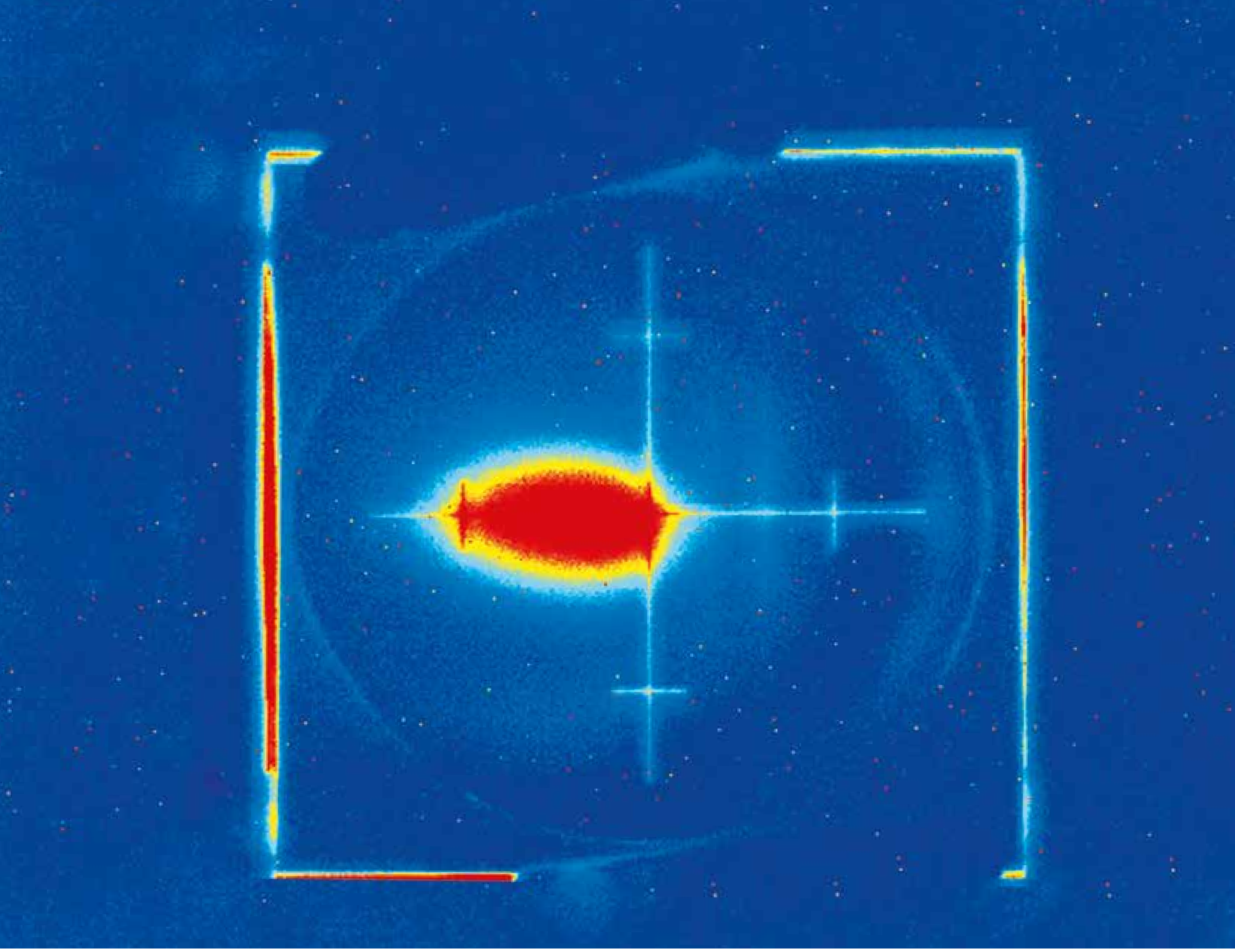

PHOTON SCIENCE 2014.

Highlights and Annual Report

Accelerators | Photon Science | Particle Physics

Deutsches Elektronen-Synchrotron
A Research Centre of the Helmholtz Association

EMBL

PIER

Helmholtz-Zentrum Geesthacht
Centre for Materials and Coastal Research

MAX-PLANCK-GESELLSCHAFT

UHH
Universität Hamburg
DER FORSCHUNG | DER LEHRE | DER BILDUNG

European XFEL

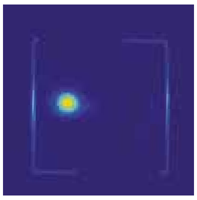

Cover

First Lasing of FLASH2 at DESY. Cross section of the SASE beam measured with a Ce:YAG screen behind the undulator line on 20 August 2014 . The picture on the left shows the optimised lasing spot measured 4 days later.
More information on the first lasing of FLASH2 can be found on page 15.

PHOTON SCIENCE 2014.

Highlights and Annual Report

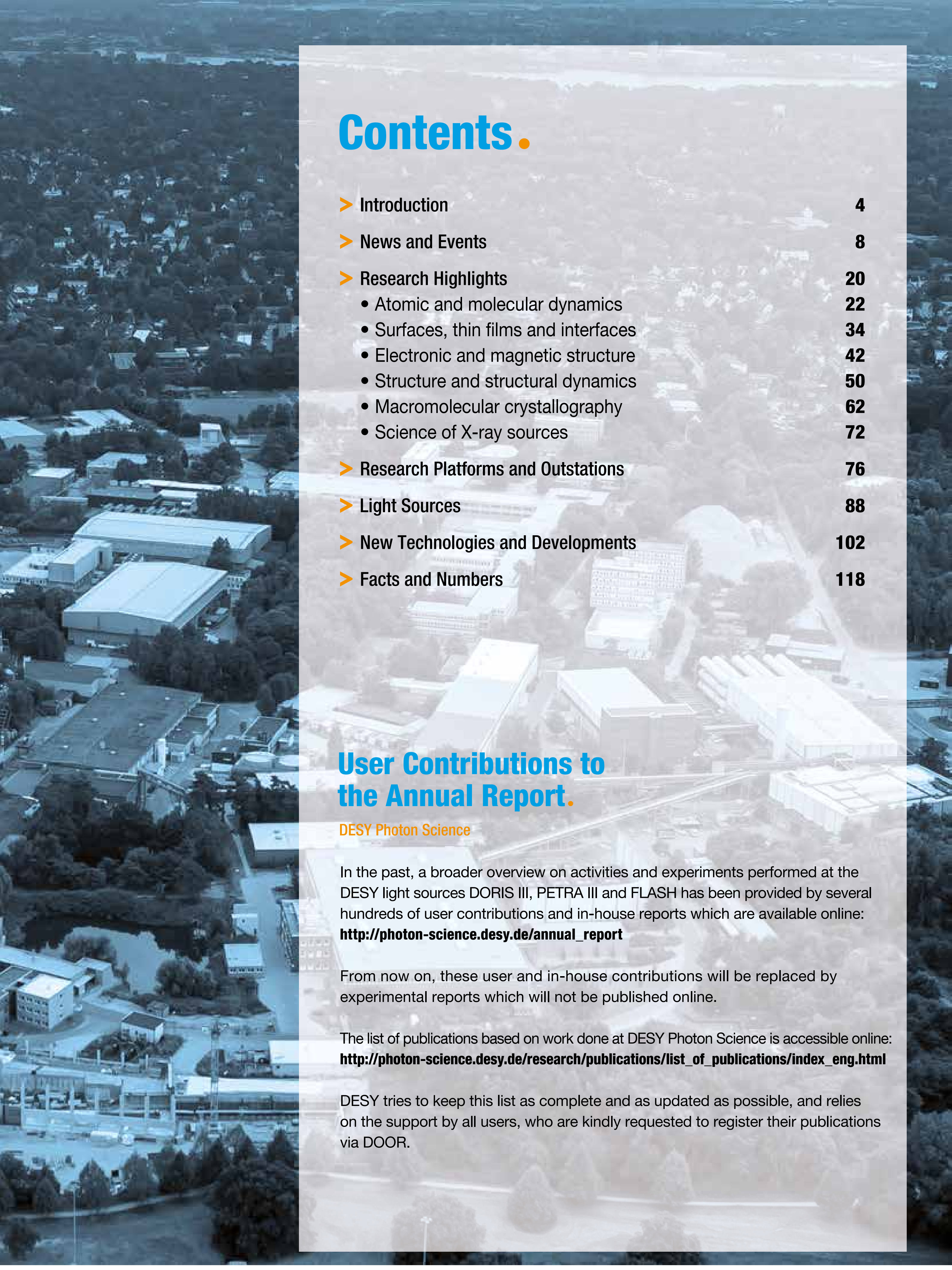

Contents.

- Introduction 4
- News and Events 8
- Research Highlights 20
  - Atomic and molecular dynamics 22
  - Surfaces, thin films and interfaces 34
  - Electronic and magnetic structure 42
  - Structure and structural dynamics 50
  - Macromolecular crystallography 62
  - Science of X-ray sources 72
- Research Platforms and Outstations 76
- Light Sources 88
- New Technologies and Developments 102
- Facts and Numbers 118

User Contributions to the Annual Report.

DESY Photon Science

In the past, a broader overview on activities and experiments performed at the DESY light sources DORIS III, PETRA III and FLASH has been provided by several hundreds of user contributions and in-house reports which are available online:
http://photon-science.desy.de/annual_report

From now on, these user and in-house contributions will be replaced by experimental reports which will not be published online.

The list of publications based on work done at DESY Photon Science is accessible online:
http://photon-science.desy.de/research/publications/list_of_publications/index_eng.html

DESY tries to keep this list as complete and as updated as possible, and relies on the support by all users, who are kindly requested to register their publications via DOOR.

The year 2014 at DESY.

Chairman’s foreword

2014, the International Year of Crystallography, has been a very successful year for DESY Photon Science.

New user facilities are being developed and new research centres are being established at DESY that exploit the unique properties of the DESY light sources, like the interdisciplinary Centre for Structural Systems Biology (CSSB). All these projects are under construction now, shaping the future of the DESY campus.

The construction of the PETRA III extensions is making rapid progress. On September 15, a tandem topping-out ceremony for both extension halls took place with the participation of Dr. Beatrix Vierkorn-Rudolph, BMBF representative and chair of the DESY Stiftungsrat, and Dr. Dorothee Stapelfeldt, the Second Mayor of Hamburg. Thanks to the excellent work of Dr. Wolfgang Drube’s project team all technical developments are on time and on specification.

At FLASH2, the extension of the free-electron laser (FEL) FLASH, a major milestone has been reached: On 20 August at 20:37, the accelerator team was able to produce the first laser light in the new FEL line. Simultaneously FLASH1, FLASH´s first FEL line, was provided with electron bunches from the same accelerator in the user mode without restrictions. With this remarkable achievement by the project team around Dr. Bart Faatz and the accelerator team around Dr. Siegfried Schreiber, FLASH is the world´s first FEL that serves two FEL lines simultaneously, a world-wide breakthrough on the way to FEL multi-user facilities.

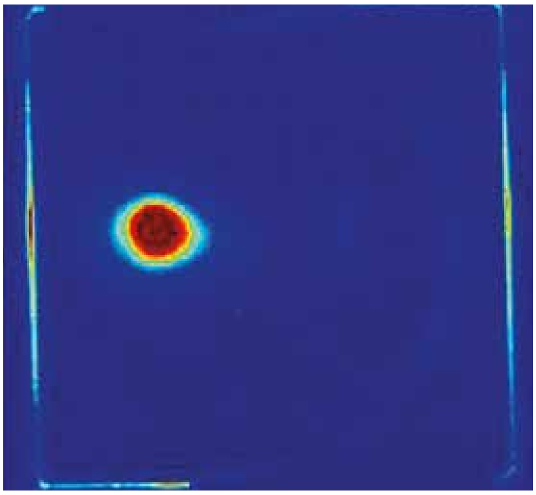

First lasing at 42 nm at FLASH2 during parallel operation with FLASH1. For the first time pulse trains of radiation at different wavelength and pulse parameters were produced in two different undulators sharing the same linear accelerator.

This achievement is of course most important for the European XFEL presently under construction. A major part of the infrastructure, the electron injector and the RF system, has already been installed in the tunnel. The first six accelerator modules are installed and the serial production of further modules is running continuously. The European XFEL teams are working hard to achieve the goal of switching on the accelerator in the summer of 2016.

Installation of one of the first accelerator modules in the tunnel of the European XFEL by workers of the DESY-led Accelerator Consortium.

With the new facilities, the work within the Photon Science division will increase in scale and complexity. For that reason we are very happy to welcome Professor Christian Schroer and Professor Wilfried Wurth as new leading scientists and scientific heads of PETRA III and FLASH, respectively. Both of them have been users at the DESY light sources for a long time and have made seminal contributions to science and instrumentation.

In future DESY will take a more strategic approach to technology transfer. To better leverage the potential for innovation at DESY, the Senate of Hamburg, DESY and the University of

Hamburg decided to build up a new business incubator on campus. With this innovation centre, enterprise foundations will be fostered and facilitated and start-ups will get support within an inspiring scientific and technological environment.

Meanwhile, two start-up companies initiated by DESY scientists are being co-funded by the Helmholtz Association. The X-Spectrum company will enter the market with a high-technology X-ray detector, and Class 5 Photonics will build very flexible femtosecond-lasers generating short pulses with high performance.

Helmut Dosch, the Chairman of the DESY Board of Directors, during the double topping-out celebration for the two PETRA III extension halls.

Celebrating the start of the business incubator on the DESY site (left to right): Helmut Dosch (Chairman of the DESY Board of Directors), Dorothee Stapelfeldt (Science Senator and Second Mayor of the City of Hamburg), Olaf Scholz (First Mayor of the City of Hamburg), Frank Horch (Economics Senator of the City of Hamburg), Dieter Lenzen (President of the University of Hamburg).

Thanks to the recent decisions of our funding bodies for the next five years, DESY is in an excellent position to further follow its ambitious plans. The comprehensive evaluation of DESY´s future strategy has been very successful and strongly supports DESY´s scientific roadmap.

I am happy to thank all our dedicated collaborators for their excellent work and commitment. ●

Helmut Dosch
Chairman of the DESY Board of Directors

Photon Science at DESY.

Introduction

The year 2014 was a very special one for DESY Photon Science. It marked the 50 year anniversary of the success story of research with synchrotron radiation at DESY. At DESY the experimental opportunities offered by this unique light were already recognized in 1964 at the synchrotron 'DESY'. For the first time, in a small laboratory, scientists characterized and explored the exceptional properties of this new radiation. Their pioneering work, in the so-called 'parasitic use' of a synchrotron dedicated to high energy physics, was worldwide one of the first nuclei for the growing research activities with synchrotron radiation. Right from the start DESY joined forces with scientists from strong partners like EMBL, MPG and many universities; they played a decisive role, in particular in the development of structural biology but also in many other fields.

The continuous development of the synchrotron radiation sources, e.g. using storage rings instead of synchrotrons, and in-house developments of advanced experimental stations and methods was and still is the basis enabling DESY to play a major role in this research field. The FLASH II and PETRA III extension projects currently being built, in combination with an own facility-related research programme at DESY Photon Science, are the latest steps in this direction.

The extension project FLASH II at DESY's free-electron laser FLASH already entered new territory. First laser light has been produced by the newly completed second free-electron laser line FLASH2 during parallel operation of the existing FLASH1 line. With this achievement, FLASH is the world's first free-electron laser that can serve two laser lines simultaneously and almost independently from each other. Before this breakthrough in August 2014, extensive construction work was necessary to build a tunnel for the second undulator line as well as a new experimental hall, suitable to host up to six new beamlines. At the same time the existing FEL line at FLASH was in full user operation from February 2014 on. About 50 proposals were submitted for the next beamtime allocation period, showing the urgent need for doubling the capacity of beamtime at FLASH. First user experiments at FLASH2 are expected to start at the end of 2015.

DESY – Hamburg site in July 2014.

The PETRA III extension project has also progressed significantly during this year. After a short operation period for users in January, PETRA III was shut down before the construction work started in February 2014. The civil engineering work for the two new experimental halls, located at the eastern and northern side of the existing "Max von Laue" hall was completed according to plan by the end of 2014. In parallel to these construction works the corresponding PETRA III tunnel sections had to be re-built to allow for the installation of the machine and new components for 11 new beamlines. The regular operation of all beamlines in the "Max von Laue" hall is scheduled to start in April 2015. Later in 2015 commissioning for the first beamlines in the extension should start. For the next beamtime allocation period about 670 proposals were submitted for the 11 DESY and HZG operated beamlines, signalling an even bigger interest in performing experiments at PETRA III than before the shutdown. Also during this year exciting research results have already been published in high-ranked journals, you will find examples in this brochure, demonstrating the excellent capabilities of PETRA III.

The establishment of the Centre for Structural Systems Biology (CSSB) is another new development on the DESY campus. The multidisciplinary and long-standing expertise of nine partners will be bundled in the field of structural biology and infection research. By this networked approach the participating institutes aim for a deeper understanding of the extremely complex questions at the root of infection processes. The foundation stone for the new CSSB building was laid in a ceremony by the end of August 2014 in the presence of the Hamburg senator for science and research. The construction work of the building, in direct neighbourhood to the PETRA III experimental halls, is advancing very well.

The DESY NanoLab, a facility for DESY Photon Science users and in-house scientists, will be a new component of the attractive offers on the DESY site. The installation of ‘made-to-measure’ equipment for structural and chemical characterization on the nanoscale made further progress, thus access to some of the DESY NanoLab techniques will be offered to the general Photon Science users already for beamtimes starting in 2015.

DESY Photon Science also strengthened the liasons with international institutions by initiating a number of new research projects and collaborations. One of the most remarkable ones is a joint research project ‘Frontiers in Attosecond X-ray Science: Imaging and Spectroscopy’ of four scientists from CFEL/DESY, the DESY machine division, Arizona State University and University of Hamburg. The European Research Council ERC granted 14 M€ to this ambitious project for the coming six years.

All research activities of DESY were evaluated in spring of this year by the Helmholtz association for the third time in the framework of the ‘Programme-oriented funding’ (POF III).

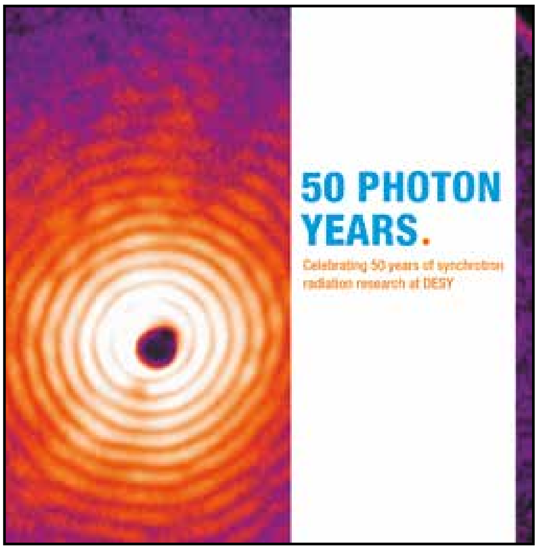

Edgar Weckert, Director Photon Science.

DESY Photon Science was very well evaluated, thus securing an excellent basis for the next five years. However, activities at Photon Science at DESY as well as at other large photon sources in Germany need a wider, long-term horizon. For this reason, a road map for the following 15–20 years is currently in preparation taking also into account the European context. We are confident that the new road map will bring us one step closer to our great goal: the next successful 50 years of research with synchrotron and FEL radiation at DESY.

Finally, I would like to thank all colleagues at DESY and users for their effort and continuous support. Let me wish all of you a personally and scientifically most successful and exciting year 2015.

Edgar Weckert
Director Photon Science

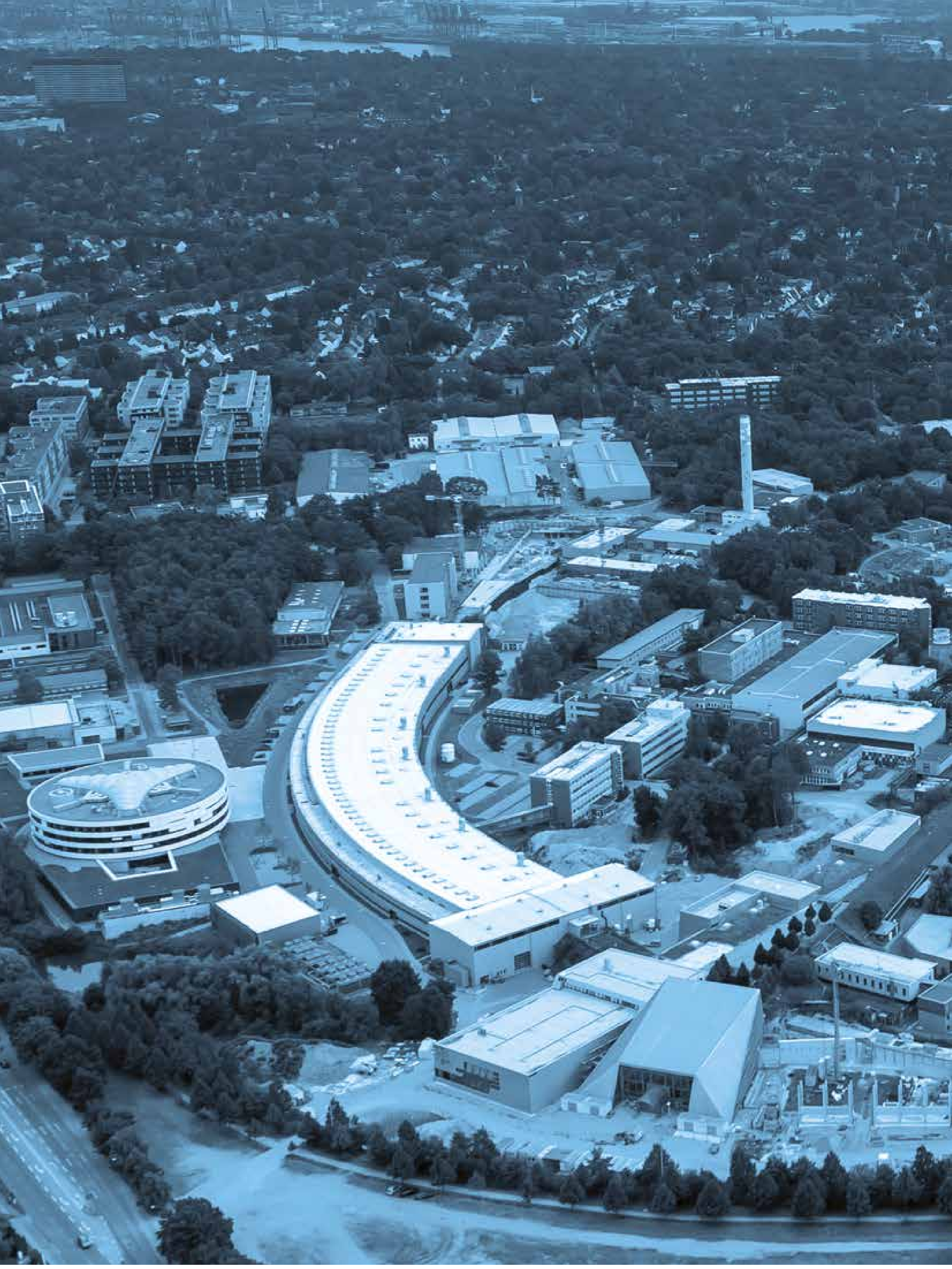

News and Events

News and Events.

A busy year 2014

January

10 January:
Start-up for the Centre for Structural Systems Biology
After a preparatory phase of two years conducted by a task force chaired by Chris Meier from University of Hamburg, the scientific committee for the new Centre for Structural Systems Biology (CSSB) took up work. It consists of one representative from each of the nine partner institutions. In its constituent meeting on 10 January 2014, Matthias Wilmanns, Head of EMBL Hamburg, was appointed founding research director. Head of the administrative office is Ina Plettner.

The goal of the interdisciplinary research centre is to understand the molecular interactions within living cells, with special focus on the investigation of pathogens. This requires the systematic analysis of the molecular building blocks, architecture, and control mechanisms of biological systems. For this aim, the CSSB scientists will use a broad range of experimental techniques, including electron microscopy and synchrotron radiation related techniques at the state-of-the-art X-ray radiation source PETRA III. The latter provides very high resolution insight down to atomic details. Moreover, the free-electron laser FLASH and the currently constructed European XFEL will offer new possibilities to observe in great detail the development of dynamic biological processes. This will help the scientists to understand the interaction of pathogens with their hosts in order to find targets for new medication, diagnostics, and vaccines.

Matthias Wilmanns (EMBL).

23 January:
Bjørn H. Wiik Prizes 2012 and 2013
In a common ceremony the Prize Committee presented a prize for the year 2012 to Kerstin Tackmann, who is working at the DESY ATLAS group honouring her contributions to the Higgs particle discovery at the ATLAS detector at LHC. The Bjørn H. Wiik Prize 2013 was awarded to Ralf Röhlsberger, DESY Photon Science. He received the award for fundamental quantum mechanical experiments with X-rays, which were mainly carried out at PETRA III. To observe for example the electromagnetically induced transparency, he used a nanometre sized platinum cavity to induce cooperative emission of many iron atoms and made use of experimental methods derived from Mössbauer spectroscopy. The novel measuring procedure opens up manifold possibilities for additional experiments, e.g. in quantum information technology.

The Bjørn H. Wiik Prize is awarded to young scientists and engineers for outstanding contributions to DESY's research programme or for technical developments that notably advance projects at DESY. The award is endowed with 3000 €. It is funded from the proceeds of donations collected in 1999 to acknowledge Bjørn H. Wiik's lifetime achievements.

At the Bjørn H. Wiik Prize ceremony.
From left to right: Eckhard Elsen, chair of the prize committee, Kerstin Tackmann, Ralf Röhlsberger, and Margret Becker-Wiik, wife of Bjørn Wiik.

29-31 January:
Joint European XFEL and DESY Photon Science Users' Meeting
About 700 participants from over 25 countries attended the joint DESY Photon Science and European XFEL Users' Meeting 2014. As in the last years current and future users of the DESY light sources and of the European XFEL met to discuss latest developments and research opportunities.

The European XFEL Users' Meeting started on Wednesday with reports on the XFEL project and the related instrumental stations and a science session addressing time-dependent phenomena. In the FLASH and FEL session on Thursday, time-resolved studies of small molecules, bio-molecules, nanoparticles, and surfaces showed the capabilities already available by using the existing X-ray free-electron laser facilities. Several satellite meetings were held in the afternoon covering different topics like X-ray nano-imaging of biological and chemical systems, perspectives of Small Angle X-ray Scattering at DESY, the PETRA III extension XAFS beamline etc.

The Friday session was devoted to status reports of the operational DESY synchrotron source PETRA III and the ongoing PETRA III extension project. Presented topics ranged from novel insights into the flow of glasses and strain engineering of semiconductor nanostructures to liquid-liquid interfaces and broad DNA sensing specificity of cGAS. A poster session on Friday afternoon featuring more than 300 presentations parallel to a vendor exhibition completed the Users' Meeting 2014.

Poster session in the foyer of the CFEL building.

February

4 February:
Official start of civil construction for the PETRA III Extension halls
The civil construction of the two new extension halls for additional ten beamlines at PETRA III has officially started on 4 February. The construction work requires the complete removal of the storage ring including the concrete ring tunnel at the sites of the new halls.

The overall PETRA III extension project comprises two new experimental hall buildings on either side of the existing large experimental hall "Max von Laue". These buildings in the North and East are making use of the long straight sections and the adjacent arcs of the PETRA III storage ring. By modifying the storage ring lattice additional insertion devices for 5 beamlines in each hall can be accommodated.

The civil construction work for the PETRA III extension hall North started with removing the soil that covers the storage ring tunnel in that area.

March

19-21 March:
13th Research Course on X-ray Science

The 13th course of this series was entitled “Correlation Functions in the Time Domain: Trends in Coherent X-ray Scattering”. The course at DESY aimed at master and PhD students and provided an introduction to all fields of X-ray Photon Correlation Spectroscopy (XPCS) research and related techniques. Another aim of the course was to assemble the XPCS community to discuss progress and trends of XPCS at modern synchrotron and free-electron laser sources. A special discussion addressed the topic “XPCS at FELs” to reconsider the conditions for XPCS experiments at LCLS and the European XFEL in terms of detectors, stability, etc. The course had 75 participants mainly from Germany and 16 international speakers, all of them XPCS experts and representatives of coherence beamlines at DESY, ESRF, APS, NSLS, LCLS, and European XFEL.

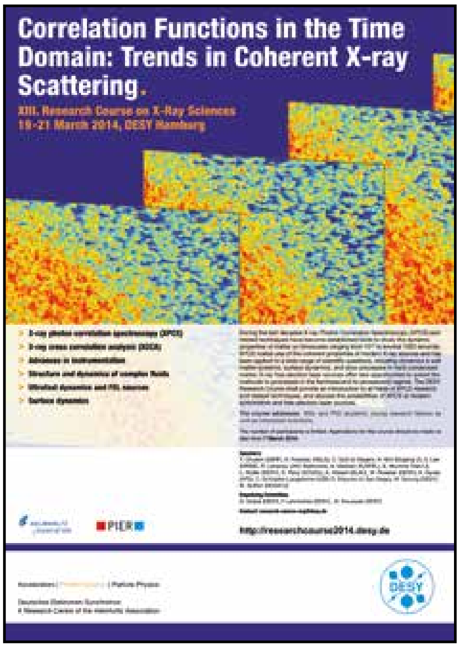

Correlation Functions in the Time Domain: Trends in Coherent X-ray Scattering.

XIII. Research Course on X-Ray Sciences
19-21 March 2014, DESY Hamburg

- X-ray photon correlation spectroscopy (XPCS)
- X-ray cross correlation analysis (XCCA)
- Advances in instrumentation
- Structure and dynamics of complex fluids
- Ultrafast dynamics and FEL sources
- Surface dynamics

http://researchcourse2014.desy.de

May

11-17 May:
International Summer School of Crystallography 2014

For a whole week the Center for Free-Electron Laser Science (CFEL) hosted 38 students attending the first International Summer School of Crystallography. The participants of 24 different nationalities, mainly PhD students, could learn the basics of crystallography. The summer school as part of the International Year of Crystallography especially dived into the mathematical background of these techniques and of related commonly used computer programs. The organizers could win Carmelo Giacovazzo from the University of Bari as tutor, who is a distinguished expert in the field of crystallography and who guided the participants through theory and history of it.

ISSC14

Hamburg, Germany
11. – 17. May 2014

First International
Summer School of Crystallography

Tutor: Prof. Carmelo Giacovazzo

Apply now:

Speakers
Prof. Henry Chapman (CFEL)
Dr. Thomas Schneider (EMBL)
Dr. Gleb Bourenkov (EMBL)
Dr. Thomas White (CFEL)
Dr. Adrian Mancuso (European XFEL)

June

2-4 June:
Science 3D Workshop

The Science 3D workshop was jointly organized by the Helmholtz-Zentrum Geesthacht (HZG), DESY, and the EU project PaNdata ODI. The The workshop at DESY served as users' meeting of the HZG imaging and tomography instruments at PETRA III and as kick-off meeting for one of the “Virtual Laboratories” within PaNdata ODI which is related to open access to tomography datasets and is being realized as a Science 3D project.

The first day of the workshop was devoted to users' experiments and scientific highlights. The goal was to present and to illustrate the results in such a way that non-experts could understand the basic ideas and concepts along the lines of the Open Access Science 3D project. This was especially aiming at school representatives in the audience who were interested in using the open access tomography database in school teaching projects. The second day focused on the HZG beamlines at PETRA III and new experimental and technological developments. The third day finally covered aspects related to new tools to optimize the data processing workflow, including software, data management, and computing resources available for users of the HZG beamlines. The workshop was well attended by about 50 participants.

A typical Science 3D object: Caecilian jaw-closing mechanics.
(T. Kleinteich, University of Kiel)

July

7-11 July:
13th International Conference on Surface X-Ray and Neutron Scattering

The 13th edition of the International Conference on Surface X-Ray and Neutron Scattering (SXNS13) took place at DESY. The organizers could welcome about 140 international participants and the conference focused on the application of surface sensitive neutron and X-ray scattering methods to investigate surfaces and interfaces in a wide range of areas in physics, chemistry, and biology. The intention was to bring together scientists from the different research areas in order to exchange new exciting scientific results and recent developments. Special emphasis was put on *in situ* characterization under processing or operation conditions.

13th Surface X-Ray and Neutron Scattering Conference

SXNS13

7 -11 July 2014

DESY, Hamburg, Germany

Exploring Surfaces and Interfaces with X-ray and Neutron Scattering Methods

www.sxns13.de

Poster prize award ceremony at the SXNS13.
From left to right: Akhil Tayal (University Indore India), Andreas Stierle (conference chair, DESY), Hsin-Yi Chen (University Göttingen), Bridget Murphy (conference co-chair, University of Kiel).

July

18 July:
Leading scientists appointed for PETRA III and FLASH

Christian Schroer and Wilfried Wurth have joined the DESY team as new leading scientists. Christian Schroer assumes the leadership of the scientific programme of DESY's synchrotron radiation source PETRA III, Wilfried Wurth becomes scientific head of the free-electron laser FLASH. Both scientists have been working as users at DESY's light sources for a long time, and made important contributions in the field of instrumentation and research.

After starting his career in theoretical physics and obtaining his doctoral degree, Christian Schroer specialised in X-ray nano research and development of X-ray optics. He worked at DESY from 2004 to 2006 and then became professor at Dresden University of Technology. According to a joint appointment procedure of the University of Hamburg and DESY, he now assumes a professorship at the University of Hamburg. As new scientific head of PETRA III, Christian Schroer will closely cooperate with Oliver Seeck, who recently took over the coordination of the PETRA III experiments.

Wilfried Wurth was professor at the University of Hamburg since 2000 and now joins DESY as well. His focus is on X-ray spectroscopy, in particular for the investigation of ultrafast processes like the real-time observation of chemical reactions at surfaces and the dynamics of electrons in solids and at interfaces. For a long time Wilfried Wurth has been one of the most prominent researchers at FLASH and, from 2007 to 2013, he was also spokesperson of the BMBF priority programme FLASH. This first priority programme in the field of condensed matter was created to bundle research at the free-electron laser within the framework of collaborative project funding.

Christian Schroer (left) and Wilfried Wurth.

22 July:
Start of DESY Summer Student Programme 2014

This year DESY could welcome a record number of 117 summer students at both its locations in Hamburg and Zeuthen. During eight weeks, the junior researchers from 28 nations got a practical insight into research at Germany's largest accelerator centre. With the summer student programme DESY offers one of the largest and most international summer schools throughout Germany.

All summer students 2014 attending the courses at the DESY Campus Hamburg.

15 female and 24 male students were selected for the part of the programme dedicated to photon science. These 39 students came from Armenia, Austria, Brazil, China, Germany, Spain, United Kingdom, Hungary, Italy, Pakistan, Poland, Portugal, Russia, Slovakia, Serbia, Thailand, Turkey, Ukraine, and the United States. They attended a special lecture series on research with photons at DESY and worked on small projects within research groups at PETRA III, FLASH, CFEL, European XFEL and University of Hamburg.

The DESY summer students 2014 working in the field of Photon Science.

August

1 August:
CFEL scientists received two prestigious ERC Grants

The European Research Council (ERC) supports the project "Frontiers in Attosecond X-ray Science: Imaging and Spectroscopy (AXSIS)" of Franz Kärtner (CFEL), Henry Chapman (CFEL), Ralph Aßmann (DESY) and Petra Fromme (Arizona State University) by an ERC Synergy Grant. The project receives 14 million Euros for the coming six years. The application was winning against more than 440 competitors. Within the project the four scientists will develop a stroboscopic technique using ultra-short light flashes in the attosecond range to record ultra-fast processes in slow motion.


Petra Fromme
(Arizona State University).


Ralph Aßmann
(DESY).


Henry Chapman
(CFEL, DESY, University
of Hamburg).


Franz Kärtner
(CFEL, DESY, University
of Hamburg).


Jochen Küpper
(CFEL, DESY, University
of Hamburg).

A second grant was awarded to Jochen Küpper (CFEL) who receives two million Euros. The council supports Küpper's project entitled "Controlling the Motion of Complex Molecules and Particles (COMOTION)" by an ERC Consolidator Grant for five years. The aim of the project is to develop methods to control for instance transport, sorting, and aligning of complex molecules like peptides and proteins, but also of larger objects, like virus particles or picoplankton.

20 August:
First simultaneous lasing of two FEL lines at FLASH

With its superconducting technology, the free-electron laser FLASH is able to deliver up to 8000 bunches per second in bursts of 800 bunches with a repetition rate of 10 Hz in normal user operation. Not many users really can make use of such long pulse trains. Therefore, the machine can be utilized more efficiently if it is able to deliver a part of the photon pulses to a different user by sharing the particle beam between two FEL undulators. Since each user has specific demands on wavelength and pulse duration, the parameters for the different users need to be tunable.

In August the FLASH team achieved a milestone towards this direction in the frame of the FLASH II project. For the first time pulse trains of radiation at different wavelength and different pulse parameters, such as repetition rate, number of bunches and pulse length were produced in two different undulators sharing the same linear accelerator.

Parallel operation of FLASH1 and FLASH2 was first achieved on 20 August, when FLASH1 was running with 250 bunches at 13.5 nm and FLASH2 was lasing with six bunches at about 42 nm. A few days later, the wavelength was confirmed by spectrometer measurements and while FLASH1 was in lasing operation, the wavelength at FLASH2 was successfully changed from 42 to 23.5 nm by changing the undulator gap.

Since first lasing was achieved, the results were repeated several times at different electron beam energies, resulting in a wavelength range between 12 and 42 nm so far. FLASH2 was operated varying between single bunch and 400 bunches at 1 MHz with a repetition rate of 10 Hz. At the longer wavelengths, gain curves have been measured, showing that


Aerial view of the FLASH facility. On the left the extension, consisting of a new tunnel with undulator and experimental hall.

saturation of the intensity has been reached. The remainder of the year was dedicated to establishing the limits of the accessible parameter range that can be offered to users. In 2015, diagnostics for radiation pulse characterization will be installed in the tunnel and in the new experimental hall. In addition, the first two experimental stations will be installed. After a commissioning phase, the first pilot experiment will take place in 2015, after which the facility will be opened to users for standard operation in 2016.

The 30 m long undulator in the FLASH2 FEL line, consisting of 12 segments, which produces the FEL radiation.

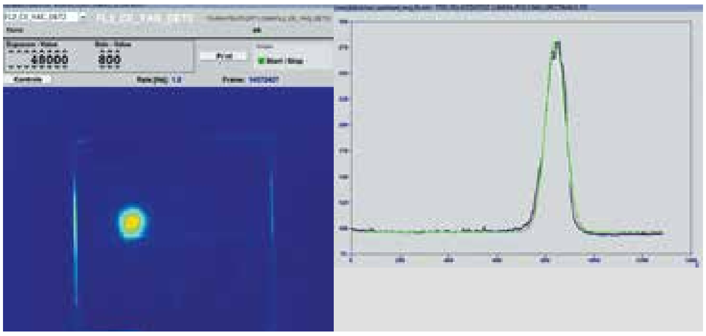

Lasing at 42 nm. On the left, the photon beam is shown on the YAG screen. On the right, the spectral measurement is shown with a centre wavelength of 42 nm and a bandwidth of ~2%.

29 August:
Foundation stone ceremony for the Centre for Structural Systems Biology

The unique interdisciplinary Centre for Structural Systems Biology (CSSB) is starting to take shape. On August 29 Hamburg's science senator Dorothee Stapelfeldt, secretary of state in Lower Saxony's science ministry Andrea Hoops, and CSSB founding director Matthias Wilmanns laid the foundation stone for the centre's new research building in presence of representatives from the nine CSSB partner institutions.

The CSSB was officially launched at the beginning of this year. From a total of eleven planned research groups, six have already been established. The group leaders have been appointed, the CSSB has been successful in attracting top researchers from, among others, Canada, Austria and Great Britain for these appointments.

The CSSB research building designed by the architects Hammes and Krause will be located in close proximity to the PETRA III experimental hall "Max von Laue". The three storey laboratory and office building will offer space of about 11000 square metres for 180 scientists.

Architect's view of the new CSSB building.

Laying of the foundation stone. From left to right: Matthias Wilmanns (CSSB founding research director), Ian Mattai (Director General EMBL Heidelberg), Jan Grapentin (Ministerial Counsellor BMBF), Verena Börschmann (DESY construction manager), Dirk Heinz (scientific director Helmholtz Centre for infection research), Bernd Kretschmär (general foreman W&F), Christian Scherf (DESY director of administration), Dorothee Stapelfeldt (science senator city of Hamburg), Rolf Horstmann (Bernhard-Nocht-Institute Hamburg), Andrea Hoops (secretary of state science ministry Lower Saxony), and Heinrich Gräner (University of Hamburg, dean of MIN faculty).

September

1 September:
Helmholtz Association funds two DESY spin-off enterprises

Two start-up companies initiated by DESY scientists were funded by the "Helmholtz Enterprise" support programme of the Helmholtz Association: The company "Class 5 Photonics" will build very flexible tuneable femtosecond-lasers generating short pulses with high pulse rates and performance. This joint spin-off of DESY and Helmholtz Institute Jena will be financed with almost 130 000 Euros. With the underlying concept the future entrepreneurs also recently won the Start-up Challenge prize of the German Competence Networks for Optical Technologies OptecNet.

The second company named "X-Spectrum" enters the market with a high-technology X-ray detector and will receive 100 000 Euros. "X-Spectrum" was founded in July 2014 by five members of the DESY detector development group (FS-DS), with DESY being 10 % shareholder of the new enterprise. The scientists developed an X-ray area detector named LAMBDA, which stands for Large Area Medipix Based Detector Array. It offers extremely high spatial resolution and high acquisition rates. The nine by three centimetres large active area of the LAMBDA detector is equipped with 750 000 pixel elements each of 55 micrometre size and can take up to 2000 images per second. Each pixel is able to detect and count single photons, but can also handle rates of more than 500 000 photons per second. This very high dynamic range is complemented with the possibility to measure the energy of the detected X-ray photons, i.e. practically taking colour pictures.

Mark J. Prandolini, Robert Riedel, and Michael Schulz (from left to right) from the Class 5 Photonics team.

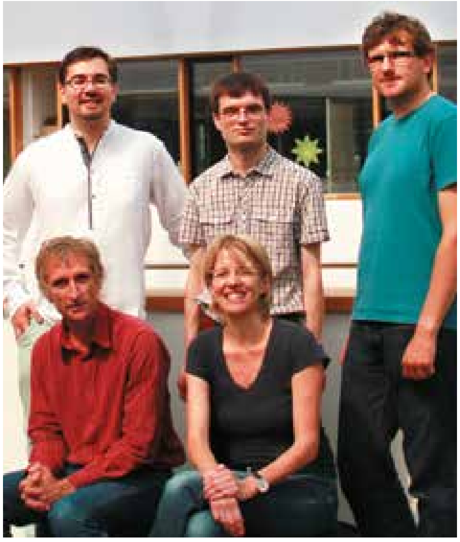

The team of X-Spectrum: (back) Julian Becker, David Pennicard, and Florian Pithan, (front) Heinz Graafsma, and Stefanie Jack.

15 September:
Double topping-out celebration for two PETRA III Extension halls

On 15 September DESY could simultaneously celebrate the topping-out of two new experimental halls for PETRA III.

PETRA III, as the world´s most brilliant X-ray source is heavily over-booked since becoming operational in 2009. The PETRA III Extension Project started in December 2013 to give more scientists access to the unique experimental possibilities of this light source and to broaden its research portfolio of offered experimental techniques. With a total ground floor of about 6000 square metres the two new experimental halls provide enough space for technical installations of up to ten additional beam lines, including additional 1400 square metres of office and laboratory space for the scientists. Beamlines and instrumentation in the new halls are under construction in close cooperation with the future user community and are, in part, collaborative research projects. Three of the future beamlines will be constructed as an international partnership with Sweden, India, and Russia.

Since February approximately 170 metres of the PETRA tunnel and accelerator were dismantled in order to start building the new experimental halls. In August, reconstruction of the accelerator sections, equipped with special magnet structures for producing X-ray radiation, begun within the already completed new tunnel areas. In September the building shells of the two halls were completed and during the next construction phase of the experimental halls in December 2014 the accelerator at the same time started to resume operation. The experiments in the PETRA III experimental hall "Max von Laue" will re-start in April 2015 and the first experimental stations in the new halls shall gradually become ready for operation from autumn 2015 until beginning of 2016.

Part of the extension's total budget of 80 million Euros comes from the expansion funds of the Helmholtz Association. Other funding is from the Federal Ministry of Research, from the Free and Hanseatic City of Hamburg and from DESY. Approximately one third of the total costs are covered by collaborative partners from Germany and abroad.

Site foreman Michael Telschow raises his glass to the new experimental hall.

October

20 October:
DESY launches Photon Science teacher training programme

DESY launched its teacher training programme “Lehrerfortbildung@DESY” in the field of research with photons. Eight teachers from the greater area of Hamburg took part in a one week training course during the autumn holidays. The teachers were directly integrated into current research projects. The aim of the programme is to motivate subject teachers to enhance their lessons with current science themes and provide them with the necessary pedagogical knowledge to communicate the fascination and fun of modern science to their pupils. In the future it is planned to offer this teacher training course every year during the autumn holidays and to develop it further.

Participants of the Photon Science teacher training programme.

28 October:
Celebrating 50 years of synchrotron radiation research at DESY

It was in 1964, when the first measurements started at the just completed ring accelerator DESY to characterise its inevitable synchrotron radiation. Initiated by these first experiments and visionary decisions of the then directorate, the use of synchrotron radiation rapidly took up speed at DESY and all over the world. 250 guests gathered at a symposium to celebrate the 50th anniversary of synchrotron radiation at DESY. In view of the many exciting perspectives presently developing in the field of research with photons at the DESY campus the symposium did not only recall the past but most of the talks given by Helmut Dosch, Stefan Eisebitt (TU Berlin), Edgar Weckert, Wilfried Wurth, and Christian Schroer rather addressed present and future opportunities.

The guests of the symposium 50 Photon Years at DESY.

30 October:
PhD thesis prize for Stephan Stern and Tigran Kalaydzhyan

The award of the Association of the Friends and Sponsors of DESY 2014 is shared in equal parts by Stephan Stern, DESY (CFEL) and University of Hamburg, and Tigran Kalaydzhyan, DESY (Theory) and University of Hamburg.

In his thesis titled „Controlled Molecules for X-ray Diffraction Experiments at Free-Electron Lasers“, Stephan Stern recorded the coherent X-ray diffraction of many identical molecules by using a special procedure for the spatial alignment. In his analysis of a specific molecule, Stern successfully deduced the size and alignment angle of the molecule in the laboratory. His thesis makes important contributions to single molecule structure determination and to possible ways of following structure changes along chemical reactions with X-ray lasers.

Tigran Kalaydzhyan graduated in the Theory Group at DESY. The title of his thesis is „Quark-gluon plasma in strong magnetic fields“ and deals with the study of the properties of elementary matter at extremely high temperatures and in the presence of strong magnetic fields.

Stephan Stern (left) and Tigran Kalaydzhyan.

November

27-28 November:
DESY and EMBL endorse their partnership

The interdisciplinary cooperation of DESY and the European Molecular Biology Laboratory (EMBL) in the field of research with photons in life science is a long-lasting and extremely successful story. The basis of this cooperation was now prolonged by a new Framework Institutional Partnership Agreement which aims to continue and strengthen the construction and operation of life science oriented research infrastructures on the DESY campus.

On the occasion of a symposium celebrating the 40th anniversary of the EMBL Hamburg Outstation the new agreement was signed by Silke Schumacher, Director International Relations of EMBL and by the Chairman of the DESY Board of Directors, Helmut Dosch.

Helmut Dosch and Silke Schumacher signing the partnership agreement between DESY and EMBL.

December

10 December:
Leibniz Prize for Henry Chapman

The German research foundation Deutsche Forschungsgemeinschaft (DFG) announced that Henry Chapman (CFEL, DESY, University of Hamburg) will be awarded one of the prestigious Gottfried Wilhelm Leibniz Prizes 2015. This important German research award honours outstanding scientists. Henry Chapman receives the 2.5-Million-Euro prize for his pioneering work in the development of femtosecond crystallography which allows to decode the structure of complex biomolecules in its natural environment at the atomic level with the help of X-ray lasers.

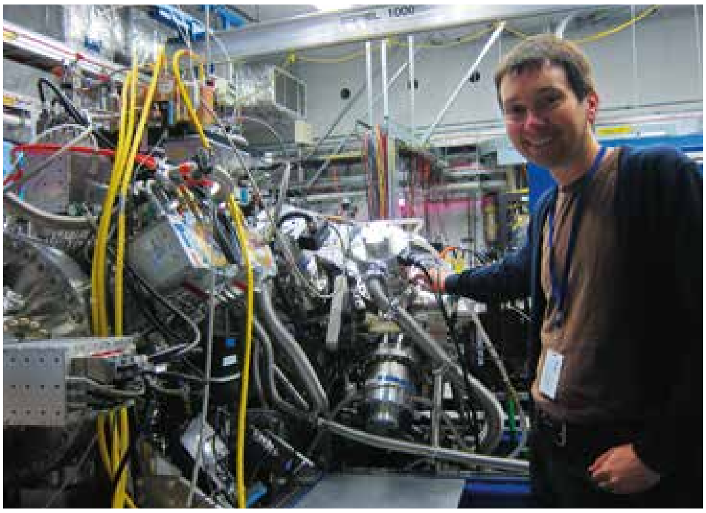

Henry Chapman.

Research Highlights.

Atomic and molecular dynamics

- Mysterious gas giants 22
- Sacrificial tamper layer 24
- Electron rearrangement in dissociating molecules 26
- Single quantum states and defined wave packets 28
- Boiling water with light faster than you can blink 30
- When is a molecule a molecule 32

Surfaces, thin films and interfaces

- High-energy SXRD for fast surface structure determination 34
- Nanoscopic control of tandem polymer solar cells 36
- Lipid molecules in driven motion 38
- Degradation in polymeric solar cells 40

Electronic and magnetic structure

- Chemical insight into resistive switching devices by HAXPES 42
- Twisted X-rays reveal spin excitations in magnetic materials 44
- Screening effects studied by VUV Raman spectroscopy 46
- Creating and controlling metastable states 48

Structure and structural dynamics

- Detection of a water-reservoir in the Earth’s deep mantle 50
- Unexpected stable stoichiometries of sodium chlorides under pressure 52
- Strong cellulose filaments with tunable nano structure 54
- Imaging living cells at nanometre resolution 56
- Decoding the nanostructure of advanced TiAl alloys 58
- From molecular complexes to nanocrystals 60

Macromolecular crystallography

- A first glimpse of photosynthesis in action 62
- First human membrane protein solved using X-FEL radiation 64
- Guiding neural networks 66
- Small beams for small crystals 68
- Macromolecular serial crystallography at PETRA III 70

Science of X-ray sources

- Electron beams from 100.000 silicon tips 72
- Pulse-by-pulse interferometry at PETRA III 74

Mysterious gas giants.

X-ray laser FLASH spies deep into giant gas planets

The large gas planets of our solar system cloak themselves with impenetrable layers of cloud, successfully keeping their secrets hidden. We know that the gas giants Jupiter and Saturn are mostly made up of hydrogen and helium – the two lightest elements. The gas gets denser as the depth increases, and most of the hydrogen must be liquid. But whether the gas giants possess a solid core is as uncertain as the exact structure of their outer layers.

Laboratory studies can help to improve our models of these planets. Using FLASH, we took a sneak peek deep into the lower atmospheric layers of these planets. The observations reveal how liquid hydrogen becomes a plasma and they provide information on the material's thermal conductivity and its internal energy exchange, which are important ingredients for planetary models.

Knowledge of thermodynamic properties of matter under extreme conditions is critical for modelling stellar and planetary interiors [1]. Of central importance are the electron-ion collision and equilibration times that determine the microscopic properties of matter related to reflectivity and thermal conductivity. On a macroscopic scale, they affect the depth of mixing layers in Jovian planets [2]. Insufficient knowledge of the transport properties in dense matter limits our ability to accurately model such complex systems.

Precise determination of the heat transfer rate from electrons to ions and atoms in dense matter requires the preparation of a uniform sample and sub-picosecond probing. To investigate dynamic processes of warm dense matter on such short time scales, pump-probe experiments are necessary, where a first pulse generates an excited state that is subsequently probed by a second pulse at well-defined time delays.

The split-and-delay capability [3] of FLASH's BL2 (see Fig. 1) is used to measure ultrafast heating of dense matter. We produce two FEL pulses of comparable intensity to volumetrically heat dense cryogenic hydrogen and probe it by soft X-ray scattering.

We employ 92 eV soft X-ray radiation to be in a regime where the photon energy is well above the plasma frequency for hydrogen at liquid density. This leads to a high penetration depth with an absorption length $l_{abs} = 11\ \mu\text{m}$, comparable to the hydrogen jet radius of $\sim 9\ \mu\text{m}$. The initial energy deposition via photo absorption is not uniform, as FEL intensities of I_0 are present at the target front side, compared to only $\sim 0.2 I_0$ at the target rear side. Yet, the generated photo-electrons with kinetic energies of 78 eV are capable of impact-ionizing several molecules and atoms within the FEL pulse duration [5]. This leads to further ionization, molecular heating, and expansion, as well as breaking of the covalent H-H bond (dissociation). All these effects lead to an almost homogeneous electron heating throughout the sample.

To describe the temporal variation of the measured scattering intensity, we have performed one-dimensional Lagrangian radiation-hydrodynamic simulations with the code HELIOS [6]. HELIOS solves the equations of motion for a fluid. We compare the predictions by HELIOS using two different equation of state (EOS) models: one model calculates the ionization via a Saha model [6], while the second one uses a Thomas-Fermi model as implemented in the quotidian EOS (QEOS [7]).

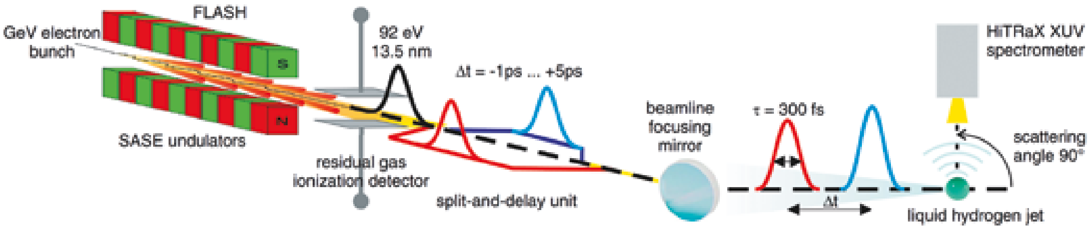

Figure 1

Schematic of the experimental setup. Horizontally polarized FEL radiation at 92 eV, 10 Hz pulse repetition rate, and duration of $\tau \lesssim 300$ fs is geometrically divided by a split-and-delay unit [3]. The pulses are subsequently focused to a $20 \times 30\ \mu\text{m}^2$ spot using an ellipsoidal mirror, yielding intensities up to $\sim 27\ \text{TW/cm}^2$ for the variable-delay branch and $\sim 19\ \text{TW/cm}^2$ for the fixed branch. The FEL pulses hit a $\sim 9\ \mu\text{m}$ radius hydrogen jet with mass density of $0.08\ \text{g/cm}^3$ and temperature of 20 K. Scattering is collected at 90° relative to the incident FEL radiation in the vertical plane. To discriminate between the scattered XUV photons and plasma self-emission or energetic particles, we employ a variable line space grating spectrograph [4]. (Copyright APS publishing group)

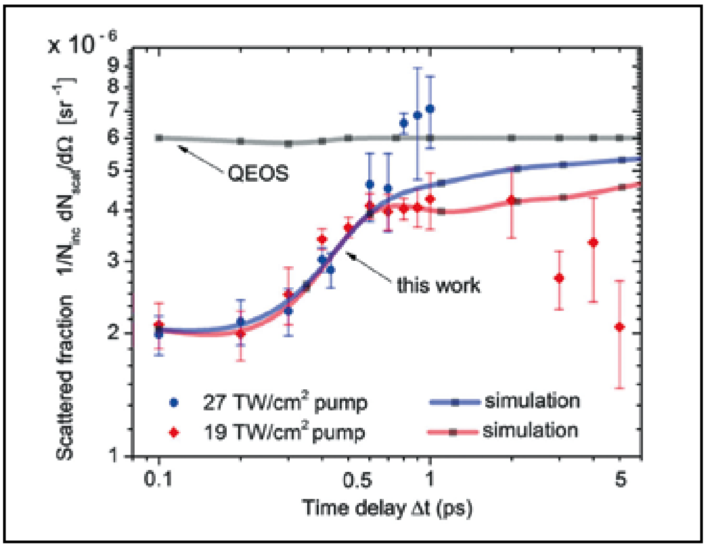

Figure 2

Temporal evolution of measured and simulated X-ray scattering. A total of 300 exposures were grouped by delay, their error bars resemble their root mean square deviations. For the blue data points, ranging from Δt = 0 ps to 1 ps only, the more intense 27 TW/cm² pulse pumps the target, while it is probed by the 19 TW/cm² pulse. The red data points, ranging from 0 to 5 ps, resemble the inverse case with a less intense pump (19 TW/cm²) than probe (27 TW/cm²) pulse. In both cases, the signal increases within the first ps. For the more intense pump the amplitude is larger. The blue and red lines show simulations based on the Saha model. In contrast, simulations based on QEOS (gray) predict no delay dependence for the structure factor *S(0)*. (Copyright APS publishing group)

Driving hydrogen from initially cryogenic molecular condensed matter to an ideal plasma poses several challenges to the employed models. We evaluated ionization models for the equation of state data and showed that a Saha-like model is superior to a Thomas-Fermi approach as implemented in the QEOS. The latter predicts about one order of magnitude too short equilibration times, generating a plasma with a structure factor *S(0)* ~ 1 well within the FEL pulse duration. Hence, a pump-probe delay dependence for *S(0)* is not predicted using the QEOS (see Fig. 2). The QEOS predicts an initially metallic state with ~40 % ionization, in contrast to experimental data being in agreement with only 4–6 % ionization.

Figure 2 shows the experimental data in comparison with the different simulations. The total scattered fraction of FEL photons rises to a peak value of 4 × 10^{-6} within 0.9 ps, remaining constant for delays up to 2 ps. We show that this dynamic behaviour is reproduced with a Saha model for ionization. In contrast, simulations using QEOS show quasi-instantaneous heating within the FEL pulse duration of ~300 fs, and hence no delay dependence is visible.

In principle, the QEOS model accounts for degenerate plasmas, important in the framework of warm and dense matter. However, is not accurate for the low temperatures and low atomic numbers found in the astrophysically relevant plasmas, dealt with in this work (the maximum electron temperature achieved in this experiment is T_e ~2.1 eV, the maximum ion temperature is T_i ~0.4 eV).

In summary, our experimental results have provided important insights on transport effects which lead to a better understanding of dense plasmas.

Contact: Ulf Zastrau, ulf.zastrau@uni-jena.de,
Sven Toleikis, sven.toleikis@desy.de

Authors

U. Zastrau[1,2], P. Sperling[3], M. Harmand[4], A. Becker[3], T. Bornath[3], R. Bredow[3], S. Dziarzhytski[4], T. Fennel[3], L. B. Fletcher[2], E. Förster[1,5], S. Göde[3], G. Gregori[6], V. Hilbert[1], D. Hochhaus[7], B. Holst[3], T. Laarmann[4,8], H. J. Lee[2], T. Ma[9], J. P. Mithen[6], R. Mitzner[10], C. D. Murphy[6], M. Nakatsutsumi[11], P. Neumayer[7], A. Przystawik[4], S. Roling[10], M. Schulz[4], B. Siemer[10], S. Skruszewicz[3], J. Tiggesbäumker[3], S. Toleikis[4], T. Tschentscher[11], T. White[6], M. Wöstmann[10], H. Zacharias[10], T. Döppner[9], S. H. Glenzer[2], and R. Redmer[3]

1. Friedrich-Schiller-Universität, Institut für Optik und Quantenelektronik, Max-Wien-Platz 1, 07743 Jena, Germany
2. SLAC National Accelerator Laboratory, 2575 Sand Hill Road, Menlo Park, California 94025, USA
3. Universität Rostock, Institut für Physik, 18051 Rostock, Germany
4. Deutsches Elektronen-Synchrotron DESY, Notkestrasse 85, 22607 Hamburg, Germany
5. Helmholtz-Institut Jena, Fröbelstieg 3, 07743 Jena, Germany
6. University of Oxford, Department of Physics, Clarendon Laboratory, Parks Road, Oxford OX1 3PU, United Kingdom
7. GSI Helmholtzzentrum für Schwerionenforschung, Extreme Matter Institute, 64291 Darmstadt, Germany
8. The Hamburg Centre for Ultrafast Imaging CUI, 22761 Hamburg, Germany
9. Lawrence Livermore National Laboratory, 7000 East Avenue, Livermore, California 94550, USA
10. Westfälische Wilhelms-Universität, Physikalisches Institut, Wilhelm-Klemm-Strasse 10, 48149 Münster, Germany
11. European XFEL, Albert-Einstein-Ring 19, 22761 Hamburg, Germany

Original publication

"Resolving Ultrafast Heating of Dense Cryogenic Hydrogen", Phys. Rev. Lett. 112, 105002 (2014). DOI: 10.1103/PhysRevLett.112.105002

References

1. N. Nettelmann et al., "Ab Initio Equation of State Data for Hydrogen, Helium, and Water and the Internal Structure of Jupiter", Astrophys. J. 683, 1217 (2008).
2. J. Leconte and G. Chabrier, "A new vision of giant planet interiors: Impact of double diffusive convection", Astron. Astrophys. 540, A20 (2012).
3. M. Wöstmann et al., "The XUV split-and-delay unit at beamline BL2 at FLASH", J. Phys. B 46, 164005 (2013).
4. R. R. Fäustlin et al., "A compact soft X-ray spectrograph combining high efficiency and resolution", JINST 5, P02004 (2010).
5. R. R. Fäustlin et al., "Observation of ultrasfast nonequilibrium collective dynamics in warm dense hydrogen", Phys. Rev. Lett. 104, 125002 (2010).
6. J. MacFarlane et al., "HELIOS-CR – a 1-D radiation-magnetohydrodynamics code with inline atomic kinetics modeling", J. Quant. Spectrosc. Radiat. Transfer 99, 381 (2006)
7. R. M. More et al., "A new quotidian equation of state (QEOS) for hot dense matter", Phys. Fluids 31, 3059 (1988)

Sacrificial tamper layer.

Transient states of highly charged ions in delayed cluster explosion

Violent forces are at work during research with free-electron lasers: every single light flash brings the analysed sample to a fast explosion. Every femtosecond counts in the experiments when decoding the molecular structure of the sample before its destruction. At FLASH, we have studied a method to delay the explosion of the sample for potentially decisive fractions of a second. A sacrificial tamper layer provides an efficient electron source for partial neutralization of highly charged ions created in the centre. The significant reduction of charge states increases the available time for recording a diffraction pattern in coherent imaging experiments.

Free-electron lasers can be used as high-speed cameras for the nanocosm. Their high-energy and short X-ray pulses allow insights into the smallest dimensions and ultra-fast processes, opening up new scientific investigation possibilities in various areas, ranging from the imaging of single molecules up to filming the motion of electrons in atoms. Coherent diffraction imaging promises to reveal the structure of molecules which cannot be prepared in crystalline form. Using time-resolved pump-probe schemes important information is obtained about how molecular reactions take place, for example during photosynthesis. However, during the measurement, the extreme intensity of each single X-ray flash inevitably transforms the investigated sample into a plasma and eventually destroys it [1]. When X-rays hit the sample, many of the bound electrons are abruptly knocked out, leaving a molecular structure of highly charged ions repelling each other and disintegrating in a Coulomb explosion. It is an open question whether sufficient scattering signal can be detected before the molecule explodes. One strategy to prevent the loss of electrons in the sample too quickly is to surround it with a shell (tamper layer) [2]. During the interaction with the X-ray light, the layer is ionised as well; however, the electrons released from the shell will be transferred into the core of the sample, thus compensating the loss of core electrons for a short time which slows down the expansion. Clusters can be used as nanoscopic model systems to test the effect of tamper layers, as so-called core-shell clusters can be generated, with a core consisting of one element surrounded by a shell consisting of another element.

For the investigation of the explosion delay, we prepared small clusters with a core consisting of about 80 Xenon atoms and a shell of about 400 Argon atoms. The composite clusters were irradiated with FLASH pulses at a wavelength of 13.5 nm which is resonant with the excitation of the 4d electron shell of Xe. At typical pulse durations of 150 fs and an average pulse energy above 100 µJ, the power density exceeds 10^{15} W/cm^2 in the focus. The interaction results in the emission of fluorescence photons from multiply charged ions. A toroidal diffraction grating diffracts and focuses the fluorescence onto a CCD camera.

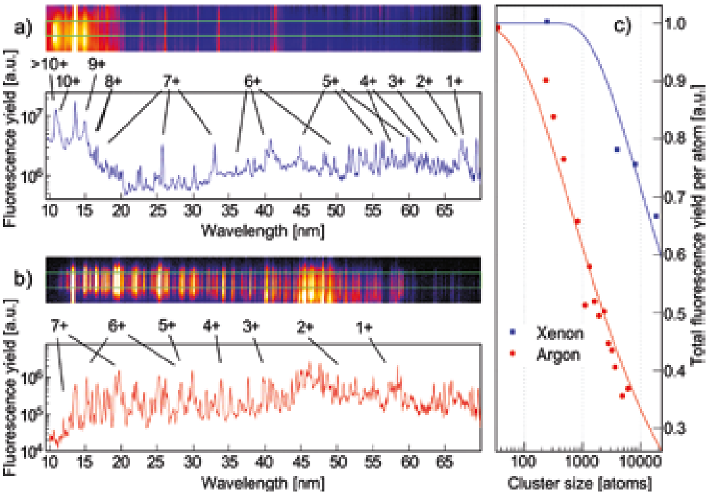

Figure 1

Typical fluorescence spectra of pure Xe clusters (a) and pure Ar clusters (b) comprising 4100 and 400 atoms, respectively. The data are recorded with an X-ray camera at a FEL intensity of approximately 2×10^{15} W/cm^2 and plotted in logarithmic scale. The same line out of the CCD chip (green rectangle) is evaluated for each spectrum. Charge states have been assigned to more than 100 fluorescence lines and a characteristic selection is given. Total fluorescence yield per atom as a function of cluster size is shown in (c).

A typical spectrum of Xe and Ar clusters is plotted in Figs. 1(a) and 1(b), respectively. The raw data is integrated vertically in a narrow region, as indicated by the green rectangle in Fig. 1, to retrieve a spectrum. In the experiments on pure Xe clusters, charge states up to at least 11+ were detected. The Ar cluster fluorescence reveals lower charge states of up to 7+ due to

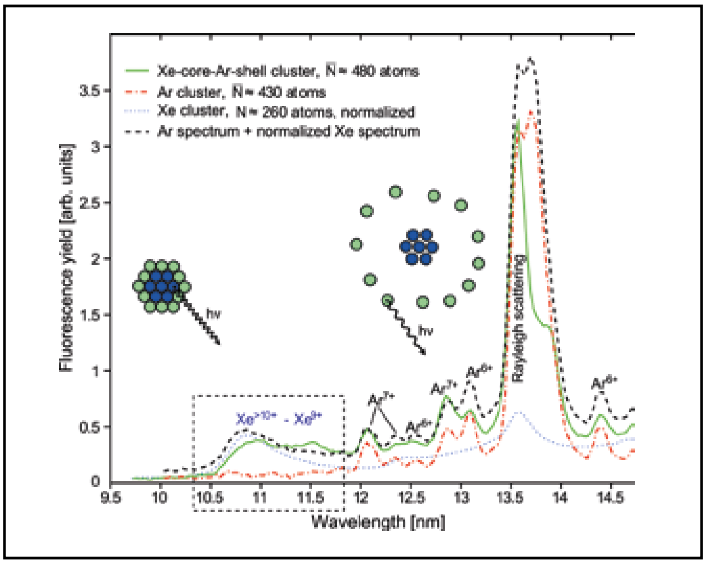

Figure 2

Comparison of the measured Xe-core-Ar-shell spectrum, the pure Ar and Xe spectra and the spectrum synthesized from the Ar- and a normalized Xe spectrum. The Xe-core-Ar-shell spectrum and the synthesized spectrum show reasonable agreement at short wavelengths where Xe charge states of at least 11+ appear. The pictographs illustrate that the time-integrated fluorescence spectrum of Xe-core-Ar-shell clusters provides information on the highly charged Xe core from early times of the interaction (left), as well as information on the Ar-shell upon Coulomb explosion (right).

both the higher ionization potential of Ar and the difference in the atomic photoabsorption cross section. In both cases, fluorescence is predominantly emitted from highly charged ions that peel off the surface during the disintegration. Note, that the fraction of surface atoms decreases with increasing cluster size as can be seen in the reduced fluorescence yield per atom in Fig. 1(c).

To push the experimental sensitivity toward processes that occur inside the cluster ion core on the sub-ps time scale when the core is still close to its initial geometry, we performed complementary fluorescence experiments on Xe-core-Ar-shell clusters. Fig. 2 shows a comparison between fluorescence spectra of core-shell clusters (green), pure Ar clusters (red), and pure Xe clusters (blue). The key finding is that composite clusters emit between 10.5 and 12 nm. This signal is absent in pure Ar clusters. We assign the fluorescence at short wavelength to the Xe ion core because it coincides with the most prominent emission lines in the pure Xe spectra. To corroborate this finding the core-shell spectrum is emulated by combining spectra of pure Ar clusters and pure Xe clusters. The similarity in the structures between 10.5 and 12 nm of the measured core-shell spectrum (green) and the emulated one (black) is clear evidence of the transient presence of highly charged Xe^q ions ($q > 10+$) in the core-shell cluster.

The Xe charge states observed in the core-shell cluster fluorescence are just as high as those in pure Xe spectra. This is a stark contrast to mass spectra, which show much lower final charge states compared to pure clusters [3]. Thus, fluorescence spectroscopy probes ultrafast radiative decay of highly charged ions in a time window which is not accessible by conventional time-of-flight mass spectrometry. In agreement with theory [4], the latter traces remnants of the interaction, where electron thermalisation followed by nonradiative recombination has already produced significantly lower charge states. Thus, a sacrificial tamper layer provides an efficient electron source for partial neutralization of highly charged ions created in the centre which in turn slows down the expansion of the cluster core.

Contact: Tim Laarmann, tim.laarmann@desy.de

Authors

L. Schroedter[1], M. Müller[2], A. Kickermann[1], A. Przystawik[1], S. Toleikis[1], M. Adolph[2], L. Flückiger[2], T. Gorkhover[2], L. Nösel[2], M. Krikunova[2], T. Oelze[2], Y. Ovcharenko[2], D. Rupp[2], M. Sauppe[2], D. Wolter[2], S. Schorb[3], C. Bostedt[3], T. Möller[2], and T. Laarmann[1,4]

1. Deutsches Elektronen-Synchrotron DESY, Notkestrasse 85, 22607 Hamburg, Germany
2. Institut für Optik und Atomare Physik, Technische Universität Berlin, Eugene-Wigner-Building EW 3-1, Hardenbergstrasse 36, 10623 Berlin, Germany
3. SLAC National Accelerator Laboratory, P.O. Box 20450, Stanford, California 94309, USA
4. The Hamburg Centre for Ultrafast Imaging CUI, Luruper Chaussee 149, 22761 Hamburg, Germany

Original publication

"Hidden Charge States in Soft-X-Ray Laser-Produced Nanoplasmas Revealed by Fluorescence Spectroscopy", Phys. Rev. Lett. 112, 183401 (2014).
DOI: 10.1103/PhysRevLett.112.183401

References

1. **R. Neutze, R. Wouts, D. van der Spoel, E. Weckert, and J. Hajdu, "Potential for biomolecular imaging with femtosecond X-ray pulses", Nature 406, 752-757 (2000).**
2. **S. P. Hau-Riege et al., "Sacrificial Tamper Slows Down Sample Explosion in FLASH Diffraction Experiments", Phys. Rev. Lett. 104, 064801 (2010).**
3. **M. Hoener, C. Bostedt, H. Thomas, L. Landt, E. Eremina, H. Wabnitz, T. Laarmann, R. Treusch, A. R. B. de Castro, and T. Möller, "Charge recombination in soft x-ray laser produced nanoplasmas", J. Phys. B 41, 181001 (2008).**
4. **E. Ackad, N. Bigaouette, S. Mack, K. Popov, and L. Ramunno, "Recombination effects in soft-x-ray cluster interactions at the xenon giant resonance", New J. Phys. 15, 053047 (2013).**

Electron rearrangement in dissociating molecules.

Real time observation of electron transfer in Coulomb exploding I_2^{n+} molecular ions

Employing an XUV-pump-XUV-probe scheme at FLASH, the critical internuclear distance up to which electrons can be transferred within a dissociating iodine molecule was determined. This property is critical for one of the most promising future free-electron laser applications: the imaging of single biomolecules. Our results are in good agreement with a classical model routinely applied in collision physics, which suggests that molecular dissociation can be described as a half-collision.

One of the most far-reaching goals of science at free-electron lasers (FELs) is to image the structure of single biomolecules with atomic resolution by measuring interference patterns of X-rays coherently scattered off the molecule [1]. This requires very intense, ultra-short light flashes. To outrun the molecular destruction during the illumination and to ensure that a snapshot of the undamaged molecule is taken, the exposure time must be shorter than the disintegration time. The relevant time scales are in the femtosecond (1 fs = 10^{-15} s) regime.

One of the unknown aspects of single-molecule imaging is the role of heavy atoms within the molecule. They absorb X-ray radiation by orders of magnitude more efficient than the much lighter carbon or hydrogen atoms. Therefore, the absorbed energy is locally deposited and, subsequently, spreads throughout the molecule via various electronic relaxation and rearrangement mechanisms. Due to photo-ionization and secondary relaxation processes, the molecule carries a positive net-charge that is distributed over the molecule, finally leading to its fragmentation. The more efficiently the charge is redistributed within the molecule, the faster it explodes. We have investigated such a scenario using iodine molecules I_2, a prototype system with two heavy constituents, by tracing electron rearrangement as a function of time and internuclear separation at FLASH.

The absorption of a single extreme-ultraviolet (XUV) photon of 87 eV already leads to multiple ionization of I_2: After the removal of an inner-shell electron via photo-ionization, the remaining excitation energy of the “hole-state” is used to emit one or two additional electrons. Thus, an XUV pulse of suitable energy creates a multiply charged molecule and triggers dissociation due to the repulsion of its positively charged constituents. After a freely adjustable time-delay a second identical pulse, the probe pulse, is shot onto the molecule and removes further electrons from one of the ionic fragments. For small delays, and correspondingly small internuclear distances, any charge asymmetry

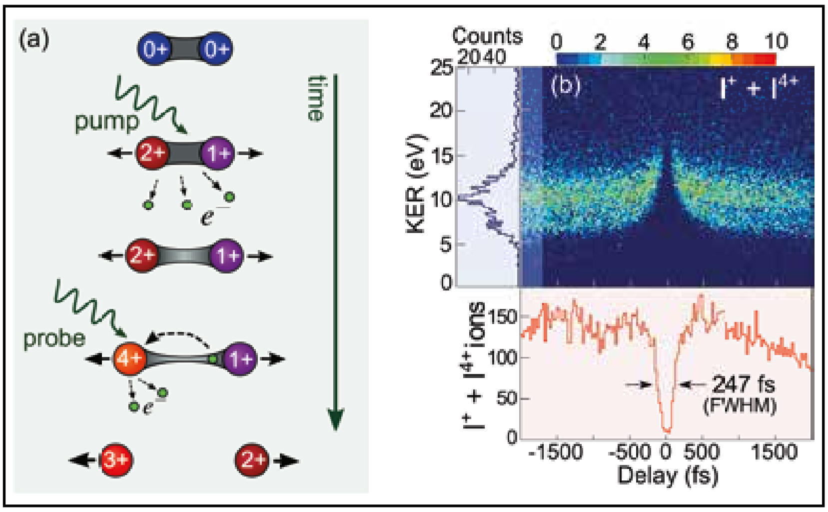

Figure 1

(a) Sketch of the pump-probe scheme. The pump pulse multiply ionizes I_2 and thereby triggers the dissociation of the molecule. The delayed probe pulse further ionizes one of the ions, which may lead to electron transfer throughout the molecule.

(b) The kinetic-energy release (KER) of $I^+ + I^{4+}$ ion pairs is plotted as a function of the pump-probe delay. Asymmetrically charged fragments can only be produced from certain delays on, when electron transfer is blocked, which manifests itself as a vanishing ion yield for small delays. A projection of all events onto the delay axis (red curve) allows to extract the critical time up to which electron transfer is possible. From the projection onto the KER axis for large delays (blue curve) we are able to conclude which intermediate charge state was populated by the pump pulse. This information is needed to convert the critical time into the corresponding internuclear distance of electron transfer, which is plotted in Fig. 2(b).

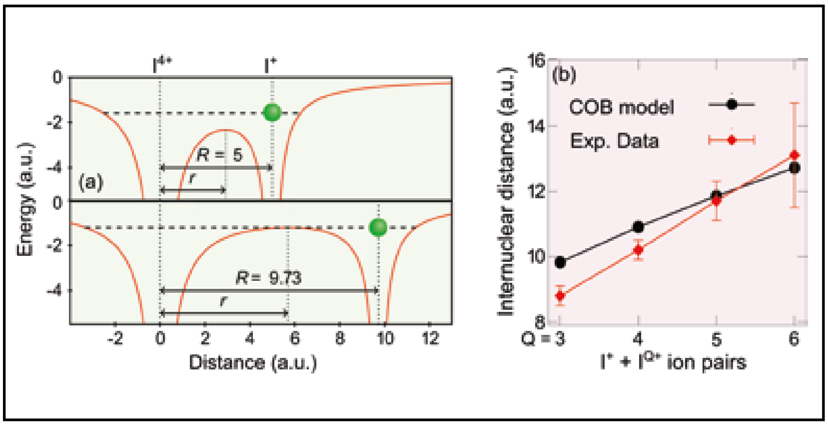

Figure 2

(a) Illustration of the classical over-the-barrier model (COB) by means of the ion pair $I^+ + I^{4+}$. Upper panel: At the equilibrium internuclear distance $R = 5$ a.u. (1 a.u. = 5.29×10^{-15} m) the combined potential barrier of the neighbouring ions is well below the binding energy of the outermost electron (shown as green sphere), thus electron transfer is possible. Lower panel: While the ions separate the barrier rises and electron transfer is blocked from a certain separation on.

(b) Critical internuclear distance for selected asymmetric ion pairs. Red diamonds show experimental data, while black dots represent the values predicted by the COB model.

which is induced by the probe pulse is balanced by electron transfer among the ions, as depicted in Fig. 1(a). However, at large delays the ionic fragments behave like individual ions and electron transfer is blocked. Thus, asymmetrically charged ion pairs can only be produced from certain delays on, as can be seen for the fragmentation into $I^+ + I^{4+}$ in Fig. 1(b). Experimentally, the critical internuclear distance up to which electron transfer is possible is determined by detecting the final charge states of the two emerging ionic fragments as a function of the time-delay between the consecutive XUV pulses. In order to do so, we employed a reaction microscope [2] in combination with the autocorrelator installed in the beamline BL2 at FLASH [3].

The results are in good agreement with an intuitive classical model that is routinely employed in ion-atom collisions, the so-called over-the-barrier model [4]. Within this model an electron can freely move between the neighbouring ions as long as the binding energy of this electron is above the combined potential of the atomic cores, as depicted in Fig. 2(a). The height of the potential barrier depends on the internuclear distance and it rises above the electronic binding energy from some critical distance on. These predicted distances are in good agreement with the experimentally determined values, which are shown in Fig. 2(b).

The geometry of our pump-probe scenario is surprisingly similar to that of a traditional ion-atom collision experiment. There, the projectile approaches the target up to a certain minimal distance, the impact parameter, and continues its trajectory with a modified momentum. In our approach, the reaction partners start from their closest distance, which is defined by the moment when the probe pulse impinges. Thus, we observe only the outgoing ions and therefore refer to the process as a “half-collision”. This “XUV-induced” half-collision offers the great advantage of a controlled impact parameter, which can be adjusted by varying the pump-probe time-delay. The kinetic energies of the ionic fragments are comparably low and they correspond well to the regime of chemical and plasma reactions. Electron transfer plays a crucial role in such processes. On the atomic level, however, these low-energetic quasi-molecular reactions are mostly unexplored because of substantial technical difficulties, in theory (many-body non-perturbative complexity) as well as in experiment (high-resolution low-energy ion beams).

Our results demonstrate that electron transfer occurs over relatively large internuclear distances of several atomic radii on time-scales faster than the molecular dissociation. Thus, locally created charges are efficiently redistributed which leads to an accelerated explosion of the molecule. Future experiments on more complex molecules relevant for X-ray imaging are planned.

Contact: Kirsten Schnorr, kirsten.schnorr@mpi-hd.mpg.de
Robert Moshammer, r.moshammer@mpi-hd.mpg.de

Authors

K. Schnorr[1], A. Senftleben[1], M. Kurka[1], A. Rudenko[2], G. Schmid[1], T. Pfeifer[1], K. Meyer[1], M. Kübel[3], M.F. Kling[3], Y.H. Jiang[4], R. Treusch[5], S. Düsterer[5], B. Siemer[6], M. Wöstmann[6], H. Zacharias[6], R. Mitzner[7], T.J.M. Zouros[8], J. Ullrich[9], C.D. Schröter[1], and R. Moshammer[1]

1. Max-Planck-Institut für Kernphysik, 69117 Heidelberg, Germany
2. J.R. Macdonald Laboratory, Kansas State University, Manhattan, Kansas 66506, USA
3. Max-Planck-Institut für Quantenoptik, 85748 Garching, Germany
4. SARI, Chinese Academy of Sciences, Shanghai 201210, China
5. Deutsches Elektronen-Synchrotron, 22607 Hamburg, Germany
6. Westfälische Wilhelms-Universität, 48419 Münster, Germany
7. Helmholtz-Zentrum Berlin, 12489 Berlin, Germany
8. Department of Physics, University of Crete, Post Office Box 2208, 71003 Heraklion, Crete, Greece
9. Physikalisch-Technische Bundesanstalt, 38116 Braunschweig, Germany

Original publication

“Electron Rearrangement Dynamics in Dissociating I_2^{n+} Molecules Accessed by Extreme Ultraviolet Pump-Probe Experiments”, Phys. Rev. Lett. 113, 073001 (2014).
DOI: 10.1103/PhysRevLett.113.073001

References

1. R. Neutze et al., “Potential for biomolecular imaging with femtosecond X-ray pulses”, Nature 406, 752 (2000).
2. J. Ullrich et al., “Recoil-ion and electron momentum spectroscopy: reaction- microscopes”, Rep. on Prog. Phys. 66, 1463 (2003).
3. M. Wöstmann et al., “The XUV split-and-delay unit at beamline BL2 at FLASH”, J. Phys. B 46,164005 (2013).
4. H. Ryufuku, K. Sasaki, and T. Watanabe, “Oscillatory behavior of charge transfer cross sections as a function of the charge of projectiles in low-energy collisions”, Phys. Rev. A 21, 745 (1980).
4. A. Niehaus, “A classical model for multiple-electron capture in slow collisions of highly charged ions with atoms”, J. Phys. B 19, 2925 (1986)

Single quantum states and defined wave packets.

Controlling the motion of molecules with electric fields

Molecules in the gas-phase can be controlled and sorted using strong electric fields [1]. Using electrostatic deflection, molecules can be separated on the basis of their shape, structure, or even quantum state. We have demonstrated this for the separation of water into the respective ground states of its two nuclear-spin isomers, *para* and *ortho*, presenting the first full separation of water nuclear-spin states. Furthermore we show how individual rotational quantum states of carbonyl sulfide can be selected and detected. Samples of carbonyl sulfide molecules, all in the absolute ground state, have been used to study non-adiabatic effects in strong laser-field alignment [2] and mixed-field orientation. Pendular state wave packet dynamics, analogous to a classical pendulum motion, was demonstrated.

The control and determination of a sample's initial state, e.g., the wave function of its constituent molecules, provides direct access to the quantum-mechanical properties and dynamics even for macroscopic samples. This control is beneficial for experiments aimed at "recording the molecular movie", i.e., the imaging of molecular dynamics using time-resolved X-ray or electron diffraction, high harmonic generation, or molecular-frame photoelectron imaging. The controlled samples also allow investigation of the microscopic details of complex chemical systems. For example, it is well known that astrochemical systems such as interstellar ices often contain highly non-thermalized spin-state distributions of molecules. For instance, the population ratio of *para* and *ortho* nuclear-spin states in water (H_2O) often differs from that expected based on the local temperature [3]. The reasons for this remain unclear and laboratory experiments on nuclear-spin conversion could help shed some light on this. Highly controlled samples of molecules, all in an identical stationary eigenstate or in the same dynamical wave packet, allow for detailed investigations of these phenomena.

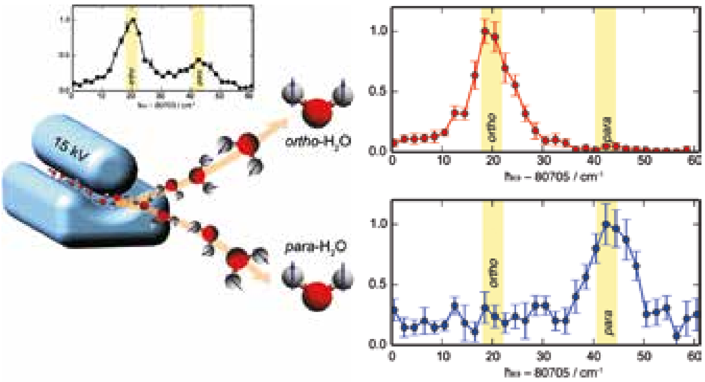

Figure 1

Separation of the *para* and *ortho* nuclear-spin isomers of water. A beam of cold water molecules is send through a strong inhomogeneous electric field dispersing and spatially separating the quantum states occupied by the nuclear-spin isomers. This was confirmed through state-specific spectroscopic detection, shown on the right for the separated beams, yielding a purity of 97 % and 74 % for *ortho*- and *para*-water, respectively.

In our experiments, target molecules are introduced into the gas-phase and are co-expanded in a high-pressure backing gas into vacuum. Supersonic molecular beams with internal temperatures of about one kelvin are produced. These are directed through an inhomogeneous electric field of ~150 kV cm^{-1} in the deflector, see Fig.1. As the effective, space-fixed, dipole moment of a molecule is a property of its individual quantum state, the device acts as an electrostatic prism for molecules according to their quantum state. The spatial distributions of molecules are subsequently probed using spectroscopic techniques. The rotational degrees of freedom of the molecules, their alignment and orientation, are controlled via strong laser fields and weak DC electric fields.

Using this experimental setup we separated both nuclear-spin isomers, *para* and *ortho*, of water. These individual species are defined by the relative orientation of the nuclear spins of the hydrogen atoms, which can be symmetric ("*ortho*") or antisymmetric ("*para*") with respect to the exchange of the two protons. According to the symmetrization postulate of quantum mechanics, the two nuclear-spin isomers must reside in distinct rovibronic (rotation-vibration-electronic) quantum states and cannot spontaneously interconvert. It is these rovibronic states that are separable with the electrostatic prism. At the low temperatures in our experiment, all molecules reside in the vibronic (vibration-electronic) ground state; *ortho* water has a ground state corresponding to the rotational state $J_{K_aK_c}=1_{01}$, while the ground state of *para* water corresponds to $J_{K_aK_c}=0_{00}$. These states exhibit significantly different Stark effects and thus deflect differently in our electric prism, shown in Fig. 1.

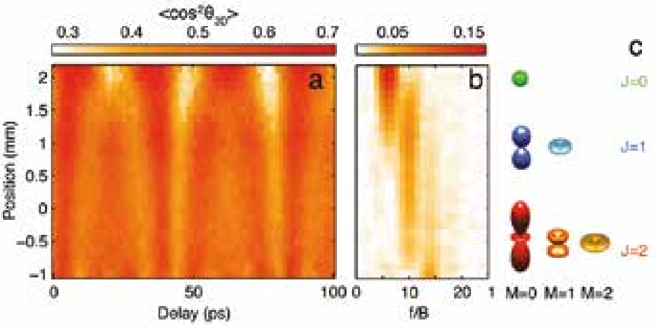

Figure 2

(a) Measured degree of laser-induced alignment as a function of time and position in the deflected molecular beam and (b) its Fourier transform, demonstrating the dispersed rotational state distribution. (c) Color-coded densities of the derived rotational wave functions.

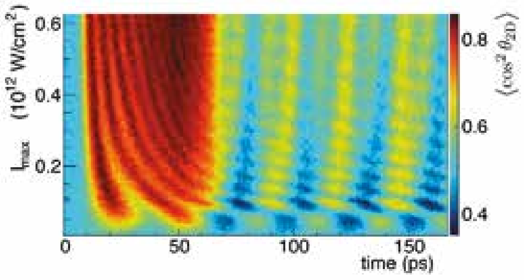

Figure 3

Degree of alignment for ground-state-selected carbonyl sulfide molecules as a function of the delay between the alignment laser and the probe laser and as a function of the intensity of the alignment laser. The pendular state wave packet motion inside the strong laser pulse is observed by the oscillations in the degree of alignment during the laser pulse (between 10 and 60 ps).

The purity of the produced quantum-state selected samples is probed using resonance-enhanced multi-photon ionization where 97 %-pure *ortho* water and 74 %-pure *para* water were produced.

Exploiting the same separation technique, we have dispersed molecular beams of carbonyl sulfide molecules according to their quantum state. We measured the state-specific angular probability densities of the individual rotational states. Combining two experiments, we determined the two relevant quantum numbers, the overall angular momentum J and its projection M onto a space-fixed axis. In a variant of rotational coherence spectroscopy a weak femtosecond laser pulse induced rotational Raman transitions and transferred population from the initial state $|J,M\rangle$ to nearest-neighbour states of the same parity, i.e., $\Delta J = 2$, $\Delta M = 0$. Subsequently, the time-dependent degree of alignment is determined for the spatially dispersed molecular beam, shown in Fig. 2(a). The coherent evolution of the rotational wave packet results in a spatially varying time-dependent beating, determined by the angular momentum J of the coupled eigenstates. Its frequency, as a function of vertical position in the dispersed beam, can be directly obtained from the Fourier transform, Fig. 2(b). In addition, we have directly observed the projection of the quantum number M of the individual rotational states through Coulomb explosion imaging of the molecular axis alignment of the dispersed samples without any laser-induced alignment. For many positions, the samples exhibit significantly non-isotropic angular distributions, a direct signature of the separation of quantum states according to their angular momentum projection. The combination of the two measurements allows to reconstruct the full quantum states as a function of position in the dispersed beam, i.e., the angular probability densities, which are depicted in Fig. 2(c).

Absolute ground-state-selected carbonyl sulfide molecules have been used to study non-adiabatic effects in laser alignment and mixed field orientation dynamics. Using 50-ps-long laser pulses, shorter than the 82 ps rotational period of ground state carbonyl sulfide, a defined wave packet of pendular states, i.e., a quantum pendulum, has been created, see Fig. 3. The wave packet motion is directly visible by the oscillations in the time-dependent degree of alignment [4]. Exploiting the combined effect of mixed laser and dc electric fields, similar rotational wave packets have been created. This wave packet exhibits very strong field-free orientation of $\langle\cos\theta\rangle = 0.6$, significantly stronger than the orientation achieved with THz pulses.

In summary, the separation of molecular eigenstates paves the way for novel experiments, from the investigation of simple quantum mechanical concepts such as the realization of a quantum pendulum or strong field-free orientation, to possible applications of nuclear-spin-purified water in hyperpolarized NMR methods with wide (bio)chemical applicability.

Contact: Jochen Küpper, jochen.kuepper@desy.de

Authors

Daniel A. Horke[1], Sebastian Trippel[1], and Jochen Küpper[1,2,3]

1. Center for Free-Electron Laser Science, DESY, 22607 Hamburg, Germany
2. The Hamburg Centre for Ultrafast Imaging CUI, University of Hamburg, 22761 Hamburg, Germany
3. Department of Physics, University of Hamburg, 22761 Hamburg, Germany

Original publications

“Separating *Para* and *Ortho* Water”, Angew. Chem. Int. Ed., 53, 11965-11968 (2014)
DOI: 10.1002/anie.201405986
“Trennung von para-und ortho-Wasser“, Angew. Chem., 126, 12159-12162 (2014)
DOI: 10.1002/ange.201405986
“Strongly driven quantum pendulum of the carbonyl sulfide molecule”, Phys. Rev. A 89, 051401R (2014). DOI: 10.1103/PhysRevA.89.051401
“Two-state wave packet for strong field-free molecular orientation”, arxiv:1409.2836 [physics]

References

1. S. Y. T. Meerakker, H. L. Bethlem, N. Vanhaecke, and G. Meijer, “Manipulation and Control of Molecular Beams“, *Chem. Rev.* 112, 4828 (2012).
2. H. Stapelfeldt and T. Seideman, “*Colloquium:* Aligning molecules with strong laser pulses“, *Rev. Mod. Phys.* 75, 543 (2003).
3. M. R. Hogerheijde, E. A. Bergin, C. Brinch, L. I. Cleeves, J. K. J. Fogel, G. A. Blake, C. Dominik, D. C. Lis, G. Melnick, D. Neufeld, O. Panić, J. C. Pearson, L. Kristensen, U. A. Yildiz, and E. F. van Dishoeck, “Detection of the Water Reservoir in a Forming Planetary System”, *Science* 334, 338 (2011).
4. Supplementary information of S. Trippel et al., Phys. Rev. A 89, 051401R (2014), https://journals.aps.org/pra/supplemental/10.1103/PhysRevA.89.051401/quantum-pendulum.mp4

Boiling water with light faster than you can blink.

Sub-picosecond extreme heating of liquid water by intense THz radiation

Water is the single most important solvent in chemistry and biology. Many chemical and biochemical reactions take place in water due to random thermal fluctuations of the solvent that provide the reactants in solution with enough energy to undertake a reactive event. Time-resolved pump-probe measurements of such thermal reactions cannot be performed in the usual way by photo-excitation with optical or UV lasers like in usual femtochemistry because they take place in the electronic ground state of the system. To overcome such fundamental limitation, we theoretically investigate strategies to bring a large amount of energy to liquid water using short and intense THz pulses. We find that it is possible to increase the temperature of water in the focus of the pulse by about 500 K within 1.5 ps.

Rather than acting as a passive environment, the dynamics of water during chemical and biological processes play a fundamental role in the solvation and stabilization of reaction intermediates. Recent THz spectroscopy measurements probing collective, low frequency modes show that water is a key actor in enzymatic reactions and protein folding [1].

Recently, the generation of THz radiation from X-ray FELs (XFELs) in full synchronization with the X-ray pulse was demonstrated [2, 3]. This opens extremely interesting avenues for pump-probe type experiments in which a THz pulse initiates a chemical process of interest in e.g. solid state or biological samples, followed by an ultrashort X-ray pulse that interrogates the system at a well-defined time delay.

In this work, we studied the response of liquid water to an intense sub-picosecond THz pulse by *ab initio* molecular dynamics (AIMD) [4]. We assumed a THz pulse characterized by a Gaussian envelope with a full width at half maximum (fwhm) of 250 fs and intensity of 5×10^{12} W/cm^2. Assuming the THz light is focused to a spot of 0.01 mm^2 this represents a total pulse energy of about 125 μJ. At a mean photon energy of $\omega = 100$ cm^{-1} (3 THz) one cycle of the electromagnetic field oscillation takes about 330 fs, meaning that our pulse is between a half and a full cycle long.

Interestingly, such a THz pulse transfers a large amount of energy to the liquid medium in a sub-ps time scale. The temperature increase as a function of time is shown in Fig. 1. After the pulse, the temperature rises from 300 K to about 800 K. It should be noted that the temperature increase is much faster than the time the liquid has to expand, meaning that the volume remains constant. Initially, the water molecules react to the strong electric field via their permanent dipoles, which try to orient with the polarization direction of the electric field of the THz pulse. This field is of the order of fractions of Volts per Angstrom and therefore only about one order of magnitude smaller than the Coulomb fields generated by atoms and electrons at chemical bonding distances. Consequently, there is a sudden break up of the hydrogen bonding structure of the liquid phase, and water molecules start to strongly vibrate against one another. Later on, on a time scale of 1 ps, the energy redistributes into intramolecular degrees of freedom, namely the O-H bond stretching and H-O-H angle bending motions, due to collisions between water monomers. Fig. 2a and Fig. 2b present energy distributions of the water molecules in the bulk as a function of time for the rotational and vibrational degrees of freedom, respectively. It can be observed how the initial 300 K Maxwell-Boltzmann distributions before the THz pulse quickly change after the pulse extending to substantially larger energies. This indicates that solvent molecules dissolved in water can potentially gain a large amount of energy from the liquid via collisional energy transfer, which is the subject of current investigations.

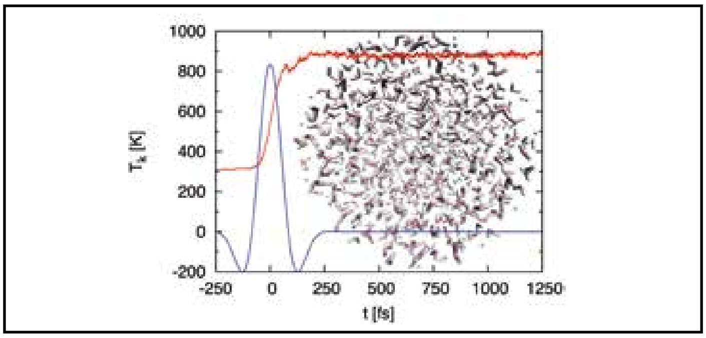

Figure 1

Temperature increase calculated as a function of time (red). The temperature shown here is a kinetic temperature proportional to the mean kinetic energy of the atoms as a function of time. After the pulse (blue), the temperature rises from 300 K to about 800 K.

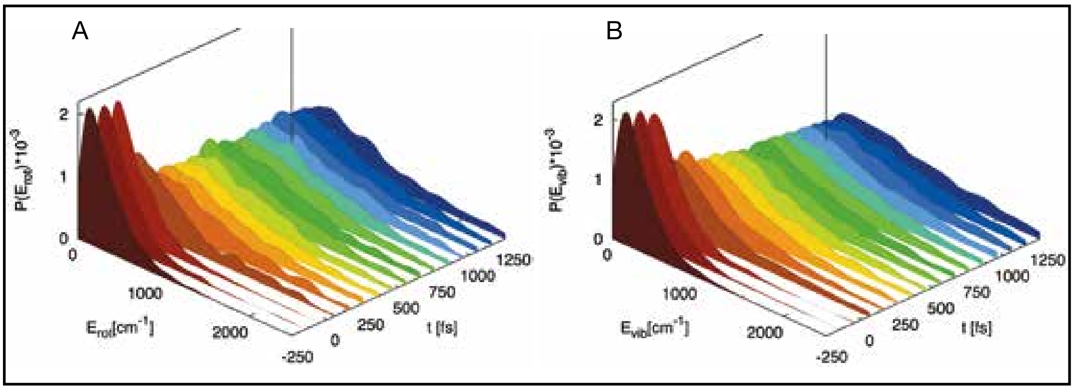

Figure 2

Probability distributions per water molecule of rotational (left) and vibrational (right) energies for different time delays. These are Maxwell-Boltzmann distributions for t = −250 fs and are normalized at all times. At the time of the pulse peak intensity around t = 0 the distributions quickly flatten and resemble equilibrium distributions at a larger temperature than before the THz pulse.

The large amount of energy per monomer transferred to the liquid changes its structure significantly disrupting the hydrogen bond network and the tetrahedral coordination of water molecules on an ultrafast time scale. In addition to the results described so far, we computed the time-resolved wide-angle X-ray scattering (TR-WAXS) signal of water as a function of time and found that the structural changes can potentially be traced by X-ray scattering measurements. The characteristics of the medium created by the THz pulse are comparable to measurements on water performed at T = 1500 K and pressure of 12 GPa [5].

Fig. 3a shows the $g_{O\text{-}O}(r)$ radial distribution function (RDF) calculated as a function of time. $g_{O\text{-}O}(r)$ evolves from having two peaks, which is indicative of the first two solvation shells around each molecule, into a flat RDF typical of a gas phase system. This change occurs between −50 and 150 fs after the start of the THz pulse. Similarly, the $g_{O\text{-}H}(r)$ RDF in Fig. 3b indicates a very fast disruption of the hydrogen bond network as seen in the disappearance of the peak at about 2 Å, which is related to the oxygen-hydrogen distance in a typical hydrogen bond.

This study shows that a sub-ps intense THz pulse, soon to be achieved at modern accelerator facilities and table-top setups, transfers a large amount of energy to liquid water and creates a hot and structureless environment. Importantly, as a consequence of collisions induced between monomers, a large amount of energy flows to intramolecular vibrations non-resonant with the pulse photon energy. These changes can be monitored by time-resolved X-ray scattering measurements of the liquid. The transient, hot environment achieved by the THz pulse may have interesting properties as a matrix to study activated chemical processes. This is the subject of on-going research.

Contact: Oriol Vendrell, oriol.vendrell@cfel.de

Figure 3

Radial distribution functions (RDF) (a) $g_{O-O}(r)$ and (b) $g_{O-H}(r)$ at different time delays under the effect of the THz pulse. Time is given in femtoseconds. The $g_{O-O}(r)$ distribution loses the double peak structure after the THz pulse and more closely resembles the RDF distribution of a gas. The $g_{O-H}(r)$ distribution loses the peak at 2 Å shortly after the pulse, indicating that hydrogen bonds are broken by the interaction with the THz pulse.

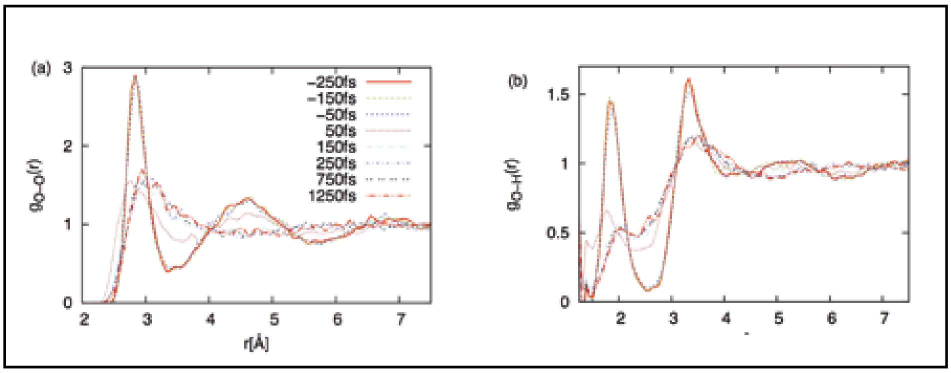

Authors

Pankaj K. Mishra[1,2,3], Oriol Vendrell[1,3], and Robin Santra[1,2,3]

1. Center for Free-Electron Laser Science, CFEL, DESY, Notkestraße 85, 22607 Hamburg, Germany.
2. Department of Physics, University of Hamburg, Jungiusstraße 9, 20355 Hamburg, Germany.
3. The Hamburg Center for Ultrafast Imaging (CUI), Luruper Chaussee 149, 22761 Hamburg, Germany.

Original publication

"Ultrafast energy transfer to liquid water by sub-picosecond high-intensity THz pulses: an *ab-initio* molecular dynamics study", Angewandte Chemie International Edition 52, 13685-13687 (2013). DOI: 10.1002/anie.201305991

References

1. S. Ebbinghaus, S. J. Kim, M. Heyden, X. Yu, U. Heugen, M. Gruebele, D. M. Leitner, and M. Havenith, Proc. Natl. Acad. Sci. 104, 20749 (2007).
2. Ulrike Frühling, M. Wieland, M. Gensch, T. Gebert, B. Schütte, M. Krikunova, R. Kalms, F. Budzyn, O. Grimm, J. Rossbach, E. Plönjes, and M. Drescher, Nat. Photon. 3, 523 (2009).
3. F. Tavella, N. Stojanovic, G. Geloni, and M. Gensch, Nat. Photon. 5, 162 (2011).
4. J. VandeVondele, M. Krack, F. Mohamed, M. Parrinello, T. Chassaing, and J. Hutter, Com. Phys. Comm. 167, 103 (2005).
5. N. Goldman and L. E. Fried, J. Chem. Phys. 126, 134505 (2007).

When is a molecule a molecule.

X-ray Free-Electron Laser measures charge transfer over large distances

The making and breaking of molecular bonds are the most fundamental processes in chemistry. Molecular bonds, both covalent and ionic, are created through the sharing or transfer of valence electrons between atomic constituents. Bond-breaking reactions are thus associated with electron rearrangement and their subsequent localization on either of the resulting (dissociating) fragments. If triggered by light, these reactions can be tracked using a timed sequence of ultra-short light pulses. Using such a pump-probe scheme, we studied the transfer of electrons between two sites of a dissociating iodomethane molecule. We used an infrared laser pulse to break the molecular bond, then created a localized source of positive charge by ionizing the iodine atom with a subsequent femtosecond X-ray pulse from a Free-Electron Laser, and observed charge transfer to the methane fragment over distances of up to 10 times the equilibrium bond length.

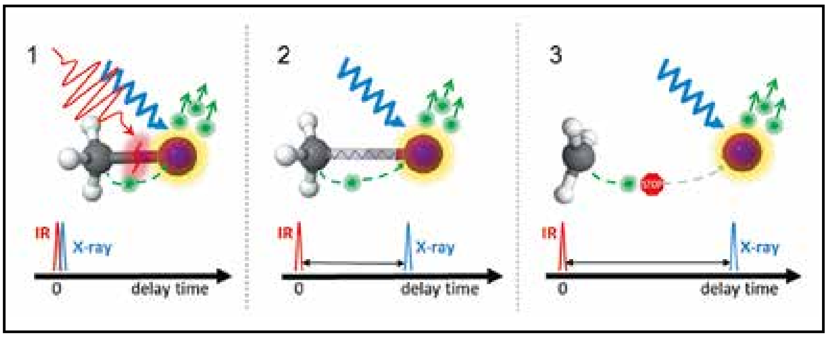

Figure 1

Schematic overview of the pump-probe experiment at three different time delays. (1) Both pulses arrive at the same time and interact with the still intact molecule. (2) With increasing delay between the IR pulse, which triggers the dissociation, and the X-ray pulse, which ionizes the iodine, the internuclear distance increases and the constituents become more isolated. Nevertheless, electrons are still able to transfer from one atom to the other. (3) At long delays and thus large internuclear distances, the atoms become fully isolated and electron transfer from the environment towards the iodine ions is no longer possible.

Chemical reactions involving the transfer or migration of electrons drive numerous important processes in physics, chemistry and biology, with practical applications ranging from X-ray astrophysics to artificial photosynthesis and molecular electronics [1]. These processes often happen on few-femtosecond or even sub-femtosecond time scales. Pump-probe spectroscopies using femtosecond optical lasers, attosecond extreme ultraviolet pulses, and ultra-short X-ray free-electron lasers (FEL) nurture the vision to trace these reactions in real time [2]. Electronic motion can be triggered by photo excitation or -ionization of valence electrons. However, valence electrons are highly delocalized, making it difficult for experimental studies to follow time-dependent charge localization. FEL sources can provide ultra-short X-ray pulses and thus open access to femtosecond time-resolved experiments employing element specific inner-shell ionization. This allows for probing electronic and nuclear dynamics with very high temporal and spatial resolution.

In our recent experimental study performed at the Linac Coherent Light Source (LCLS), we employed femtosecond X-ray pulses to directly map charge transfer dynamics upon inner-shell ionization of iodomethane molecules (CH_3I). As sketched in Fig. 1, we first dissociated the molecule using a femtosecond infrared (IR) laser, and then ionized the system with an intense X-ray pulse of 1.5 keV photon energy arriving after a controlled time delay. The X-ray pulse predominantly interacted with the iodine M-shell electrons, creating high charge states of iodine through sequential absorption of multiple photons, similar to observations made earlier for xenon [3]. By precisely measuring the kinetic energies of all ionic fragments created in this two-step process, we were able to disentangle different reaction channels initiated by the IR pulse and, thus, to determine the dissociation velocities of the individual channels. This enabled us to study the electron transfer after ionization by the FEL pulse as a function of internuclear separation between the iodine ion and the neutral methyl group fragment (CH_3).

As the time between the initial dissociation by the IR pulse and the X-ray pulse arrival increases, the molecular fragments depart from each other, changing the system from a bound molecule into separated atoms. Thereby, the kinetic energy of the iodine ion itself served as an indicator for the existence of charged neighbours, which would change the energy due to Coulomb repulsion of positive charges. The two-dimensional colour map in Fig. 2 shows the kinetic energy of the iodine ions as a function of pump-probe delay. In this way, we were able to investigate the probability of charge, namely electrons, being transferred from the neutral methyl group to the iodine ion. As is also shown in Fig. 2, the charge transfer probability decreases from one to zero as a function of delay-time, i.e. internuclear separation. The distance at which charge transfer effectively stops increases with higher charge states of iodine. For the case of iodine 14+ as well as for higher charge states, charge transfer was observed for distances exceeding 20 Angstroms, which is about 10 times the equilibrium bond length of the carbon-iodine bond in CH_3I. We have shown that this distance can be estimated from a classical over-the-barrier model developed earlier for ion-atom collisions [4]. Similar results have been recently obtained at FLASH for electron transfer after iodine O-shell dissociation in an XUV-pump – XUV probe experiment [5].

The present study was facilitated by the availability of a cross-correlation system between optical and FEL X-ray pulses on a shot-by-shot basis [6]. This allowed us to precisely measure the time delay and to sort the data after the measurements in order to overcome the time resolution that is otherwise limited by the ~300 fs jitter between the optical and the accelerator based system. With the cross-correlation measurements, we were able to achieve a temporal resolution of about 110 fs.

The CAMP chamber [7], which was used for the experiment at the LCLS, has now been installed at the BL1 beamline of FLASH as a permanent endstation that is available to all users for imaging and pump-probe experiments.

This study shows the capabilities of FELs to study chemical dynamics in experiments utilizing well-synchronized optical pulses and X-ray pulses. Planned upgrades improving the synchronization and decreasing the pulse duration will soon allow for detailed studies of processes where electron migration and nuclear motion happen on similar time-scales and the Born-Oppenheimer approximation, which allows separating electronic and nuclear motion, is no longer valid.

Contact: Benjamin Erk, benjamin.erk@desy.de
Artem Rudenko, rudenko@phys.ksu.edu

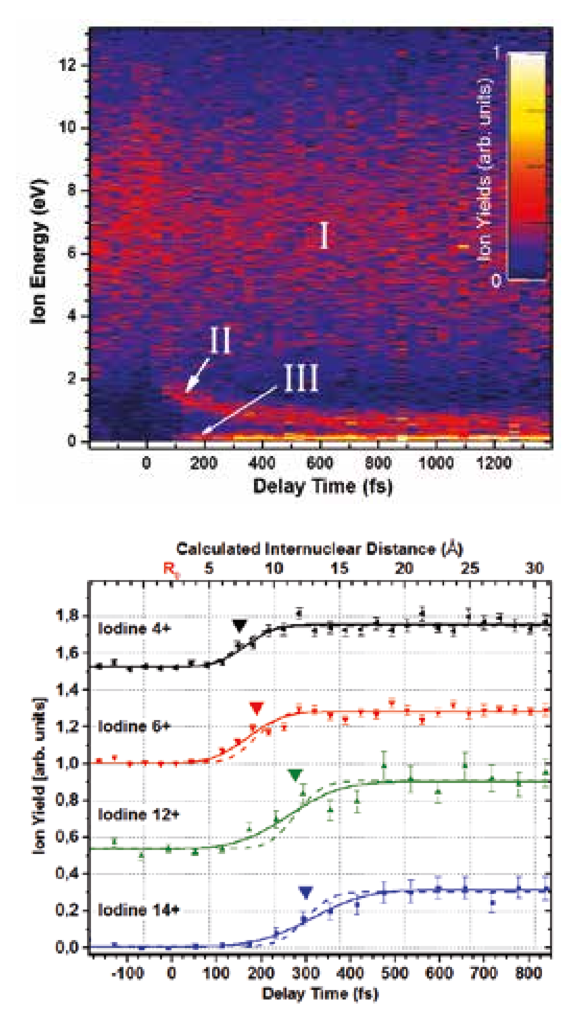

Figure 2

Top: Kinetic energy of iodine 6+ ions as a function or IR – X-ray delay. The lowest energy channel III represents iodine ions which have a neutral fragmentation partner and thus are not influenced by Coulomb repulsion. Bottom: Delay-dependent yields of iodine fragments of this low-energy channel from the iodomethane dissociation into I^{n+} and neutral CH_3. As the iodine charge increases, the distance, up to which charge transfer can occur, also increases. The experimentally determined critical distance, where charge transfer can no longer occur, agrees well with predictions from a simple classical model which are indicated as coloured triangles.

Authors

Benjamin Erk[1,2,3], Rebecca Boll[1,2,3], Sebastian Trippel[4], Denis Anielski[1,2,3], Lutz Foucar[2,5], Benedikt Rudek[2,3,6], Sascha W. Epp[2,3], Ryan Coffee[7], Sebastian Carron[7], Sebastian Schorb[7], Ken R. Ferguson[7], Michele Swiggers[7], John D. Bozek[7], Marc Simon[8,9], Tatiana Marchenko[8,9], Jochen Küpper[4,10,11], Ilme Schlichting[2,5], Joachim Ullrich[6,2,3], Daniel Rolles[1,2,5], and Artem Rudenko[12,2,3]

1. DESY Photon Science, 22607 Hamburg, Germany
2. Max Planck Advanced Study Group at CFEL, 22607 Hamburg, Germany
3. Max-Planck-Institut für Kernphysik, 69117 Heidelberg, Germany
4. Center for Free-Electron Laser Science, CFEL, DESY, 22607 Hamburg, Germany
5. Max-Planck-Institut für Medizinische Forschung, 69120 Heidelberg, Germany
6. Physikalisch-Technische Bundesanstalt, 38116 Braunschweig, Germany
7. Linac Coherent Light Source, SLAC National Accelerator Laboratory, 94025 Menlo Park, CA, USA
8. Sorbonne Universités, UPMC Université Paris 06, Laboratoire de Chimie Physique Matière et Rayonnement, 75005 Paris, France
9. CNRS, Laboratoire de Chimie Physique Matière et Rayonnement, 75005 Paris, France
10. Department of Physics, University of Hamburg, 22761 Hamburg, Germany
11. The Hamburg Centre for Ultrafast Imaging (CUI), 22761 Hamburg, Germany
12. J. R. Macdonald Laboratory, Department of Physics, Kansas State University, Manhattan, KS 66506, USA

Original publication

"Imaging charge transfer in iodomethane upon x-ray photoabsorption",
Science 345, 288 (2014). DOI: 10.1126/science.1253607

References

1. V. May and O. Kühn, "Charge and energy transfer dynamics in molecular systems", Wiley-VCH, Weinheim, 2011.
2. F. Lepine, M. Yu. Ivanov, and M. J. J. Vrakking, "Attosecond molecular dynamics: fact or fiction?", Nature Photon. 8, 195 (2014).
3. B. Rudek et al., "Ultra-Efficient Ionization of Heavy Atoms by Intense X-Rays", Nature Photon. 6, 858 (2012).
4. A. Niehaus, "A classical model for multiple-electron capture in slow collisions of highly charged ions with atoms", J. Phys. B 19, 2925 (1986).
5. K. Schnorr et al., "Electron Rearrangement Dynamics in Dissociating I_2^{n+} Molecules Accessed by Extreme Ultraviolet Pump-Probe Experiments", Phys. Rev. Lett. 113, 073001 (2014).
6. S. Schorb et al., "X-ray-optical cross correlator for gas-phase experiments at the LCLS free-electron laser", Appl. Phys. Lett. 100, 121107 (2012).
7. L. Strüder et al., "Large-format, high-speed, x-ray pnCCDs combined with electron and ion imaging spectrometers in a multipurpose chamber for experiments at 4th generation light sources", Nucl. Inst. Meth. A 614, 483 (2010).

High-energy SXRD for fast surface structure determination.

Probing a model catalyst under working conditions

Understanding the interaction between surfaces and their surroundings is crucial in many materials science fields, such as catalysis, corrosion, and thin-film electronics, but existing characterization methods have not been capable of fully determining the structure of surfaces during dynamic processes. We demonstrate how the use of high-energy photons (85 keV), in combination with a large two-dimensional detector for surface X-ray diffraction, increases the data acquisition speed by several orders of magnitude and enables structural determinations of surfaces on time scales suitable for *in situ* studies. We illustrate the potential of high-energy surface X-ray diffraction by determining the structure of a palladium surface *in situ* during catalytic carbon monoxide oxidation

Surface X-ray diffraction (SXRD) is one of few methods available for surface structure determination under ambient conditions. Due to the broken periodicity at the surface, the diffraction pattern (or the reciprocal lattice) will, in addition to Bragg reflections originating from the bulk, include so-called crystal truncation rods (CTRs), which connect the Bragg reflections *perpendicular* to the surface. In case the in-plane periodicity at the surface differs from that of the underlying bulk, additional superstructure rods arise in reciprocal space, and the shapes, positions and directions of these CTRs and superstructure rods hold detailed information about the atomic surface structure.

A schematic map of the reciprocal lattice of the Pd(100) crystal surface used in our study, including Bragg reflections (blue spots) as well as CTRs (blue lines) is shown in Fig. 1A. With a certain orientation between the incoming X-ray beam and the sample, the Ewald sphere defines the surface within reciprocal space that is giving rise to the diffraction pattern. In order to probe a certain point in reciprocal space, the sample is rotated such that the Ewald sphere intersects this point, and the detector is placed so that it collects the corresponding diffracted beam. Traditionally, point or small two-dimensional (2D) detectors are used to measure a limited part of reciprocal space simultaneously. Consequently, exploring 2D maps from a substantial part of reciprocal space is very time consuming, and mapping of the 3D reciprocal space with high resolution was hardly feasible even with synchrotron radiation.

By increasing the energy of the X-ray beam from the conventional 10 – 30 keV to 85 keV, as done in this study, the diffraction angles get smaller and a significant part of reciprocal space can be measured simultaneously by a stationary, large 2D detector. The grey surface intersecting the map of the reciprocal lattice in Fig. 1A shows the part of the Ewald sphere which is probed by the detector in our experiment. The corresponding detector image is shown in Fig. 1B, where the CTRs intersecting the Ewald sphere are clearly visible together with the shadows of tungsten pieces placed in front of the detector in order to protect it from the high intensity of the Bragg reflections. To map out the reciprocal space, the sample (and hence the reciprocal lattice) is rotated around the surface normal, such that the Ewald sphere scans through the reciprocal space. The result is a 3D data set of the diffraction from the sample surface, the scan takes on the

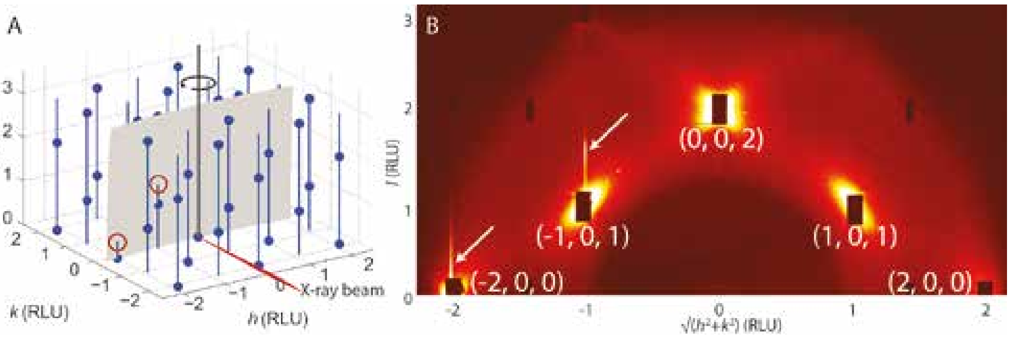

Figure 1

(A) Illustration of how CTRs from a clean Pd(100) surface cross the Ewald sphere during sample rotation. The rotational axis for the measurements is shown. (B) The corresponding detector image in which the Bragg reflections from the Pd substrate are indexed, and the lines where CTRs cross the Ewald sphere are marked with arrows. The dark rectangles at the position of Pd Bragg reflections stem from absorbers protecting the detector.

order of 10 minutes. This enables full surface structure determinations *in situ* during catalytic reactions, which has not been possible before.

We illustrate the power of High-Energy (HE)SXRD by studying the surface oxide formed on Pd(100) during CO oxidation under semi-realistic conditions at PETRA III beamline P07. The surface oxide, as known from *ex situ* UHV studies, is a single PdO(101) plane exhibiting a ($\sqrt{5}\times\sqrt{5}$)-R27° periodicity (hereafter denoted $\sqrt{5}$), as shown in Fig. 2A [1,2]. The corresponding diffraction is summarized in Fig. 2. In Fig. 2B, we show the result of combining 900 detector images to render the maximum-intensity result for each pixel. Such a projection onto the rotational plane provides a direct view of all the CTRs (indexed below the image) and superstructure rods (indexed above) within the probed volume. One can immediately identify the different structures present at the surface and draw some qualitative conclusions. For instance, the X-ray scattering intensity corresponding to the superlattice rods contains no Bragg reflections, indicating that the oxide film is very thin. To allow comparison of the results obtained by HESXRD with those expected from LEED, which is the most common surface diffraction method used under UHV conditions, we show a slice in the *hk*-plane of the HESXRD data around $l = 0.5$ reciprocal lattice unit (RLU) (Fig. 2C). Projected onto the data is a map of the reciprocal lattice corresponding to the Pd(100) substrate (green squares) and the surface oxide (red dots and circles). A zoom-in (Fig. 2D) shows the spots at $(h, k) = (0.4, -0.8)$, $(0.6, -0.8)$, $(0.8, -0.6)$, and $(0.8, -0.4)$, corresponding to the periodicity of the $\sqrt{5}$ structure. It is, however, apparent that these spots are not perfectly in the $\sqrt{5}$ periodicity but that there is a stress-induced mismatch between the oxide and the substrate, as has been reported previously [2].

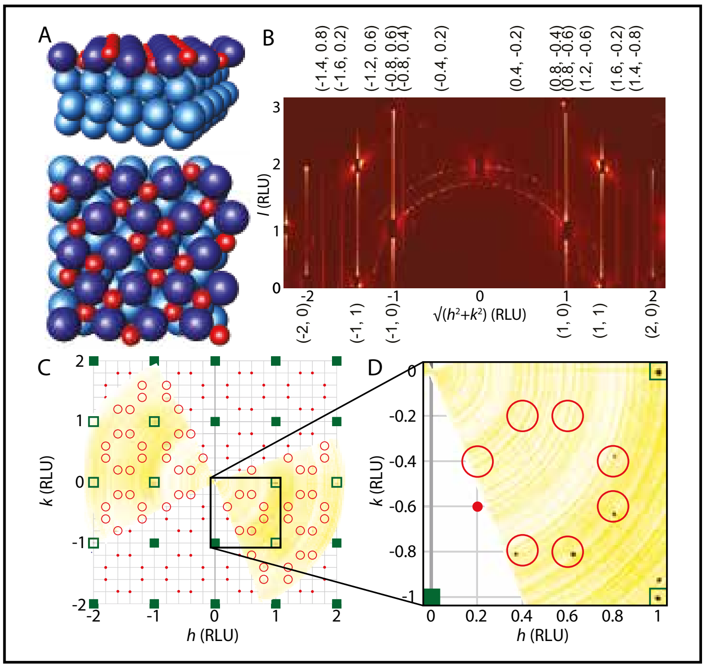

Figure 2

In situ HESXRD data from the surface oxide on Pd(100) measured during CO oxidation. (A) Side and top view of the oxygen-induced ($\sqrt{5}\times\sqrt{5}$)-R27° surface structure. The structure is an O-Pd-O trilayer corresponding to one PdO(101) plane [1,2]. (B) All images collected during the rotational scan combined into a single image in which the CTRs and superlattice rods are indicated. (C) In-plane view (*hk*-plane around $l = 0.5$) of the angular range measured in the current experiment. The Pd CTRs (squares) and surface oxide superlattice rods (circles) are indicated. (D) Magnification of reciprocal space showing the superlattice reflections. The reflections are not in the middle of the red circle, directly revealing the mismatch between the PdO(101) and the Pd(100) substrate.

In addition to providing a complete data set for qualitative analysis, as illustrated in Fig. 2, the quality of the data is good enough in order to extract data for quantitative analysis of the atomic positions. Hence, a full surface structure determination can be performed in the order of 10 min, instead of around 10 hours with conventional SXRD. Further, a single detector image reveals a significantly larger part of reciprocal space, which means we can follow dynamic processes at the surface with a subsecond time resolution. For more details, see the original publication and [3].

Contact: Johan Gustafson, johan.gustafson@sljus.lu.se

Authors

J. Gustafson[1], M. Shipilin[1], C. Zhang[1], A. Stierle[2,3], U. Hejral[2,3], U. Ruett[2], O. Gutowski[2], P.-A. Carlsson[4], M. Skoglundh[4], and E. Lundgren[1]

1. Synchrotron Radiation Research, Lund University, Box 118, 221 00 Lund, Sweden
2. Deutsches Elektronen-Synchrotron (DESY), 22603 Hamburg, Germany
3. Fachbereich Physik Universität Hamburg, Jungiusstrasse 9, 20355 Hamburg, Germany
4. Competence Centre for Catalysis, Chalmers University of Technology, 412 96, Göteborg, Sweden

Original publication

"High-Energy Surface X-ray Diffraction for Fast Surface Structure Determination", Science 343, 758-761, (2014). DOI: 10.1126/science.1246834

References

1. **M. Todorova, E. Lundgren, V. Blum, A. Mikkelsen, S. Gray, J. Gustafson, M. Borg, J. Rogal, K. Reuter, J. N. Andersen, M. Scheffler, "The Pd(100)–($\sqrt{5}\times\sqrt{5}$)R27°-O surface oxide revisited", Surf. Sci. 541, 101-112 (2003).**
2. **P. Kostelnik, N. Seriani, G. Kresse, A. Mikkelsen, E. Lundgren, V. Blum, T. Šikola, P. Varga, M. Schmid, "The Pd(100)-($\sqrt{5}\times\sqrt{5}$)R27°-O surface oxide: a LEED, DFT and STM study", Surf. Sci. 601, 1574-1581 (2007).**
3. **M. Shipilin, U. Hejral, E. Lundgren, L. R. Merte, C. Zhang, A. Stierle, U. Ruett, O. Gutowski, M. Skoglundh, P.-A. Carlsson, J. Gustafson, "Quantitative surface structure determination using *in situ* high-energy SXRD: Surface oxide formation on Pd(100) during catalytic CO oxidation", Surf. Sci. 630, 229-235 (2014).**

Nanoscopic control of tandem polymer solar cells.

X-ray imaging paves the way for novel solar cell production

The highly coherent beam delivered via the nano-focusing lenses at beamline P06 enabled an unprecedented 3D resolution of a complete polymer solar cell. We used ptychographic tomography to verify the integrity of the delicate intermediate layer of a roll-coated tandem polymer solar cell. The preparation of this intermediate layer proved to be critical for the performance of the tandem solar cell, coated entirely from solution, to ensure a defect-free and electronically functional recombination layer. The intermediate layer has sufficient solvent resistance to survive the coating with subsequent layers. We have documented this with high-resolution 3D microscopy that also illustrates some of the requirements to achieve this.

The realization of a complete polymer solar cell, where the different layers are coated from solutions onto a flexible substrate, results in a fully scalable production process. The solar cells can be produced fast and cheap, and in almost any desired length – up to several 100 metres long serially connected solar cell modules have already been manufactured. However, the energy harvesting efficiency is not very high (1.6 % power conversion efficiency) [1]. To increase the efficiency, much interest is focused on extending the technology to tandem solar cells, where two such single junction solar cells are stacked onto each other. Each of these absorbs a different part of the solar spectrum, so that the resulting tandem polymer solar cell converts more of the incoming sunlight into electric energy.

Each added layer in the multilayer coating presents new challenges: Already coated material may be dissolved by the solvent from the following layer, causing complete failure of the solar cell. We were able to prevent this by using a combination of two different polymer dispersions and zinc oxide in the intermediate layer as shown in Fig. 1a. The polymer dispersions consist of poly(3,4-ethylenedioxythiophene), which is conducting, and polystyrene sulfonate (PEDOT:PSS). This layer combination was able to withstand dissolution during coating of the second solar cell from chlorobenzene, protecting the integrity of the underlying first solar cell.

To investigate the morphology of the intermediate as well as the other layers of the tandem solar cell, we used the coherent X-ray beam at P06 at PETRA III to reveal finest details of the delicate solar cell structure, consisting of twelve individual layers altogether. We employed ptychographic tomography to examine the layer structure in detail. The method reconstructs the three-dimensional shape and electron density of the sample from the way it diffracts the incoming X-rays. For a full 3D reconstruction a great number of overlapping X-ray diffraction images have to be recorded from all sides. The advantage of ptychography is that it yields a higher resolution than conventional X-ray imaging alone and a better sensitivity

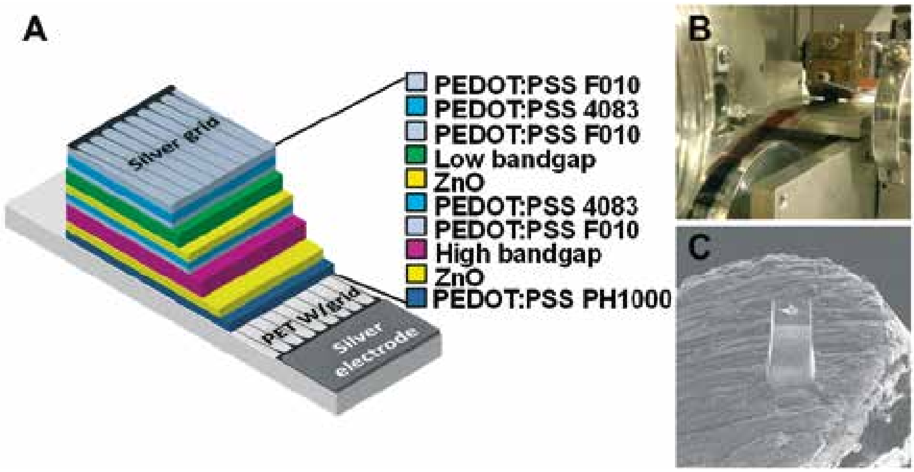

Figure 1

a) Layer architecture of the tandem polymer solar cell. The intermediate layer constitutes ZnO + PEDOT:PSS 4083 and F010.

b) Coating test of an active layer of poly(3-hexyl)thiophene/fullerene on the *in situ* grazing incidence small angle X-ray scattering setup at DTU [5] used to determine solvent resistance of the intermediate layer.

c) The tandem solar cell cut out with focused ion beam to a prism of 2.3 × 2.3 μm^2 in cross-section for ptychographic tomography.

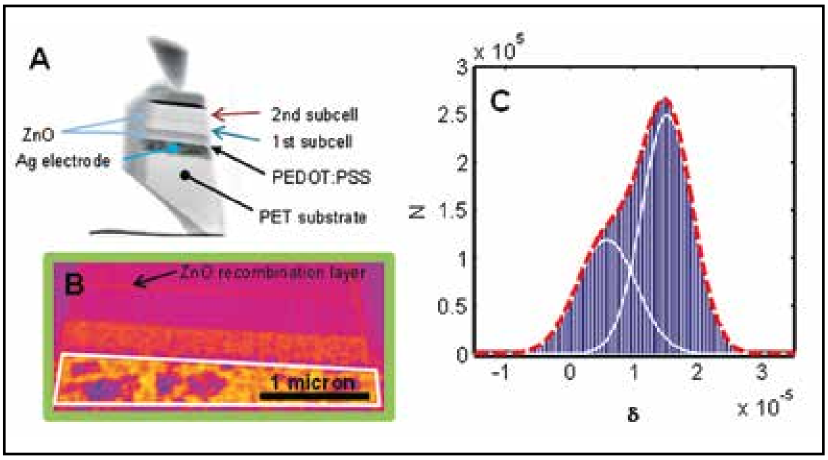

Figure 2

a) A single 2D ptychographic phase contrast projection of the polymer tandem solar cell stack (two microns across). The triangular pin on top of the sample is the tip of the needle used to manipulate the sample during microscopy. b) A slice through the 3D volume of the polymer tandem solar cell, reconstructed from ptychographic projections. The 40 nm thin ZnO layer is seen in the top of the image. The white polygon shows part of the “Flextrode” substrate electrode, consisting of nano-particulate silver, with a coating of PEDOT:PSS. c) Histogram of refractive indices in the reconstructed silver electrode volume outlined in b), fitted by two Gaussian functions corresponding to silver and PEDOT:PSS, showing the very high porosity with just 60 % of the electrode volume occupied by solid silver. The void space is filled by matter with a refractive index that matches PEDOT:PSS.

for density variations in soft material consisting of mainly low atomic number elements. And, as opposed to electron microscopy, X-ray ptychography can also look deep inside the sample.

The principle of ptychography is to collect far-field diffraction patterns from the sample, illuminated by a localized coherent beam in a large number of overlapping steps, thus introducing a redundancy in the data set by oversampling, which is exploited to recover the phase information by iterative algorithms. With this method, we obtain the complex-valued projections of phase shifts through an extended sample, i.e. the usual requirement of coherent diffractive imaging, that the entire sample is illuminated by the coherent beam, is lifted. By combining phase projections from different angles, we obtain the 3D distribution of the X-ray refractive index which is directly related to electron density [2]. Because the size of the beam, focused by compound refractive lenses [3], is just 250 nm, the many overlapping illuminations limits the size of the sample to a few microns across, which was cut out from a functional solar cell using focused ion beam milling (see Fig. 1c).

With 3D ptychography of the highest spatial resolution achieved so far at P06, we were able to image the complete roll-coated tandem solar cell, verifying the integrity of the 40 nm thin zinc oxide layer in the intermediate layer that successfully preserved the underlying layers from solution damage. We also found that the combination of the good conductivity of a porous silver electrode with the good film forming ability of a conducting polymer that infiltrates the silver electrode (Fig. 2b and c), constitutes a substrate electrode with a smooth surface for the coating of the subsequent layers (“Flextrode” [4]). This allows the coating of very thin layers at very high speeds, still forming contiguous layers without pinholes.

Looking into the complete structure can also provide valuable information for a possible optimization of the device and the production process. In principle the devices are manufactured without knowing what the internal structure looks like in detail. But knowing the structure tells us which parameters we can modify, and which factors are important for the device architecture, for example the special type of substrate electrode, and the formulation of the intermediate layer.

The resulting polymer tandem solar cell converts 2.67 % of the incoming sunlight into electric energy, which is a factor of 7–8 below the efficiency of conventional solar cells. This is, however, the first example of a roll-to-roll coated tandem solar cell where the efficiency of the tandem device actually exceeds that of the individual sub-cell devices by themselves. The true tandem performance is confirmed by a high open-circuit voltage, close to the sum of the sub-cell voltages.

Contact: Jens Wenzel Andreasen, jewa@dtu.dk

Authors

Henrik F. Dam[1], Thomas R. Andersen[1], Emil B. L. Pedersen[1], Karl T. S. Thydén[1], Martin Helgesen[1], Jon E. Carlé[1], Peter S. Jørgensen[1], Juliane Reinhardt[2], Roar R. Søndergaard[1], Mikkel Jørgensen[1], Eva Bundgaard[1], Frederik C. Krebs[1] and Jens W. Andreasen[1]

1. Department of Energy Conversion and Storage, Technical University of Denmark (DTU), 4000 Roskilde, Denmark
2. Deutsches Elektronen-Synchrotron DESY, 22607 Hamburg, Germany

Original publication

“Enabling Flexible Polymer Tandem Solar Cells by 3D Ptychographic Imaging”, Advanced Energy Materials (2014) DOI: 10.1002/aenm.201400736

References

1. P. Sommer-Larsen, M. Jørgensen, R. R. Søndergaard, M. Hösel, F. C. Krebs, ”It is all in the Pattern – High-Efficiency Power Extraction from Polymer Solar Cells through High-Voltage Serial Connection”, Energy Technol. 1, 15-19 (2013)
2. M. Guizar-Sicairos, A. Diaz, M. Holler, M. S. Lucas, A. Menzel, R. A. Wepf, O. Bunk, “Phase tomography from x-ray coherent diffractive imaging projections”, Opt. Express 19, 21345 (2011).
3. C. G. Schroer, O. Kurapova, J. Patommel, P. Boye, J. Feldkamp, B. Lengeler, M. Burghammer, C. Riekel, L. Vincze, A. van der Hart, M. Küchler, ”Hard x-ray nanoprobe based on refractive x-ray lenses”, Appl. Phys. Lett. 87, 124103 (2005).
4. M. Hösel, R. R. Søndergaard, M. Jørgensen, F. C. Krebs, “Fast Inline Roll-to-Roll Printing for Indium-Tin-Oxide-Free Polymer Solar Cells Using Automatic Registration”, Energy Technol. 1, 102-107 (2013).
5. L. H. Rossander, N. K. Zawacka, H. F. Dam, F. C. Krebs, J. W. Andreasen, ”*In situ* monitoring of structure formation in the active layer of polymer solar cells during roll-to-roll coating”, AIP Advances 4, 087105 (2014).

Lipid molecules in driven motion.

Non-equilibrium dynamics of membranes studied by time-resolved diffraction

The molecular structure and dynamics of lipid model bilayers has been intensively studied as a model system for biological membranes, and also as a paradigmatic soft matter system. A characteristic spectrum of thermal shape and density fluctuations is described by dispersion relations, quantifying important physical properties of lipid membranes. However, investigations at high spatial and temporal resolution have to date been limited to thermal equilibrium. Generically, however, biological membranes are out-of-equilibrium. Using time resolved X-ray diffraction, utilizing the 40 bunch timing mode at the PETRA III storage ring for stroboscopic illumination, it became now possible to study out-of-equilibrium structural dynamics of lipid membranes, driven by surface acoustic waves for well controlled excitation. The results show that the internal bilayer structure begins to oscillate in response to the excitation.

The membrane as nature's most important interface is constantly subjected to external forces, for example due to osmotic pressure differences, the coupling to an active cytoskeleton, or to membrane proteins such as ion channels or pumps. These effects may change structural, dynamical and mechanical properties on a fundamental level [1], but are extremely challenging to track down. For a simple reason: biomolecules are by nature very mobile, and even without external forces they vibrate, turn and stretch considerably at ambient temperature. Because these movements constantly overlap, the membrane structure and dynamics can in most cases be experimentally determined only as an average [2]. In order to directly track the molecular dynamics, both the spatial and the temporal resolution have to be matched to molecular scales, and the excitation of membrane modes has to be synchronized to the probing picosecond X-ray pulses.

Using this stroboscopic approach in recent experiments carried out at beamline P08 [3,4], the molecular structure and nanosecond dynamics of lipid membranes was investigated subject to controlled electroacoustic excitation, see Fig. 1. A stack of lipid membranes was driven from equilibrium by coupling of a surface acoustic wave (SAW) into the film. The SAW standing wave emits a coherent phonon into the lipid stack, so that the membranes are forced to oscillate at MHz rate. For the experiment, the membrane vibrations needed to be precisely synchronized with the X-ray pulse frequency so that the X-ray flashes captured the movement of the membranes during different phases of the oscillation cycle. The reflection of X-ray light from the aligned membranes was then recorded at different phases (times), thereby giving access to the time-dependent structural changes. It was found that the forced oscillation is accompanied by a unexpected changes in the density profile of the bilayer. Instead of only a simple harmonic displacement of the bilayer (e.g. its centre of mass), the internal structure of the bilayer began to vibrate.

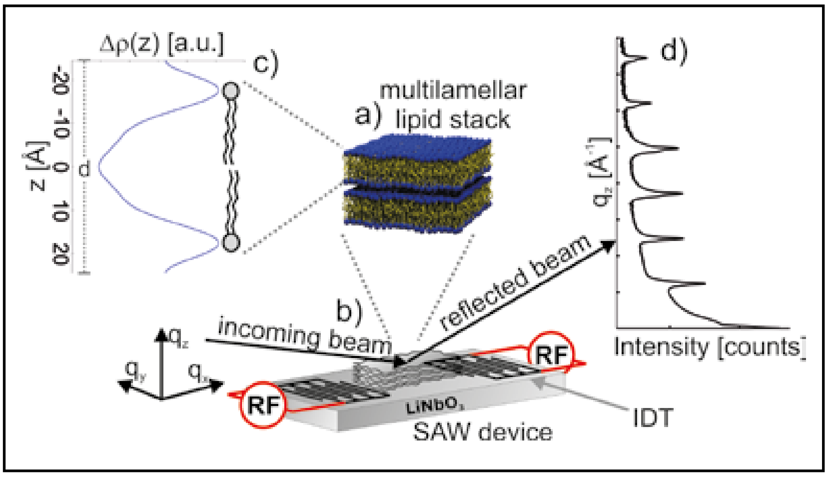

Figure 1

(a) Multilamellar stacks of lipid bilayers deposited on the piezoelectric LiNbO$_3$ substrate of a surface acoustic wave (SAW) device. (b) By application of a RF-signal to the interdigital transducers (IDTs), standing waves or propagating SAW pulses are induced. The ultrafast response of (c) the averaged bilayer electron density profile is measured by (d) time resolved (phase-locked) X-ray reflectivity experiments.

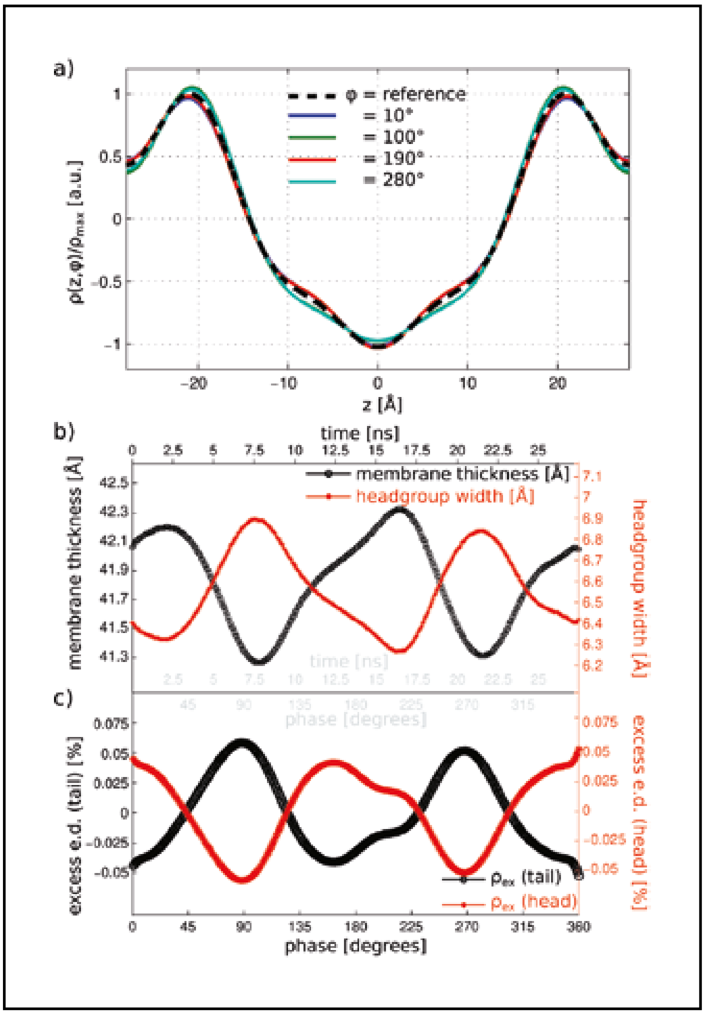

Figure 2

Structural dynamics of the lipid bilayer in response to the acoustic excitation by the SAW, as quantified by the time resolved electron density profile, shown for selected phase angles along with the equilibrium reference profile (dashed line). Pronounced variations of the resulting relative electron density are observed. The density variations are accompanied by a variation of membrane thickness. (b) Characteristic bilayer parameters (membrane thickness and headgroup width) extracted from the profile. The maxima in the headgroup width are accompanied by minima of the membrane thickness, and (c) a reduction of the electron density in the headgroup region (negative excess density) compensated by a density increase in the tail region (positive excess density).

SAWs have previously been shown to induce induce a number of phenomenal dynamic effects in soft matter films and samples deposited on top of the piezoelectric substrate, such as phase separation [5]. To some extent the electro-acoustic fields can mimic the effects of external forces which act on biomolecular assemblies or membranes in a biological environment. Up to now, however, the limited experimental resolution has impeded clear cut explanations of many such phenomena, since the spatial and temporal scales of the molecular dynamics have not been accessed. Using time-resolved diffraction in the 40 bunch mode of PETRA III with 192 ns bunch spacing, which eliminates the need of a chopper, structural resolution on the sub-nm scale can now be combined with temporal resolution on the picosecond scale. This has enabled the present observations. From the data shown in Fig. 2, one can infer how a macroscopic acoustic wave couples to the arrangement and conformations of lipids and water. The periodic changes in thickness and density can be explained by collective stretching and compression of the lipid molecules. Estimations show that inertia effects can explain the response of the ‘soft’ system, given the experimental velocities and accelerations on the order of 1 nm/ns and 1 nm/ns^2, respectively. These values are close to what can be expected also in a biological system and shows that collective conformational changes on molecular scales can be an important component in the response to externally applied forces.

Contact: Tim Salditt, tsaldit@gwdg.de

Authors

Tobias Reusch[1], Florian J. R. Schülein[3], Jan-David Nicolas[1], Markus Osterhoff[1], Andre Beerlink[4], Hubert J. Krenner[3], Marcus Müller[2], Achim Wixforth[3], Tim Salditt[1]

1. Institut für Röntgenphysik, Georg-August-Universität Göttingen, Friedrich-Hund-Platz 1, 37077 Göttingen, Germany
2. Institut für Theoretische Physik, Georg-August-Universität Göttingen, Friedrich-Hund-Platz 1, 37077 Göttingen, Germany
3. Lehrstuhl für Experimentalphysik I, Universität Augsburg, Universitätsstr. 1, 86159 Augsburg, Germany
4. Deutsches Elektronen-Synchrotron DESY, Notkestrasse 85, 22605 Hamburg, Germany

Original publication

“Collective Lipid Bilayer Dynamics excited by Surface Acoustic Waves”. Phys. Rev. Lett. 113, 118102 (2014). DOI: 10.1103/PhysRevLett.113.118102

References

1. S. Ramaswamy, J. Toner, and J. Prost, “Nonequilibrium fluctuations, traveling waves, and instabilities in active membranes.” Phys.Rev. Lett. 84, 3494, (2000).
2. M. C. Rheinstädter, W. Häussler, T. Salditt, “Dispersion Relation of Lipid Membrane Shape Fluctuations by Neutron Spin-Echo Spectrometry”, Phys. Rev. Lett. 97, 48103 (2006).
3. T. Reusch , F.. J. R. Schülein, C. Böhmer, M. Osterhoff, A. Beerlink, H. J. Krenner, A. Wixforth, Tim Salditt, “Standing surface acoustic waves in $LiNbO_3$ studied by time resolved X-ray diffraction at PETRA III”, AIP Advances 3, 072127 (2013).
4. O. H. Seeck et al., “The high resolution diffraction beamline P08 at PETRA III”, J. Synchrotron Rad. 19, 30 (2012).
5. M. Hennig, M. Wolff, J. Neumann, A. Wixforth, M. F. Schneider, and J. O. Raedler, “DNA concentration modulation on supported lipid bilayers switched by surface acoustic waves”, Langmuir 27, 14721 (2011).

Degradation in polymeric solar cells.

A live broadcast

As efficiencies of organic photovoltaics have crossed the symbolic 10 % limit, their breakthrough as a versatile and cheap source of electricity becomes more and more evident. These non-toxic devices can be easily produced on a large scale and allow for a very broad field of application due to their mechanical flexibility and optional transparency. A challenge still to overcome arises, however, from their limited lifetime. Thus, fundamental understanding of all involved device degradation mechanisms is essential. We show the first *in-operando* grazing incidence small angle X-ray scattering study of such a solar cell addressing the morphological degradation: By simultaneously probing both, the electrical characteristics and the active layer's morphology, we find a coarsening of nanostrucures accompanied by a loss of current output. The presented model, which fully explains the loss of current by the observed structural changes, gives direct evidence of morphological degradation in organic photovoltaics for the first time

A promising approach to produce organic photovoltaics comes from polymer-fullerene blend thin films as active layers, where interpenetrating domain networks of both materials on a nanometre scale form upon film application from a mature blend solution. In such a so-called bulk heterojunction type active layer [1], visible light can be efficiently converted into electric current. In order to improve both, efficiency and lifetimes of these photovoltaic films, it is, however, necessary to fully understand the nano morphology and the structure-function relation [2] of active layers after fabrication and during operation. Advances in modern scattering techniques, especially in the field of grazing incidence small angle X-ray scattering allow for ongoing growth of the understanding of the blend film morphology [3]. In particular, recent progress at the Micro- and Nanofocus X-ray Scattering beamline P03 at PETRA III (MiNaXS) [4] enables high-quality data even with short X-ray exposure times on the order of subseconds [5]. With such a high beam brilliance, *in situ* scattering studies on polymer-based solar cells have become possible. In this very first *in-operando* study, we follow structural changes of the active layer in real time and provide direct evidence for morphological degradation on a nanometre scale in a polymer-based model solar cell.

Therefore, an operational poly(3-hexylthiophene-2,5-diyl): phenyl C_{60} butyric acid methyl ester (P3HT:PCBM) bulk-heterojunction solar cell was simultaneously probed by grazing incidence small angle X-ray scattering (GISAXS) and current-voltage (IV) tracking: In order to avoid oxidation of the solar cell as a well known degradation mechanism, it was kept under vacuum condition during the whole 7-hour experiment. The solar cell was illuminated with artificial sun light mimicking the solar spectrum (AM1.5G conditions) and cooled (< 45 °C) during the continuous tracking of IV curves. Using the microfocused X-ray beam of the MiNaXS beamline, GISAXS data of the active layer were taken before and during illumination with visible light and IV tracking. A schematic representation of the used *in-operando* setup is shown in Fig. 1.

From the GISAXS measurements we infer that pure polymer domains occur at different length scales from a few nm up to 150 nm. Amongst them we isolate a prominent intermediate

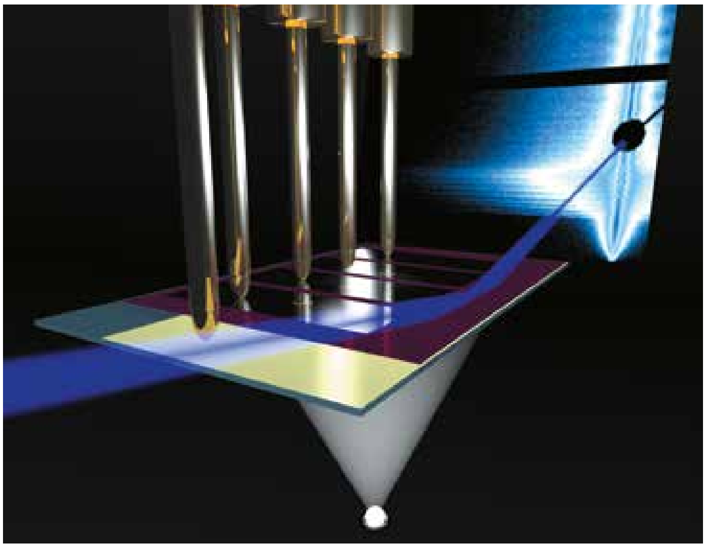

Figure 1

In-operando GISAXS and current-voltage tracking on a polymer-fullerene solar cell. Schematic illustration of the experimental setup used to evidence morphological changes in polymer-based solar cells as a driving force to degradation. An operational solar cell is placed in an evacuated chamber to suppress oxidation. Electrical contacts (golden rods coming from the top) allow for continuous current-voltage tracking, while the solar cell is illuminated with artificial sun light (bright spot at the bottom). The highly intense focused X-ray beam (blue beam) of beamline P03 at the PETRA III storage ring impinges the polymer-fullerene blend film close to its electrical contacts under a shallow angle and scatters towards a 2D detector, where grazing-incidence small angle X-ray scattering data are obtained after different durations of solar cell operation.

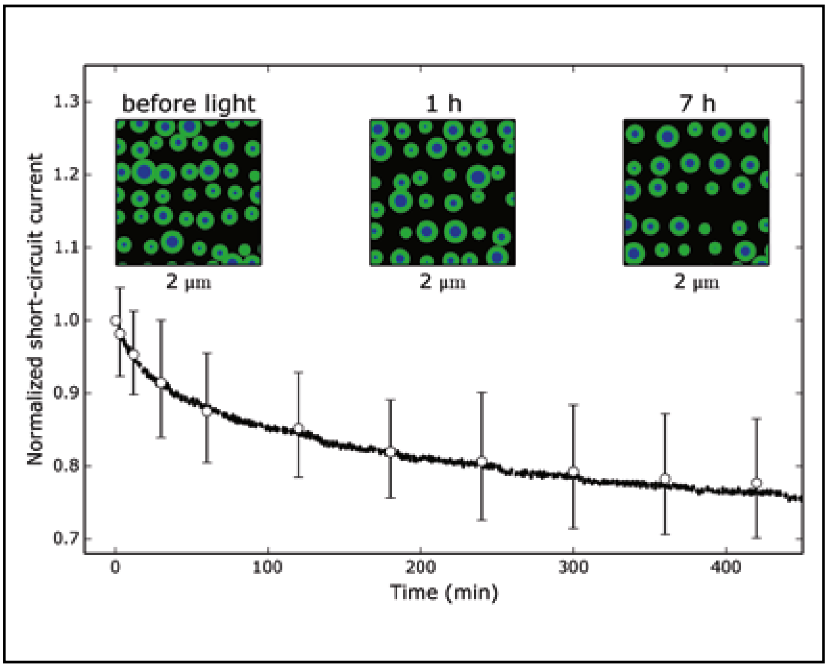

Figure 2

Correlation of morphology and current output. The dashed black line displays the measured short-circuit current. The open symbols show the short-circuit current as expected from the GISAXS findings and the model described above. The inlets show an illustration of active domain morphology (green rings) around pure polymer domains (blue circles) in an inactive matrix (black) as obtained from Monte-Carlo simulations based on GISAXS findings before and after one and seven hours of solar cell operation. Hereby, active domains grow with time while their inter distance increases simultaneously. The latter increase outweighs the domain growth and leads to the loss of short-circuit current.

length scale with feature radii on the order of 30 to 40 nm and a corresponding inter distance between 300 and 400 nm. As the size of these domains is similar to the typical exciton diffusion length in the polymer under investigation, these domains are assumed to mainly determine the electrical current generation. While mean radii and distances are found to be 34 and 310 nm in the beginning of the experiment, we observe both to grow monotonically to 40 and 370 nm, respectively during the first seven hours of solar cell operation. In the same time, the short-circuit current (black line in Fig. 2) decreases by roughly 25 %.

We introduce a geometrical 2D model to explain the generation of current in the active layer. In this model, pure polymer domains are assumed as the centres (blue dots in the inlets of Fig. 2) of active areas (green disks in the inlets of Fig. 2) which allow for current generation. Hereby, photons that are absorbed within a certain fixed distance to these centres contribute to electricity generation whereas photons that are absorbed at a further distance do not. On the basis of this model, we are able to calculate the short circuit current density at different times exclusively from the feature radii and inter distances obtained from the *in-operando* GISAXS measurements (open data points in Fig. 2). The growth of both, the size of active areas and their inter distance, display concurring effects, where the domain growth is beneficial for the current output whereas the growing distance is not. Finally, the increase of distance outweighs domain growth and leads to a loss of current output. This scenario is schematically depicted in the inlets of Fig. 2, which show exemplary illustrations of the morphology at different times as obtained from our Monte-Carlo simulation based on the GISAXS findings.

From the excellent agreement of measured and predicted short circuit current we conclude that the loss of short circuit current is mainly driven by the morphological changes that occur during solar cell operation, giving a first evidence for morphological degradation of polymer solar cells on a nanometre scale. These findings may pave the way to more stable polymer solar cells.

Contact: Peter Müller-Buschbaum, muellerb@ph.tum.de

Authors

Christoph J. Schaffer[1], Claudia M. Palumbiny[1], Martin A. Niedermeier[1], Christian Jendrzejewski[1], Gonzalo Santoro[2], Stephan V. Roth[2], and Peter Müller-Buschbaum[1]

1. Technische Universität München, Physik-Department, Lehrstuhl für Funktionelle Materialien, James-Franck-Str. 1, 85748 Garching, Germany
2. DESY Photon Science, Notkestr. 85, 22607 Hamburg, Germany

Original publication

“A Direct Evidence of Morphological Degradation on a Nanometer Scale in Polymer Solar Cells”, Advanced Materials 25, 6760-6764 (2013). DOI: 10.1002/adma.201304187

References

1. C. J. Brabec et al., “Polymer-Fullerene Bulk-Heterojunction Solar Cells”, Advanced Materials 22, 3839-3856 (2010).
2. M. A. Ruderer et al., “Solvent-Induced Morphology in Polymer-Based Systems for Organic Photovoltaics”, Advanced Functional Materials 21, 3382-3391 (2011).
3. P. Müller-Buschbaum, “The Active Layer Morphology of Organic Solar Cells Probed with Grazing Incidence Scattering Techniques”, Advanced Materials, DOI: 10.1002/adma.201302854 (2014).
4. A. Buffet et al., “P03, the microfocus and nanofocus X-ray scattering (MiNaXS) beamline of the PETRA III storage ring: the microfocus endstation”, Journal of Synchrotron Radiation 19, 647-653 (2012).
5. Kuhu Sarkar et al., “Monitoring Structural Dynamics of *In situ* Spray-Deposited Zinc Oxide Films for Application in Dye-Sensitized Solar Cells”, ChemSusChem 7, 2140-2147 (2014).

Chemical insight into resistive switching devices by HAXPES.

Probing the Ti / $Pr_{0.48}Ca_{0.52}MnO_3$ interface

Complex transition metal oxides may exhibit large electrically driven changes of resistance, thereby attracting considerable attention for the development of non-volatile storage devices. We have used core-level Hard X-ray Photoelectron Spectroscopy (HAXPES) to prove experimentally that resistive switching in Ti / $Pr_{0.48}Ca_{0.52}MnO_3$ / $SrRuO_3$ (Ti / PCMO / SRO) thin film heterostructures depends on a redox process occurring on the Ti side of the Ti / PCMO interface. The resistance states are determined by the amount of oxidized Ti ions in the stack, which is varied through a reversible redox-reaction leading to the formation and shortening of an insulating tunnel barrier.

Resistance random access memories (RRAMs) utilize two or more electrically induced resistive states of a system to act as data storage devices [1, 2]. Besides a large variety of binary oxides, also complex transition metal oxides exhibiting different resistance states at opposite polarities, e.g., manganites, titanates, and zirconates, could be employed as RRAMs. In particular, for many manganites the high and low resistive state currents scale with the electrode area, thereby implying that the mechanisms related to forming and switching among the resistive states take place beneath the whole area of the electrodes [3-5].

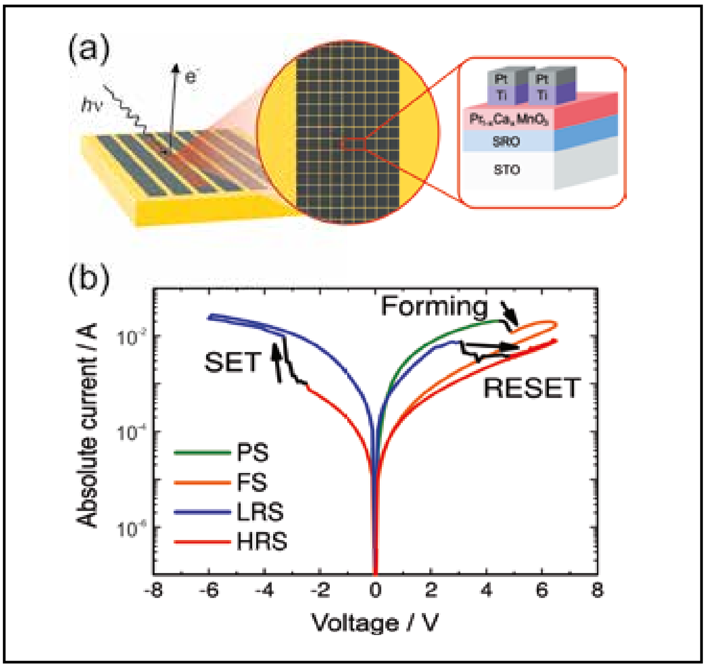

Figure 1

(a) Schematics of the patterned samples for the HAXPES measurements. The devices consisted of 30 nm SRO as bottom electrode and 20 nm PCMO epitaxial thin films, both grown *in situ* by pulsed laser deposition on TiO_2-terminated $SrTiO_3$ (001). The 7 nm Ti top electrode and the 3 nm of Pt capping layer were subsequently deposited by DC sputtering, then the Ti / Pt top electrode stack was patterned using photolithography.

(b) Typical I(V) curve of the Pt / Ti / PCMO / SRO / STO stack investigated by HAXPES. The voltage is applied to the Pt top electrode and the SRO is set on ground potential. The colours curves identify the electrical path passing from pristine (PS) to formed (FS) states, followed by switching between low (LRS) "SET" and high (HRS) "RESET" resistive states.

A crucial role in this process is played by the chemical states of the materials at the boundaries of these heterostructures which can be significantly different from the bulk. This feature concerns also the initial electro-forming treatment consisting of strong voltage stress application which is required to set and / or improve the change of the resistance for many perovskite compounds.

We have investigated this topic for Ti / $Pr_{0.48}Ca_{0.52}MnO_3$ / $SrRuO_3$ (Ti / PCMO / SRO) thin film devices through probing the Ti / PCMO interface by core-level HAXPES. This technique is able to provide sensitivity to the bulk up to 20 – 25 nm, thus large enough to perform non-destructive studies of deep regions and buried interfaces. In our study, the detection of small but significant chemical changes occurring at the Ti / PCMO boundary for two reversible resistance states of the device provides the spectroscopic proof of the correlation between redox-state and charge-carrier transport at this interface. These effects, being less pronounced with respect to those previously observed by us for the electro-forming treatment [6], have not been reported for a similar system so far.

The HAXPES measurements were performed at beamline P09 of the PETRA III source. The experimental geometry, summarized in Fig. 1(a), was chosen to maximize the bulk sensitivity for HAXPES measurements, with the angle between the incident X-ray beam and the electron analyzer set to 90° and the

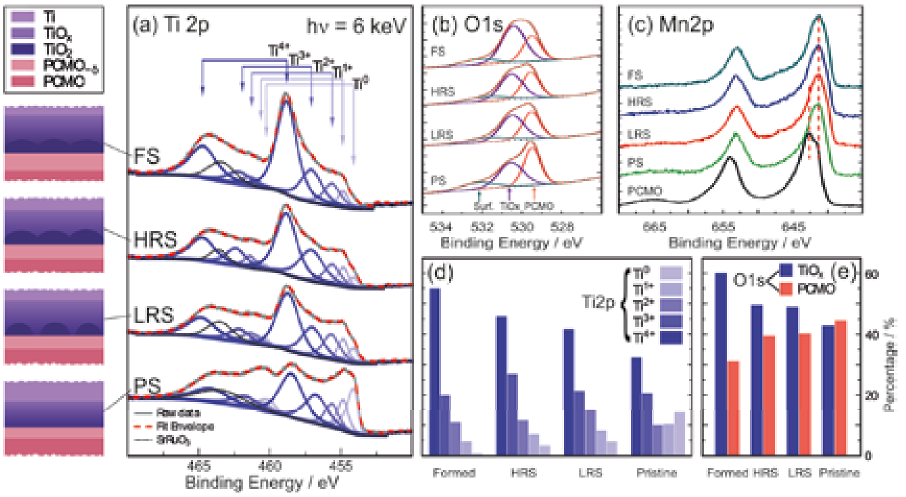

Figure 2

(a–c) Ti 2p, O 1s and Mn 2p HAXPES spectra for the four resistive states, sorted from low resistance (pristine) to high resistance (formed). The spectrum named PCMO refers to the unpatterned bare film used as reference sample. (d, e) Area percentages for the components of the Ti 2p and O 1s spectra, respectively. On the left, the qualitative model of the Ti/PCMO interface for each resistive state is reported. The sketches indicate the progressive oxidation for the Ti layer due to electromigration of oxygen ions promoted from the underlying PCMO while passing from low to high resistance states.

X-ray beam impinging on the sample at a grazing angle of 2°. The photon energy was set at 6 keV, with an overall resolution of 0.35 eV. All the measurements were performed at room temperature. Due to the large footprint of the X-ray beam, device arrays consisting of 50 × 50 μm^2 electrodes grouped in 7 stripes of 0.8 mm width, and spaced by 10 μm from each other, were fabricated. Every electrode in the stripe has been subjected to an identical electrical treatment.

The structure of the devices is reported in Fig. 1(a), while exemplary current–voltage behaviour is shown in Fig. 1(b). Considering the electrical behaviour, the initial resistance state after deposition of the top electrode is referred to as “pristine state” (PS). Electro-forming of the device is achieved by applying a positive voltage sweep, and is called “formed state” (FS). After forming, a negative voltage sweep sets the system into the “low resistance state” (LRS), and a subsequent sweep to a positive voltage resets the system into the “high resistance state” (HRS). The resistance of the four states can be sorted according to the order PS < LRS < HRS < FS.

The influence of the electrical treatment on the oxidation state of the top Ti electrode is shown in Fig. 2(a). The Ti 2p HAXPES spectra recorded for each resistive state exhibit distinct features corresponding to metallic Ti^0 and fully oxidized Ti^{4+}, respectively, particularly evident for the Ti $2p_{3/2}$ peak. The analysis of the spectra recognizes also the contribution of intermediate valence terms. The distribution of the fractional intensity for all Ti valence states is shown in Fig. 2(d). Noticeably, a monotonous decrease for the metallic Ti^0 line and increase of Ti^{4+} component with increasing resistance occurs. In a similar manner, Fig. 2(b) and Fig. 2(e) depict the O 1s spectra and the area percentage of their three constituent peaks, respectively. Similarly to the trend of the Ti spectra, a spectral weight transfer from the O1s terms to PCMO and TiO_x is observed. Moreover, the Mn 2p spectra representative of the PCMO layer, shown in Fig. 2(c), have a low binding energy shoulder at the Mn $2p_{3/2}$ line for all states, indicating a shift of the average Mn valence towards Mn^{3+} slightly enhanced by the electrical treatment, in agreement with oxygen removal from the PCMO.

The bulk sensitivity of the HAXPES spectra demonstrates that a redox-reaction is induced at the Ti/PCMO interface through electrical biasing, as qualitatively sketched in Fig. 2, thereby influencing the resistance of both Ti and PCMO layers and implying a direct role of the interfacial oxide in the resistivity of the device. This information has been essential to present a device model, inclusive of the chemical changes and the movement of oxygen vacancies expected from the direction of the applied field, which fits all the resistive states in a consistent way with a limited number of physically reasonable parameters.

Contact: Francesco Borgatti, francesco.borgatti@cnr.it

Authors

Francesco Borgatti[1], Anja Herpers[2], Christian Lenser[2*], Chanwoo Park[2], Francesco Offi[3], Giancarlo Panaccione[4], Stephan Menzel[2], Rainer Waser[2], and Regina Dittmann[2]

1. CNR – Istituto per lo Studio dei Materiali Nanostrutturati (ISMN) via P. Gobetti 101, 40129 Bologna, Italy
2. Peter Grünberg Institute Research Center, 52425 Jülich, Germany
3. CNISM and Dipartimento di Scienze Università Roma Tre, 00146 Rome, Italy
4. CNR – Istituto Officina dei Materiali (IOM) Laboratorio TASC, S.S.14, Km 163.5 34149 Trieste, Italy

*current address: Laboratory for Electrochemical Interfaces, Department of Nuclear Science and Engineering, Massachusetts Institute of Technology, 77 Massachusetts Avenue, Cambridge, MA 02139, USA

Original publication

“Spectroscopic Proof of the Correlation between Redox-State and Charge-Carrier Transport at the Interface of Resistively Switching Ti/PCMO Devices”, Adv. Mater. 26, 2730-2735 (2014).
DOI: 10.1002/adma.201304054

References

1. R. Waser and M. Aono, Nat. Mater. 6, 833 (2007).
2. R. Waser, R. Dittmann, G. Staikov, and K. Szot, Adv. Mater. 21, 2632 (2009).
3. A. Sawa, Mater. Today 11, 28 (2008).
4. M. Hasan, R. Dong, H. J. Choe, D.S. Lee, D. J. Seong, M. B. Pyun, and H. Hwang, Appl. Phys. Lett. 92, 202102 (2008).
5. R. Meyer, L. Schloss, J. Brewer, R. Lambertson, W. Kinney, J. Sanchez, and D. Rinerson, Proc. NVMTS, 54 (2008).
6. F. Borgatti, C. Park, A. Herpers, F. Offi, R. Egoavil, Y. Yamashita, A. Yang, M. Kobata, K. Kobayashi, J. Verbeeck, G. Panaccione, and R. Dittmann, Nanoscale 5, 3954 (2013).

Twisted X-rays reveal spin excitations in magnetic materials.

A proposed radar trap for spin waves

Collective magnetic excitations with energies ranging from neV to eV form the basis for dynamic processes involving the spin degree of freedom in condensed matter. The low-energy regime, however, is largely inaccessible for X-ray spectroscopic techniques that could reveal dynamical properties on atomic length scales. In order to reach a sufficient energy resolution an extremely narrow spectral bandwidth is required which reduces the useful photon flux to impractical values. On the other hand, if the photon polarization – instead of the photon energy – could be employed as carrier of spectral information, the energy resolution would be decoupled from the bandwidth of the probing X-rays. Resonant X-ray scattering from spinwaves exhibits exactly this property: it results in a polarization precession of the scattered X-rays from which information of the spinwave spectrum can be obtained independent of the X-ray spectral bandwidth.

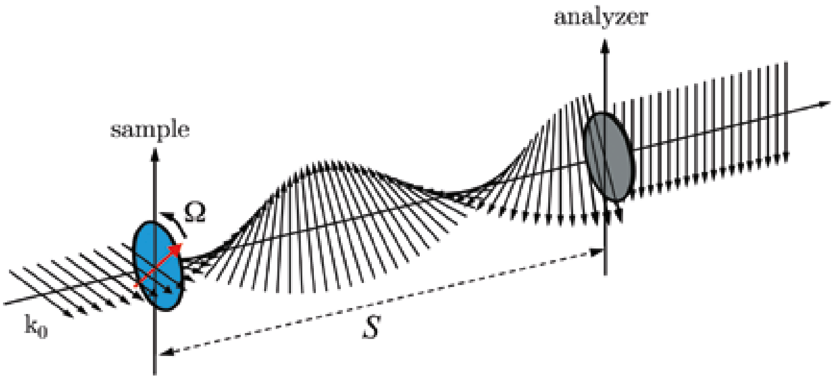

Figure 1

A half-wave plate where the anisotropy axis (e.g. the magnetization direction) rotates with angular frequency Ω converts incident linear polarization into a polarization that precesses with angular frequency 2Ω. The polarization state of the scattered photons is analysed as function of distance *S* by a linear polarizer that projects out a certain linear polarization state.

Great parts of modern information technology rely on the dynamics of magnetic materials on length scales that bridge several orders of magnitude. The rapid evolution of this field has been driven by questions like “How can a magnetic bit on a hard disk be switched most efficiently? How can magnetic spins be used as carrier of information in next-generation computers? What role does magnetism play in new types of high-temperature superconductivity?” A detailed investigation of these and related subjects requires to unravel the spectrum of magnetic excitations on relevant spatial and time scales with an energy resolution which is presently not available in the field of X-ray spectroscopy. Moving the resolution limit of magnetic spectroscopies into the regime of low-energy excitations eventually requires to abandon the paradigm to encode spectral information in the energy of the photons. It turns out that the photon polarization can carry spectral information instead, provided the scattering process is polarization sensitive. In this way it will be possible to decouple the energy resolution from the spectral bandwidth and to obtain µeV resolution with eV bandwidth, for example.

It is known since more than a century that circularly polarized light exerts a torque on an optically anisotropic element like a half-wave plate when transmitted through it [1,2]. Conversely, if the half-wave plate rotates, work is done on circularly polarized light which manifests itself in a frequency shift of the light [3]. This is the key to the spectroscopic method proposed here: The X-ray optical properties of a magnetic material resemble those of a half-wave plate provided the material exhibits an anisotropy that leads to X-ray linear dichroism. Then the precessing magnetic moments of a spin wave in such a material act like a rotating half-wave plate for X-rays, resulting in a time-dependent polarization rotation of the scattered photons that contains spectral information about the spinwaves.

The frequency shift of photons caused by a rotating half-wave plate is also known as the angular Doppler effect [4], in close analogy to the linear Doppler effect: A mirror that moves with linear velocity $\boldsymbol{v}$ leads to a linear Doppler shift $\boldsymbol{q}\cdot\boldsymbol{v}$ of the light which is reflected with momentum transfer $\boldsymbol{q}$. In case of back-reflection the light has experienced a reversal of its linear momentum, i.e. $\boldsymbol{q} = 2k_0$. A half-wave plate essentially acts as a back reflecting mirror in angular space because it reverts the spin angular momentum (helicity) of the photons transmitted through it, i.e., converting left-circular into right-circular

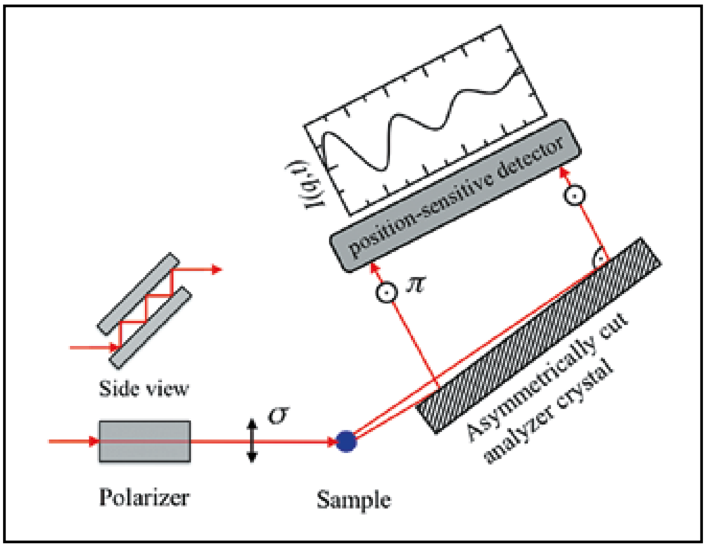

Figure 2

Scheme of the proposed experimental setup. The incident radiation from the source is σ-polarized with very high purity. The analyser, adjusted to momentum transfer q, selects the π-polarized component of the scattered radiation which is mapped onto a position sensitive detector, yielding the intermediate scattering function $I(q,t)$, of the magnetic excitations in the sample.

polarization and vice versa. Correspondingly, a half-wave plate (HWP) rotating with angular velocity Ω imparts an angular Doppler shift of $\Omega \cdot \boldsymbol{L}$ on the light that has experienced an angular momentum transfer of $\boldsymbol{L} = 2\hbar$ resulting from the reversal of its angular momentum. Therefore, when horizontally polarized light A_H interacts with a rotating HWP, its left- and right-circular components A_+ and A_- experience opposite frequency shifts of $\pm 2\Omega$, respectively: $[A_H]_{circ} = e^{-i2\Omega t} A_+ + ie^{i2\Omega t} A_-$. This can be visualized by writing it in a linear polarization basis, consisting of horizontal and vertical polarization unit vectors A_H and A_V: $[A_H]_{lin} = A_H \cos 2\Omega t + A_V \sin 2\Omega t$ which means that the polarization of the photons performs a precessional motion upon propagation in space, as illustrated in Fig. 1. If one of the two linear polarization components is filtered out by a linear polarizer and detected afterwards, one obtains a signal that oscillates with frequency $4\,\Omega$, corresponding to the frequency difference of the two circular polarization components.

Due to the opposite energy shifts of the circular polarization components there is no net energy transfer to a linearly polarized photon scattered off the sample. Instead, the information about the spinwave frequency is contained in the frequency difference between left- and right circular polarization components. Accordingly, the whole spinwave spectrum at a given momentum transfer is encoded in the precession of the photon's polarization as it evolves during propagation after the scattering process. In case of a distribution of spinwave frequencies, the photon polarization vectors fan out due to different precession frequencies so that the amplitude of the effective polarization vector of the photon is reduced. Thus, if the polarization is analysed as function of the propagation distance $\boldsymbol{S}$ behind the sample one obtains a quantity that resembles the intermediate scattering function $I(q,t)$ of inelastic X-ray scattering, with $t = \boldsymbol{S}/c$ being the propagation time of the photons from the sample to the analyser.

In order to ease the recording of $I(q,t)$ for a given q, the scattered radiation should be analysed by an asymmetrically cut single crystal with a Bragg angle very close to 45°, as illustrated in Fig. 2. In this geometry, unwanted polarization components are strongly suppressed and the function $I(q,t)$ is recorded by a one-dimensional detector. With realistic values for crystal dimensions and detector resolution, spinwaves within a range of 1–100 GHz can be detected. A unique feature of this proposed setup is that $I(q,t)$ for a given momentum transfer q can be recorded with a single shot of an X-ray laser, e.g., in combination with a pump-probe excitation scheme. If phase-locked to a periodic excitation process, similar studies can be done in a stroboscopic manner also at conventional synchrotron radiation sources.

Contact: Ralf Röhlsberger, ralf.roehlsberger@desy.de

Author

Ralf Röhlsberger
Deutsches Elektronen-Synchrotron DESY, Notkestraße 85, 22607 Hamburg, Germany

Original publication

"Polarization precession spectroscopy for high-resolution studies of spin waves",
Phys. Rev. Lett. 112, 117205 (2014). DOI: 10.1103/PhysRevLett.112.117205

References

1. J. H. Poynting, "The wave motion of a rotating shaft and a suggestion as to the angular momentum in a beam of circularly polarised light", Proc. Roy. Soc. (London) A82, 560 (1909).
2. R. A. Beth, "Direct detection of the angular momentum of light", Phys. Rev. 48, 471 (1935).
3. B. A. Garetz and S. Arnold, "Variable frequency shifting of circularly polarized laser light via a rotating half-wave retardation plate", Opt. Commun. 31, 1 (1979).
4. B. A. Garetz, "Angular Doppler Effect", J. Opt. Soc. Am. 71, 609 (1981).

Screening effects studied by VUV Raman spectroscopy – Every electron counts.

Magnetic excitations in correlated spin ladder compounds

Low-energy quasi-particle excitations are of high relevance as they drive the thermodynamic behaviour of condensed matter materials. Particularly important are transition metals in the form of transition-metal oxides. Examples are copper-oxide compounds such as the cuprates, which manifest high temperature superconductivity a still poorly understood phenomenon. A new VUV-Raman spectrometer with high resolution and a strong rejection of the elastic Rayleigh line at FLASH enables us to study the delicate interplay between electronic structure and low-energy quasi-particle excitations. We have shown the influence of electronic screening processes on the resulting superexchange energies as a consequence of the charges located next to the metal on the oxygen sites. Local enhancement of the superexchange shows that the understanding of the individual behaviour of these electrons is extremely important.

The magnetic superexchange energy is determined by the ratio between kinetic and Coulomb energies [1]. In a simple picture one can consider this process as a nearest neighbour effect between two essentially identical metal sites having effectively only one electron. The motion of the electron is enhanced with an increase of the hopping matrix element. However, once the electron has moved to its neighbouring site, it will meet another electron with negative charge in the same orbital. This results in an increase in Coulomb repulsion. What happens next, strongly depends on the ratio between the hopping matrix element t representing the kinetic energy and the on-site repulsion U representing the Coulomb repulsion for two electrons in the same orbital [2]. If t is much larger than U, the electrons will form a Fermi-Liquid with small corrections to the ideal metallic behaviour. Vice versa, if t is much smaller than U, it is clearly unfavourable to move on to the next site and the electron has to hop back to the empty site. Since no net motion of charge occurs, this yields an insulating state and the only electronic degree of freedom that can be changed is the spin [1, 2]. Therefore, in a situation where the Coulomb on-site repulsion dominates one expects an insulating spin oriented ground state that is driven by the magnetic superexchange energy $J \approx t^2/U$.

However, an important question remains: How do the other electrons in the materials react to this back and forth motion of the electron? As known from traditional electrodynamics the other electrons will modify the effective movement and the effective energy scales associated with the superexchange process. This is known as the downfolding of the manyfold of possible electronic motions within different bands of a solid into one single and effective band [3]. In other words, before this downfolding takes place the energies associated with the superexchange process are the so called ‘bare orbital energies’. After the downfolding one obtains ‘effective’ energies at typically lower values [3]. The situation described above is substantially modified if other electrons do not ‘play along’, which implies that their energy scales are mixing and are not well separated. An example are cuprates, where the original electrons are located at the oxygens which the electrons have ‘to cross’ in order to establish the effective superexchange interaction. Since superconductivity is a property of doped

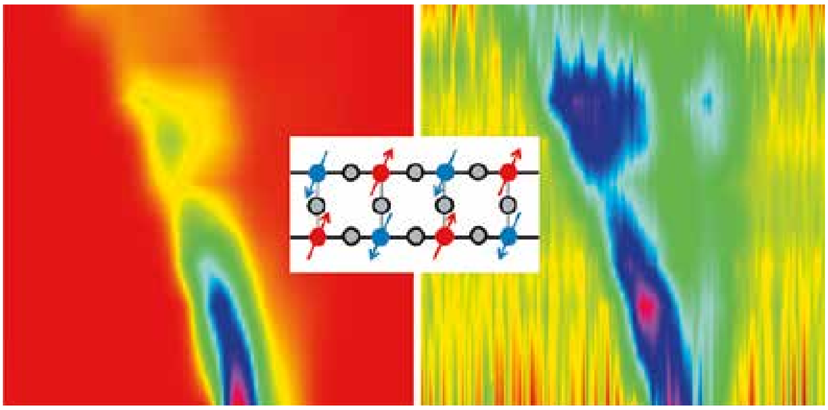

Figure 1

Resonance profile, i.e. change of the intensity of the magnetic excitations as a function of the incident photon energy of FLASH along the rungs (left) and legs (right) of the correlated spin ladder compound depicted in the inset. The resonance excitation energy is given with respect to the elastic scattering signal (Raman shift). The resonance enhancements allow the determination of the orbital energies that are relevant for the superexchange process. The spin ordering of the copper d-orbitals, which is the result of the superexchange between adjacent spin sites denoted as red and blue arrows, develops across the oxygen atoms (grey circles). Our study determines the role of the hole (missing electron) in the oxygen orbitals on the superexchange process between neighboring spin sites.

cuprates the role and the influence of the charge modification at the oxygen for the superexchange process at the transition metal needs to be evaluated.

In order to address this question we have studied isostructural doped and undoped spin-ladder compounds at the VUV-Raman instrument of FLASH. Of particular importance is that the instrument suppresses the typically dominant elastic line by several orders of magnitude and is therefore capable of studying low energy excitations. Using spin ladder compounds we were able to investigate phonons and more importantly two-magnon excitations as a function of incident photon energy. The resonance energy (see Fig. 1) is determined by the orbital $M_{3,2}$ energies plus the on-site repulsion U that is seen by the electrons at the transition-metal site [4, 5]. On the other hand the measurement of the two-magnon peak allows the determination of the superexchange energy (of the order a few 100 meV). The simultaneous measurement of both quantities reveals all parameters relevant to the superexchange process (J, t, U). When comparing doped and undoped samples, we can deduce how the charge modification at the oxygen changes the parameters responsible for the superexchange energy. Amazingly, it is to a large degree the Coulomb on-site repulsion that is most affected by the doping of charge into the oxygen. Normally, one would not expect any change of an energy scale that is associated with the local interaction of two electrons in one orbital. However, this view ignores the relevance of all the other electrons that are responsible for the transformation of the 'bare' U into an 'effective' U [3]. With the appropriate downfolding, and considering an anisotropic charge distribution, the effective Coulomb on-site repulsion can even become smaller and anisotropic, and this is seen in our experiment. In turn this can even result in an enhancement of the magnetic superexchange energy J when charge is doped, which is counterintuitive to a simple one-band picture. The understanding of the competing energy scales in these correlated materials and how they change with doping is a key aspect for the understanding of transition-metal oxide materials and the validity of derived models.

Contact: Michael Rübhausen, michael.ruebhausen@desy.de
ruebhausen@physnet.uni-hamburg.de
Andrivo Rusydi, phyandri@nus.edu.sg

Authors

A. Rusydi[1,2,3], A. Goos[1], S. Binder[1], A. Eich[1], K. Botril[1], P. Abbamonte[4], X. Yu[3], M. B. H. Breese[2,3], H. Eisaki[5], Y. Fujimaki[6], S. Uchida[6], N. Guerassimova[7], R. Treusch[7], J. Feldhaus[7], R. Reininger[8], M. V. Klein[4], and M. Rübhausen[1,2]

1. Institut für Angewandte Physik, Universität Hamburg, Jungiusstraße 11, 20355 Hamburg, Germany and Center for Free Electron Laser Science (CFEL), Notkestraße 85, 22607 Hamburg, Germany
2. NUSSNI-NanoCore Department of Physics, National University of Singapore, Singapore 117542, Singapore
3. Singapore Synchrotron Light Source, National University of Singapore, Singapore 117603, Singapore
4. Physics Department and Frederick Seitz Materials Research Laboratory, University of Illinois, Urbana, Illinois 61801, USA
5. Nanoelectronics Research Institute, AIST, 1-1-1 Central 2, Umezono, Tsukuba, Ibaraki 305-8568, Japan
6. Department of Superconductivity, University of Tokyo, Bunkyo-ku, Tokyo 113, Japan
7. DESY Photon Science, Notkestraße 85, 22607 Hamburg, Germany
8. Advanced Photon Source, Argonne National Laboratory, Argonne, Illinois 60439, USA

Original publication

"Electronic Screening-Enhanced Hole Pairing in Two-Leg Spin Ladders Studied by High-Resolution Resonant Inelastic X-Ray Scattering at Cu M Edges",
Phys. Rev. Lett. 113, 067001 (2014). DOI: 10.1103/PhysRevLett.113.067001

References

1. **J. Hubbard, Proc. R. Soc. A 276, 238 (1963).**
2. **M. B. J. Meinders, J. van den Brink, J. Lorenzana, and G. A. Sawatzky, Phys. Rev. B 52, 2484 (1995).**
3. **M. Imada and T. Miyake, J. Phys. Soc. Jpn., 79, 112001 (2010).**
4. **P. Kuiper et al., Phys. Rev. Lett. 80, 5204 (1998).**
5. **M. G. Cottam and D. J. Lockwood, Phys. Rev. B 31, 641 (1985).**

Creating and controlling metastable states.

Liquid electrolyte gating in VO_2 thin films

Vanadium dioxide (VO_2) exhibits a temperature-driven insulator-to-metal transition, characterized by a change in resistance of over 5 orders of magnitude, making it interesting for both fundamental physics and device applications. It has long been a goal to induce a metallic state in VO_2 using electric fields, however the fields achieved by conventional devices are not sufficient. Recently, this metallization was accomplished by gating with a liquid electrolyte, where much higher electric fields can be realized. Using hard X-ray photoelectron spectroscopy, we showed this metallic phase to be distinct from the metallic state induced by temperature. Our results indicate the potential of liquid electrolyte gating to create and control new electronic states in materials.

The development of new states at oxide interfaces and surfaces is of considerable significance both scientifically and technologically. VO_2 exhibits a temperature-driven metal-to-insulator transition accompanied by a structural transformation from a rutile structure (high-temperature metallic phase) to a monoclinic structure (low-temperature insulator phase). This transition between phases with such contrasting electrical properties near room temperature motivates the control and tailoring of the VO_2 electronic states. The use of conventional solid dielectrics as a gate material (in the field-effect transistor geometry) induces moderate values of electric fields that are not sufficient to modify the electronic states of VO_2. However, using ionic liquid electrolyte gate dielectrics, which provide much larger electric fields, Jeong et al. [1] and Nakano et al. [2] were able to induce a metallic state below the metal-to-insulator transition temperature. Moreover, these authors showed this process to be reversible [1].

Jeong et al. [1] also showed that the metallic state in the VO_2 was non-volatile and persisted when the gate voltage was reduced to zero and even after the ionic liquid was completely removed from the VO_2 surface. They provided strong evidence that the gate-induced metallicity in VO_2 was accompanied by the formation of oxygen vacancies due to the oxygen migration from the film to the electrolyte. The investigations of the electronic properties in these systems were restricted to electronic transport measurements. The aim of our work was to use hard X-ray photoelectron spectroscopy to directly probe the modifications in the electronic structure induced by electrolyte gating.

A schematic of the device and measurement setup is shown in Fig. 1(a). The experiment was performed at beamline P09 at PETRA III using 3.0 keV photon energy and linearly polarized light. The valence band of the VO_2 film was measured in the pristine insulating monoclinic (120 K) and metallic rutile (350 K)

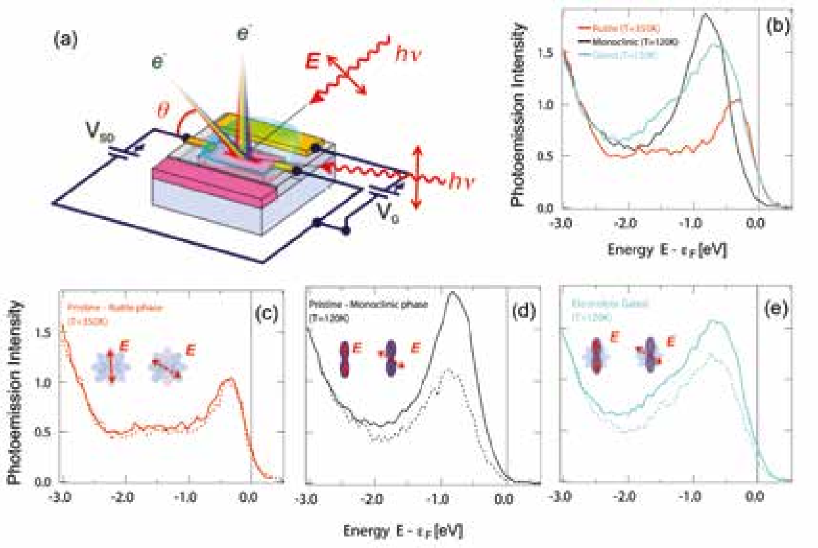

Figure 1

(a) Experiment and device schematic. The gate electrode, of area of 4 × 10 mm², and the electrical contacts to the channel are shown in yellow. The VO_2 channel (pink) of size 2 × 6 mm² is set at a distance 0.5 mm from the gate. The semi-transparent turquoise droplet is the ionic liquid. The substrate is shown in blue. The linearly polarized light impinges the sample at an incidence angle of 5° and 60° for near-normal ($\theta = 85°$) and off-normal ($\theta = 30°$) photoemission measurements, respectively. (b) Valence band spectra at near-normal emission condition measured at 3.0 keV for VO_2 in the rutile (350 K), gated (120 K) and monoclinic (120 K) states. Subfigures (c), (d) and (e) show the valence band spectra for the three phases at light incidence angles of 5° (solid line) and 60° (dashed line). Inset figures depict the relationship between the orbital polarization and the electric field direction *E* of the light in each case.

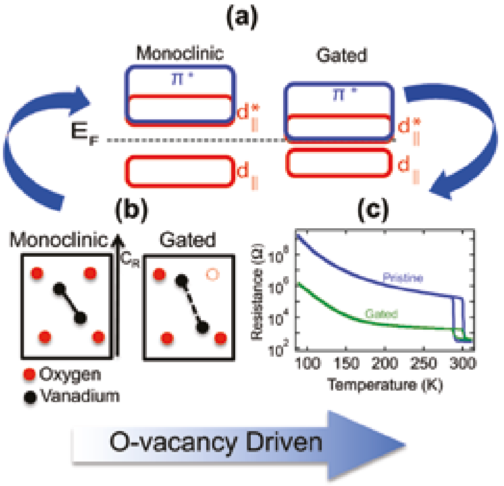

Figure 2

The interconnection between crystal structure, electronic structure and transport properties in low temperature monoclinic and liquid electrolyte gated VO_2. (a) Modifications in the band diagram can be described by a reduction of $d_{||}$ band splitting (see text).
(b) Structural changes induced by electrolyte gating: the electrochemical reaction produces oxygen vacancies in VO_2. In the gated structure, the V-V distances are larger than in the monoclinic phase.
(c) Temperature-dependent resistance of a pristine film and after electrolyte gating: the gated phase presents reduced resistivity at low temperatures. The small hysteresis is due to the fabrication process or incomplete gating.

phases as well as the gated (120 K) state, as shown in Fig. 1(b). Note that the valence band of the gated state cannot be decomposed into a combination of valence band spectra from the rutile and monoclinic phases. This confirms that the gate-induced metallic phase is distinct from the temperature-induced rutile phase. The intensity at the peak maximum in photoemission of the vanadium 3*d* band in the monoclinic is much higher than in the rutile phase. The gated phase eexhibits a peak intensity between that of the rutile and monoclinic phases. This behaviour can be explained as a consequence of the coupling between the light electric field vector and the electronic orbital arrangements in this compound [3]. Figures 1(c)–(e) show the dependence of the 3*d* band photoemission intensity on the light incident angles. The vanadium 3*d* states form two bands near E_F: the $d_{||}$-band, originating from the overlap of the *d*-orbitals which are oriented along the rutile c-axis; and the π*-band, an antibonding state arising from the hybridization of *d*-orbitals and oxygen *2p* states. In the rutile phase, both bands are filled resulting in a homogeneous spatial distribution of 3*d* states, as sketched in the inset of Fig 1(c). Therefore, the photoemission intensity does not present a strong dependence on the light electric field direction. By contrast, the monoclinic phase has a strong dimerization of vanadium atoms (Fig. 2(b)) resulting in a strong orbital polarization. That is, only the $d_{||}$ band is occupied at energies near the Fermi energy E_F. The light electric field at low incident angles couples with the $d_{||}$ states resulting in an enhanced photoemission intensity in comparison to high incident angles (Fig. 1(d)). In the gated phase, the angular dependence is smaller, which can be ascribed to a partial orbital polarization (Fig. 1(e)). A smaller orbital polarization is a direct consequence of the reduced vanadium dimerization, as shown schematically in Fig. 2 (b).

Our results are summarized in Fig. 2. We conclude that the low temperature monoclinic structure and the associated V-V dimerization of the insulating phase is retained but modified by electrolyte gating (Fig. 2(b)). The V-V distance is increased in the gated phase and is consistent with the creation of oxygen vacancies, as proposed by Jeong et al. (Fig. 2(b)). Larger V-V distances imply a smaller *d*-orbital overlap, decreasing the $d_{||}$ band splitting without lifting the orbital polarization. This is accompanied by a charge redistribution due to the removal of oxygen, populating empty states at E_F (Fig. 2(a)). Additionally, the gated sample shows a substantial increase in spectral weight at E_F, reflecting the enhanced conductivity at low temperatures (Fig. 2(c)).

Our work ultimately shows that the gate induced metallic state in VO_2 has a distinct electronic structure from that of the rutile metallic phase of the pristine film. This result suggests that liquid electrolyte gating is a potential pathway to reversibly create and control new phases in materials.

Contact: Julie Karel, julie.karel@cpfs.mpg.de
Carlos Viol Barbosa, carlos.barbosa@cpfs.mpg.de

Authors

Julie Karel[1], Carlos E. Viol Barbosa[1], Janos Kiss[1], Jaewoo Jeong[2], Nagaphani Aetukuri[2], Mahesh G. Samant[2], Xeniya Kozina[3], Eiji Ikenaga[3], Gerhard H. Fecher[1], Claudia Felser[1] and Stuart S. P. Parkin[2]

1. Max-Planck-Institut für Chemische Physik fester Stoffe, 01187 Dresden, Germany
2. IBM Almaden Research Center, San Jose, California 95120, USA
3. Japan Synchrotron Radiation Research Institute, SPring-8, Hyogo 679-5148 Japan

Original publication

"Distinct Electronic Structure of the Electrolyte-Gate Induced Conducting Phase in Vanadium Dioxide Revealed by High Energy Photoelectron Spectroscopy", ACS Nano 8, 5474 (2014).
DOI: 10.1021/nn501724q

References

1. J. Jeong, N. Aetukuri, T. Graf, T. D. Schladt, M. G. Samant, S. S. P. Parkin, "Suppression of Metal-Insulator Transition in VO_2 by Electric Field–Induced Oxygen Vacancy Formation", Science 339, 1402-1405 (2013).
2. M. Nakano, K. Shibuya, D. Okuyama, T. Hatano, S. Ono, M. Kawasaki, Y. Iwasa, Y. Tokura, "Collective Bulk Carrier Delocalization Driven by Electrostatic Surface Charge Accumulation", Nature 487, 459-462 (2012).
3. M. W. Haverkort, Z. Hu, A. Tanaka,W. Reichelt, S. V. Streltsov, M. A. Korotin, V. I. Anisimov, H. H. Hsieh, H. J. Lin, C. T. Chen, et al., "Orbital-Assisted Metal-Insulator Transition in VO_2", Phys. Rev. Lett. 95, 196404 (2005).

Detection of a water-reservoir in the Earth's deep mantle.

Hydrous ringwoodite trapped in super deep diamonds

Whether or not huge volumes of water are stored in the deep Earth is a matter of ongoing scientific controversy. Inclusions trapped in diamonds having a super deep origin (> 410 km depth) are suitable to solve this question. Our combined study using synchrotron X-ray fluorescence, X-ray diffraction, Raman and infrared spectroscopic data yield the first evidence for the terrestrial occurrence of ringwoodite, a high-pressure polymorph of olivine, only stable in the lower part of the transition zone of the Earth's mantle at a depth between about 520 and 660 km. The water-rich nature of this inclusion, indicated by infrared absorption is direct evidence that, at least locally, the transition zone is hydrous, to about 1.5 wt%.

Based on phase transitions of its main component olivine, the Earth's mantle is subdivided into an upper mantle (< 410 km depth), a lower mantle (> 660 km depth) and a so-called transition zone in between. Experimental data have shown that although most mineral phases of the Earth's mantle are essentially dry, the two high pressure polymorphs of olivine, wadsleyite and ringwoodite are able to capture enormous amounts of fluids in the form of OH-groups in their crystal structures, enabling the TZ to store several times the amount of today's oceans [1]. Until now it was still an open question if the transition zone is more like a dry sponge or one of the Earth's main water reservoirs [2,3].

Ultradeep diamonds, originating from the deep mantle [4], allow unique insights into the material constituting the Earth's transition zone. These diamonds should provide the best opportunity for finding both wadsleyite and ringwoodite. In this study, we focused on diamonds from the Juina district of Mato Grosso, Brazil, in a search for ultrahigh-pressure inclusions. Alluvial deposits in this region contain abundant diamonds that originate in the Earth's transition zone or even the lower mantle.

In this work the first identification of terrestrial ringwoodite was successfully performed by means of Raman spectroscopy. The detailed measurements yield not only information about the existing mineral phases but also about the residual pressure in the inclusion. Beside ringwoodite a second deep mantle phase, walstromite-structured $CaSiO_3$, was identified. In contrast to ringwoodite, which largely avoided retrogression, the Ca-rich phase is reverted from its higher pressure $CaSiO_3$-perovskite precursor. Within the deep Earth, ringwoodite and former $CaSiO_3$-perovskite coexisted at pressures above 15 GPa, which is in the transition zone. The compressive stress imposed on the inclusion yields internal pressures of between 1.7 and 2.3 GPa [5] and was estimated by measuring the pressure induced Raman shift of the main diamond band in the immediately adjacent diamond.

Micro-X-ray fluorescence and absorption spectroscopy (μXRF / XAS) measurements were performed at beamline L of the DORIS III synchrotron facility at DESY. Measurements were made using a confocal detection scheme that enables direct non-destructive extraction of three-dimensional elemental / chemical state information from an internal microscopic

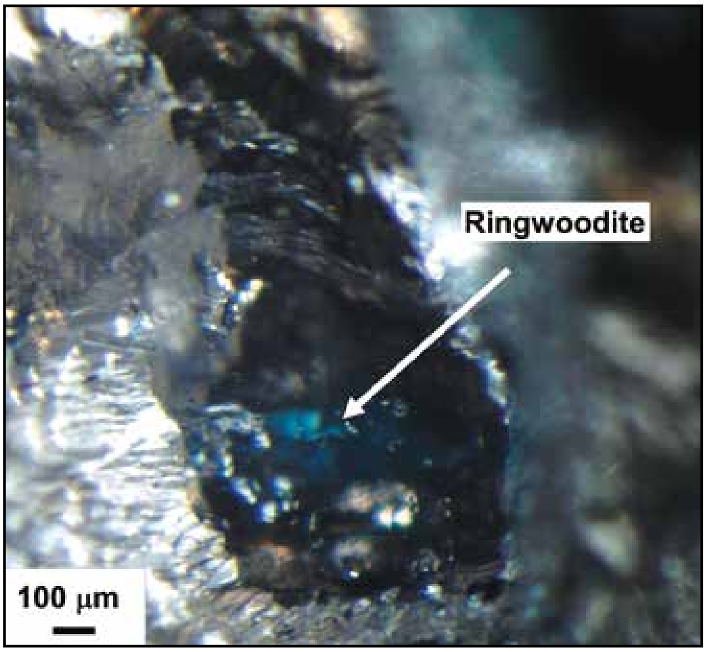

Figure 1

Light microscopic image of the hydrous ringwoodite (JUc29) enclosed in a diamond from the Juina area. The typical blue colour of ringwoodite found in high pressure experiments can be seen. The photograph is courtesy of Dr. Mederic Palot (University of Alberta, CA).

Figure 2

Three-dimensional confocal µXRF view of a two-phase ringwoodite-walstromite inclusion within the JUc29 diamond, showing Ca (red) and Fe (green) low-intensity isosurfaces for confocal µXRF, with blue representing the diamond host (derived from scatter intensity).

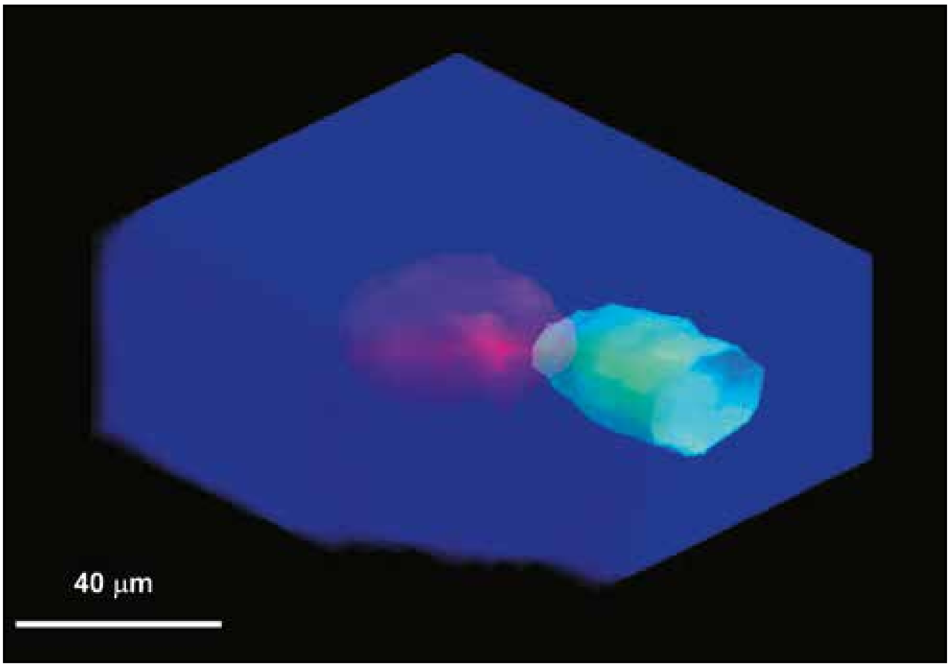

volume element of approximately 22 µm × 22 µm × 16 µm (full width at half maximum). The confocal detection mode ensures that the measurements are insensitive to surface features, recording information only from the depth of the inclusion. Fe and Ca confocal µXRF measurements were recorded with an excitation energy of 7200 eV and were combined to produce the three-dimensional confocal micro X-ray fluorescence view of the two-phase inclusion shown in Fig. 2. The synchrotron X-ray tomography shows the inclusion to form part of a pair, with a Ca-rich (red) and a Fe-bearing (green) phase immediately adjacent.

Single-crystal X-ray diffraction of the Fe-bearing phase revealed the main four diffraction peaks of ringwoodite, in their relative order of expected intensity thus providing the definitive proof that this high pressure polymorph is preserved within the diamond.

In order to measure the water-content of the sample and to test the transition zone water hypothesis, FTIR-spectroscopy was applied. The spectra of sample JUc29 show strong OH absorption, clearly indicative of significant H_2O content, and are consistent with a minimum estimate between 1.4 and 1.5 wt % H_2O, derived by integrating the FTIR-spectra.

The comprehensive microanalytical study of this unique find of a hydrous ringwoodite enclosed in diamond from Brazil enabled us to solve one of the long lasting questions of the Earth and showed that at least locally the Earth's transition zone has stored high amounts of water. In addition, our finding was a key factor in promoting new seismological searches for water in the deep Earth [6].

Contact: Frank Brenker, f.brenker@em.uni-frankfurt.de

Authors

Frank E. Brenker[1], D. Graham Pearson[2], Laszlo Vincze[3], Bart Vekemans[3], Geert Silversmit[3], Sylvia Schmitz[1], Fabrizio Nestola[4], John McNeill[5], Lutz Nasdala[6], Mark T. Hutchison[7], Sergei Matveev[2,8], and Kathy Mather[5]

1. Geoscience Institute – Mineralogy, Goethe University, Altenhöferallee 1, 60438 Frankfurt, Germany
2. Department of Earth and Atmospheric Sciences, 1-26 Earth Sciences Building, University of Alberta, Edmonton, Alberta T6G 2E3, Canada
3. Department of Analytical Chemistry, Ghent University, Krijgslaan 281 S12, B-9000 Ghent, Belgium
4. Dipartimento di Geoscienze, Università di Padova, 35137 Padua, Italy
5. Department of Earth Sciences, Durham University, Durham DH1 3LE, UK
6. Institut für Mineralogie und Kristallographie, Universität Wien, Althanstrasse 14, 1090 Wien, Austria
7. Trigon GeoServices Ltd, 2780 South Jones Boulevard, #35-15, Las Vegas, Nevada 89146, USA
8. Department of Earth Sciences, Utrecht University, Budapestlaan 4, 3584 CD Utrecht, Netherlands

Original publication

"Hydrous mantle transition zone indicated by ringwoodite included within diamond", Nature 507, 221-224 (2014). DOI: 10.1038/nature13080

References

1. D. L. Kohlstedt, H. Keppler, and D. C. Rubie, "Solubility of water in the α, β and γ phases of $(Mg,Fe)_2SiO_4$", Contrib. Mineral. Petrol. 123, 345-357 (1996).
2. A. Kelbert, A. Schultz, and G. Egbert, "Global electromagnetic induction constraints on transition-zone water content variations", Nature 460, 1003-1006 (2009).
3. X. Huang, Y. Xu, and S. Karato, "Water content in the transition zone from electrical conductivity of wadsleyite and ringwoodite", Nature 434, 746-749 (2005).
4. B. Harte, "Diamond formation in the deep mantle: the record of mineral inclusions and their distribution in relation to mantle dehydration zones", Mineral. Mag. 74, 189-215 (2010)
5. A. K. Kleppe, A. P. Jephcoat, and J. R. Smyth, "Raman spectroscopic study of hydrous γ-Mg_2SiO_4 to 56.5 GPa", Phys. Chem. Miner. 29, 473-476 (2002).
6. B. Schmandt, S. D. Jacobsen, T. W. Becker, Z. Liu, and K. G. Dueker, "Dehydration melting at the top of the lower mantle", Science 344, 1265-1268 (2014).

Unexpected stable stoichiometries of sodium chlorides under pressure.

Metallic "salt"

Sodium chloride (NaCl) is a typical ionic compound, and often used to explain how ionic bond works in elementary chemistry. Elements Na and Cl are thought to combine with only 1:1 ratio: one Na can donate one electron to Cl, so that both of them have full shell electron configuration, to form a stable compound. However, based on theoretical calculations of materials with a variable stoichiometry, a number of new compounds with unexpected stoichiometry should become stable at high pressures: they are $NaCl_3$, $NaCl_7$, Na_3Cl, Na_2Cl, and Na_3Cl_2. We have synthesized $NaCl_3$ (two different modifications) and Na_3Cl at high pressures. Na_3Cl is a two dimensional metal material which hints that unexpected stoichiometry compounds could be a new resource of functional material. The new finding will evoke the rethinking about the electron interaction and bonding model at extreme conditions. Further exploration will be helpful to solve puzzles in planetology and geoscience.

The high-pressure behaviour of NaCl has been extensively studied experimentally [1-3] at pressures up to 304 GPa and by *ab initio* simulations [4-6], and a very simple behaviour was observed – at 30 GPa the rocksalt structure was found to transform into the CsCl (B2-type) structure. Metallization of NaCl is generally expected to occur at several hundred GPa [6]. Theoretical calculations based on *ab initio* evolutionary algorithm USPEX [7] demonstrate stability of materials with stoichiometries other than 1:1 (Fig. 1(a)) and complex behaviour similar to that of intermetallides. This manifests the breakdown of traditional chemical rules in what was long thought to be the simplest binary chemical system. The calculated phase diagram features unexpected compounds – cubic (SG *Pm3n*, Fig 1(b)) and orthorhombic (SG *Pnma*) $NaCl_3$ are stable above 20 GPa, $NaCl_7$ above 142 GPa, and Na_3Cl_2, Na_2Cl, and Na_3Cl are stable above 120 GPa, 100 GPa and 77 GPa, respectively. For the Na-rich side of the phase diagram – tetragonal Na_3Cl (space group *P4/mmm*), tetragonal (SG *P4/m*) and orthorhombic (SG *Cmmm*) Na_3Cl_2, and three phases of Na_2Cl – one tetragonal (SG *P4/mmm*), and two orthorhombic (SG *Cmmm and Imma*) phases are predicted. In the entire explored pressure region, NaCl is also a stable compound, i.e. will not spontaneously decompose into other compounds. This means that to obtain the newly predicted compounds it is not sufficient just to compress NaCl, but one must do so at high temperatures (to overcome kinetic barriers) and with excess of either Na or Cl.

Inspired by these predictions, high-pressure experiments have been performed in a laser heated diamond anvil cell (DAC) at 10–80 GPa on the Na-Cl system in the excess of chlorine and sodium. Laser heating at 55–80 GPa results in a chemical reaction, which was detected by a sudden increase in temperature near and above 2000 K and is consistent with the predicted exothermic chemical reaction. The reaction products were examined by visual observations, optical and Raman confocal spectroscopy, and by synchrotron X-ray

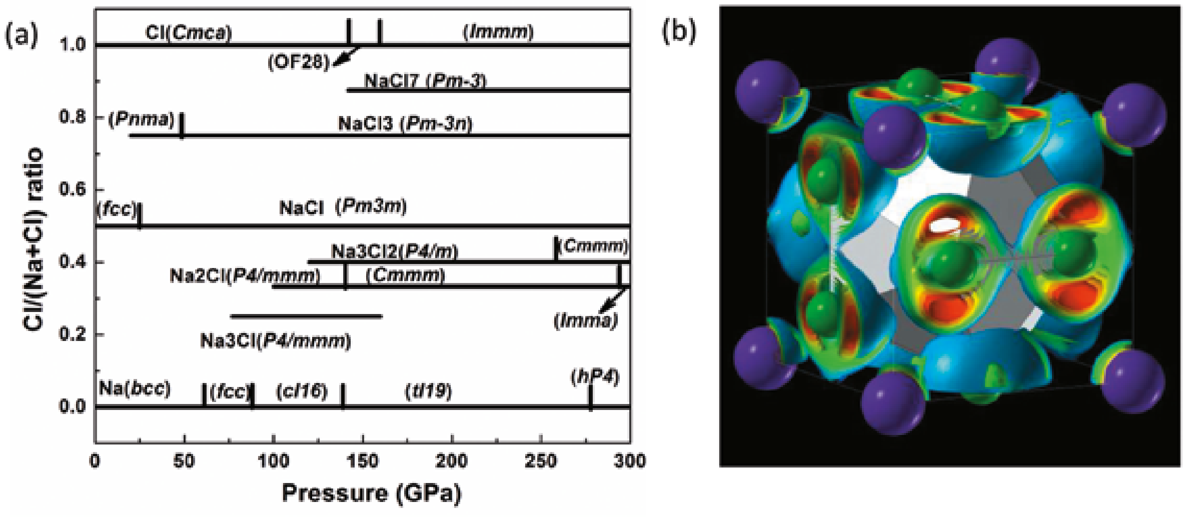

Figure 1

(a) Pressure-composition phase diagram of the Na-Cl system and

(b) electron localization function of cubic $NaCl_3$, Na and Cl atoms are shown in blue and green, respectively.

diffraction at room temperature. Synchrotron X-ray diffraction (XRD) data were collected at GeoSoilEnviroCARS, APS, Chicago and Extreme Conditions Beamline P02.2 at PETRA III, which have online laser heating capabilities. The probing X-ray beam size was about 2–5 μm.

In the case of loading with excess of chlorine, X-ray diffraction measurements show new Bragg peaks after laser heating. At higher pressures these Bragg peaks can be indexed either in a cubic *Pm3n* $NaCl_3$ unit cell, or with a mixture of the cubic and the orthorhombic *Pnma* $NaCl_3$ unit cell. With pressure decreasing below 54 GPa, after laser heating, only the peaks of the orthorhombic $NaCl_3$ are present in the XRD patterns. We have obtained the lattice parameters and the unit cell volume for the two structures as functions of pressure for the decompression sequence. As seen from Fig. 2(a) there is a perfect agreement between the experimental and the theoretical equation of state (EOS) for both $NaCl_3$ structures. Raman spectra of the reaction products show a set of lines distinct from those of Cl_2. Two different “spectral families” can be observed: (i) a broad feature between 250 and 500 cm^{-1} which is in agreement with predicted Raman frequencies of cubic $NaCl_3$ and (ii) a set of narrow bands with frequencies very close to the predicted ones for the orthorhombic $NaCl_3$. Based on a practically perfect agreement of the experimental findings with the theoretically predicted symmetry, lattice parameter and lattice dynamics for both cubic and orthorhombic $NaCl_3$ compounds, we suggest that we synthesized two new Cl-rich materials, the stoichiometry of which is $NaCl_3$.

Also in the case of loading with excess of sodium, X-ray diffraction measurements show new Bragg peaks after laser heating. The XRD pattern usually also contains peaks from unreacted cubic B1 or B2 NaCl and bcc or fcc sodium. These Bragg peaks can be indexed in a tetragonal *P4/mmm*-Na_3Cl unit cell for the whole pressure range of this study. The lattice parameters of the new material agree well with the theoretically predicted *P4/mmm* Na_3Cl in a wide pressure range of 27–70 GPa and, as seen from Fig. 2(b), there is a perfect agreement between the experimental and the theoretical EOS. Having in mind that both cubic NaCl and Na are Raman inactive the appearance of narrow Raman lines, after laser heating, signals the formation of a new compound. From the above it is evident that both the experimental techniques show a perfect agreement of the experimental findings with the theoretically predicted symmetry, lattice parameter and lattice dynamics for the tetragonal Na_3Cl compound. Consequently, we suggest that we synthesized a new Na-rich material, with the stoichiometry Na_3Cl.

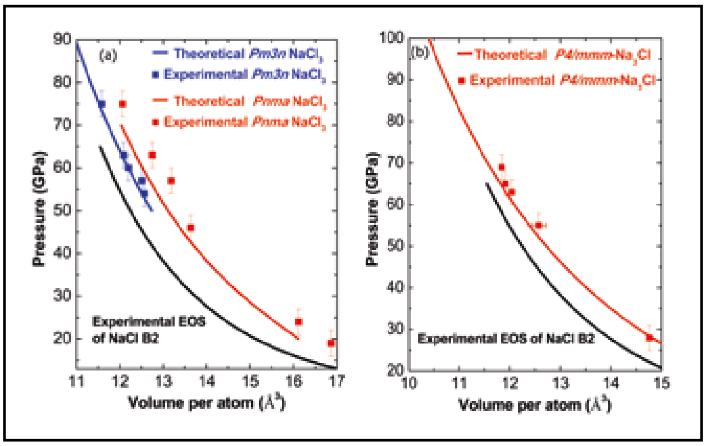

Figure 2

(a) EOS for two different $NaCl_3$ structures and (b) EOS for the tetragonal Na_3Cl structure. Theoretical predictions are indicated by solid lines and experimental data by squares and circles.

Contact: Alexander F. Goncharov,
agoncharov@carnegiescience.edu,
Zuzana Konôpková, zuzana.konopkova@desy.de,
Artem R. Oganov, artem.oganov@sunysb.edu

Authors

W. Zhang[1,2], A. R. Oganov[2,3,4], A. F. Goncharov[5,6], Q. Zhu[2], S. E. Boulfelfel[2], A. O. Lyakhov[2], E. Stavrou[5], M. Somayazulu[5], V. B. Prakapenka[7], Z. Konôpková[8]

1. Department of Applied Physics, China Agricultural University, Beijing 100080, China.
2. Department of Geosciences, Center for Materials by Design, and Institute for Advanced Computational Science, State University of New York, Stony Brook, NY 11794, USA.
3. Moscow Institute of Physics and Technology, 9 Institutskiy Lane, Dolgoprudny City, Moscow Region 141700, Russia.
4. School of Materials Science, Northwestern Polytechnical University, Xi’an 710072, China.
5. Geophysical Laboratory, Carnegie Institution of Washington, 5251 Broad Branch Road NW, Washington, DC 20015, USA.
6. Center for Energy Matter in Extreme Environments and Key Laboratory of Materials Physics, Institute of Solid State Physics, Chinese Academy of Sciences, 350 Shushanghu Road, Hefei, Anhui 230031, China.
7. Center for Advanced Radiation Sources, University of Chicago, Chicago, IL 60637, USA.
8. Deutsches Elektronen-Synchrotron DESY, Notkestr. 85, 22607 Hamburg, Germany

Original publication

“Unexpected Stable Stoichiometries of Sodium Chlorides”, *Science* 342, 1502 (2013).
DOI: 10.1126/science.1244989

References

1. T. Sakai, E. Ohtani, N. Hirao, and Y. Ohishi, “Equation of state of the NaCl-B2 phase up to 304 GPa”, J. Appl. Phys.109, 084912 (2011).
2. D. L. Heinz and R. Jeanloz, “Compression of the B2 high-pressure phase of NaCl”, Phys. Rev. B 30, 6045-6050 (1984).
3. W. A. Bassett, T. Takahash, H.-K. Mao, and J. S. Weaver, “Pressure-induced phase transformation in NaCl”, J. Appl. Phys. 39, 319 (1968).
4. S. Ono, “The equation of state of B_2-type NaCl”, J. Phys. Conf. Ser. 215, 012196 (2010).
5. S. Froyen and M. L. Cohen, “Structural properties of NaCl”, Phys. Rev. B 29, 3770-3772 (1984).
6. X. Chen and Y. Ma, “High-pressure structures and metallization of sodium chloride”, Europhys. Lett. 100, 26005 (2012).
7. A. R. Oganov, A. O. Lyakhov, and M. Valle, “How evolutionary crystal structure prediction works – and why”, Acc. Chem. Res. 44, 227 (2011).

Strong cellulose filaments with tunable nano structure.

X-ray scattering reveals nano structure during assembly and in the final filaments prepared from cellulose nanofibrils

Cellulose nanofibrils originate from e.g. trees and can be obtained by disintegrating pulp fibres into fibrils, which are approximately 5 nm wide and typically 1 μm long. The fibrils are constructed of cellulose molecules in a near-crystalline order. These fibrils have considerable potential as building blocks for new bio-based materials. However, in order to fully utilise this potential, the nanostructure of macroscopic materials must be controlled. In this work, wide- and small angle X-ray scattering (WAXS and SAXS) measurements at the beamline P03 at PETRA III are used to investigate an assembly process that accomplishes this control. The mechanical properties of the filaments are similar to cellulose fibres from trees at the same fibrillar alignment.

Nature presents a wide range of materials with impressive properties. In many cases, these properties are determined by the micro- and nanostructure of the materials. Cellulose fibres in e.g. trees are one example and their main structural components are cellulose nanofibrils [1]. During the last decade, processes have been developed to make utilisation of cellulose nanofibrils viable as the basis for new bio-based materials for paper, textile, or engineering applications. Films and filaments have been prepared from cellulose nanofibrils [2,3], but previous works has not been able to reproduce the strength reported for cellulose fibres from trees.

In this work we combine flow-focusing [4] with a surface potential controlled transition from a state of dispersion to a gel state of cellulose nanofibrils in water [5]. In this way we achieve a controlled assembly of cellulose nanofibrils into filaments. The key to success lies in creating and locking the nanostructure in a continuous process. This has been demonstrated by WAXS of the final filaments and *in situ* SAXS during the assembly process.

In flow focusing, a central stream is focused by two or more outer sheath flows. This flow is typically set up in a channel system as shown in Fig. 1a. The channel contours are indicated with white lines. In our flow focusing system a central flow consisting of 0.3 mass percentage cellulose nanofibrils dispersed in water enters from the left. The sheath flows consisting of water and positive ions enter from the top and the bottom. In Fig. 1a polarized light is used to visualize the alignment of the fibrils due to the stretching of the central flow during focusing. A higher birefringence can be observed in the regions where fibrils are highly aligned. The aligned fibril structure is then "frozen" in a gel state by ions diffusing from the sheath flows into the central stream, thereby inducing dispersion to gel transition [5].

However, the polarized microscopy only allows for relative measurements of fibril alignment and accurate quantification of the alignment is not straightforward. Therefore, SAXS is used to precisely quantify the fibril alignment during flow focusing. Figure 1b shows SAXS patterns from the positions marked with green squares in Fig. 1a. The red circles in Fig. 1b denote a constant SAXS intensity and it is clearly seen that the circle in the first image is deformed into an ellipse further downstream. This deformation is a footprint of fibril alignment.

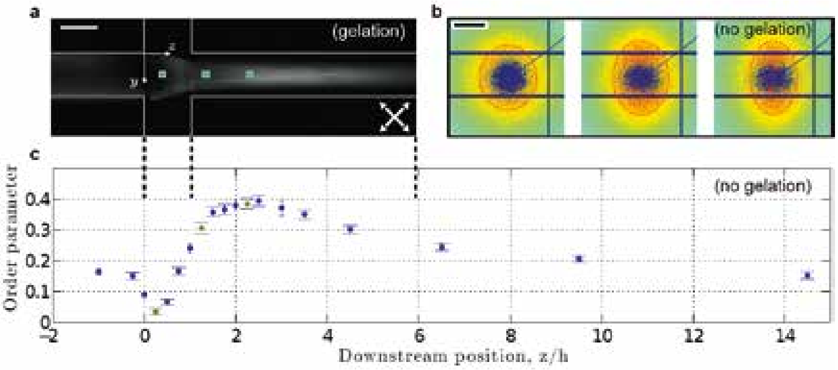

Figure 1

Alignment and de-alignment of fibrils in the channel. (a) A sodium chloride solution focusses a cellulose nanofibrils dispersion. The channel is placed between two crossed polarization filters rotated 45° from the vertical axis (white arrows). (b) SAXS diffractograms before, during and after the acceleration by pure water in the channel, where the red ellipse corresponds to a constant intensity. The locations are marked with green squares around blue markers in (a). (c) Order parameter from acceleration by pure water calculated from SAXS data as a function of the downstream distance normalized with the channel width h of 1 mm. The scale bar in (a) is 1 mm and in (b) 0.5 nm^{-1}.

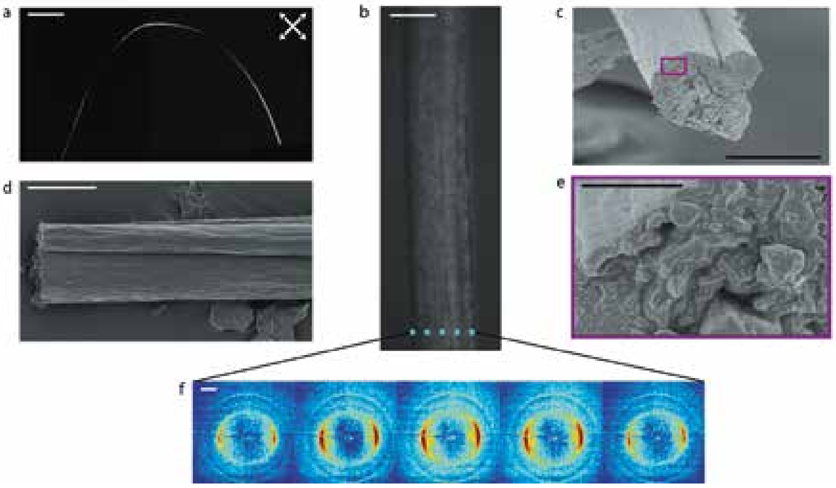

Figure 2

Images and diffractograms of a dried filament. (a) Image of a single filament placed between two crossed polarization filters rotated 45° with respect to the vertical axis (white arrows), the scale bar represents 10 mm. (b) Image of a filament in a light microscope. (c – e) SEM images of a filament, where the outlined squares are close-ups. The scale bars are 20 μm in (b – d) and 2 μm in (e). (f) Diffractograms from a horizontal scan of a filament shown in (b), where the filament has a diameter of ~30 μm, the region covered by each diffractogram is indicated with blue rectangles in (b). The scale bar in (f) is $10\ \mathrm{nm}^{-1}$.

From the SAXS patterns, the order parameter S can be derived as the mean value of the second order Legendre polynomial fit to the scattered intensity. A full horizontally aligned state corresponds to $S = 1$, no alignment at all to $S = 0$, and a perpendicular alignment corresponds to $S = -0.5$. In Fig. 1c, the order parameter from several positions along the channel is shown. The stretching of the flow gives an increase of the order parameter to around 0.4 at 2.5 mm after the inlet of the sheath flows. Figure 1c shows a case where no ions were used that induce the dispersion gel / transition. Therefore, the alignment is decreased behind the point of maximum alignment due to Brownian diffusion as the fibrils are transported further downstream.

If an increased ionic strength is used in the outer sheath flows, a gel thread is ejected from the channel. After drying of this gel thread, a filament is obtained. Figure 2 shows a polarized light image, scanning electron microscopy images, and WAXS diffractograms of a dried filament. The polarized light visualizations in Fig. 2a show that the filament is birefringent meaning the dried fibrils are well aligned. The electron microscopy images in Figs. 2(c – e) show that the filament is smooth and homogeneous. The WAXS diffractograms in Fig. 2f are taken across the filaments at the positions indicated with blue rectangles with a $1.5 \times 1.2\ \mu\mathrm{m}^2$ micro-focused beam (the size of the rectangles approximately corresponds to the beam size). The WAXS data show that the fibril alignment is consistent throughout the cross section of the filament; thus no distribution of the alignment along the wire diameter is present. The final nanostructure can be controlled by the strength of stretching in the central focused flow, the streamwise position at which gelation is induced in the channel and the drying conditions.

The combination of controlled alignment and assembly in flow focusing with WAXS and SAXS measurements of the process and final material provides a complete platform that can be used to further investigate the fibril behaviour during assembly, paving the way for high-performance filaments based on cellulose by increasing the interval of fibril alignment that can be obtained. The thorough understanding of the important factors in the process is also key to the successful scale-up for preparation of fibres for textiles. Successful production of textiles from cellulose nanofibrils could provide an alternative for viscose, Lyocell, and maybe even cotton with a reduced environmental footprint.

Contact: Fredrik Lundell, frlu@kth.se

Authors

Karl M.O. Håkansson[1,2], Andreas Fall[1,3], Fredrik Lundell[1,2], Shun Yu[4], Christina Krywka[5,6], Stephan V. Roth[4], Gonzalo Santoro[4], Mathias Kvick[1,2], Lisa Prahl-Wittberg[1,2], Lars Wågberg[1,3], and L. Daniel Söderberg[1,2,7]

1. Wallenberg Wood Science Center, KTH Royal Institute of Technology, Stockholm SE-100 44, Sweden
2. Linné FLOW Centre, KTH Mechanics, KTH Royal Institute of Technology, Stockholm SE-100 44, Sweden
3. Department of Fibre and Polymer Technology, KTH Royal Institute of Technology, Stockholm SE-100 44, Sweden
4. Deutsches Elektronen-Synchrotron DESY, 22607 Hamburg, Germany
5. Ruprecht Haensel Laboratory, University of Kiel, 24098 Kiel, Germany
6. Helmholtz-Zentrum Geesthacht, Institute for Materials Research, 21502 Geesthacht, Germany
7. Innventia AB, PO Box 5604, Stockholm SE-114 86, Sweden

Original publication

“Hydrodynamic alignment and assembly of nanofibrils resulting in strong cellulose filaments”, Nat. Comm. 5, 4018 (2014). DOI: 10.1038/ncomms5018

References

1. **S. J. Eichhorn, A. Dufresne, M. Aranguren, N. E. Marcovich, J. R. Capadona, S. J. Rowan, C. Weder, W. Thielemans, M. Roman, S. Renneckar, W. Gindl, et al., “Review: current international research into cellulose nanofibres and nanocomposites”, J. Mater. Sci. 45, 1-33 (2010).**
2. **H. Sehaqui, N. E. Mushi, S. Morimune, M. Salajkova, T. Nishino, “Cellulose nanofiber orientation in nanopaper and nanocomposites by cold drawing”, Appl. Mater. Interfaces 4, 1043-1049 (2012).**
3. **S. Iwamoto, A. Isogai, T. Iwata, “Structure and mechanical properties of wet-spun fibers made from natural cellulose nanofibers”, Biomacromolecules 12, 831-836 (2011).**
4. **P. J. A. Kenis, R. F. Ismagilov, G. M. Whitesides, “Microfabrication inside capillaries using multiphase laminar flow patterning”, Science 285, 83-85 (1999).**
5. **A. B. Fall, S. B. Lindström, O. Sundman, L. Ödberg, L. Wågberg, “Colloidal stability of aqueous nanofibrillated cellulose dispersions”, Langmuir 27, 11332-11338 (2011).**

Imaging living cells at nanometre resolution.

A combination of nano-diffraction and microfluidics

X-rays offer high resolution imaging of unstained, unsliced samples, thereby providing a complementary method to visible light and electron microscopy. In order to apply the emerging techniques to biological samples and in particular to whole living cells a number of challenges have to be overcome. We have developed an X-ray compatible microfluidic sample environment for biological cells, providing them with nutrients throughout the measurements. This approach enables us to directly compare chemically fixed and living cells. By analysing the scattered X-ray intensity, we find fixation-induced structural changes on the order of 30 to 50 nm.

Imaging cells at high spatial and temporal resolution is an important aim in life-sciences as many biological processes can only be understood when followed on its relevant length and times scales. Ideally, these methods capture the studied system in its natural, hydrated state with no or only minimal invasion in physiological processes. Visible light fluorescence and electron microscopy have emerged as two powerful complementary techniques to image cells. Electron microscopy provides the highest spatial resolution to date and is widely used for structural studies of cellular components. One major drawback, however, is the extensive sample preparation including fixation, staining, and slicing. Complementary, living cells are routinely studied via visible light fluorescence microscopy owing to fluorescent proteins (e.g. green fluorescent protein) that can be directly expressed in the cells. This approach provides molecule specificity as one great advantage, but at the same time the tagging with fluorescent proteins potentially influences cellular behaviour.

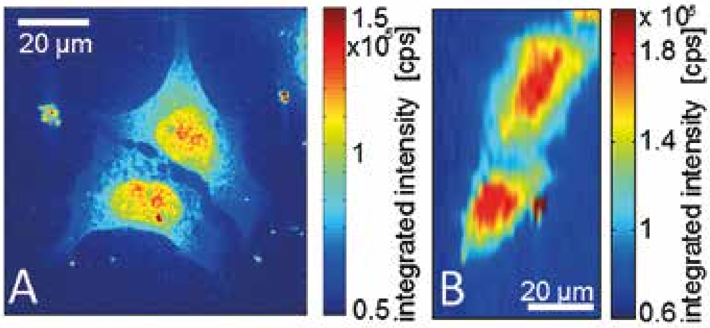

Figure 1

Scanning X-ray diffraction dark field images of A) chemically fixed (symmetric steps) and B) living cells (asymmetric steps). The colour scale shows the total scattered intensity per pixel. The nuclei of the cells are recognized by particularly strong scattering.

X-ray imaging has the potential to complement these established methods and overcome some of the challenges. Hard X-rays provide high penetration depth and nanoscale resolution due to the small wavelength. In recent years, the challenge to focus hard X-rays to small spots thus avoiding averaging effects in complex, heterogeneous samples has successfully been tackled and beams with nanometre diameter are now available [1]. This advancement paves the way for imaging techniques [2,3] where the sample is scanned with a small step size, approximately corresponding to the beam size and employing different imaging modes such as phase or dark field contrast. One major challenge remains: radiation damage by the impact of the highly energetic beams on the sample and, naturally, this is particularly severe in soft matter and biological samples. Recent developments, including fast scanning algorithms and adapted sample environments, help to reduce radiation damage.

In general, when studying biological systems and above all living cells, a suitable sample environment is one key to success. We have chosen microfluidic devices in which the adherent cells are grown and constantly flushed with medium or buffer during the measurements [4]. Thus, the cells are constantly supplied with nutrients and wastes are flushed away. Additionally, the constant liquid flow likely has a positive cooling effect and damaging radicals, which are produced by the incoming radiation, are transported away. We chose eukaryotic cells [5] containing a nucleus for our studies, which grow readily on the silicon nitride windows incorporated in the microfluidic devices as entry windows for the X-rays.

The measurements were performed at the P10 beamline of PETRA III using the Göttingen Instrument for Nano-Imaging with X-rays (GINIX) [6]. The beam was focused down to a few hundred nanometres using two Kirkpatrick-Baez (KB)

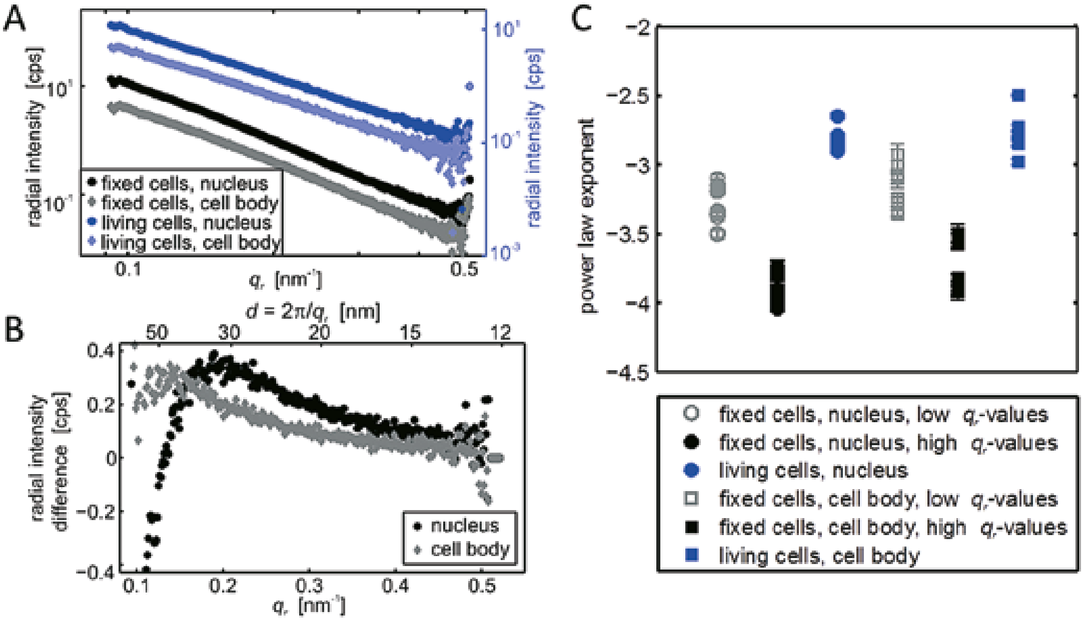

Figure 2

A) Scattered intensity of fixed (black, grey) and living (blue) cells, separately for nuclei and cell periphery.
B) Subtracted intensity ("living – fixed cells"). Regions, where the curves adapt values > 0 show structures destroyed upon chemical fixation, whereas regions with values < 0 correspond to emerging structures.
C) Power law exponents for fits to the data shown in A. Reproducibly, the exponents for living cells are larger than for fixed cells.

mirrors. The sample was scanned through the beam and the scattered signal was recorded in each position. We generated dark field images, where each pixel represents the total scattered intensity for the respective scan position, as shown in Fig. 1. Clearly, the cell nuclei can be distinguished from the cell periphery by their stronger overall scattering.

For our study, we compared living cells with chemically fixed cells, as widely employed in the life and natural sciences. In addition to the real space dark field images, each recorded pixel yields the information encoded in a full scattering pattern and in order to access this information, we analysed the scattered intensity of the living and fixed cells separately for the nuclei and for the cell periphery (see Fig. 2A). In Fig. 2B, the difference between these curves (data for fixed cells subtracted from the data for living cells) is shown. The lower abscissa shows the scattering vector q_r and the upper abscissa shows the corresponding structure size $d = 2\pi/q_r$. We clearly observe both emerging and destroyed structures upon chemical fixation in the range of a few tens of nanometres. Power law fits to the data shown in Fig. 2A yield exponents, which clearly differ for fixed (black symbols) and living (blue symbols) cells. The data for fixed cells were fitted separately for two different power laws to better describe the data.

X-ray imaging allows us to directly compare fixed and living cells, as fixation is no prerequisite for the technique, by contrast to other nanoscale imaging methods like electron microscopy. The differences we observed agree with earlier assumptions of the influence of fixatives and can now be directly measured. Importantly, the observed structural changes are found in a size range of tens of nanometres which is nowadays also reached by visible light fluorescence microscopy, owing to the advent of superresolution microscopy.

The combination of scanning diffraction imaging with nanometre X-ray beams and microfluidic sample environments as demonstrated here has the potential to complement other cellular imaging methods by bridging exactly the gaps left between electron microscopy and visible light microscopy.

Contact: Sarah Köster, sarah.koester@phys.uni-goettingen.de

Authors

Britta Weinhausen[1], Oliva Saldanha[1], Robin N. Wilke[1], Christian Dammann[1], Marius Priebe[1], Manfred Burghammer[2,3], Michael Sprung[4], and Sarah Köster[1]

1. Institute for X-Ray Physics, University of Göttingen, 37077 Göttingen, Germany
2. European Synchrotron Radiation Facility, 71 avenue des Martyrs, 38000 Grenoble, France
3. Department of Analytical Chemistry, Ghent University, 9000 Ghent, Belgium
4. Deutsches Elektronen-Synchrotron DESY, Notkestrasse 85, 22607 Hamburg, Germany

Original publication

"Scanning X-Ray Nanodiffraction on Living Eukaryotic Cells in Microfluidic Environments", Phys. Rev. Lett. 112, 088102 (2014).
DOI: 10.1103/PhysRevLett.112.088102

References

1. A. Schropp, P. Boye, J. M. Feldkamp, R. Hoppe, J. Patommel, D. Samberg, S. Stephan, K. Giewekemeyer, R. N. Wilke, T. Salditt, et al., "Hard x-ray nanobeam characterization by coherent diffraction microscopy", Appl. Phys. Lett. 96, 091102 (2010).
2. O. Bunk, M. Bech, T. H. Jensen, R. Feidenhans'l, T. Binderup, A. Menzel, and F. Pfeiffer, "Multimodal x-ray scatter immaging", New J. Phys. 11, 123016 (2009).
3. B. Weinhausen, J.-F. Nolting, C. Olendrowitz, J. Langfahl-Klabes, M. Reynolds, T. Salditt, and S. Köster, "X-ray nano-diffraction on cytoskeletal networks", New J. Phys. 14, 085013 (2012).
4. B. Weinhausen and S. Köster, "Microfluidic devices for X-ray studies on hydrated cells", Lab Chip 13, 212 (2013).
5. R. Windoffer, S. Wöll, P. Strnad, and R. E. Leube, "Identification of Novel Principles of Keratin Filament Network Turnover in Living Cells", Mol. Biol. Cell 15, 2436 (2004).
6. T. Salditt, S. Kalbfleisch, M. Osterhoff, S. P. Krüger, M. Bartels, K. Giewekemeyer, H. Neubauer, and M. Sprung, "Partially coherent nano-focused x-ray radiation characterized by Talbot interferometry", Opt. Express 19, 9656 (2011).

Decoding the nanostructure of advanced TiAl alloys.

Real-time insights into the precipitation behaviour

Titanium aluminides based on the ordered γ-TiAl phase have attracted attention in aircraft and automotive industries due to their potential as structural light-weight materials in high-temperature application. With the intention to broaden the temperature range of usage, further alloy development is required. Alloying with carbon improves the mechanical properties at elevated temperatures by solid solution and / or precipitation hardening. However, the direct observation of the ongoing precipitation mechanism was difficult so far. Thus, we studied the precipitation behaviour and thermal stability of perovskite-type carbides Ti_3AlC in an advanced TiAl alloy for the first time by means of *in situ* small-angle X-ray scattering in combination with *ex situ* high-energy X-ray diffraction as well as transmission electron microscopy.

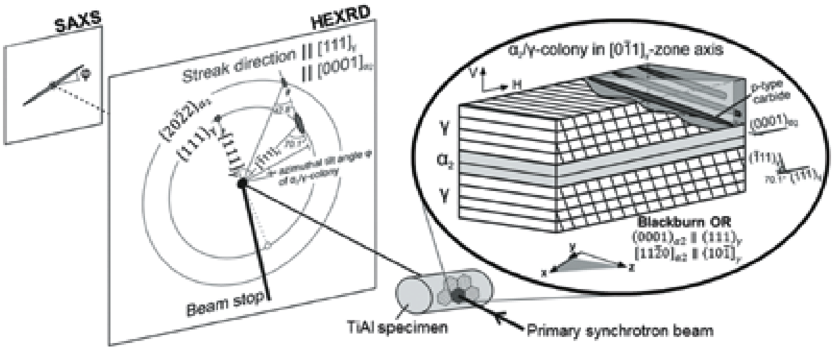

Figure 1

Experimental setup of the conducted synchrotron experiment. The monochromatic beam with an energy of 100 keV is guided through the sample which is situated in a modified quenching and deformation dilatometer device DIL 805 A / D from Baehr Thermoanalyse. The diffraction patterns are recorded with a Perkin Elmer XRD 1621 Flat Panel detector in experimental hutch EH 3, whereas a mar345 Image Plate detector located behind in EH 4 is used to record the signal from small-angle scattering. The cylindrical sample with a size of 5 mm in diameter and 10 mm in length was heated inductively. H = horizontal, V = vertical (related to the crystal-coordinate system of the γ-phase).

Advanced intermetallic γ-TiAl based alloys, e.g. TNM alloys with a nominal composition of Ti-43.5Al-4Nb-1Mo-0.1B (in at %), have found application as turbine blades or turbo-charger wheels in modern high-performance aircraft and automotive engines due to their low density, high strength and creep-resistance up to 750 °C as well as their good oxidation and burn resistance [1]. However, efficiency and engine performance is steadily improving with increasing operation temperatures, demanding more creep-resistant structural light-weight materials. In order to increase the high-temperature capability of γ-TiAl based alloys and thus to widen their range of use, alloying concepts with C are being investigated. Carbon is reported to increase the creep strength and hardness at elevated temperatures by solid solution hardening and / or formation of needle-shaped precipitates of perovskite-type Ti_3AlC carbides, depending on the solubility limit of the constituent phases and the thermal history. Nevertheless, detailed investigations of the precipitation behaviour are still lacking. Therefore, it is needed to clarify the role of alloy composition on the formation and evolution of carbides and thus on their influence on microstructure and mechanical properties.

Starting from a supersaturated TNM-1C alloy the precipitation kinetics and thermal stability of p-type carbides Ti_3AlC during isothermal annealing at 750 °C and ensuing re-heating to 1200 °C is quantified by means of *in situ* small-angle X-ray scattering (SAXS) using synchrotron radiation. Complementary, the formed hierarchical structures on the nano-scale, i.e. p-type carbide precipitates within ultra-fine γ-lamellae of the α_2/γ-colonies, were investigated by means of monochromatic high-energy X-ray diffraction (HEXRD) in combination with transmission electron microscopy (TEM).

The experiments were carried out at the HZG high-energy materials science beamline HEMS (P07) at PETRA III. A sketch of the experimental setup is depicted in Fig. 1. The SAXS data were recorded with a sample-to-detector distance of 11.654 m and a frame rate of 20 images per hour. Slits made of pure tungsten minimized undesired scattering and ensured a low background. Data evaluation was performed by means of the program Fit2D with respect to azimuthal integration followed by a fitting procedure of the derived scattering curves with the program SANSFit based on a least-square method iteration [2-5].

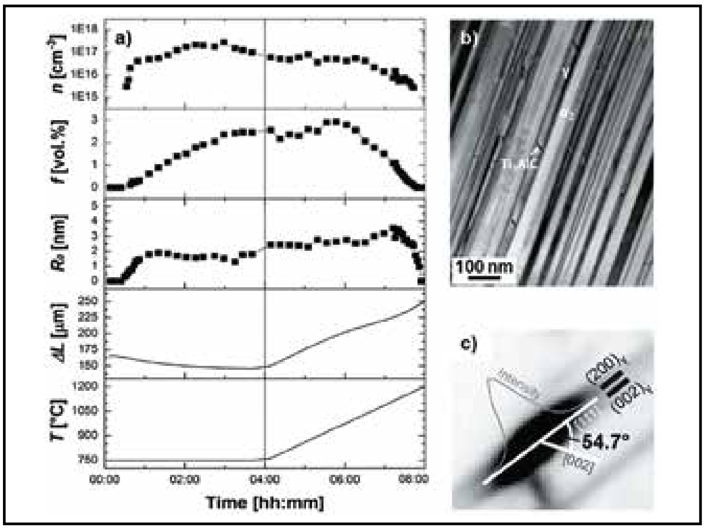

Figure 2

a) Progress of temperature T and length change ΔL of the dilatometer sample during heat-treatment. Additionally, the median radius R_0 of the needle-shaped p-type carbide precipitates, their volume fraction f and their number density n are given;

b) TEM bright-field image of p-type carbides aligned within a characteristic γ-lath and

c) the HEXRD image section after precipitation annealing at 750 °C for 4 h corresponds to a detail of the streaked (002)γ and (200)γ reflections.

The conducted *in situ* SAXS experiment allows determining the precipitation behaviour during isothermal annealing at 750 °C as well as to investigate the thermal stability of p-type carbides during further heating to 1200 °C with a rate of 2 K/min based on the evaluation of the scattering curves in Fig. 2a. It was found that p-type carbide formation takes place after an incubation time of 30 min within the γ-laths, previously formed from supersaturated α_2-grains. Thus, the phase-transformation sequence takes the form

$$\alpha_{2,ss}\text{-Ti}_3\text{Al} \rightarrow \alpha_2\text{-Ti}_3\text{Al} + \gamma\text{-TiAl and } \gamma\text{-TiAl} \rightarrow \text{p-Ti}_3\text{AlC}.$$

After ageing for 4 h at 750 °C, the carbide precipitates exhibit a mean radius of 1.7 nm with a monodisperse size distribution. The aspect ratio of the elongated carbides of 7, as verified by TEM (Fig. 2b), correlates with a carbide length of 23.8 nm. In view of the mean γ-lamellae thickness of 13.8 nm (see also Fig. 2b), the precipitates must grow at an inclined angle to the lamella walls. The thickness D of γ-laths and the radius R of p-type carbides can be correlated by the geometrical relation $D = 2\mu R \times \cos(54.7°)$ according to the orientation relationship $(001)_\gamma \parallel (001)_p$ and $(010)_\gamma \parallel (010)_p$. The geometrical correlation is valid as long as the size of p-type carbides is controlled by the small dimension of γ-lamellae.

The SAXS data are in good agreement with the evaluation of diffraction streaks from the two-dimensional HEXRD patterns using the Scherrer Equation (Fig. 2c). There, the occurrence of diffraction streaks, i.e. anisotropic peak broadening, was found to originate from the finite thickness of γ-laths and the geometrical relation between the monochromatic X-ray beam and the structure of an α_2/γ-colony within the polycrystalline TNM-1C material. Diffraction streaking implies that the 70.1° tilted $(-111)_\gamma$ lattice planes are in diffraction condition, which do not exhibit a strong superordinate structure when compared to $(111)_\gamma$ lattice planes which are by definition parallel to $(0001)_{\alpha2}$.

The combination of SAXS and HEXRD, applying the modified quenching and deformation dilatometer, were successfully used to study *in situ* the intrinsic hierarchical nanostructure of complex intermetallic TiAl alloys during annealing without time-consuming TEM effort. This approach offers unique opportunities for investigating various aspects of importance for the development of TiAl alloys and other precipitation hardened alloy systems. In future, fast simultaneously working detector systems combined with the high brilliance of the PETRA III storage ring will allow a precise structural evolution of fast precipitation sequences.

Contact: Svea Mayer, svea.mayer@unileoben.ac.at

Authors

Emanuel Schwaighofer[1], Peter Staron[2], Boryana Rashkova[1], Andreas Stark[2], Norbert Schell[2], Helmut Clemens[1], and Svea Mayer[1]

1. Department of Physical Metallurgy and Materials Testing, Montanuniversität Leoben, 8700 Leoben, Austria
2. Institute of Materials Research, Helmholtz-Zentrum Geesthacht, 21502 Geesthacht, Germany

Original publication

"*In situ* small-angle X-ray scattering study of the perovskite-type carbide precipitation behavior in a carbon-containing intermetallic TiAl alloy using synchrotron radiation", Acta Mater. 77, 360-369 (2014). DOI: 10.1016/j.actamat.2014.06.017

References

1. H. Clemens and S. Mayer, "Design, processing, microstructure, properties, and applications of advanced intermetallic TiAl alloys", Adv. Eng. Mater. 15, 191-215 (2013).
2. A. P. Hammersley, S. O. Svensson, M. Hanfland, A. N. Fitch, and D. Häusermann, "Two-dimensional detector software: from real detector to idealised image or two-theta scan", High Pressure Res. 14, 235-248 (1996).
3. K.-D. Liss, A. Bartels, H. Clemens, S. Bystrzanowski, A. Stark, T. Buslaps, F.-P. Schimansky, R. Gerling, C. Scheu, and A. Schreyer, "Recrystallization and phase transitions in a γ-TiAl-based alloy as observed by *ex situ* and *in situ* high-energy X-ray diffraction", Acta Mater. 54, 3721-3735 (2006).
4. P. Staron, U. Christoph, F. Appel, and H. Clemens, "SANS investigation of precipitation hardening of two-phase γ-TiAl alloys", Appl. Phys. A 75, 1-3 (2002).
5. T. Schmoelzer, K.-D. Liss, P. Staron, S. Mayer, and H. Clemens, "The contribution of high-energy X-rays and neutrons to characterization and development of intermetallic titanium aluminides" Adv. Eng. Mater. 13, 685-699 (2011).

From molecular complexes to nanocrystals.

In situ total scattering studies of WO_3

Time resolved total scattering has been used to unravel the mechanism of WO_3 nanoparticle formation from an aqueous precursor under hydrothermal conditions. Pair distribution function (PDF) analysis of total scattering data reveals that a precursor structure consisting of corner- and edge-sharing WO_6 octahedra undergoes reorientation before forming the nanoparticles. This structural transformation is the key to the formation of different hexagonal phases of WO_3.

Tungsten oxide (WO_3) is an interesting material for applications in solar cells, smart windows and gas sensors due to its excellent electrochemical, electrochromic, photochromic and gas sensing properties [1-3]. The characteristics of WO_3 can be tailored by tuning the nanostructure composition, as well as the specific synthesis procedures. Therefore, rational design of nanoparticles with desirable properties requires fundamental insight into the reaction mechanisms leading to the formation of the crystalline nanoparticles from precursor solution. It is thus crucial to gain knowledge about the reaction pathway in order to optimize the formation process.

In situ total scattering studies of the formation and growth of nanoparticles during sub- and supercritical synthesis provides information about the precursor structure in the solutions. It also reveals how these precursor complexes undergo structural changes before forming solid precipitates, which eventually transform into nanocrystals. The pair distribution function is used to analyze the precursor structure since it reveals structural information from solutions, amorphous solids as well as from crystals [4]. Time resolved total scattering data can be obtained at high energy synchrotron beamlines for X-ray diffraction. The reaction mechanism under solvothermal conditions can be followed in a specifically designed *in situ* reactor [5].

In the current study at the powder diffraction station of beamline P02 at PETRA III, a solution of ammonium metatungstate $(NH_4)_6H_2W_{12}O_{40} \cdot xH_2O$ in water was heated under high pressure of 250 bar. Time resolved data collection was started before the heater was switched on. Figure 1 (a,b) shows the evolution of the PDF in time. Modelling of the data reveals that a complex precursor structure exists in the solution (Fig. 1c). It consists of edge and corner sharing WO_6 octahedra. A representative data set obtained 25 sec after initiation of heating was subjected to structural modelling analysis, and it revealed that WO_6 octahedra form a cluster by corner and edge sharing (Fig. 1(d)). The first two noticeable peaks at 1.87 Å and 2.22 Å correspond to W-O bond distances. The third peak (3.28 Å) corresponds to W-W distances that arise due to edge sharing of WO_6 octahedra, whereas the peak at 3.68 Å arises due to W-W distances of corner sharing of WO_6 octahedra. The presence of a noticeable peak at 6.02 Å is due to the second coordination sphere of W-W bond distances and it supports the formation of the cluster. It is of interest to note that the absence of any correlations in the PDF beyond a distance

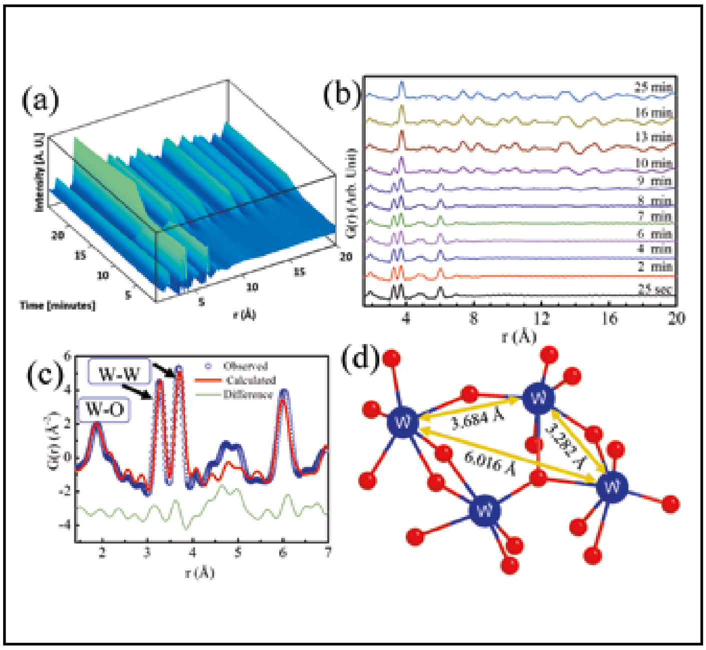

Figure 1

(a) Evolution of PDFs with respect to time at 250 °C reaction temperature, measured at beamline P02.1. (b) Selected PDFs illustrating the reaction progress at 250 °C. (c) PDF for the precursor solution. (d) Molecular cluster present in the precursor solution.

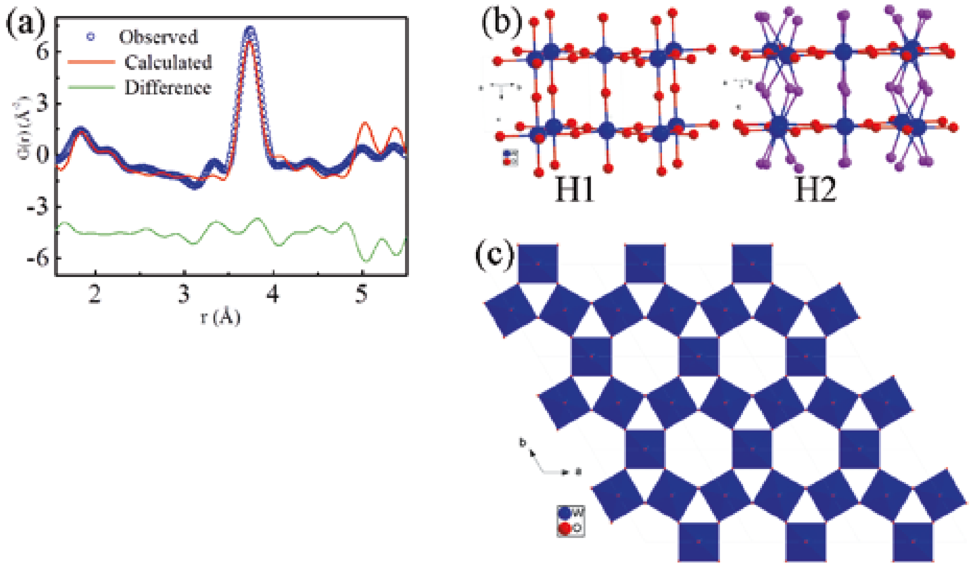

Figure 2

a) PDF fitted with the H2 model for local structure only.

b) The H1 and H2 crystal structures.

c) Packing diagram of WO_3.

of about 7 Å indicates the presence of local ordering only. While heating the solution, the precursor structure gradually undergoes a reorientation converting the edge sharing octahedra to corner sharing octahedra before forming the nanoparticles. While the octahedra locally become reoriented there is no evidence of long range order. After 10 minutes of heating, the nuclei in the solution abruptly cluster together and form crystalline particles. The sudden formation of nanocrystals is also confirmed by *in situ* powder X-ray diffraction. Rietveld refinement was carried out with the last data set of the time-resolved experiment. WO_3 crystallizes in a hexagonal crystal system with space group *P6/mmm* (H1). Although the long range order in the H1 structure could be fitted with the ordered H1 model, the short range local order could not be fitted. The peak at 2.22 Å could be explained by the nearest-neighbor W-O bond distance of the H1 model. However the local order could be fitted with another hexagonal phase (space group $P6_3/mcm$ *(H2)*) [6].

The *in situ* experiment resembles the hydrothermal reaction scale in a laboratory autoclave synthesis, as the same product was obtained. However, the other hexagonal phase H2 of WO_3 was obtained in a continuous flow reactor starting from the same precursor solution. In the flow reactor the reaction time is very short in comparison to the autoclave. Therefore it may be suggested that in case of flow synthesis the octahedra in the precursor complex do not have sufficient time to reorient themselves into the ordered H1 structure, which results in half occupied disordered oxygen positions (H2 structure).

In conclusion, *in situ* X-ray scattering studies allow us to follow reaction mechanisms for the formation of solids from solution and to determine the dynamics associated with it. The present study on WO_3 establishes the complex precursor structure and the reaction pathways and it also rationalizes the formation of two different hexagonal phases of tungsten oxide.

Contact: Bo B. Iversen, bo@chem.au.dk

Authors

Dipankar Saha[1], Kirsten M. Ø. Jensen[1], Christoffer Tyrsted[1], Espen D. Bøjesen[1], Aref Hasen Mamakhel[1], Ann-Christin Dippel[2], Mogens Christensen[1], and Bo B. Iversen[1]

1. Center for Materials Crystallography, Department of Chemistry and iNANO, Aarhus University, Langelandsgade 140, 8000 Aarhus, Denmark
2. Deutsches Elektronen-Synchrotron DESY, Notkestr. 85, 22607 Hamburg, Germany

Original publication

"*In Situ* Total X-Ray Scattering Study of WO_3 Nanoparticle Formation under Hydrothermal Conditions", *Angew. Chem. Int. Ed.* 53(14), 3667-3670 (2014)
DOI: 10.1002/anie.201311254

References

1. H. Zheng, Y. Tachibana, and K. Kalantar-zadeh, "Dye-Sensitized Solar Cells Based on WO_3", Langmuir 26, 19148-19152 (2010).
2. G. A. Niklasson and C. G. Granqvist, "Electrochromics for smart windows: thin films of tungsten oxide and nickel oxide, and devices based on these", J. Mater. Chem. 17, 127-156 (2007).
3. D. T. Gillaspie, R. C. Tenent, and A. C. Dillon, "Metal-Oxide Films for Electrochromic Applications: Present Technology and Future Directions", J. Mater. Chem. 20, 9585-9592 (2010).
4. T. Egami and S. J. Billinge, "Underneath the Bragg peaks: structural analysis of complex materials", Pergamon, 2012.
5. J. Becker, M. Bremholm, C. Tyrsted, B. Pauw, K. M. O. Jensen, J. Eltzholt, M. Christensen, and B. B. Iversen, "Experimental setup for *in situ* X-ray SAXS/WAXS/PDF studies of the formation and growth of nanoparticles in near-and supercritical fluids", J. Appl. Crystallogr. 43, 729-736 (2010).
6. B. Gerand, G. Nowogrocki, J. Guenot, and M. Figlarz, "Structural study of a new hexagonal form of tungsten trioxide", J. Solid State Chem. 29, 429-434 (1979).

A first glimpse of photosynthesis in action.

Making molecular movies of the light sensitive protein photosystem II responsible for oxygen production

The intense, femtosecond duration X-ray pulses produced by X-ray free-electron lasers enable time-resolved measurements with a femtosecond 'shutter speed' in addition to the ability to determine the structure of radiation sensitive proteins through the principle of 'diffraction before destruction' [1, 2]. These unique properties were exploited with the aim to understand the process of photosynthesis in action. Photosynthesis is the chemical reaction responsible for turning sunlight and water into oxygen plus energy.

Photosynthesis is responsible for the majority of atmospheric oxygen and thus for sustaining life on earth, as well as all of the earth's fossil fuel reserves. Photosystem II (PS II) is the molecule responsible for capturing light and using this energy to split water into oxygen and hydrogen, which is then used as an energy source in subsequent reactions. PS II acts as a catalyst in the splitting of water - it facilitates the splitting of water but is not consumed, thus a single molecule of photosystem II may catalyse many cycles of oxygen splitting. The splitting process requires the absorption of four photons, each of which triggers a separate stage of the reaction. This much is known from previous studies, but to date no one has been able to observe the reaction in progress. However, being sensitive to light the most interesting part of this protein is also the most challenging to study as it is easily damaged during the process of imaging. The femtosecond duration pulses from X-ray free-electron lasers (FELs) provide a unique way in which to address this problem.

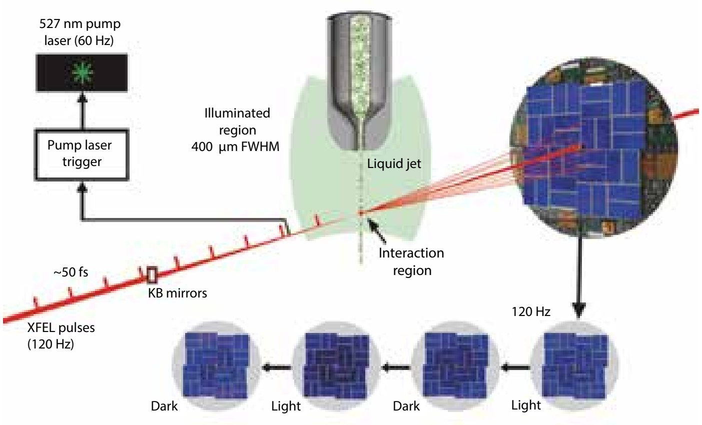

Figure 1

Serial crystallography delivers fresh sample to the interaction region for each X-ray pulse, and each crystal is exposed only once to the beam. For time resolved studies, the crystal stream is exposed to two subsequent optical laser pulses at 527 nm separated by approx. 200 µs before the stream interacts with the X-ray FEL beam 570 µs after the second pump pulse. Triggering the pump laser at half the FEL repetition rate allows for alternating collection of X-ray diffraction patterns from the S1 dark state and the double-excited S3 state shown in Fig. 2.

Measurements were performed using the newly developed technique of serial femtosecond crystallography (SFX) [1, 2], in which a stream of protein crystals flows across the FEL beam and each crystal is exposed to the X-ray beam only once, as illustrated in Fig. 1. Delivery of fresh sample to the interaction region for each measurement ensures that each crystal is free from radiation damage at the time of exposure to the X-rays. Continuously replenishing the sample makes it possible to study reactions where multiple cycles of excitation would result in either a mixture of states, or where the reaction is not reversible prohibiting the accumulation of signal over many cycles of excitation. Meanwhile, the power of X-ray FELs enables a diffraction pattern to be captured using a single femtosecond duration X-ray pulse, reducing the effects of radiation damage observed in the measured structure to almost negligible levels.

Still frames of photosystem II as it splits water into hydrogen and oxygen were recorded using the LCLS at SLAC in a pump-probe scheme with an optical pump and an X-ray probe, as shown in Fig. 1. Nano-crystals of photosystem II complex were extracted from bacteria that employ photosynthesis as their energy source, a cyanobacteria called *Thermosynechococcus elongatus*. The photosystem II catalytic water splitting cycle is illustrated in Fig. 2. It involves four light excitations to complete one cycle in which two water molecules are converted into oxygen and protons. The most interesting part of the cycle is after two flashes, as this is where the largest structural changes occur. Each crystal was no more than a few microns in size and was exposed to two flashes of visible laser light separated by approx. 200 µs to bring the water splitting process to the S_3 state. At this point in the cycle, 570 µs after the second laser pulse, synchronised X-ray pulses from the LCLS captured X-ray diffraction patterns with an exposure time of ~30 fs, short enough to freeze-frame the water splitting process at different stages. This enabled observation of how the molecular structure of the photosystem II complex changed during the process.

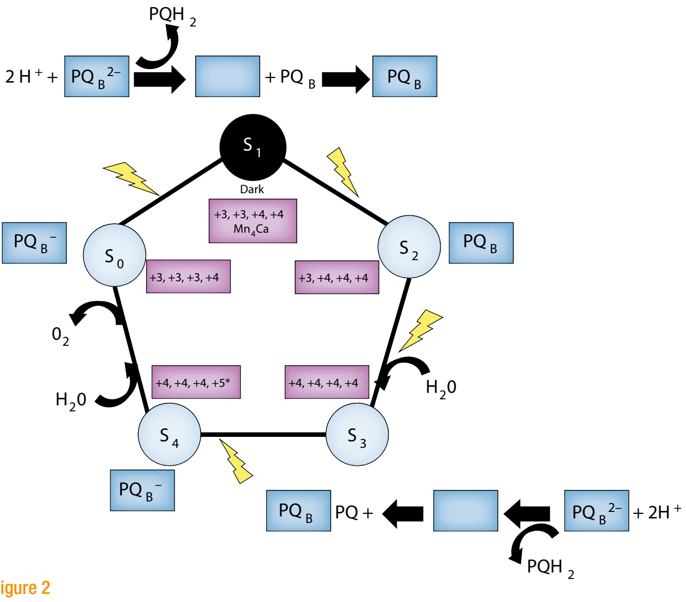

Figure 2

The cycle of the oxygen-evolving complex (OEC) in photosystem II. The oxidation state of the 4 manganese ions in the Mn_4CaO_5 cluster changes after each of the charge separation events, initiated by a flash of light. Also shown in this figure is the reduction of the plastoquinone which serves as the terminal electron acceptor of photosystem II responsible for charge migration.

This time-resolved SFX study captures PS II after two flashes of light and provides experimental evidence for structural changes occurring in the S_3 state of the oxygen-evolving complex (OEC) of PS II, shown in Fig. 3. Although only at modest resolution of 5 Å, changes in the electron density of the manganese cluster, which is responsible for catalysing the water splitting process, were just visible. They are accompanied by structural changes in the OEC and at the acceptor side of PS II. The change in this cluster is suggestive of an increase of the distance between the cubane and the 'dangler' Mn and distortion in the cubane in the S_3 state, which could allow an essential second water molecule to bind in higher S-states, as is consistent with recent theoretical modeling [3]. Our observations also reveal an overall decrease in the dimension of the entire cluster in the S_3 state due to the lack of Jahn-Teller distortion of Mn atoms at +4 oxidation states.

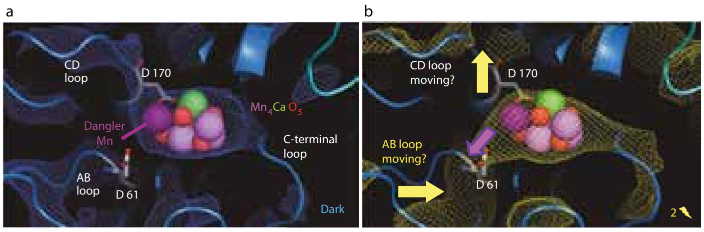

Figure 3

Structure of the Mn_4CaO_5 cluster for dark (S_1) and double-excited (S_3) state. (A) shows S_1 in blue and (B) S_3 in yellow at a contour level of 1.5 σ with the structural model 3ARC from Umena et al. [4]. The figure shows that the Mn cluster and its surrounding protein environment may undergo significant conformational changes in the transition from the dark S_1 to the double-excited S_3 state.

Catalysis plays a big role in many fields of chemistry, and the techniques developed here offer huge potential not only for the study of photosynthesis, but also for the study of catalysis in general. Observing catalysis in action may lead to insights that in turn lead to the development of even more efficient catalysts. A deeper understanding of photosynthesis could for instance aid the development of better solar cells and might advance the quest for biochemistry's holy grail, artificial photosynthesis. Extension of this experiment to high resolution studies of all the S-states is underway and will lay the foundation for unraveling three-dimensional, high resolution structures of all stages of the water oxidation process.

Contact: Anton Barty, anton.barty@desy.de
Henry Chapman, henry.chapman@desy.de
Petra Fromme, pfromme@asu.edu

Authors

C. Kupitz, S. Basu, I. Grotjohann, R. Fromme, N. A. Zatsepin, K. N. Rendek, M. S. Hunter, R. L. Shoeman, T. A. White, D. Wang, D. James, J.-H. Yang, D. E. Cobb, B. Reeder, R. G. Sierra, H. Liu, A. Barty, A. L. Aquila, D. Deponte, R. A. Kirian, S. Bari, J. J. Bergkamp, K. R. Beyerlein, M. J. Bogan, C. Caleman, T.-C. Chao, C. E. Conrad, K. M. Davis, H. Fleckenstein, L. Galli, S. P. Hau-Riege, S. Kassemeyer, H. Laksmono, M. Liang, L. Lomb, S. Marchesini, A. V. Martin, M. Messerschmidt, D. Milathianaki, K. Nass, A. Ros, S. Roy-Chowdhury, K. Schmidt, M. Seibert, J. Steinbrener, F. Stellato, L. Yan, C. Yoon, T. A. Moore, A. L. Moore, Y. Pushkar, G. J. Williams, S. Boutet, R. B. Doak, U. Weierstall, M. Frank, H. N. Chapman, J. C. H. Spence, and P. Fromme

Full author and affiliation details at www.nature.com/nature/journal/v513/n7517/full/nature13453.html

Original publication

"Serial time-resolved crystallography of photosystem II using a femtosecond X-ray laser", *Nature* 513, 261-265 (2014), doi:10.1038/nature13453.

References

1. H. N. Chapman et al., "Femtosecond X-ray protein nanocrystallography", Nature 470, 73-77 (2011).
2. S. Boutet et al., "High-Resolution Protein Structure Determination by Serial Femtosecond Crystallography", Science 337, 362-364 (2012).
3. H. Isobe et al., "Theoretical illumination of water-inserted structures of the $CaMn_4O_5$ cluster in the S_2 and S_3 states of oxygen-evolving complex of photosystem II: full geometry optimizations by B3LYP hybrid density functional", Dalton Trans 41, 13727-13740 (2012).
4. Y. Umena, K. Kawakami, J.-R. Shen, and N. Kamiya, "Crystal structure of oxygen-evolving photosystem II at a resolution of 1.9Å", Nature 473, 55-60 (2011).

First human membrane protein solved using X-FEL radiation.

Atomic structure of a human serotonin receptor at ambient temperature

The new method of serial femtosecond crystallography is applied to probing microcrystals of a human serotonin receptor, using an X-ray free-electron laser (X-FEL). The unique properties of X-FELs (high intensity, short pulse duration) enable us to overcome the bottleneck of radiation damage and the need for large, well-diffracting crystals typical for conventional X-ray crystallography. We were able to solve the room temperature structure of a member of a medically important superfamily of human membrane proteins from crystals out of reach for a conventional source.

G-protein coupled receptors (GPCRs) represent one of the most pharmaceutically prominent protein families, which are targets of 30 – 40 % of all prescriptive drugs. Their main function is to sense the presence of signalling molecules outside the cell, in order to trigger an intracellular response appropriate to the stimulus. Hence, by either inhibiting or activating these receptors, it is possible to specifically counteract a variety of diseases on a molecular level.

GPCRs are difficult to analyse by X-ray crystallography, due to high flexibility, low production yields and low stability of the receptor after extraction from membranes, leading to very small crystals. Conventional crystallographic experiments are generally limited by the need of large, well-diffracting crystals, which are particularly difficult to obtain for membrane proteins. A variety of improvements on the level of protein engineering, crystallization methods and the availability of modern synchrotrons, allowed for the first high-resolution GPCR structure of the human β_2-adrenergic receptor to be solved in 2007 [1], a work that contributed to the Nobel Prize in Chemistry 2012. Microfocus beamlines with X-ray beams of less than 10 μm FWHM are readily available, but typically long exposure times of several seconds are required to record weak high-resolution reflections. During these exposures, the crystals suffer severe radiation damage and typically require merging of data from multiple crystals.

The method of serial femtosecond crystallography (SFX) [2] (Fig. 1) makes use of ultrashort X-FEL pulses (< 50 fs) to outrun radiation damage. Due to the very high brilliance (> 10^{12} photons / pulse) of the X-ray beam of LCLS, it is possible to obtain interpretable diffraction patterns from individual microcrystals. The sample is completely vaporized due to the interaction with the X-rays, making it necessary to continuously replace the crystals in the beam. The typically used delivery technique is the Gas Virtual Dynamic Nozzle (GVDN) system [2], where a stream of microcrystals in aqueous solution is delivered into the interaction region. The disadvantage of GVDN is the high flow rate,

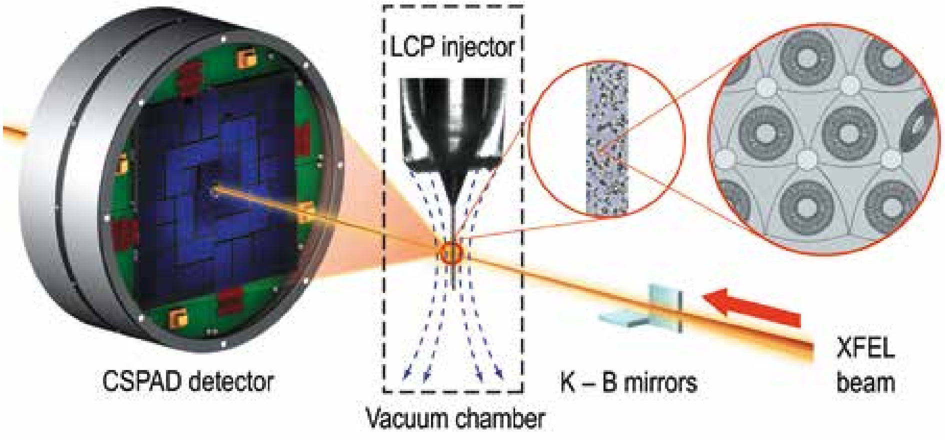

Figure 1

Scheme of the experimental setup for SFX data collection using the LCP injector. Microcrystals grown in LCP (right) injected into the interaction region (centre) inside a vacuum chamber and probed with the microfocus X-FEL beam. Diffracted rays are detected by the Cornell-SLAC Pixel Array Detector, CSPAD (left).
(Science 342, 1521 (2013)).

requiring 10 – 100 mg of crystallized protein for a complete dataset, which is practically unachievable for many human membrane proteins including GPCRs.

One of the methods that enable GPCR crystallography is the crystallization of the proteins in lipidic cubic phase (LCP, Fig. 1) [3]. LCP forms a 3D matrix made of lipids and water, mimicking the cell membrane and providing a stabilizing environment for GPCRs. LCP crystallization often leads to well-ordered but small crystals that are ideal for SFX. We have turned an apparent disadvantage of LCP, its highly viscous gel-like texture, into an advantage by designing a special LCP microextrusion injector [4] that enables a better control over the flow allowing for a more efficient use of protein microcrystals. The LCP injection system (Fig. 1), which has been developed jointly by Arizona State University and The Scripps Research Institute, typically requires less than 300 μg of crystallized protein, making it very attractive for structural studies of challenging targets.

The combination of GPCR crystallization in LCP with the exciting new technique of serial femtosecond crystallography has allowed us to solve the first human membrane protein structure at ambient temperatures to near-atomic resolution. As a model system we used microcrystals of the serotonin receptor 5-HT_{2B} in complex with the anti-migraine drug ergotamine. This receptor is of high medical relevance, since its malfunction is the cause of a variety of diseases, behavioural effects and is the target of hallucinogenic drugs.

A total of 152651 crystal diffraction patterns were collected within 10 hours, of which finally 32819 were indexed and integrated to a final dataset, with the software package CrystFEL [5]. The structure obtained at ambient temperature was compared to the previous synchrotron structure of the same receptor at cryogenic conditions [6]. The overall structure and quality of the X-FEL structure is very similar to the synchrotron structure, however some important details differ, most likely due to the temperature difference during data collection and apparent radiation damage in the synchrotron structure (Fig. 2). By careful analysis of temperature factors (Debye-Waller 'B' factors) it was possible to identify more dynamic regions, namely loop regions, which are involved in protein-protein interactions necessary for signalling.

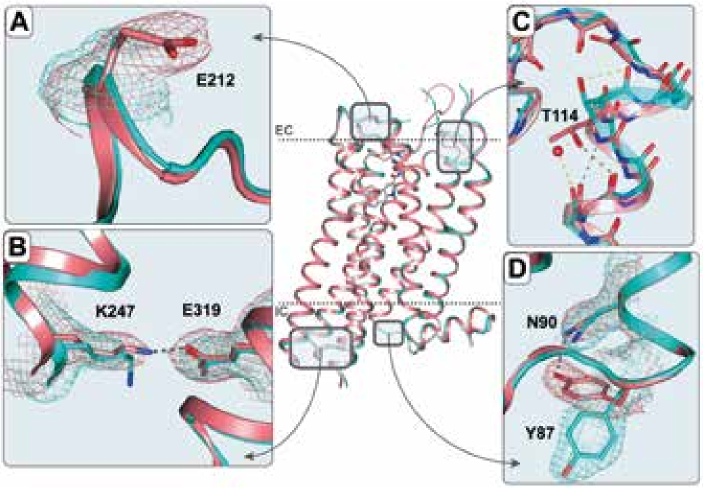

Figure 2

Comparison of synchrotron (cyan) and SFX structure (light red). Close-ups represent a selection of structural differences. A) Missing side chain in synchrotron structure, most likely due to radiation damage, B) Salt bridge intact in SFX structure, C) and D) conformational difference in SFX structure, probably due to room-temperature measurements (Science 342, 1521 (2013)).

SFX enabled us to probe a GPCR structure in a physiologically more accurate manner, and the general understanding of the structure and function of this highly important family of membrane proteins can be improved. By further improving technical details, such as sample handling, background scattering, dynamic range of detectors and data processing, higher quality data could be obtained in the near future.

Contact: Cornelius Gati, cornelius.gati@desy.de
Henry N. Chapman, henry.chapman@desy.de
Vadim Cherezov, vcherezo@scripps.edu

Authors

Wei Liu, Daniel Wacker, Cornelius Gati, Gye Won Han, Daniel James, Dingjie Wang, Garrett Nelson, Uwe Weierstall, Vsevolod Katritch, Anton Barty, Nadia A. Zatsepin, Dianfan Li, Marc Messerschmidt, Sébastien Boutet, Garth J. Williams, Jason E. Koglin, M. Marvin Seibert, Chong Wang, Syed T. A. Shah, Shibom Basu, Raimund Fromme, Christopher Kupitz, Kimberley N. Rendek, Ingo Grotjohann, Petra Fromme, Richard A. Kirian, Kenneth R. Beyerlein, Thomas A. White, Henry N. Chapman, Martin Caffrey, John C. H. Spence, Raymond C. Stevens, Vadim Cherezov

Full author and affiliation details at
www.sciencemag.org/content/342/6165/1521

Original publication

"Serial Femtosecond Crystallography of G Protein-Coupled Receptors",
Science 342, 1521-1524 (2013). DOI: 10.1126/science.1244142

References

1. S. G. F. Rasmussen et al., "Crystal structure of the human beta2 adrenergic G-protein-coupled receptor", Nature 450, 383-7 (2007).
2. H. N. Chapman et al., "Femtosecond X-ray protein nanocrystallography", Nature 470, 73-7 (2011).
3. M. Caffrey and C. Porter, "Crystallizing membrane proteins for structure determination using lipidic mesophases", J. Vis. Exp. (2010). DOI: 10.3791/1712
4. U. Weierstall et al., "Lipidic cubic phase injector facilitates membrane protein serial femtosecond crystallography", Nat. Commun. 5, 3309 (2014).
5. T. A. White et al., "CrystFEL: a software suite for snapshot serial crystallography", J. Appl. Crystallogr. 45, 335-341 (2012).
6. D. Wacker et al., "Structural features for functional selectivity at serotonin receptors", Science 340, 615-9 (2013).

Guiding neural networks.

How the guidance molecule netrin-1 pulls and pushes axons to their destination

Neurons are specialized cells and important components of the nervous system and extend axons over large distances to build up neural networks. So-called guidance cue proteins steer the axons towards their destination by triggering the release of specific signals which attract or repel receptors sitting on the tip of the axon. One such group of proteins – netrins – can cause both attraction and repulsion effects. A crystal structure of the protein netrin-1 in complex with one of its receptors – DCC – shows that netrin-1 can bind to two molecules of DCC simultaneously. One of these binding sites is specific to DCC but the other is a unique generic binding site. Follow-up experiments performed by neuroscientists from the Dana-Farber Cancer Institute in Boston (USA) and Peking University (China) show that the generic site can be occupied by another receptor. Netrin-1 acts as a switch board to trigger either attraction or repulsion, depending on the receptors present at the tip of the axon. These findings also add to our understanding of the behaviour of migrating cells including the process of tumour metastasis.

Neurons project axons that move and grow in response to chemical signals, the release of which is triggered by proteins known as guidance cues. Receptors which recognize and respond to these cues sit on the tip of the axon in the so-called growth cone. The receptors then translate the cues into movement, causing the neuron to move towards or away from the released chemicals, so steering the axon to its final destination. Of particular interest are the group of guidance proteins known as netrins which are able to trigger both attraction and repulsion responses, depending on the receptor present on the axon growth cone. But just how one molecule can trigger two conflicting responses has long been a mystery within the field. Netrin-1 interacts with two receptors that produce different signalling outcomes – the receptor DCC causes an attraction response while interaction with the receptor UNC5 together with DCC causes repulsion.

Although it has been known for some time that DCC is involved in neuron signalling, it was actually first discovered in an entirely different context. DCC, or Deleted in Colorectal Cancer, was initially discovered as a marker for colon cancer, where its absence is associated with a malignant state of the disease. Recent work indicates that the absence of the DCC receptor in colon cells promotes tumour metastasis [1] and desensitizes the tumour cells to a netrin-1 dependent apoptotic pathway [2]. Also here netrin-1 plays an important role. Without netrin, the netrin / DCC signalling complex breaks down and the cell dies. Tumour cells avoid this apoptotic pathway by switching off the production of DCC. The netrin receptor UNC-5 (uncoordinated 5) was first discovered in the nematode worm, where its absence results in uncoordinated movements. This receptor too is associated with apoptosis, indicating both netrin receptors can process extra-cellular signals that can drastically change the behaviour of the cell.

Despite its apparently important role in several cellular processes, the structure of netrin was unknown. We worked closely together with teams from Harvard and Peking University to resolve the structure of netrin and how it interacts with its receptors on a molecular level. The Wang group from Harvard provided us with DCC fragments, which we then combined with netrin-1 and submitted into the automatic crystallization pipeline available at the Sample Preparation and Characterization facility at EMBL Hamburg. Together with our collaborators we followed the crystallization experiments and the growth of the single crystals closely via the web interface. The crystals were then mounted on the EMBL beamlines by hand. The crystal structure was determined on the EMBL microfocus beamline P14 and the behaviour of the complex in solution was studied using Small Angle X-ray Scattering at the EMBL BioSAXS beamline P12. The structural data of netrin-1 in complex with the receptor DCC shows that netrin-1 can actually bind to two molecules of DCC simultaneously (Fig. 1). However, while one of these binding sites is specific to DCC, the second is a generic site capable of taking either DCC or UNC-5 receptors. This non-specific binding site is very unusual and explains how netrin-1 can switch from triggering an attraction to triggering a repulsion effect (and vice versa). The Zhang group from Peking University performed repulsion and attraction assays on neurons containing DCC and UNC-5 receptors to verify the structural observations.

Key to this work was the close and effective team work between Boston, Hamburg and Beijing, but also the immediate and direct access we had to the beamlines and sample characterisation facilities at PETRA III. The close proximity of the labs and beamlines ensured that the precious sample was used efficiently. In the near future, the integration of the lab facilities at the beamlines will be further enhanced with a

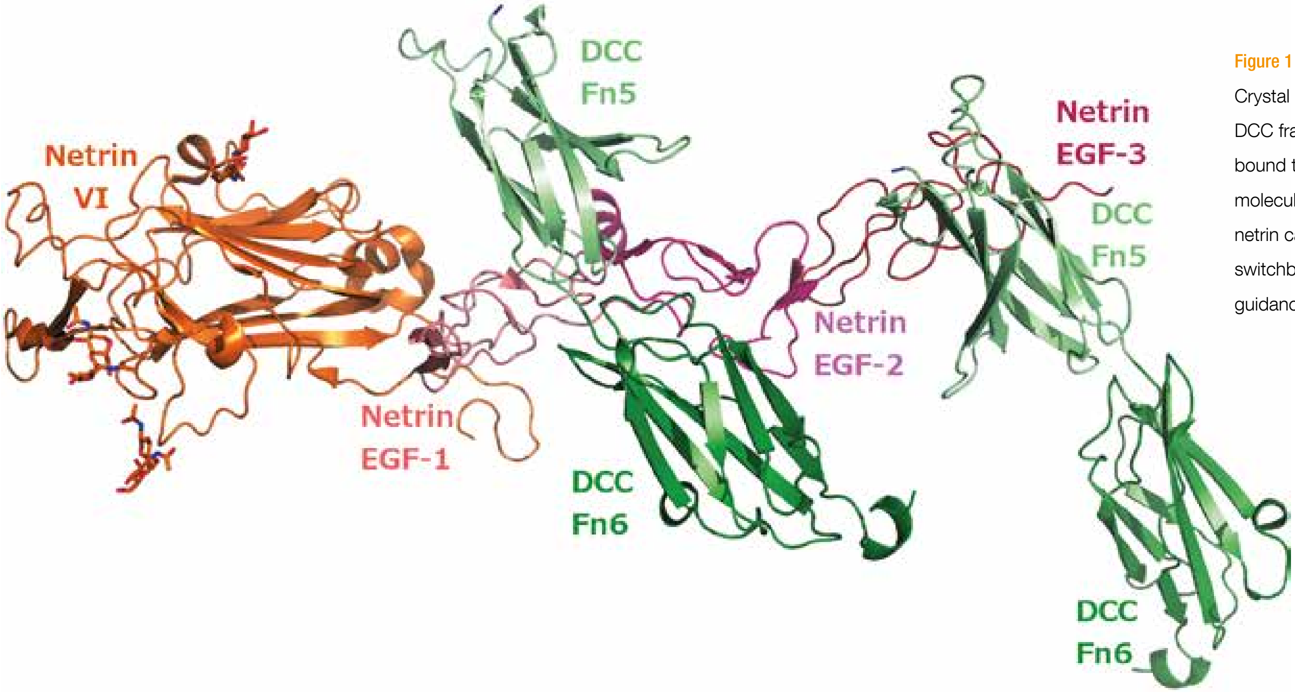

Figure 1
Crystal structure of two DCC fragments (in green) bound to one netrin-1 molecule, showing how netrin can act as a switchboard in axon guidance.

robotic system to harvest crystals, and with on-line purification and biophysical characterization set-ups on the BioSAXS beamline P12.

Our experiments also showed that the second interaction site requires negatively charged sulphate ions to maintain contact between the proteins. In a cellular environment these sulphate ions are probably replaced by larger sugar like molecules called heparan sulphates. It was already known that heparan sulphates influence neuronal wiring but it seems that these molecules may also determine which receptor binds to netrin and subsequently how the cell responds. We are now investigating what role this so-called sugar code plays in netrin / receptor interactions. This particular mode of interaction could be very interesting for drug design, with the idea that by exploiting these interactions we could possibly interfere with netrin biology and influence a range of cell migration pathways including tumour metastasis and apoptosis processes.

Contact: Rob Meijers, r.meijers@embl-hamburg.de

Authors

Lorenzo I. Finci[1,2], Nina Krüger[3], Xiaqin Sun[1], Jie Zhang[1], Magda Chegkazi[3], Yu Wu[1], Gundolf Schenk[3], Haydyn D. T. Mertens[3], Dmitri I. Svergun[3], Yan Zhang[1,4], Jia-huai Wang[1,2], and Rob Meijers[3].

1. State Key Laboratory of Biomembrane and Membrane Biotechnology, College of Life Sciences, Peking University, Beijing, 100871, China
2. Dana-Farber Cancer Institute, Harvard Medical School, Boston, MA 02215, USA
3. European Molecular Biology Laboratory (EMBL), Hamburg Outstation, Notkestrasse 85, 22603 Hamburg, Germany
4. PKU-IDG / McGovern Institute for Brain Research, Peking University, Beijing, 100871, China

Original publication

"The Crystal Structure of Netrin-1 in Complex with DCC Reveals the Bifunctionality of Netrin-1 As a Guidance Cue", Neuron 83, 839-849 (2014). DOI: 10.1016/j.neuron.2014.07.010

References

1. **P. Krimpenfort, J.-Y. Song, N. Proost, J. Zevenhoven, J. Jonkers, and A. Berns, "Deleted in colorectal carcinoma suppresses metastasis in p53-deficient mammary tumours", Nature 482, 538-541 (2012).**
2. **L. Mazelin, A. Bernet, C. Bonod-Bidaud, L. Pays, S. Arnaud, C. Gespach, D. E. Bredesen, J.-Y. Scoazec, and P. Mehlen, "Netrin-1 controls colorectal tumorigenesis by regulating apoptosis", Nature 431, 80-84 (2004).**

Small beams for small crystals.

A novel method for determining macromolecular structures from micrometre sized crystals

Macromolecular crystallography is a powerful tool for obtaining detailed structural information about biological macromolecules, however it is limited by the size of crystals available for measurements, radiation damage occurring during the experiment, and the dimensions of the X-ray beam available. The crystal structure of *T. brucei* procathepsin B was determined using a suspension of *in vivo* grown microcrystals mounted in a standard nylon loop for crystallographic data collection on a microfocus synchrotron beamline. The resulting structural model is consistent with that obtained at a free-electron laser source, providing mutual validation and demonstrates potential opportunities for combining data from serial femtosecond crystallography for the determination of high-resolution structures of micrometre sized crystals.

Crystal structure determination of biological macromolecules at synchrotrons is typically limited by the availability of sufficiently sized crystals and by the fact that crystal quality deteriorates during data collection due to radiation damage to the sample. Growing large enough crystals for crystallography from biomolecules such as proteins is notorious for being difficult and time consuming. Large molecules and protein complexes are particularly difficult or seemingly impossible to crystallise to suitable sizes. In such cases it would be very advantageous to be able to use microcrystals for analysis. Advanced third generation synchrotrons with fine X-ray beams can now determine the structures of crystals with volumes less than 1000 μm^3 and a number of biomolecules have been measured at such facilities. At free-electron laser (FEL) facilities a serial femtosecond crystallography (SFX) experiment typically involves flowing a suspension of microcrystals across a very fine and intense X-ray beam. This results in an extremely large number (many tens of thousands or more) of single crystal X-ray diffraction images. New methods and tools such as CrystFEL [1] – a suite of programs for processing diffraction data – have been developed to process and handle these large volumes of data. In a recent study by Redecke et al. [2] the crystal structure of the enzyme *T. brucei* procathepsin B (TbCatB) was resolved using the SFX approach, and provided the first new biological insights using FEL pulses. The TbCatB enzyme is of particular medical interest since studies have shown that knocking out the gene encoding the enzyme was lethal for the parasite which causes the so-called sleeping sickness in Africa, making TbCatB an important potential drug target [3].

Figure 1

Crucial for the success of this experiment was the high-precision vertical MD3 microdiffractometer at the P14 beamline – developed by scientists and engineers at EMBL Hamburg and EMBL Grenoble – and the micrometre sized high-flux X-ray beam at the PETRA III storage ring.

Inspired by this recent success and key developments in the field of serial femtosecond crystallography, scientists from the Center for Free-Electron Laser Science (CFEL) at DESY, the European Molecular Biology Laboratory (EMBL) and the Universities of Hamburg and Lübeck embarked on an experiment to determine the crystal structure of *T. brucei* procathepsin B using synchrotron radiation. Microcrystals were first grown in baculovirus infected insect cells before being isolated and purified. For measurement on the EMBL microfocus beamline P14 at the PETRA III storage ring (Fig. 1), a small volume of the crystalline suspension containing approximately 5000 crystals was mounted in a standard nylon loop. A serial helical scan approach (Fig. 2) was used during data collection. Here, the loop was rotated during exposure while being simultaneously translated and using a fine X-ray beam of 5 μm in diameter often creating multiple exposures of the same crystal and so reducing systematic data collection errors. Diffraction data from 80 *T. brucei* procathepsin B crystals with an average volume of 9 μm^3 were combined making them some of the

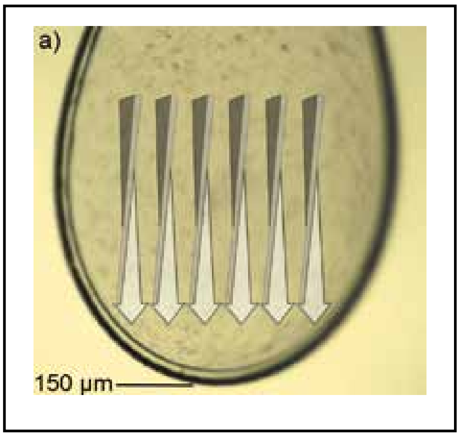

Figure 2

Schematic macroscopic illustration of the serial helical line-scan approach using a standard cryogenic loop, imaged with the inline microscope.

smallest protein crystals that have been analysed with synchrotron radiation to date. A complete data set was assembled to 3.0 Å resolution.

The resulting structural model from the synchrotron data is consistent with the model built on the data collected at the free-electron laser by Redecke et al. [2], providing mutual validation of both experiments.

Compared with current implementations of SFX the serial synchrotron crystallography approach requires relatively few crystals making it potentially useful for a first round of measurements to adjust parameters before using the crystal intensive SFX approach. At present, one of the major limitations in serial synchrotron crystallography is the unfavourable high level of background scatter with respect to the small signal originating from the small crystals. To reduce the background scatter by reducing the beam size such that it matches the crystal size, P14 will be upgraded with compound refractive lenses in the context of a Röntgen-Ångström-Cluster project. There are also several approaches being followed to develop novel crystal mounting techniques reducing the amount of material surrounding the crystal thereby reducing the unwanted background scatter from such non-crystalline material.

Building on developments initially made for the analysis of XFEL based serial crystallography data, the method of serial synchrotron crystallography with serial helical scans is conceptually simple and widely applicable. It will become available as a standard protocol on beamline P14 in 2015.

Contact: Henry Chapman, henry.chapman@desy.de
Lars Redecke, redecke@chemie.uni-hamburg.de
Thomas Schneider, thomas.schneider@embl-hamburg.de

Authors

Cornelius Gati[1], Gleb Bourenkov[2], Marco Klinge[3], Dirk Rehders[3], Francesco Stellato[1], Dominik Oberthür[1,4], Oleksandr Yefanov[1], Benjamin P. Sommer[4,5], Stefan Mogk[5], Michael Duszenko[5], Christian Betzel[4], Thomas R. Schneider[2], Henry N. Chapman[1,6], and Lars Redecke[3]

1. Center for Free-Electron Laser Science (CFEL), Deutsches Elektronen-Synchrotron DESY, Notkestrasse 85, 22607 Hamburg, Germany
2. European Molecular Biology Laboratory (EMBL), Hamburg Outstation, Notkestrasse 85, 22607 Hamburg, Germany
3. Joint Laboratory for Structural Biology of Infection and Inflammation, Institute of Biochemistry and Molecular Biology, University of Hamburg, and Institute of Biochemistry, University of Lübeck, Notkestrasse 85, 22607 Hamburg, Germany
4. Institute of Biochemistry and Molecular Biology, University of Hamburg, Notkestrasse 85, 22607 Hamburg, Germany
5. Interfaculty Institute of Biochemistry, University of Tübingen, Hoppe-Seyler-Strasse 4, 72076 Tübingen, Germany
6. Institute of Experimental Physics, University of Hamburg, Luruper Chaussee 149, 22761 Hamburg, Germany.

Original publication

“Serial crystallography on in vivo grown microcrystals using synchrotron radiation”, IUCrJ 1, 87-94 (2014). DOI: 10.1107/S2052252513033939

References

1. **T. A. White, R. A. Kirian, A. V. Martin, A. Aquila, K. Nass, A. Barty and H. N. Chapman, “CrystFEL: a software suite for snapshot serial crystallography”, J. Appl. Cryst. 45, 335-341 (2012).**
2. **L. Redecke, K. Nass, D. P. DePonte, T. A. White, D. Rehders, A. Barty, F. Stellato, M. Liang, T. R. M. Barends, S. Boutet, G. J. Williams, M. Messerschmidt, M. M. Seibert, A. Aquila, D. Arnlund, S. Bajt, T. Barth, M. J. Bogan, C. Caleman, T. Chao, R. B. Doak, H. Fleckenstein, M. Frank, R. Fromme, L. Galli, I. Grotjohann, M. S. Hunter, L. C. Johansson, S. Kassemeyer, G. Katona, R. A. Kirian, R. Koopmann, C. Kupitz, L. Lomb, A. V. Martin, S. Mogk, R. Neutze, R. L. Shoeman, J. Steinbrener, N. Timneanu, D. Wang, U. Weierstall, N. A. Zatsepin, J. C. H. Spence, P. Fromme, I. Schlichting, M. Duszenko, C. Betzel and H. N. Chapman, “Natively Inhibited Trypanosoma brucei Cathepsin B Structure Determined by Using an X-ray Laser”, Science 339, 227-230 (2013).**
3. **A. H. Fairlamb, “Chemotherapy of human African trypanosomiasis: current and future prospects”, Trends Parasitol. 19, 488-494 (2003).**

Macromolecular serial crystallography at PETRA III.

Synchrotron facilities benefit from FEL science

The development of X-ray free-electron lasers (FELs) and of the method of serial femtosecond crystallography (SFX) to obtain structural information of biological macromolecules at near atomic resolution has caused a paradigm shift in structural biology. It is now possible to use protein crystals that are smaller in volume than 1 μm^3 for crystallographic experiments, by recording and merging many tens of thousands of snapshot diffraction patterns from individual crystals. New software such as CrystFEL and Cheetah was developed to cope with the challenging data processing of such experiments. These new capabilities and concepts are very appealing for modern high-brightness synchrotron radiation facilities since they open up high-throughput and automated measurements with sub-millisecond exposures and reduced dose. To demonstrate this potential, we adapted FEL methods and software to perform the first successful serial synchrotron crystallography experiment at room temperature.

X-ray crystallography is to date the most widely used method to obtain models of biological macromolecules at atomic resolution. The bottleneck to structural information in this case is the need to crystallise the object of interest. The most important systems, membrane bound receptors and large macromolecular complexes, are difficult to crystallise and often only yield weakly diffracting, very small crystals. However, small crystal size does not necessarily prevent high resolution information to be obtained: powder diffraction achieves this by simultaneously exposing millions of crystallites, but loses orientational information. Our insight is that by measuring powder diffraction one grain at a time we can orient each pattern in three dimensions and build up a complete set of single-crystal structure factors.

The development of X-ray free-electron lasers (FELs) that produce intense pulses of tens of femtoseconds in duration opened up data collection from room-temperature crystals before the rapid onset of disorder [1, 2]. This method of serial femtosecond crystallography (SFX) introduced a number of innovations, such as data collection from a flowing suspension of crystals in a liquid jet with high-frame-rate detectors, and software to process millions of detector frames [3] and to merge data from the hundreds of thousands of single-crystal diffraction patterns [4]. We have now applied these innovations to use with synchrotron radiation (SR). Exposure times are measured in milliseconds rather than femtoseconds. However, the dose requirement for any single crystal is reduced by only recording a single "still snapshot" at a single orientation.

In order to test the feasibility of SR serial room temperature measurements, experiments were carried out at the PETRA III beamline P11 by flowing a suspension of chicken-egg lysozyme crystals (with a typical size of 4 × 4 × 6 μm^3) at room temperature through a capillary positioned across the 6 × 9 μm^2 focussed X-ray beam. We recorded 25 images per

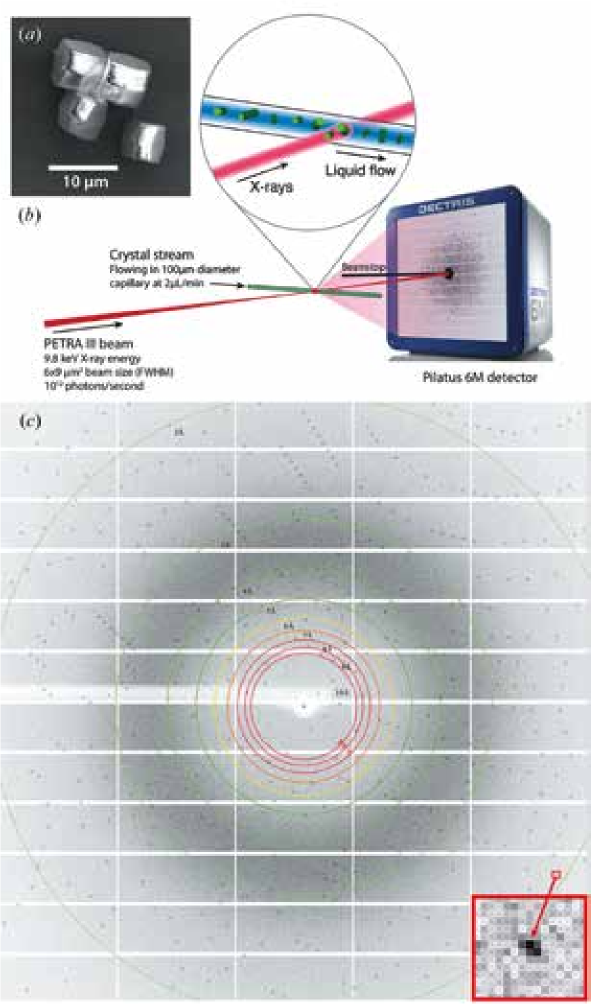

Figure 1

(a) SEM micrograph of the lysozyme microcrystals used for the serial crystallography measurements, (b) a sketch of the experimental setup for protein serial crystallography at PETRA III – P11 beamline, (c) a single crystal diffraction pattern. The circles show predicted positions of Bragg peaks. Bragg spots can be observed up to the centre edge of the detector, as shown by the red arrow that indicates a Bragg spot located at 2.05 Å resolution.

second using a PILATUS 6M detector in a shutterless mode. The data collection time per image was 10 ms, giving a detector dead-time of 75 %. The actual exposure time of a crystal was governed by the time it took a crystal to traverse the X-ray beam, which was no more than about 3 ms.

More than 1.5 million diffraction images were recorded. Of these, about 200000 “hits” were found (that is, images containing Bragg spots). These frames were processed using CrystFEL [4] to automatically index each pattern, providing the lattice vectors of the crystal oriented in the laboratory frame. More than 40000 patterns were indexed and integrated and then further processed using conventional crystallography programs. We refined a structural model of chicken egg-lysozyme against the data to 2.1 Å resolution by molecular replacement, starting from a model of human lysozyme and clearly observing the differences in the sequence in the electron density map. After model building and refinement to convergence we obtained quality metrics of $R_{work}/R_{free} = 0.18/0.23$, and found that while these metrics became worse as the number of patterns were reduced, a total of 5000 indexed patterns (2 hours of sample run time) was enough to achieve the slightly worse, but still reasonable values of $R_{work}/R_{free} = 0.22/0.28$.

In the broader context, this work is part of an effort to make use of the software and hardware developments of SFX at X-ray FEL facilities, which have spurred new ideas for macromolecular crystallography with SR. The trend began at PETRA III with an innovative approach for serial crystallography on cryogenically cooled samples. In that case, 9 μm^3 *in vivo* grown crystals were used to solve the structure of *Trypanosoma brucei* procathepsin B [5] (see the Research Highlight in this section).

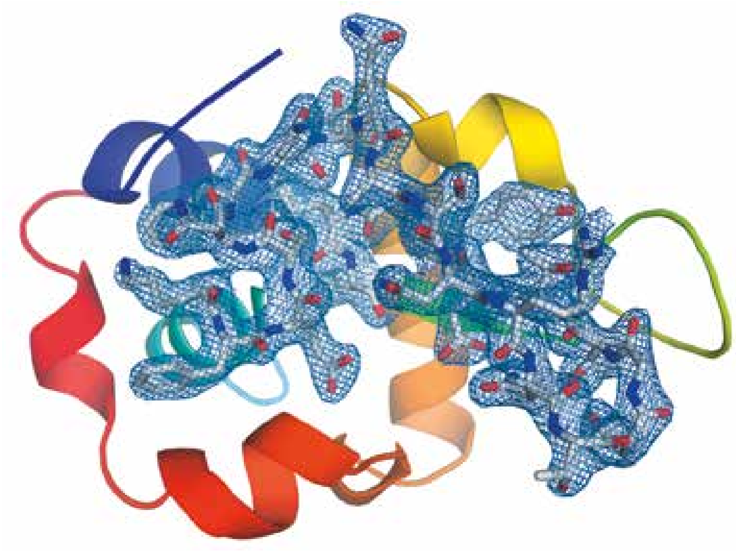

Figure 2

Electron density map of lysozyme at 2.1 Å resolution calculated from 40233 single crystal indexed diffraction patterns.

These new approaches open up the possibility for time-resolved measurements at millisecond timescales, either through flow-mixing techniques or by photoexcitation. Given its roots with X-ray FELs, the method is demonstrably scalable to even shorter exposure times and higher frame rates that are becoming available with modern detectors [6] and high-brightness beams from upgraded facilities. Our results show that we can successfully adapt methods from FEL science to synchrotrons and thus widen the bottleneck of crystallization by using more often occurring microcrystals for crystallography at synchrotrons.

Contact: Francesco Stellato, francesco.stellato@roma2.infn.it
Dominik Oberthuer, dominik.oberthuer@desy.de
Henry N. Chapman, henry.chapman@desy.de

Authors

Francesco Stellato[1], Dominik Oberthuer[1,2,3], Mengning Liang[1], Richard Bean[1], Cornelius Gati[1], Oleksandr Yefanov[1], Anton Barty[1], Anja Burkhardt[4], Pontus Fischer[4], Lorenzo Galli[1,3], Richard A. Kirian[1], Jan Meyer[4], Saravannan Panneerselvam[4], Chun Hong Yoon[1,5], Fedor Chervinskii[6], Emily Speller[7], Thomas A. White[1], Christian Betzel[2,8], Alke Meents[4], Henry N. Chapman[1,3,8]

1. Center for Free-Electron Laser Science, DESY, Notkestrasse 85, Hamburg 22607, Germany
2. Institute of Biochemistry and Molecular Biology, University of Hamburg, Hamburg 22607, Germany
3. Department of Physics, University of Hamburg, Luruper Chaussee 149, Hamburg 22607, Germany
4. DESY Photon Science, Hamburg 22607, Germany
5. European XFEL GmbH, Albert Einstein Ring 19, Hamburg 22761, Germany
6. Moscow Institute of Physics and Technology, 141700 Moscow, Russian Federation
7. Department of Physics, University of York, Heslington, York YO10 5DD, UK
8. The Center for Ultrafast Imaging, CUI, Luruper Chaussee 149, Hamburg 22761, Germany

Original publication

“Room-temperature macromolecular serial crystallography using synchrotron radiation”, IUCrJ 1, 204-212 (2014). DOI: 10.1107/S2052252514010070

References

1. **H.N. Chapman et al., ”Femtosecond X-ray protein nanocrystallography”, Nature 470, 73-77 (2011).**
2. **S. Boutet et al., “High-resolution protein structure determination by serial femtosecond crystallography”, Science 337, 362-364 (2012).**
3. **A. Barty et al., “Cheetah: software for high-throughput reduction and analysis of serial femtosecond X-ray diffraction data”, J. Appl. Cryst. 47, 1118-1131 (2013).**
4. **T.A. White et al., “CrystFEL: a software suite for snapshot serial crystallography”, J. Appl. Cryst. 45, 335-341 (2012); T. A. White et al., “Crystallographic data processing for free-electron laser sources”, Acta Cryst. D 69, 1231-1240 (2013).**
5. **C. Gati et al., “Serial crystallography on in vivo grown microcrystals using synchrotron radiation”, IUCrJ 1, 87-94 (2014).**
6. **B. Henrich et al., “The adaptive gain integrating pixel detector AGIPD a detector for the European XFEL”, Nucl. Instr. Meth. Phys. Res. A 633, S11-S14 (2011).**

Electron beams from 100.000 silicon tips.

Nanostructured ultra-fast optical field-emitter arrays

Femtosecond ultra-bright electron sources with spatially structured emission are a potentially enabling technology for free-electron lasers, compact coherent X-ray sources, electron diffractive imaging, and attosecond science. Here, we report the design, modelling, fabrication, and experimental characterization of a novel ultrafast optical field emission cathode comprised of a large (> 100 000 tips), dense (4.6 million tips · cm^{-2}), and highly uniform (< 1 nm tip radius deviation) array of nanosharp high-aspect-ratio silicon columns. Such field emitters offer an attractive alternative to UV photocathodes while providing a direct means of structuring the emitted electron beam. Detailed measurements and simulations show pC electron bunches can be generated in the multiphoton and tunnelling regime.

Ultra-fast-pulsed (< 1 ps), ultra-bright high-current electron sources are an enabling technology for free-electron lasers, electron diffractive imaging [1] and compact coherent X-ray generators [2]. State-of-the-art ultra-fast cathodes are flat surfaces that use highly reactive materials to lower the work function and increase the quantum efficiency of single-photon absorption for ultraviolet (UV) pulses; these devices have short lifetimes, and need to be fabricated and operated in ultra-high vacuum. Multiphoton-triggered field emission cathodes are an attractive alternative to circumvent these issues. Strong-field electron tunnelling from solids without damage occurs when the electric field of high-intensity optical pulses interacts with field enhancing structures to bend down the potential barrier at the surface such that the electron's tunnelling time is shorter than one optical cycle, with the potential for attosecond electron pulse generation [3].

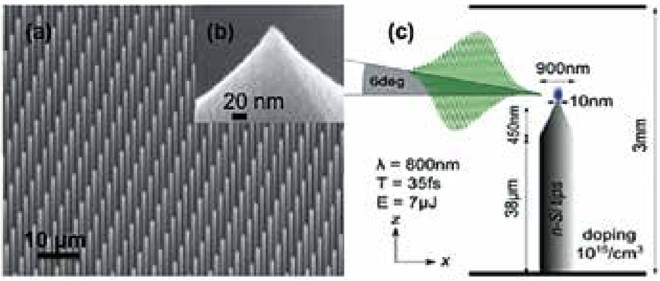

Figure 1

Images and schematic of emitter structure: (a) Scanning electron microscope (SEM) image of uniform array of high-aspect-ratio Si columns with 5 µm pitch. (b) SEM close-up of a single tip. (c) Schematic of a single 800 nm pulse interacting with a single silicon tip. λ is the laser wavelength, T is the pulse duration and E is the laser pulse energy.

Much of the previous work on nanostructured photo-triggered field emission cathodes has focused on single metal tips that are serially manufactured; in this work, we used standard complementary metal–oxide–semiconductor (CMOS) wafer-level fabrication techniques to create massively multiplexed arrays of nano-sharp high-aspect-ratio single-crystal silicon pillars with high uniformity (> 100 000 tips, 4.6 million tips · cm^{-2}), resulting in greatly enhanced array electron emission (Fig. 1). Eventually this may also enable the generation of attosecond electron pulses with considerable charge, i.e. hundreds of femtocoulomb from a single-cycle near IR drive source along with a THz source for charge extraction [4].

In a field emitter array, a broad tip radii distribution causes severe array sub-utilization because the emission current has an exponential dependence on the local surface electric field at the tips, which is inversely proportional to the tip radii. For ultra-fast electron source applications, achieving a homogeneous charge distribution in the bunch is strongly desired, thereby making small variations in the tip dimensions essential. Here, we developed a fabrication process that attains small tip variation across the array as a result of the diffusion-limited oxidation step that sharpens the tips and identify the parameter range in the current-voltage-optical excitation diagram, where strong-field emission occurs and charging effects are negligible.

The high electric field of ultra-short laser pulses combined with the field enhancement of the nano-sharp silicon tip array resulted in large current emission at small laser energies (Fig. 2a). While the overall quantum efficiency (QE, inset Fig. 2a) does not exceed 10^{-6}, this is high considering that only a very small fraction of the emitter surface is utilized, as the tip diameter is sub-10 nm and the tip spacing is 5 µm (i.e., about 3 millionths of the total array area emit electrons).

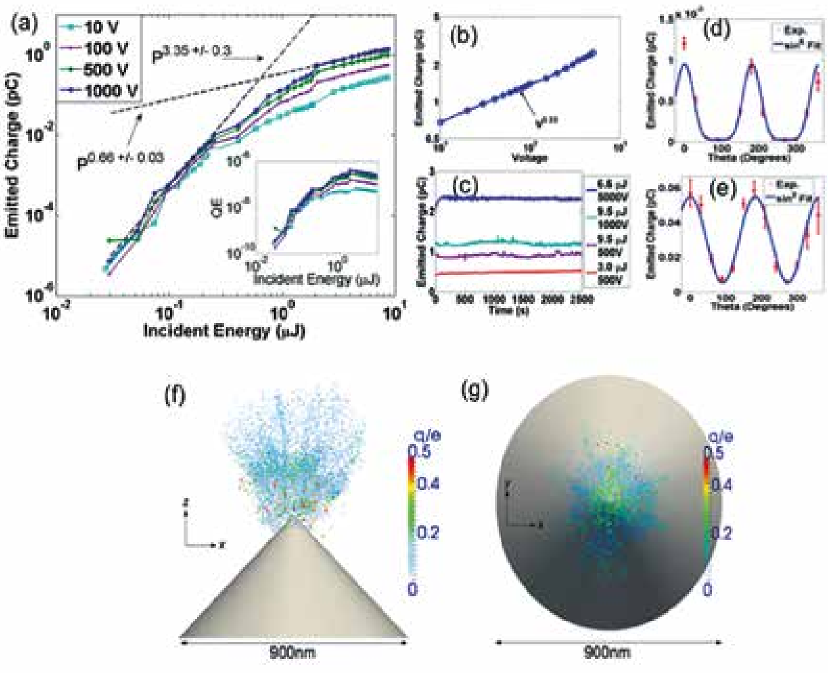

Figure 2

Experimental results: (a) Emitted charge and overall quantum efficiency (QE) as a function of laser pulse energy for various anode bias voltages. A 3-photon emission growth is shown in current at low intensities, and then a bend-over when tunneling sets in. (b) Log-log plot of emitted charge versus bias-voltage at fixed incident pulse energy of 10.8 µJ. The < 1 slope indicates that the emission is not fully space charge limited. (c) Stability of emitted current from the photocathode over time showing stable output. In (d) and (e) the polarization was changed continuously from 0° (along the tip) to 360° to show the effect of polarization on charge yield. (d) At an incident pulse energy of 37 nJ, the current increases with the third power of pulse energy ($\sin^6(\theta)$). (e) At 180 nJ, the emission is in the tunnelling regime so the current increases linearly ($\sin^2(\theta)$) with pulse energy. (f, g) Computed emitted charge profile due to field emission at the tip with 70 V anode bias at t = 120 fs: (f) side-view and (g) top-view of the charge profile including space-charge and image charge effects. The density of points and the colour code represent the charge density. Each point represents a charge emitted at a specific time step due to the existing local electric field. 1000 electrons are emitted from each tip, which are visualized by more than 50000 particles with charges equal to fractions of an electron charge.

Assuming the same field enhancement at the tip, the overall QE could be further increased by more than one order of magnitude through a reduction of tip spacing using the same fabrication methods that we employed. At low energy (< 0.2 µJ), we observe 3-photon emission (power dependence slope of ~3.4 shown in Fig. 2a). Above 0.2 µJ the power dependence reduces to a slope of ~1. For the case of single tips, such a bend-over in current yield occurring near a Keldysh parameter of about 2 is in agreement with the expected field enhancement in the structure. This regime is commonly referred to as the strong-field or tunnelling regime of electron emission. To further demonstrate the effect of electric field enhancement on tip emission, the charge yield is measured while rotating the polarization angle (θ) (Fig. 2d and Fig. 2e). For both low and high pulse energies, peak emission occurs when the polarization was along the axis of the tip, and minimum emission for the orthogonal polarization. For the case of high pulse energies, the polarization followed a $\sin^2(\theta)$ dependence, while for low energies that of a $\sin^6(\theta)$ dependence, corresponding to the tunnelling and multi-photon emission regions, respectively. Fig. 2c shows four different cathode currents on four different sample locations with the beam being unblocked at time zero at an unexposed area. All four curves show stable current emission after 8 million pulses with the highest curve equal to 2.3 pC of charge per pulse, which is important for electron source applications where surviving millions of cycles at high charge output is required.

We also modelled the emission from a single tip in the time domain using excitation conditions shown in Fig. 1 and an expanded Fowler-Nordheim [5, 6] electron emission model, accounting for space charge and Coulomb-blockade effects by adding the fields of a moving charge to the time domain Maxwell solver. Figures 2(g) and 2(f) show the charge distribution from a single tip. The model reproduces many of the experimentally observed features and clarifies space charge effects and the formation of a virtual cathode for extraction of large charges at limited extraction fields.

Contact: Franz X. Kärtner, franz.kaertner@cfel.de

Authors

Michael E. Swanwick[1], Phillip D. Keathley[2], Arya Fallahi[3], Peter R. Krogen[2], Guillaume Laurent[2], Jeffrey Moses[2], Franz X. Kärtner[2,3], and Luis F. Velásquez-García[1]

1. Microsystems Technology Laboratories, Massachusetts Institute of Technology, Cambridge, USA
2. Dept. of Electrical Engineering and Computer Science and Research Laboratory of Electronics, Massachusetts Institute of Technology, USA
3. Center for Free-Electron Laser Science CFEL, DESY, Dept. of Physics, University of Hamburg and "The Hamburg Centre for Ultrafast Imaging" (CUI), Hamburg, Germany

Original publication

"Nanostructured Ultrafast Silicon-Tip Optical Field-Emitter Arrays", Nano Lett. 14, 5035-5043 (2014). DOI: 10.1021/nl501589j

References

1. P. Baum and A. H. Zewail, "Attosecond electron pulses for 4D diffraction and microscopy", Proc. Natl. Acad. Sci. 104, 18409-18414 (2007).
2. W. S. Graves, F. X. Kärtner, D. E. Moncton, and P. Piot, "Intense superradiant X-rays from a compact source using a nanocathode array and emittance exchange", Phys. Rev. Lett. 108, 263904 (2012).
3. M. Krüger, M. Schenk, and P. Hommelhoff, "Attosecond control of electrons emitted from a nanoscale metal tip", Nature 475, 78-81 (2011).
4. L. J. Wong, A. Fallahi, and F. X. Kärtner, "Compact electron acceleration and bunch compression in THz waveguides", Opt. Express 21, 9792-9806 (2013).
5. R. H. Fowler and L. Nordheim, "Electron emission in intense electric fields", Proc. R. Soc. Lond. Ser. A 119, 173-181 (1928).
6. S. V. Yalunin, M. Gulde, and C. Ropers, "Strong-field photoemission from surfaces: Theoretical approaches", Phys. Rev. B 84, 195426 (2011).

Pulse-by-pulse interferometry at PETRA III.

Photon correlations measured at a synchrotron radiation source

Synchrotrons and free-electron lasers are nowadays the principal sources of high-brilliance hard X-ray radiation. With the ongoing development of coherent X-ray sources, including diffraction limited storage rings (DLSR), measurements of the transverse coherence properties of X-rays become increasingly important and are vital for the success of coherence-based applications. These measurements can provide important information on the source parameters, such as the photon source size, and can be used, in principle, in a feedback system. To explore this question, Hanbury Brown – Twiss interferometry was performed at PETRA III.

Intensity interferometry, pioneered by the experiment of Hanbury Brown and Twiss (HBT) [1,2], is an exemplary technique to investigate fundamental properties of partially coherent radiation. Originally designed as a robust setup to determine the size of stars, it led to the development of new concepts in statistical optics and especially initiated research in the field of quantum optics [3]. In this work, measurements of second-order intensity correlation functions were performed at PETRA III by implementing HBT interferometry.

The key quantity in a HBT experiment is the normalized second-order intensity correlation function

$$g^{(2)}(r_1, r_2) = \langle I(r_1)\cdot I(r_2)\rangle / (\langle I(r_1)\rangle\langle I(r_2)\rangle)$$

where $I(r)$ is the intensity measured at position r and $\langle \ldots \rangle$ denotes the average over a large ensemble of independent single pulse measurements. Using the Gaussian moment theorem, it can be shown that the intensity correlation function originating from thermal (chaotic) sources can be described in terms of the amplitude correlation function, also known as the complex coherence function $\gamma(r_1, r_2)$, as

$$g^{(2)}(r_1, r_2) = 1 + \zeta\,|\gamma(r_1, r_2)|^2,$$

where $\zeta = 1/M_l$ is the contrast value, $M_l = T/\tau_c$ is the number of longitudinal modes of the radiation field, T is the time resolution or pulse duration for pulsed sources, and τ_c is the coherence time, which scales inversely with the bandwidth and can typically be tuned. The modulus of the complex coherence function $|\gamma(r_1, r_2)|$ is a measure of the visibility of interference fringes in a Young's double pinhole experiment.

In this work, the new adaptive gain integrating pixel detector (AGIPD) is used to measure intensity correlations. This detector operates at a frame rate of multiple MHz, is able to resolve individual synchrotron pulses, and has an exemplary spatial

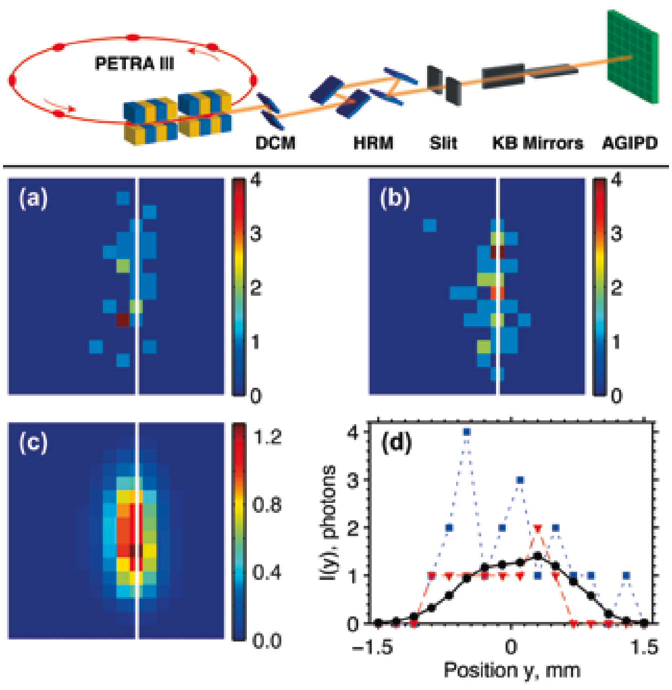

Figure 1

Top panel: Generic scheme of Hanbury Brown – Twiss interferometry performed at PETRA III. Synchrotron radiation is generated by the two 5 m undulators, monochromatized to 1 meV by a combination of a double crystal monochromator (DCM) and a high-resolution monochromator (HRM), and finally transmitted through a slit system and set of KB mirrors. Individual synchrotron radiation pulses are recorded with the AGIPD.

Bottom panel: Measured intensities. (a), (b) Typical intensity profiles of individual synchrotron radiation pulses recorded at the AGIPD. (c) Average intensity profile. (d) Vertical line scans along the white lines in (a)–(c) through typical single pulses [red triangles (a), blue squares (b)] and average intensity profile [black circles (c)].

resolution, which eliminates the necessity of a beam splitter. Additionally, it measures intensity correlations at different relative positions across the beam simultaneously, which allows for full coherence characterization in a single measurement. For our experiment, we used an AGIPD 0.4 assembly, which is a 16 × 16 pixel prototype of the AGIPD [4].

The experiment shown in Fig. 1(a) was performed at the Dynamics Beamline P01 at the high-brilliance storage ring PETRA III at a photon energy of 14.4 keV. The detector was synchronized to the bunch repetition frequency of PETRA III (5.2 MHz), and about 3×10^5 intensity profiles of individual synchrotron pulses were recorded [see Figs. 1(a), 1(b)]. Figure 1(c) shows the average intensity profile. The pulses have significantly different profiles due to both the chaotic nature of the radiation and the low count rates. At synchrotron sources, the latter factor dominates the intensity fluctuations due to a small degeneracy parameter, which is the average number of photons in a single mode.

The result of the second-order correlation function analysis along the vertical line shown in Figs. 1(a-c) is presented in Fig. 2(a). The normalized correlation function $g^{(2)}(y_1, y_2)$ shows the expected behaviour of maximum values for small separations between the pixels and a smooth falloff for larger separations. To determine the transverse coherence length and contrast, we extract the intensity correlation function $g^{(2)}(\Delta y)$ from $g^{(2)}(y_1, y_2)$ (see Fig. 2(b)). The data shown in Fig. 2(b) are well reproduced by a Gaussian function fit, which yields a transverse coherence length of $l_c = 0.68$ mm (rms) and a contrast value of $\zeta = 1.7\,\%$. The contrast is in good agreement with an estimate using PETRA III bunch parameters. We have used the results of the transverse coherence measurements to determine the size of the synchrotron source. Using the Gaussian Schell model [5], where the coherence function is homogeneous across the beam and all functional dependencies are described by Gaussian functions, we found a source size of 7.8 μm. This value is in excellent agreement with the photon source size $\sigma_y = 7.5$ μm estimated from the design electron beam parameters of the PETRA III storage ring.

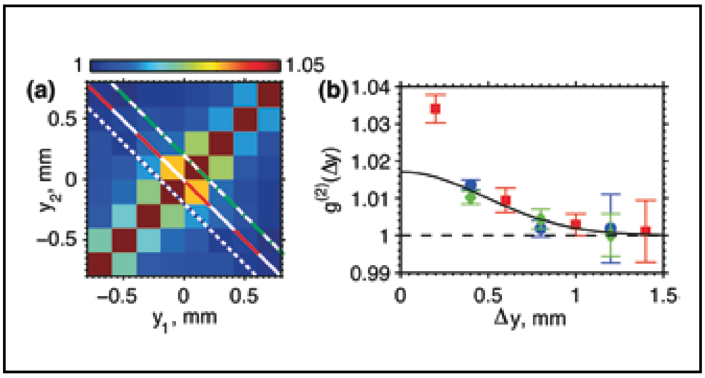

Figure 2

Intensity correlation analysis. (a) The normalized intensity correlation function $g^{(2)}(y_1, y_2)$. (b) The normalized intensity correlation $g^{(2)}(\Delta y)$ as a function of Δy. Fit by a Gaussian function (black solid line) provided transverse coherence length values of $l_c = 0.68$ mm (rms).

In summary, we have demonstrated successful intensity correlation measurements performed in the spatial domain with hard X-rays at the storage ring PETRA III. The success of our measurements was based on the use of the prototype AGIPD detector that measures intensity profiles of individual synchrotron pulses with the rate of about 5 MHz. Using this pixelated detector, we were also able to record the intensity correlation function at different relative spatial separations simultaneously, which is unique compared to previous measurements. We anticipate that this technique can be extended to XFELs [6] and will provide a valuable diagnostic tool for next generation X-ray sources. Because of the large frame rate, the final AGIPD detector will certainly be useful for a variety of experiments at high-brilliance X-ray sources, for example, for studies of the dynamics of matter from the nano- to microsecond time scales. We also anticipate that the unprecedented combination of outstanding temporal and spatial resolution of AGIPD will initiate new developments in the biological and materials sciences at high-brilliance X-ray sources.

Contact: Ivan Vartaniants, ivan.vartaniants@desy.de

Authors

A. Singer[1], U. Lorenz[1], A. Marras[2], A. Klyuev[2], J. Becker[2], K. Schlage[1], P. Skopintsev[1,3], O. Gorobtsov[1,4], A. Shabalin[1], H.-C. Wille[1], H. Franz[1], H. Graafsma[2,5], and I. A. Vartanyants[1,6]

1. Deutsches Elektronen-Synchrotron DESY, Notkestraße 85, D-22607 Hamburg, Germany
2. Center for Free-Electron Laser Science CFEL, Notkestrasse 85, D-22607 Hamburg, Germany
3. Moscow Institute of Physics and Technology (State University), Dolgoprudny, 141700 Moscow Region, Russia
4. National Research Center "Kurchatov Institute," Kurchatov Square 1, 123182 Moscow, Russia
5. Mid Sweden University, S-851 70 Sundsvall, Sweden
6. National Research Nuclear University, "MEPhI," 115409 Moscow, Russia

Original publication

"Intensity Interferometry of Single X-Ray Pulses from a Synchrotron Storage Ring", Phys. Rev. Lett. 113, 064801 (2014). DOI: 10.1103/PhysRevLett.113.064801

References

1. R. Hanbury Brown and R. Q. Twiss, "Correlation between Photons in two Coherent Beams of Light", Nature (London) 177, 27 (1956).
2. R. H. Brown and R. Q. Twiss, "A Test of a New Type of Stellar Interferometer on Sirius", Nature (London) 178, 1046 (1956).
3. R. J. Glauber, "The Quantum Theory of Optical Coherence", Phys. Rev. 130, 2529 (1963).
4. J. Becker et al., "Performance tests of an AGIPD 0.4 assembly at the beamline P10 of PETRA III", JINST 8, P06007 (2013).
5. I. A. Vartanyants and A. Singer, "Coherence Properties of Hard X-Ray Synchrotron Sources and X-Ray Free-Electron Lasers", New J. Phys. 12 035004 (2010).
6. A. Singer et al., "Hanbury Brown-Twiss Interferometry at a Free-Electron Laser" Phys. Rev. Lett. 111, 034802 (2013).

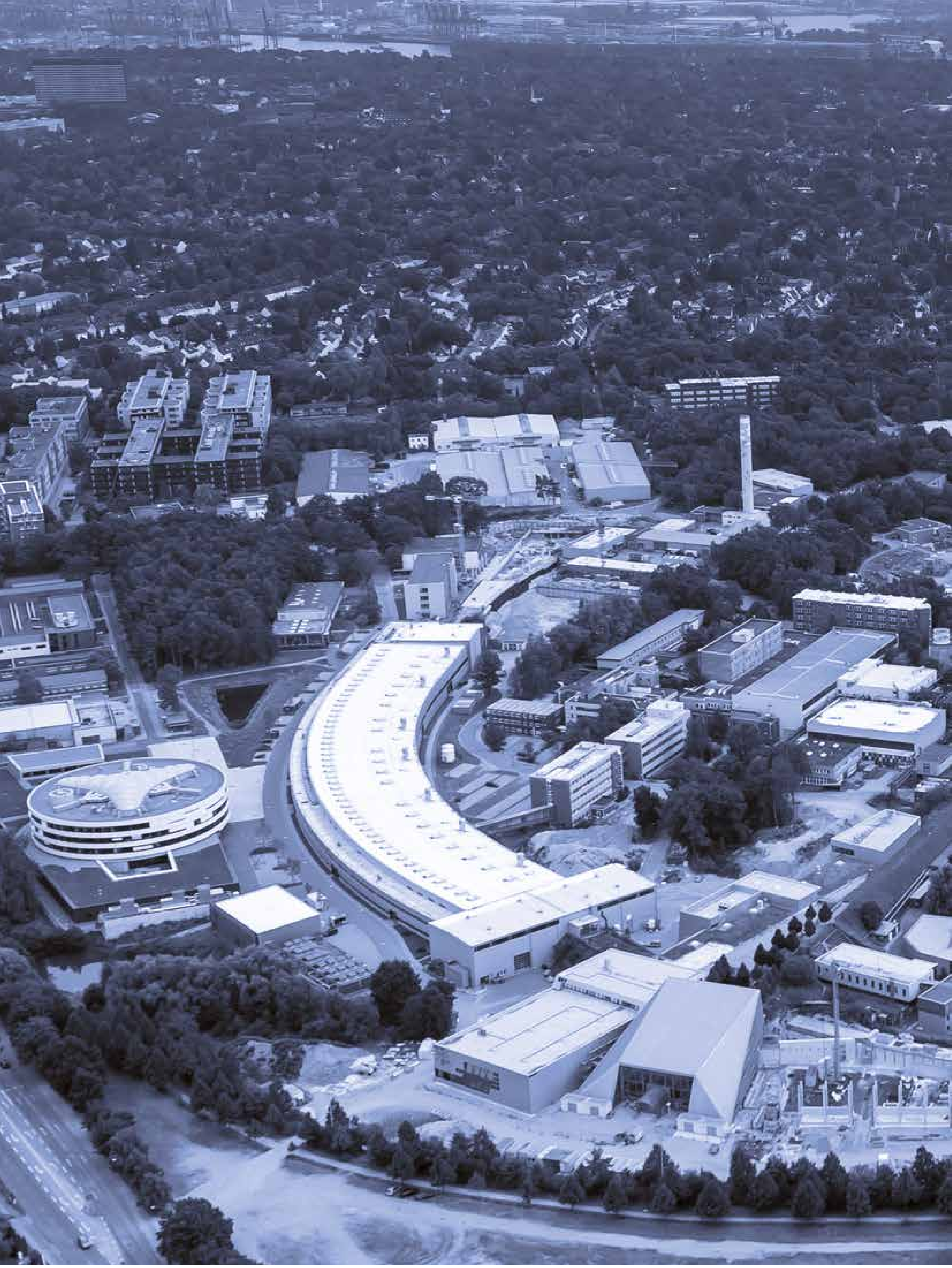

Research Platforms and Outstations.

- Center for Free-Electron Laser Science CFEL 78
- EMBL Hamburg Unit 80
- Helmholtz-Zentrum Geesthacht Outstation at DESY 82
- University of Hamburg on the DESY site 84
- Centre for Structural Systems Biology CSSB 86
- DESY NanoLab 87

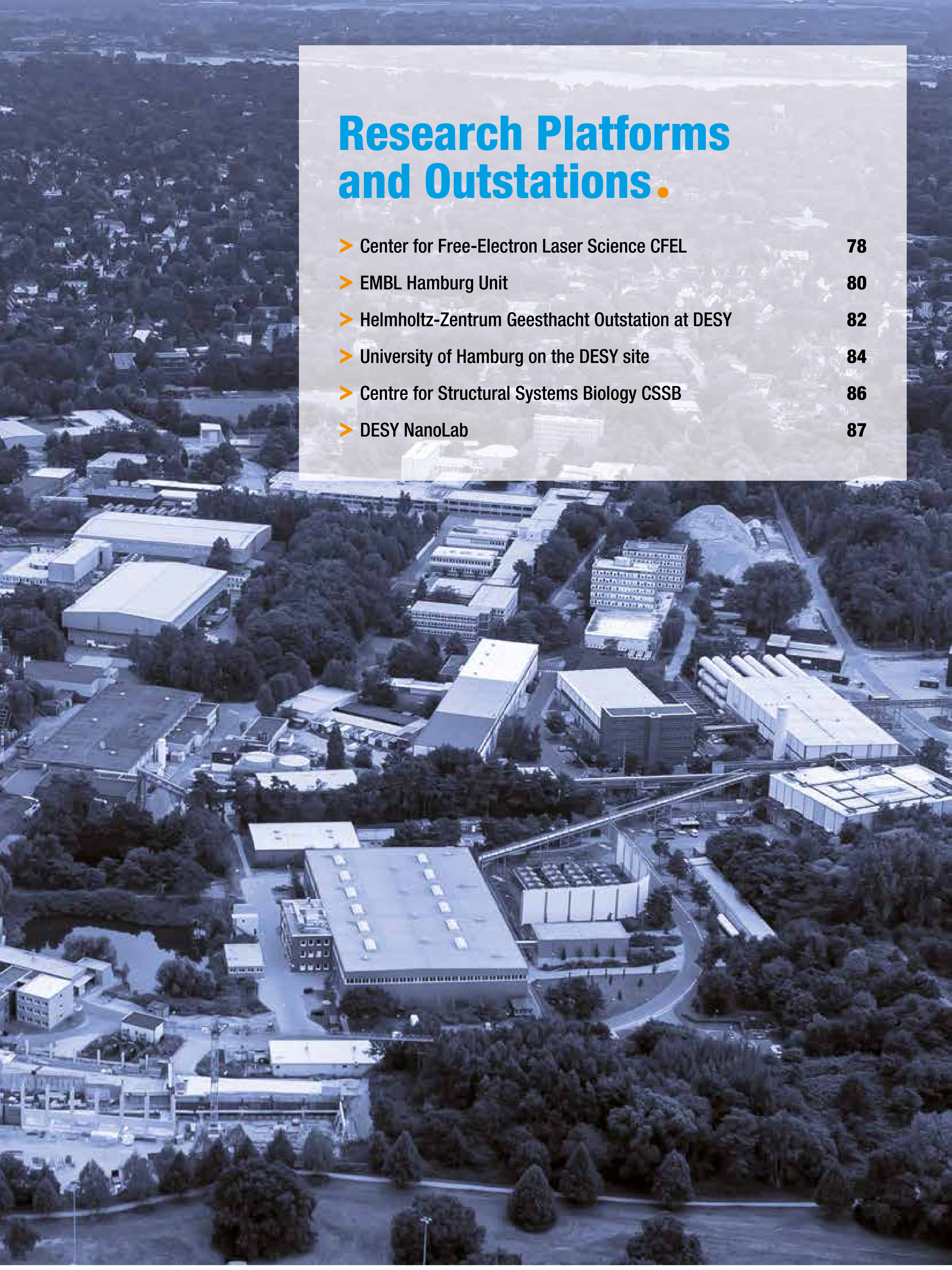

Center for Free-Electron Laser Science CFEL.

Three institutions working successfully together within CFEL

Figure 1

Angel Rubio presenting at the CFEL Colloquium on 7 November 2014.

In 2014, CFEL successfully passed the seven-year itch and increased its success in all areas. The three institutional partners in CFEL, Deutsches Elektronen-Synchrotron DESY, Max Planck Society (MPG) and the University of Hamburg (UHH), keep up the collaborative spirit of the starting years and with the recent new appointments the future looks even brighter. The CFEL building itself is now tightly packed with scientists, engineers and students, and the last year founded MPI (Max Planck Institute for the Structure and Dynamics of Matter) just started with the planning of their new building. Additional to the space the MPI uses in CFEL, a second research complex for two more divisions is planned. The third MPI director Angel Rubio started in November 2014 and introduced his research field to the colleagues with a talk within the CFEL colloquium series (Fig. 1). Angel Rubio will build up the theoretical division of the MPI with a research focus on the properties of condensed matter. The tools his group applies range from *ab initio* calculations and time-dependent modelling to density functional theory.

The cluster of excellence The Hamburg Centre for Ultrafast Imaging (CUI) in which all leading CFEL scientists participate, appointed two new CFEL based groups. Junior Professor Ulrike Frühling investigates ultrafast dynamical processes in atomic and molecular systems. Professor Arwen Pearson will strengthen CFEL's research in the field of experimental biophysics. Her activities are focused on the question how the dynamics of bio-macromolecules (enzymes, membrane proteins) is related to their biological function. To this end Arwen Pearson also develops new methods for time-resolved X-ray crystallography.

CFEL successfully hosted its first International Summer School of Crystallography (ISSC 14) in Hamburg (Fig. 2). As part of the International Year of Crystallography 2014, Professor Carmelo Giacovazzo gave focused lectures on the basics of crystallography, as well as the basics of modern phasing methods in protein crystallography and many other topics. The participants also learned modern applications of macromolecular crystallography using advanced light sources, such as 3rd generation synchrotrons and XFELs. The summer school was organized by Cornelius Gati from DESY's CFEL Division for Coherent Imaging in cooperation with CUI, PIER (Partnership for Innovation, Education and Research), the IMPRS UFAST (International Max Planck Research School for Ultrafast Imaging and Structural Dynamics) and the European XFEL.

Again, several of our colleagues were successful in their work and received awards. Stephan Stern from the Coherent Imaging Division was honoured with a PhD Thesis Award from the "Association of the Friends and Sponsors of DESY" for his work on Controlled Molecules for X-ray Diffraction Experiments at FELs. The MPI Director R. J. Dwayne Miller will be awarded the E. Bright Wilson Award in Spectroscopy from the American Chemical Society "for the development of femtosecond electron diffraction and coherent spectroscopic methods for the direct

Figure 2
Participants from 24 countries at the ISSC 14 from 11 – 17 May 2014.

observation and control of chemical dynamics at the atomic level" in 2015. Jacob Burgess of the Dynamics of Nanoelectronic Systems Max Planck Research group received a Humboldt Research Fellowship and a NSERC Postdoctoral Fellowship and Nicole Teschmit from the Controlled Molecule Imaging Group received a prestigious Kekulé Mobility Fellowship from the Chemical Industry Fund (FCI). Zheng Li – a former CFEL PhD student from the CFEL Theory Division – won a Peter Paul Ewald Fellowship of the VolkswagenStiftung allowing him to continue his research career as postdoc at the LCLS. Finally, Wilfried Wurth, division head at the CFEL Advanced Study Group of the Hamburg University, was appointed as the new scientific head of FLASH.

Another great success was the funding with 14 million euros by the EU of a project which aims for high resolution time lens for the nanocosm. With a so-called ERC Synergy Grant, the European Research Council supports the project "Frontiers in Attosecond X-ray Science: Imaging and Spectroscopy" (AXSIS) of Franz Kärtner and Henry Chapman (both CFEL, DESY and University of Hamburg), Dr. Ralph Aßmann (DESY) and Professor Petra Fromme (Arizona State University). This is the second funded ERC Synergy Grant involving the Center for Free-Electron Laser Science. The focus of this project is to develop the ability to film ultra-fast processes in slow motion. The four scientists will build a kind of stroboscope with ultra-short light flashes in the attosecond range. To reach atomic resolution, these light flashes will be in the short-wavelength X-ray region of the spectrum. This will allow insights into so far unobservable processes of nature. The attosecond source will be based on a novel, laser-driven particle accelerator technology which will emit X-ray radiation with much shorter pulses than possible so far. This technology can revolutionise the understanding of structure and function at the molecular and atomic level and unravel fundamental processes in chemistry and biology, e.g. the dynamics of light absorption, of electron transport and of the protein structural changes during photosynthesis – one of the major unsolved problems of structural biology.

The ERC Consolidator Grant project "Controlling the Motion of Complex Molecules and Particles" (COMOTION) of Jochen Küpper also started this year. This project aims at developing methods to control, e.g. to transport, to sort, and to align complex molecules and particles. This includes biological samples such as peptides, proteins, viruses, and picoplankton as well as artificial nanoparticles. The team will develop sources to create beams of these molecules in the gas phase and to immediately quick-freeze them. The molecules are then transported through pipes and funnels formed from laser light and electric fields. They are sorted according to their shapes and structures, as well as aligned and oriented in space. First successful experiments on *para* and *ortho* water are presented in the "Research Highlights" section of this volume.

Contact: Ralf Koehn, ralf.koehn@cfel.de

EMBL Hamburg Unit.

Integrated structural biology research and services with synchrotron radiation

Research activities at EMBL Hamburg focus on challenging structural biology projects. Scientific highlights in 2014 have involved the groups of Thomas Schneider and Rob Meijers. Thomas, together with EMBL Hamburg staff scientist Gleb Bourenkov and members of the Chapman group (CFEL/DESY) and Redecke group (University of Lübeck), reproduced the structure of a heavy glycosylated protein β–cathepsin, which was previously only determined with data obtained from the LCLS X-ray free electron laser facility at Stanford. They used a new method called Serial Synchrotron Crystallography (SSX), which adopts new data collection approaches developed for X-ray free electron laser applications. This work was jointly published in the IUCr Journal. In work published in the journal *Neuron*, the Meijers group, together with collaborators in Harvard and Beijing, showed how netrin-1 steers axon guidance through the DCC receptor. In a second paper published in PLoS Pathogens, Rob Meijers and co-workers used structural and functional studies to unravel how the bacteriophage endolysin targets *Clostridium* bacteria. Details of these works can be found in the "Research Highlights" section of this report. More about publication highlights from EMBL Hamburg research groups in 2014 can be seen at *www.embl-hamburg.de* The EMBL Hamburg Unit also welcomed new group leader Christian Löw recruited as part of EMBL's commitment to the on-campus Centre for Structural Systems Biology (CSSB). His work focuses on the structure, function and dynamics of integral membrane proteins, opening up a new field of structural biology research to EMBL.

The EMBL Hamburg Unit is also a major provider of leading research services in structural biology. Specifically, it offers access to three synchrotron radiation beamlines (P12, P13, P14) at the PETRA III synchrotron radiation source for applications in small angle X-ray scattering (SAXS) of biological samples and macromolecular X-ray crystallography (MX), a Sample Preparation and Characterization (SPC) facility, and various computational services for applications in structural biology. From February 2014, the PETRA III storage ring has been shutdown to allow for major construction works so EMBL was only able to welcome users to the EMBL beamlines during January 2014.

During user operation at the SAXS beamline P12, over 20 external groups were allocated beamtime. During the subsequent shutdown period a multilayer monochromator for improved flux was installed. It will provide a bandwidth between 1.5 and 2.5 %, delivering an intense beam with a flux up to 5×10^{14} photons/second. This flux will allow SAXS data to be collected in the sub-millisecond range, paving the way for ultra-fast time resolved experiments. Using a new sample chamber, it will be possible to routinely perform automated wide-angle scattering data collection, yielding more detailed information about the internal structure of macromolecular and colloidal systems. In agreement with the strong demand for the in-line size exclusion chromatography (SEC) coupled with SAXS measurements (SEC-SAXS) an automated system was installed allowing the analysis of thousands of data frames. The buffer corrected frames are analysed with available SAXS tools and concentration and molecular weight of samples can be assigned from simultaneous light scattering and refractive index measurements. Data frames across the elution peak with consistent radius of gyration values are averaged to produce the final SAXS curve, which is passed down-stream modules for complete analysis and *ab initio* modeling.

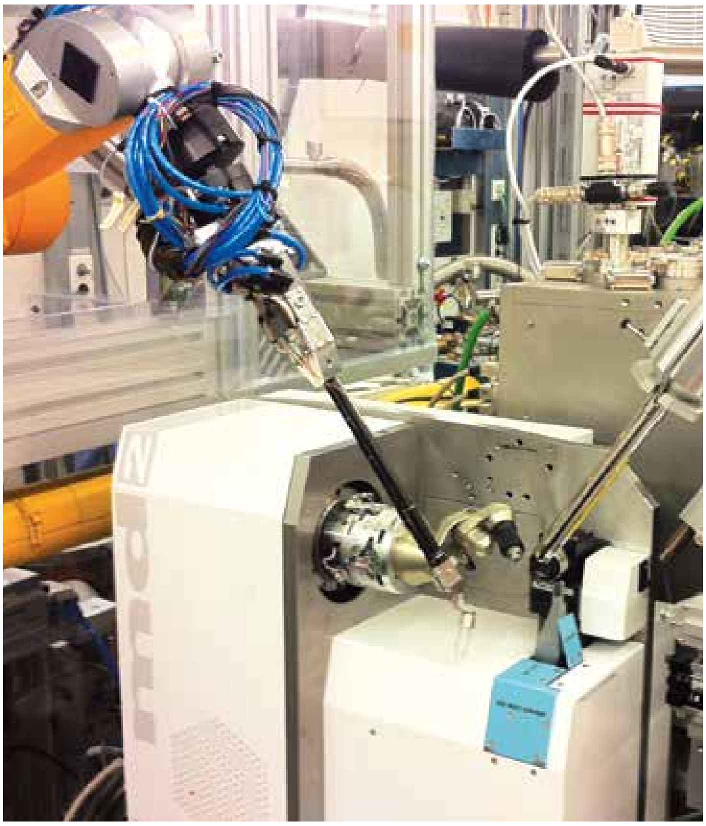

Figure 1

On P13, a crystal mounting robot 'MARVIN' (entering from top left) was taken into operation in 2013. The system is based on an industrial six-axes robotic system and transfers sample from a storage Dewar onto the diffractometer ('md2' bottom) with a cycle time of less than 40 sec.

Figure 2

Celebrating 10 years of bilateral cooperation between EMBL Hamburg and EMBL Grenoble.

From left to right: Head of EMBL Hamburg Matthias Wilmanns, Chairman of DESY Board of Directors Helmut Dosch, Director General of ESRF Francesco Sette, Head of EMBL Grenoble Stephen Cusack, Director General of EMBL Iain Mattaj, EMBL Grenoble Team Leader Florent Cipriani, and EMBL Hamburg Group Leader Thomas Schneider.

Users visiting the EMBL Beamline P13 in early 2014 benefited from the new MARVIN sample changer (Fig. 1) and the rapid tunability over the energy range 4–17 keV. During the subsequent shutdown, the MD2 micro-diffractometer was upgraded to allow data collection on P13 with samples smaller than 5 microns in size. At beamline P14, energy tuning and X-ray fluorescence scans software was established in early 2014, making it possible to carry out multiple anomalous dispersion experiments. The macromolecular crystallography data acquisition software and user interfaces underwent an upgrade, which involved implementation of the newest version of the MxCuBE interface for data collection, installation of the ISPYB data management system and deployment of the EDNA software package for on-line data analysis. A wealth of new experimental options has also been installed, including X-ray based sample localization, automated strategy determination, queued multi-crystal data collection, line- and mesh-scans combined with automated data processing. Serial Synchrotron Crystallography (SSX) will also be offered as a standard option in the future.

The Sample Preparation and Characterization (SPC) facility at EMBL presently consists of an integrated full-scale facility equipped with state-of-the-art equipment to carry out purification and characterization of macromolecular samples using techniques such as circular dichroism and isothermal titration calorimetry. New homemade thermal shift assays for checking sample stability have been tested on more than 250 different protein constructs and are now provided to many laboratories throughout Europe. Users can also take advantage of the crystallization platform, which provides commercial screens to crystallize both soluble and membrane proteins. Users can design their own screen with a new screen builder liquid handling robot. A web-interface facilitates booking of experiments and allows external researchers to monitor crystallization experiments remotely.

In 2014 EMBL has established new collaborative relationships across Northern Germany. EMBL is a partner of the Centre for Structural Systems Biology (CSSB, see separate article) and in January, the Head of EMBL Hamburg, Matthias Wilmanns, was appointed founding director. In May, EMBL established an important alliance with the University Clinical Center Hamburg-Eppendorf (UKE), the main aim being to join forces in biomedical research and training activities by way of a strategic bilateral partnership.

2014 has also been a year of celebrations at EMBL. In April 2014, EMBL Units in Hamburg and Grenoble celebrated ten years of a strong bilateral collaboration, specifically, but not exclusively, related to several synchrotron instrumentation projects. Yearly meetings aim to support and structure the ongoing collaborative projects. The celebratory symposium in Grenoble (Fig. 2), organized by the Heads of the EMBL Units – Matthias Wilmanns from EMBL Hamburg, and Stephen Cusack from EMBL Grenoble – showcased and acknowledged the efforts made by the meeting participants over the years and highlighted success stories of the collaborative work. 2014 also marks the 40th anniversary of EMBL. In addition to celebrations at the central laboratory in Heidelberg, EMBL Hamburg is organizing an anniversary symposium and celebrations in Hamburg on the 27th – 28th November 2014. DESY and EMBL have agreed on the renewal of their successful partnership and the signing ceremony took place during this event.

Contact: Matthias Wilmanns,
matthias.wilmanns@embl-hamburg.de

Helmholtz-Zentrum Geesthacht Outstation at DESY.

Our instruments are true GEMS

After many successful experiments at our PETRA III beamlines and a lively user feedback in our annual satellite workshop to the DESY Photon Science Users Meeting in January 2014, the German Engineering Materials Science Centre (GEMS), the outstation of Helmholtz-Zentrum Geesthacht (HZG) at DESY, has certainly been established as an important brand for synchrotron radiation research in engineering materials science.

At the High-Energy Materials Science beamline (HEMS, P07, jointly operated with DESY; highest in demand of all PETRA III beamlines) the granite sub-structure for the grain mapper has been completed and the motor control implementation is finalised by the end of the year 2014. A line focus below 1 μm was achieved by using one-dimensional compound refractive lenses at 38 keV. During the long PETRA III extension shut-down several beamline components were redesigned to enlarge the available experimental space in hutch EH3. The gas handling system was enlarged to accommodate new *in situ* instrumentation, i.e. a sputter deposition system for industrially relevant growth rates. The chamber is currently being manufactured and planned for installation in January 2015 within a Röntgen Ångström Cluster project in cooperation with Linköping University, Sweden. The industrial partner SECO Tools has completed the design for an *in situ* cutting rig.

GEMS provides a number of complex sample environments for *in situ* experiments mainly in the field of engineering materials science. These allow for time-resolved studies of “real world” processes, providing information that is not accessible in *ex situ* experiments. These studies require complex sample environments that are usually developed in cooperation with HZG in-house groups. Before the PETRA III shutdown, the *in situ* laser welding experiment FlexiLas (Fig. 1) has been extensively used. First measurements were performed with a new gradient furnace for tomography and diffraction for the study of the solidification of Mg alloys in cooperation with the HZG Magnesium Innovation Centre (MagIC). GEMS and MagIC will construct a new *in situ* experiment for studying the *in situ* roller casting process for Mg alloys (FlexiRoll). *In situ* diffraction and radiography experiments shall be carried out on the solidification and subsequent deformation of new Mg alloys for lightweight construction. As a first approach to ultra-fast free-electron laser experiments at the European XFEL the grinding process of metals will be studied *in situ* using a special device at GEMS synchrotron beamlines in collaboration with RWTH Aachen.

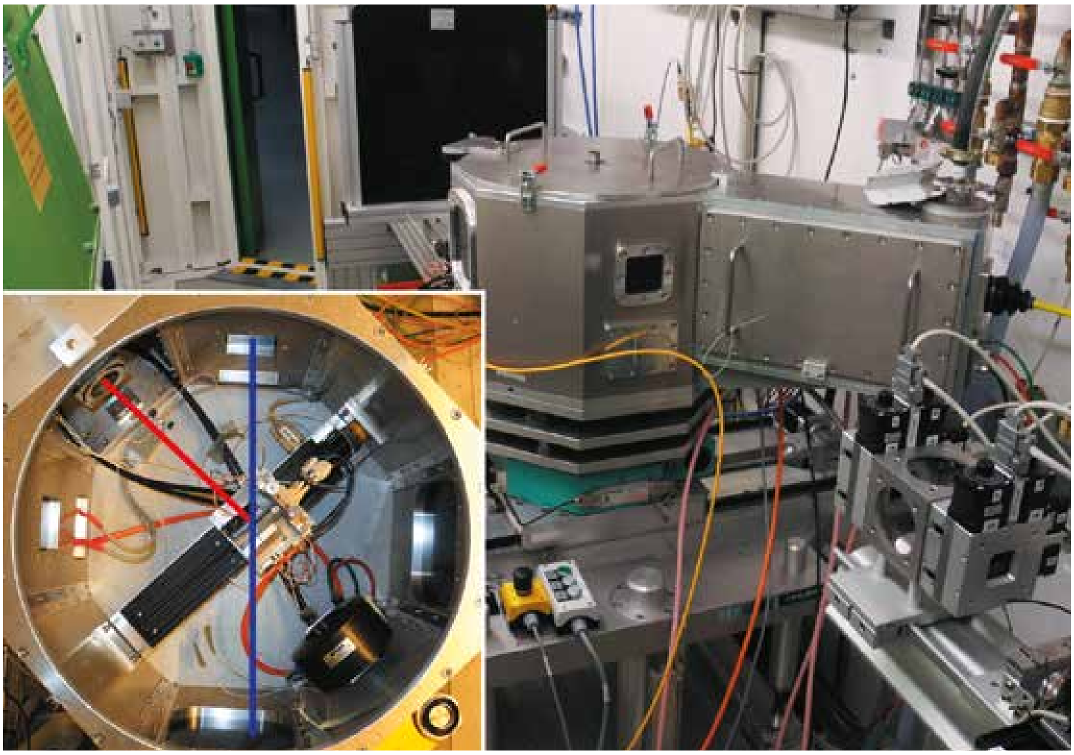

Figure 1

The *in situ* laser beam welding chamber (FlexiLas) at P07B (side station), which has been built and operated together with the colleagues from the HZG laser welding group (Jie Liu, Nikolai Kashaev). The inset shows the interior of the welding chamber with the heating device for preheating TiAl samples to 700 °C prior to welding. The red and blue lines indicate the laser and photon beams, respectively.

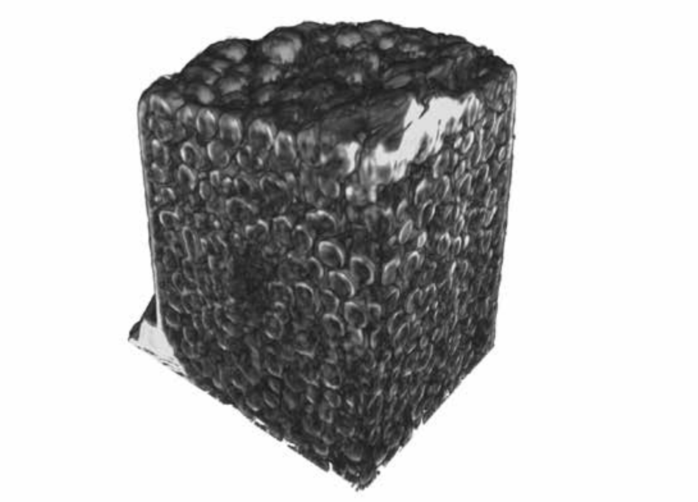

Figure 2

Three-dimensional nanotomographic reconstruction of a ZrO_2 photonic glass used for the determination of the packing fraction. Sample by Jefferson do Rosario (TUHH, SFB986, see text). Experimental parameters: 17.4 keV photon energy at IBL, voxel size 68 nm, resolution (2D) 200 nm, base dimension 18 x 18 μm^2, nominal sphere diameter 2μm.

In the field of X-ray imaging, high- and lower energy X-rays are used at HEMS and at the Imaging Beamline (IBL, P05), respectively. At HEMS, grating-based phase contrast was successfully applied in first user experiments. In 2014, a dedicated setup for differential phase contrast (DPC) was designed including a sample manipulator, a cell for liquid environment and an alignment system for the gratings. This system will be installed and tested early in 2015. Micro tomography with absorption contrast has become a routine tool at IBL, including the combination with *in situ* techniques (see above). The first successful nanotomography scan in the dedicated IBL hutch was completed in February 2014. The image shown in Fig. 2 is a three-dimensional reconstruction of a photonic glass sample made from small zirconium spheres (experiment within SFB 986, see below). The new IBL double multilayer monochromator was delivered in September 2014 and will be installed by the end of the year 2014. Its high flux will enable fast tomographic techniques.

In the beginning of 2014, a first study with a pressure cell (up to 3.5 kbar) on the intermolecular interaction between nanoparticles and biomolecules was performed at BioSAXS (P12, operated by EMBL together with HZG). The design phase of a high flux mode (double multilayer monochromator) is finished, the components have been ordered and the construction is in progress. The scattering tube is being modified for an additional wide-angle scattering option.

At the Nanofocus Endstation of P03 (a collaboration with CAU Kiel and DESY) it has been shown that scanning X-ray nanodiffraction is an excellent tool for materials science. This strong scientific focus is best demonstrated by the wide range of experiments already performed with *in situ* sample environments: stretching cells for tensile tests, a cryostream for temperature control, magnetic field application, a nanoindentation apparatus and a high pressure cell – all of these methods were successfully combined with the high spatial resolution provided by the nanofocused beam. The photon flux is currently limited by the relatively low acceptance of the nanofocusing mirrors, which in turn is a consequence of the requirement for an intermediate focus. In collaboration with the Karlsruhe Institute of Technology (KIT) we are currently exploring the applicability of a novel type of large aperture X-ray lenses to directly demagnify the undulator source into a nanofocus.

GEMS has adopted an important role in the Collaborative Research Centre SFB 986 (“Tailor-Made Multi-Scale Materials Systems – M^3”), which is coordinated by Hamburg University of Technology (TUHH), by providing the perfect tools for structural characterization of many new materials created within the project (see also Fig. 2). In 2014, a new *in situ* heating device enabling high temperature studies of phase transitions in doped zirconia microparticles was designed and constructed.

In the framework of the Helmholtz Initiative for Mobile/Stationary Energy Storage Systems, HZG is involved in the development of new energy storage materials by the department of Hybrid Materials Systems in collaboration with GEMS. Several successful experiments have been carried out in 2014 using both X-ray and neutron diffraction in order to characterise materials used in Li-ion batteries.

GEMS as part of the Helmholtz programme “From Matter to Materials and Life” was very positively reviewed in April 2014. GEMS was judged a world leader in the field of the complementary use of photons and neutrons in engineering materials science, such that its concept should serve as a role model for other facilities. Our continuous efforts to expand the interactions with industrial scientists and to increase the use by industry shall be continued. An example of this successful interaction can be seen in the “Research Highlights” section of this report, published in Acta Materialia 77, 360–369 (2014). We invite our users to actively take part in these exciting future developments of GEMS.

Contact: Martin Müller, martin.mueller@hzg.de
Andreas Schreyer, andreas.schreyer@hzg.de

University of Hamburg on the DESY site.

Photon Science – A Research Focus Area

Figure 1

Top: An artist view of the new Center for Hybrid Nanostructures (CHYN) which will host six university groups.

Bottom: A picture of the real building place (24 November 2014). One of the university buildings close to the DESY side entrance can be recognized behind the trees.

Photon Science is one of the key research areas of the faculty of mathematics, informatics and natural sciences of the University of Hamburg. In the past year a number of new appointments have been made which further strengthen the cooperation with DESY on the Campus Bahrenfeld.

Several new positions have been created within the Cluster of Excellence "The Hamburg Center for Ultrafast Imaging (CUI): Structure, Dynamics and Control of Materials on the Atomic Scale", www.cui.uni-hamburg.de. The goal of CUI, which is a joint activity of the University of Hamburg and DESY together with partners from the Max Planck Society, EMBL and the European XFEL, is an interdisciplinary effort towards imaging atoms and molecules on an ultrafast time scale to understand the interplay between structure and function. It brings together experts from physics, chemistry, biology and medicine and creates new groups at the borderline between these disciplines. One of the new groups is led by Prof. Arwen Pearson from Leeds. Her research is aimed at understanding how macromolecular structure leads to function, using X-ray crystallography as a major tool. Two new junior groups with main activities in Photon Science were also established. The positions were filled with Prof. Ulrike Frühling, research area: ultrafast dynamics in atoms and molecules, and Prof. Martin Trebbin, research area: structures on the nano- and mesoscale. The Hamburg Prize in Theoretical Physics sponsored by the Joachim Herz Foundation which is awarded by CUI on a yearly basis was given in 2014 to Prof. Antoine Georges, Collège de France and Ecole Polytechnique, Palaiseau, for outstanding contributions to condensed matter physics, in particular for methods to describe strongly correlated systems. The Prize was awarded during the CUI International Symposium 2014 (Fig. 2).

The ties between DESY and the University of Hamburg have been further strengthened last year by two new DESY appointments. Prof. Christian Schroer, who was appointed as scientific head of the PETRA III facility, also holds a full professor position at the University of Hamburg. His research focus is X-ray nanomicroscopy and novel X-ray optics. Prof. Wilfried Wurth, who is a full professor at the University of Hamburg since 2000 with a research focus on X-ray spectroscopy and applications to ultrafast dynamics in solids and at interfaces, was appointed as the new scientific head of the free-electron laser facility FLASH.

Cooperation in nanoscience will be strongly enhanced by the establishment of the new Center for Hybrid Nanostructures (CHYN) on the Campus headed by Prof. Robert Blick. Here the City of Hamburg decided to fund a new research building which will include state-of-the-art instrumentation for nanoscience and sophisticated cleanroom facilities (Fig. 1). The new centre will create strong synergies with the recently established DESY NanoLab. Both facilities will provide complementary techniques for the preparation and characterization of nanostructures and will thus ideally complement the opportunities for nanoscience at PETRA III and FLASH.

DESY and the university have established PIER – a Partnership for Innovation, Education and Research as a platform to foster their long-standing collaboration. One of the strong pillars of PIER is the PIER Helmholtz Graduate School. The goal of the PIER Helmholtz Graduate School is to combine the unique scientific opportunities on the Campus Bahrenfeld with excellent PhD training for candidates from Germany and abroad. In a very tight competition up to six outstanding students are granted PhD scholarships by the private Joachim Herz Foundation. The activities within PIER complement the strong network of excellence in education on the graduate level between DESY and the university. In Photon Science this is manifested for example through joint master courses in modern X-ray physics and accelerator based photon sources, jointly supervised PhD thesis work, and joint teaching activities in the DFG funded Collaborative Research Centre SFB 925 and the Cluster of Excellence CUI. A recent event (Fig. 3) was the “PIER graduate week 2014”, an interdisciplinary workshop and lecture week for PhD students, which took place from 6 – 9 October 2014. These activities on the graduate level are complemented by a very successful master program on “Modern X-ray physics” where lectures are given by members of DESY Photon Science and the physics department of the university.

Figure 3

One of the poster sessions during the PIER graduate week at DESY October 2014.

Figure 2

During the CUI International Symposium at DESY, November 2014.

Contact: Wilfried Wurth, wilfried.wurth@desy.de

Centre for Structural Systems Biology CSSB.

Taking shape and gathering speed

Figure 1

CSSB directorate and guests (from left to right): Martin Hällberg (Karolinska Institute, Stockholm, Sweden), Chris Meier (University of Hamburg, deputy CSSB research director), Matthias Wilmanns (EMBL, CSSB research director), Tim Gilberger (Bernhard Nocht Institute for Tropical Medicine, Hamburg, and University of Hamburg), Dietmar Manstein (Hannover Medical School), Jörg Labahn (Research Center Jülich), Edgar Weckert (DESY, Director Photon Science), Verena Börschmann (DESY, CSSB building construction), Christian Löw (EMBL), Ina Plettner (DESY, head of CSSB office), Kay Grünewald (Heinrich Pette Institute and University of Hamburg), Thomas Marlovits (UKE, deputy CSSB research director).

The Centre for Structural Systems Biology (CSSB) is a new research centre on DESY campus in life sciences, focusing on research topics in infection biology, complemented by X-ray based structural biology, including electron microscopy und systems biology approaches. Pursuing this combination of themes and methods is without precedence worldwide. CSSB has nine members at present, three universities and six research institutes, from Northern Germany.

2014 has been CSSB's first year with a proper governance structure, including the establishment of a council and a directorate with delegates from all nine partners (Fig. 1). Matthias Wilmanns, who heads the Hamburg Unit of the European Molecular Biology Laboratory (EMBL), has been appointed as the founding research director of the CSSB. Chris Meier, professor of organic chemistry, from the University of Hamburg and Thomas Marlovits, professor of structural and systems biology of bacteria, from the University Medical Center Hamburg-Eppendorf (UKE), are CSSB deputy directors. The directorate meets about every six weeks at alternating partner sites. The new CSSB office is headed by the biologist Ina Plettner.

Figure 2

CSSB building construction site close to the experimental hall “Max von Laue” (November 3, 2014, DESY Webcam).

Six CSSB partners have now completed their initial recruitments, two of them in 2014: Kay Grünewald from the University of Oxford, a leading expert in electron microscopy of viral particles, got a joint appointment by the University of Hamburg and the Heinrich Pette Institute. Kay's main initial task will be, together with Thomas Marlovits from the UKE, setting up a major infrastructure in state-of-the-art electron microscopy at the CSSB. Christian Löw, working before at the Karolinska Institute in Stockholm, Sweden, has accepted an EMBL group leader position and will focus on integral membrane proteins, mainly by X-ray crystallography.

The construction of the new CSSB building with an overall area of close to 11000 m^2, of which about 3000 m^2 will be used for laboratory experiments with specific requirements to work with pathogenic material, is proceeding rapidly (Fig. 2). The foundation stone was laid at the end of August in a ceremony in the presence of the Hamburg senator for science and research, Dr. Dorothee Stapelfeldt. CSSB faculty is eagerly awaiting to move into their common building from various interim sites.

Contact: Ina Plettner, ina.plettner@desy.de
Matthias Wilmanns, matthias.wilmanns@embl-hamburg.de

DESY NanoLab.

Implementing state-of-the-art equipment

In 2014, the installation of the first set of sophisticated equipment for atomic scale structural and chemical characterization took place in the DESY NanoLab current location in building 3. For compositional and electronic structure characterization, a dedicated setup for X-ray photoemission spectroscopy was installed (see Fig. 1). The ultrahigh vacuum (UHV) chamber is equipped with a hemispherical electron energy analyzer. Al and Mg Kα radiation are available, monochromatized for improved energy resolution. The chamber is equipped with a liquid-N_2 cryostat and sample heating. The setup has been fully commissioned and already produces state-of-the-art electron spectroscopy data. To enable sample exchange with the existing setups for surface characterization and growth, as well as Fourier Transform Infrared spectroscopy, a 3.5 m long UHV transfer chamber with base pressure of 4×10^{-11} mbar was integrated into the laboratory. This required a major rearrangement of the existing equipment. The UHV spectroscopy and microscopy laboratory has been completed in December 2014 by the installation of a variable temperature STM/AFM system, also connected to the sample transfer tunnel.

To enable fast morphological characterization of samples, a field emission scanning electron microscope was installed in the basement of building 3. The system allows imaging at low acceleration voltages which is crucial for the high resolution imaging of nanostructures on insulating substrates. It is equipped with a platinum precursor inlet, allowing local electron beam assisted deposition of Pt atoms, e.g. as markers or electrodes, which is important for a reproducible nano-object coordinate system transfer from the electron microscope to the PETRA III beamline endstations. Furthermore, the X-ray laboratory took up operation with the X-ray reflectometer (Mo Kα radiation) being operative as first instrument. As second instrument a six circle grazing incidence diffractometer (Cu Kα radiation) is currently commissioned. On both instruments a linear Mythen detector or point detector can be installed. Both instruments can carry large sample environments up to 60 kg weight, allowing important pre-studies prior to synchrotron experiments. Access to the DESY NanoLab techniques was offered to the general Photon Science users for the first time in the latest call for proposals for PETRA III, attracting considerable interest.

Figure 1

X-ray photoemission setup at the DESY NanoLab.

The planning of the future home of the DESY NanoLab, the Photon Science Building, which comprises high standard laboratory and office space, had to be modified to fit a reduced budget. This will be partially compensated for by dedicated space in the PETRA III and former DORIS halls. The construction work for the new building is planned to start end of 2015.

Contact: Andreas Stierle, andreas.stierle@desy.de

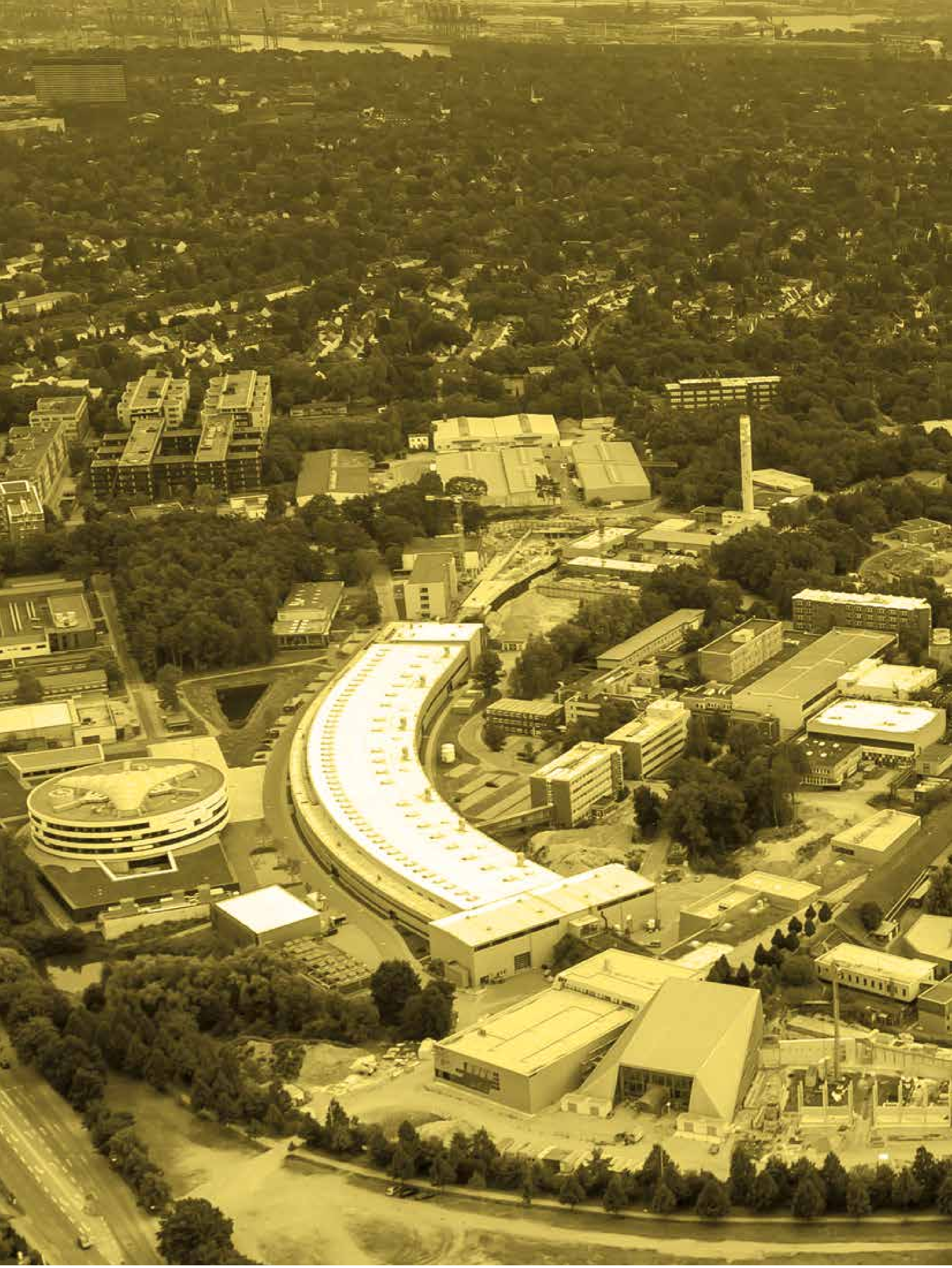

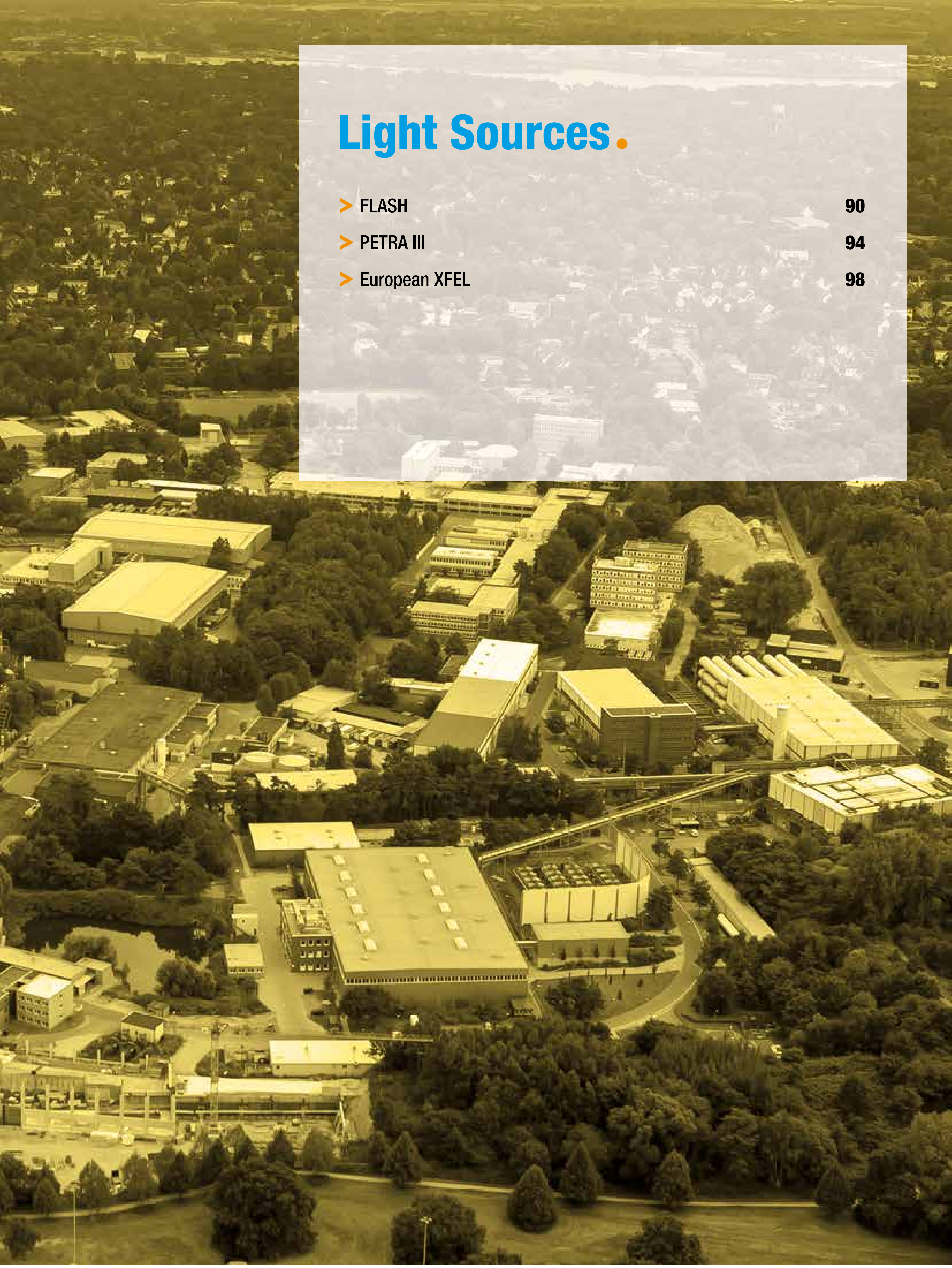

Light Sources.

> FLASH 90

> PETRA III 94

> European XFEL 98

FLASH.

Simultaneous lasing of the two FEL lines FLASH1 and FLASH2

FLASH – more specifically the first free-electron laser (FEL) FLASH1 – is in full operation for users again, after a long interruption due to construction work for the second FEL line, FLASH2.

The fifth user period started in February 2014 and will end in April 2015. 25 user projects and six in-house research experiments are scheduled in nine beamtime blocks with a total of about 440 shifts including the time needed for machine tuning and wavelength changes. The actual time distribution from 1 January to 1 December 2014 is shown in Figure 3; this period covers the first six beamtime blocks with a total of 3630 hours, including 781 hours (21.5 %) for set-up and tuning and 159 hours of downtime (4.4 %), i.e. 2690 hours were actually delivered to the experiments. A fairly large amount of time (3376 hours) was also scheduled for accelerator and FEL studies which are regularly needed to maintain and continuously improve the performance of the facility.

The experiments at FLASH cover a wide range of research areas: atomic and molecular physics (30 % of the projects), condensed matter physics (24 %), new methods including coherent X-ray imaging and FEL physics (18 %), chemistry (13 %), warm dense matter (7 %), life science (4 %) and nanoscience (4 %). Approximately 90 % of the allocated user beamtime is dedicated to time-resolved experiments which either combine the ultrashort FEL pulses with optical laser or THz pulses or make use of one of the XUV split-and-delay units integrated in the beamlines or in the experimental systems. These units divide the FEL beam into two parts which can be delayed with respect to each other, thus allowing XUV-pump XUV-probe experiments with ultimate time resolution, independent of any pulse arrival time jitter coming from the accelerator.

After a short break in May 2015, user experiments on FLASH1 will continue with the sixth user period. 50 proposals were submitted for this new beamtime period, which will start in June and last until the end of 2015. The proposals were reviewed and ranked by the international project review panel in November 2014. Up to twenty user projects and four in-house research experiments will receive beamtime in this period. From 2016 onward, it is intended to operate FLASH1 and FLASH2 fully parallel, thereby doubling the amount of user experiments. Consequently, it is planned to introduce a regular schedule with two user periods per

Figure 1

Aerial view of the FLASH facility at DESY including the new tunnel and the new FLASH2 experimental hall (in the lower left corner) and the construction site of the PETRA Extension North in early July 2014.

year and deadlines for proposal submission in spring and autumn for the first and second half of the following year, respectively.

In the meantime and in parallel to the user experiments on FLASH1, the new FLASH2 FEL is being commissioned. Several weeks were reserved for dedicated studies in 2014 in order to establish parallel operation of the two FELs.

First lasing was observed near 40 nm wavelength in August while FLASH1 was running in parallel for user experiments with long pulse trains (250 pulses per train) at 13.5 nm (see cover and the News and Events section for more details). Further studies are currently ongoing to determine the limits of the parameter space which can be used in parallel operation, such as bunch charge and compression. The commissioning is currently done with preliminary photon diagnostics in the tunnel. In the beginning of 2015, some of these components will be removed and the complete photon diagnostics and the mirrors steering the FLASH2 photon beam into the experimental hall will be installed in the tunnel. The two plane mirrors provide a beam offset and allow for collimation and radiation shielding within the tunnel, therefore no further shielding is needed in the experimental

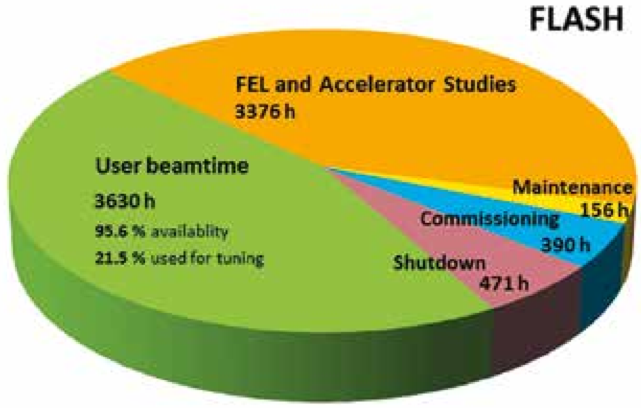

Figure 3

FLASH operation statistics for the time period 1 January – 1 December 2014. The last user beamtime block in December 2014 with ~ 500 h of scheduled beamtime is not included.

Figure 2

Front of the new FLASH2 experimental hall.

hall. In addition, the newly designed mirror chambers provide the necessary degrees of freedom to compensate beam displacements in the tunnel and to steer the FEL beam into the experimental hall at a constant position and angle.

Subsequent to the final construction work in the FLASH2 tunnel, all the basic photon diagnostics for users including monitors for pulse energy, beam position and wavelength, will be installed in the new experimental hall in a more than 10 m stretch from the wall where the FEL beam enters the hall (the orange wall in the centre of Fig. 4). After the diagnostics section the FEL beam can be diverted by plane mirrors to different experimental stations.

The first mirror chamber together with two photon beamlines will be mounted in the second half of 2015. Two plane mirrors

Figure 4
Photograph of the new FLASH2 experimental hall with the office space for users on the left (painted red) and the hutch for the optical pump-probe laser (painted grey) on the right. The picture is taken against the future FEL beam from the position of the experiment at the end of the central beamline FL24. The photon beamline connecting the tunnel with the experimental hall and crossing the PETRA tunnel is already mounted in order to avoid interference with PETRA III operation.

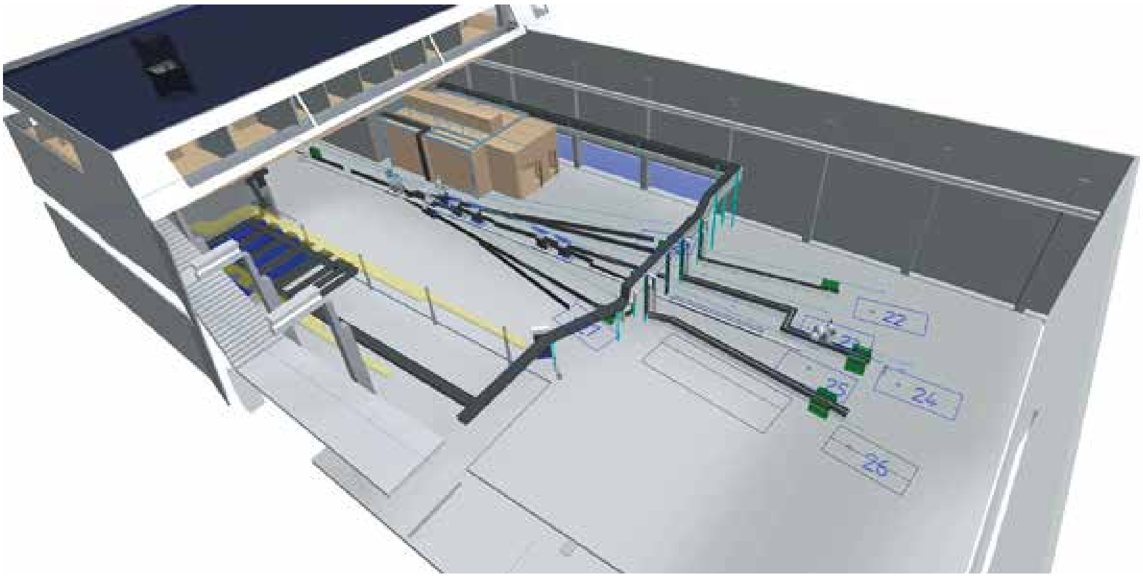

Figure 5
Preliminary layout of the infrastructure and the first three photon beamlines FL22, FL24 and FL26 in the new FLASH2 experimental hall.

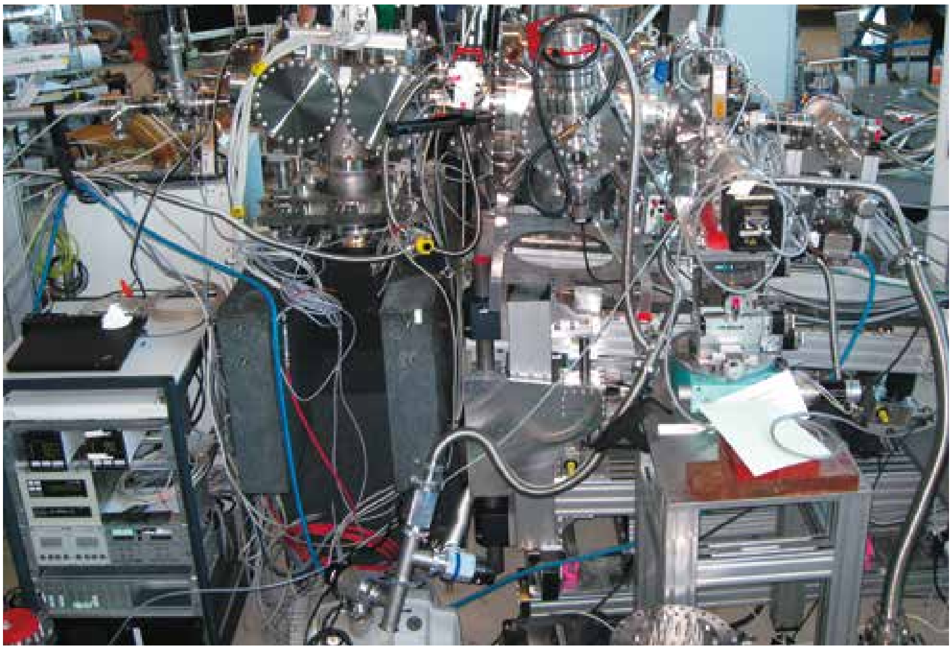

Figure 6

The CAMP chamber just mounted as permanent end station on beamline BL1.

can be moved into the beam and deflect it either left into beamline FL22 or right into beamline FL26 (see Fig. 5). When the mirrors are retracted, the FLASH2 FEL beam passes on through the central beamline FL24. The first two beamlines planned to become operational by the end of 2015 are FL24 – initially without focusing optics – and FL26 including the “reaction microscope” which will be set up by the Max-Planck-Institut für Kernphysik (MPIK) Heidelberg as permanent end station for atomic and molecular physics.

With up to seven additional photon beamlines on FLASH2 it will be possible to further increase the efficient use of the FEL beams by setting up several permanent experimental end stations while still leaving a sufficient number of open ports allowing flexible mounting of specific experimental equipment brought by user groups.

The first two permanent end stations are currently under commissioning in the FLASH1 hall, the CAMP chamber on BL1 and the Raman spectrometer on PG1. Beamline BL1 has been refurbished and a multi-purpose experimental chamber mounted together with suitable Kirkpatrick-Baez (KB) focusing optics. The experimental system, also known as the CAMP chamber, was originally built by the Advanced Study Group (ASG) of the Max-Planck-Society at CFEL and used for numerous experiments on the Linac Coherent Light Source (LCLS) in the US. In the future it will be operated by the FLASH group of the DESY Photon Science division.

The KB system was built by a research group at TU Berlin with special funds from the ministry for education and research (BMBF). A recent picture of the end station during commissioning is shown in Figure 6. The PG1 branch is equipped with a two-stage, high-resolution XUV grating spectrometer for inelastic scattering (Raman) experiments. This system was built in collaboration with a group at University of Hamburg also with funds from BMBF. After significant modifications and improvements needed for the precise alignment of the FEL refocusing optics and the spectrometer tanks, the instrument is now in the final commissioning phase. First user experiments are planned on both end stations during the coming months.

Contact: Josef Feldhaus, josef.feldhaus@desy.de

PETRA III.

Extensions for the future

The year 2014 was characterized by the shutdown for the PETRA extension work. After a short run period for users in January the operation stopped on 3 February. Instantaneous, the machine group started to take apart the sections of the storage ring at the sites of the new PETRA III experimental halls in the North and the East.

During the January run 576 hours of X-ray beam were made available for user operation on all 14 beamlines. 74 experimental sessions have been performed by users of DESY and HZG beamlines P01–P11.

The shutdown period was used – among many other projects – to update the DOOR user administration software. Right on time for the call for proposals published in June 2014 this new system was operational. This call with deadline 3 November resulted in a new record value of 668 proposals. For the first time also long-term proposals (LTPs) have been accepted for PETRA III beamlines. LTPs are valid for two years with the option to add one more year and have been installed for users who significantly contribute to one of the beamlines P01–P11. In total, a number of 22 LTPs have been submitted. Currently all proposals are in the evaluation process and results of the review will be sent to the users in early 2015. After a short period of beamline set-up and commissioning in March 2105 regular operation of PETRA III for users is scheduled for 27 April 2015 until November 2015.

Storage ring tunnel

The storage ring tunnel has been rebuilt to accommodate the new optics and front end devices for the new extension beamlines P21–P25 and P61–P66. This includes a new magnet server system to optimize the operation of PETRA III and the installation of a second diagnostics beamline. The machine modifications needed for the new soft X-ray beamline P66 will be done in the next shutdown planned end of 2015.

As a consequence of the modifications and in particular the installation of the new magnetic lattice for the extension beamlines it is expected that the operation of the PETRA III machine starts with a 10–20 % larger horizontal emittance as compared to the operation in 2013, i.e. 1.2 nmrad. However, by careful tuning the original value of 1 nmrad may be regained.

Beamlines and Experiments

The implementation of new hardware and software for the experiments comprised in particular the upgrade of the beamline control system (see also the article in the “New Technologies and Developments” section of this report). All computers at DESY beamlines are now using Debian Linux as the operating system and the control software is currently being switched to ‘Sardana’. This control software is part of the Tango software package developed by a collaboration of large scale facilities in Europe including DESY. This upgrade of the software is compatible with the data format Nexus/HDF5 and is necessary for an optimal use of high-throughput detectors such as the Eiger (DECTRIS) or the LAMBDA detector, which is a development of the DESY detector group. The new control software Sardana will be available before the user run starts in spring 2015. These improvements are complemented by the exchange of the central file server for detector data and additional 10 GB data transfer lines from the experimental hall to the central server at DESY.

In addition the cooling water system has been upgraded and the coolers of the electronic racks of the PETRA III experiments have been refurbished in order to improve the reliability of the cooling water system.

Due to severe radiation damage, which has been detected during the last runs, the magnet structures of the undulators

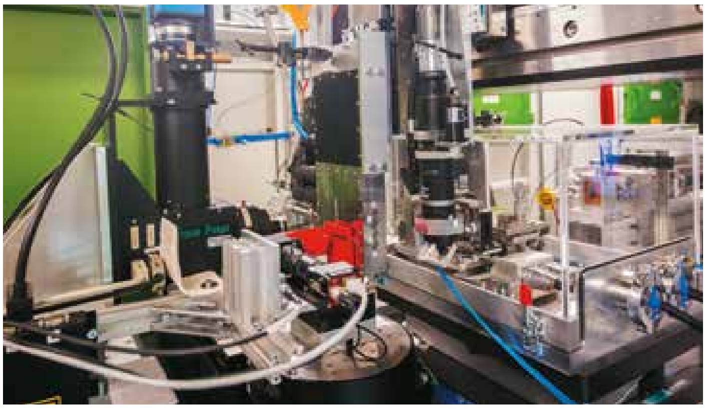

Figure 1

Maia detector in a backscattering geometry at the PETRA III beamline P06. The X-ray beam comes from the right. The detector is positioned just right of the sample holder (red rectangle). The beamstop is the red cylinder. This setup was commissioned together with Jan Garrevoet (Ghent University).

Figure 2

Aerial view of the PETRA III experimental hall "Max von Laue" at DESY including the two construction sites of the PETRA extension in the East (in the lower right corner) and in the North (in the upper left corner) in July 2014.

P02 and P08 are being remagnetised. Both undulators will be back in place before the restart of PETRA III. The mechanism of the radiation damage and suitable preventive measures are subject to further investigations.

Very good progress has been achieved in reducing the vibrations of the standard monochromators cooled by liquid nitrogen. The design of the internal liquid nitrogen cooling system has been altered at selected monochromators, resulting in a reduction of the vibrations by a factor of two and an accuracy now better than 100 nrad rms. In the future, these modifications will be applied to other monochromators.

In addition to the upgrade in software and hardware mentioned above, major improvements have been made or are in preparation at the following beamlines:

- At the High Resolution Dynamics beamline P01 a new multichannel analyzer for inelastic scattering has been installed.
- A robot for automated sample change will be put into operation at beamline P02.1.
- At the Small Angle Scattering Beamline P03 a microfocus option will be available in spring 2015.
- The Hard X-Ray Micro Probe beamline P06 is now permanently equipped with an energy dispersive Maia detector (Fig. 1).
- At the High Resolution Diffraction beamline P08 a pump-probe laser system is being installed by University of Kiel.
- At the Coherence Applications beamline P10 a bio laboratory complying with bio safety level 2 (S2) is being installed. This laboratory will be operational and accessible for PETRA III users in 2015. The rheometer has been upgraded, too.
- At the Bio-Imaging and Diffraction beamline P11 a full field/scanning transmission microscope has been installed which will be operated with the sample positioned in a vacuum vessel. Also, a Kirkpatrick-Baez mirror focusing system has been included for micro diffraction experiments.

In 2014 the three PETRA III beamlines, which were the first to accept users from 2010 on, have been evaluated by external committees: the High Resolution Diffraction beamline P08, the Magnetic Resonance Scattering and Hard X-ray Photoemission Spectroscopy beamline P09 and the Coherence Applications beamline P10. All three got a very positive feedback from the reviewers. They stated that the beamlines have fully achieved the design specifications, offer a world-class instrumentation and have already produced scientific results of the highest international standard.

Contact: Oliver H. Seeck, oliver.seeck@desy.de
Rainer Wanzenberg, rainer.wanzenberg@desy.de

Figure 3

Removal of the PETRA III storage ring in the arc sections (February 2014).

PETRA III Extension

The civil engineering and storage ring reconstruction for the PETRA III extension began as scheduled following the machine shutdown on 3 February 2014. Contracts had been signed with two different companies for the construction of the two experimental halls. While earth moving activities on both construction sites in the East and the North were ongoing around the PETRA III tunnel, this section of the storage ring was completely removed at a total length of 160 m in just about three weeks. The first milestone was the demolition and removal of the concrete tunnel after it had been completely exposed. These arc sections of the tunnel had to be rebuilt as part of the new experimental halls. Moreover the remaining part of the existing ring tunnel next to the new buildings had to be stabilized with rather complex measures to prevent it from sliding down into the construction pit. This had been a demanding procedure especially at the eastern hall where the experimental floor lies about 4 m below ground level.

Another important civil engineering milestone was the completion of the new tunnel sections which had to be accomplished on a very tight time schedule since it determined the starting point of the machine reinstallation. Both companies managed to meet the scheduled date. The installation of machine and beamline components started on 30 July (North) resp. 13 August (East) and the initial progress was quite impressive because the tunnel rapidly filled up with a new storage ring section and beamline front ends.

On a sunny late summer afternoon, 15 September, DESY celebrated the “twin topping-out” of both experimental halls. While the construction of the experimental halls was continuing around the outside of the completed tunnel sections, inside, the

Figure 4

Demolition of the PETRA III ring tunnel section in the East (March 2014).

Figure 5

Reinstallation of the machine and beamline frontends (started in August 2014).

Figure 6

Digging at the site of hall east. The remaining tunnel is seen on the right (March 2014).

newly assembled machine and beamlines was heavily being worked on. The mandatory machine interlock tests will be completed before the Christmas Holidays so that the technical commissioning of the machine may start at the beginning of January 2015. Regular user operation at beamlines in the experimental hall “Max von Laue” is scheduled to resume in April 2015. After the machine restart, the completion of the new experimental halls and the implementation of the experiment infrastructure and beamlines will continue in parallel to the operation for users in the experimental hall “Max von Laue”.

The preparatory work for the implementation of the first beamlines at the PETRA III extension, the X-ray absorption instruments P64 and P65 in the northern hall, is in an advanced stage. Both beamline frontends are planned to be completed before the machine startup, the optics and experiment hutches will be set up in spring 2015. In parallel to the installation of the technical hall infrastructure, the X-ray optical components and other beamline instrumentation will be built up. It is planned to start beamline commissioning in July 2015. Beam for first user experiments at both beamlines is expected to be available in late summer 2015.

All technical design reports of phase 2 undulator beamlines P21–24 have been reviewed and the first beamlines will be built up starting in fall 2015. For the completion of the beamline frontends, additional machine shutdowns are required, the first one is planned for November 2015. The beamline commissioning will start in 2016. The design report of the damping wiggler beamline P61 (phase 3) will be presented in spring 2015.

Figure 7

Casting of the base plate for hall north (April 2014).

Figure 8

Civil engineering of hall east (August 2014).

Figure 9

First construction phase of hall east completed (November 2014).

A special beamline is P66, the only bending magnet source for user experiments at PETRA III. It will be used for time-resolved VUV spectroscopy in continuation of the very successful activities at the former Superlumi instrument at DORIS III. The new experimental station will be located in a separate hutch on top of the PETRA III ring tunnel and the initial construction work has already begun.

A complete list of all PETRA III beamlines is available in a table at the end of this booklet.

Contact: Wolfgang Drube, wolfgang.drube@desy.de
Michael Bieler, michael.bieler@desy.de

European XFEL.

A year of steady progress

At the European XFEL, 2014 has been a year of steady progress. The year saw the start of many crucial installations and constructions: the first accelerator modules, the first support components in the photon tunnels, the first of the instrument enclosures in the experiment hall, and the start of the construction of the headquarters building in Schenefeld. Industrial partners completed mechanical production of all the X-ray-generating undulator segments, and the work on tuning the segments for tunnel installation is nearing completion. Scientists in the instrument groups furthered development of the tools with which users will investigate matter in ultrahigh detail.

Due to unforeseen supply chain and assembly challenges in the linear accelerator section of the facility, the date of first beam and the start of user operation had to be rescheduled in January to the end of 2016 and middle of 2017, respectively. The schedule adjustment was already announced at the European XFEL and DESY Photon Science Users' Meeting in January 2014.

Installations of infrastructure also began in the tunnel that will contain the SASE1 undulator. These activities included casting the concrete sockets for optical components and installing the aluminum supports for the ultrahigh vacuum system of the beamline. The first beamline vacuum components were installed during the autumn. In the experiment hall, engineers installed the complex ductwork for the air conditioning system, which is needed to maintain precise conditions inside the hall. Another set of ducts will deliver similar climate control in the photon tunnels next year.

Figure 1

Aerial view of the Schenefeld site in July 2014. The European XFEL runs from the DESY site in Hamburg to the research site in Schenefeld. The headquarters building is under construction (centre-left). The undulator systems will begin in the underground tunnels near European XFEL's Osdorfer Born site (upper right-hand corner), and the X-ray flashes they generate will be used for research in the experiment hall beneath the headquarters building. (Photo credit: European XFEL)

Also in the experiment hall, the first instrument enclosure, a heavy concrete experiment hutch for the High Energy Density science (HED) instrument, was completed in late summer. Tendering also was done on the lead hutches for the SASE1 beamline, in which the Single Particles, clusters, and Biomolecules and Serial Femtosecond Crystallography (SPB/SFX) instrument and the Femtosecond X-Ray Experiments (FXE) instrument will be installed. The construction of those hutches will begin early in 2015, and they are expected to be ready for the installation of the instruments in early 2016. Also, the final two instrument technical design reports, for the Spectroscopy and Coherent Scattering (SCS) and HED instruments, were completed and published. In summer, a new grant for HED and the Helmholtz International Beamline for Extreme Fields at the European XFEL (HIBEF) user consortium was approved by UK funding agencies.

Now scientists and engineers are focusing on detailed installation planning throughout the tunnels and experiment hall, which is expected to be the major effort during the years 2015 and 2016. In the photon tunnels the infrastructure installations are finished for the SASE1 and SASE3 beamlines. The installation of the undulator system and the photon beamline components has started. For the SASE2 beamline, the infrastructure installation is the next step. The installation of the final high quality floor has been finished. In parallel with these construction and installation activities, the planning of hutches and infrastructure for the instruments has gone on. The planning activities for the hutches and infrastructure of SASE3 concluded at the end of the 2014. Installation planning for the instruments themselves is in full swing since first components need to be mounted before the start of the hutch construction in 2015. Meanwhile, procurement began on many system components, including special super flat X-ray mirrors, X-ray monochromators, X-ray beam transport components, and optical laser systems. Further development and testing continues on diagnostics, detectors, and control systems.

The work on the undulator systems, of central importance for the facility, is in full swing in terms of construction and continues to make good progress. In July, the mechanical production of the 91 undulator segments needed for startup configuration of the SASE1, SASE2, and SASE3 undulator systems was completed. The European XFEL undulator group continues with the magnetic measurements and tuning of these segments to guarantee that all of them fulfil XFEL specifications so that all SASE systems will perform as planned. As of October, the group has fully tuned 78 segments, which are now waiting for the installation in the tunnel. Other major components of the undulator systems are coming in at a steady pace. At the close of 2014, all quadrupole movers and intersection control racks were delivered and accepted. The last phase shifters will arrive in early 2015.

Figure 2

The L1 section of the European XFEL electron accelerator.

Figure 3

At the Accelerator Module Test Facility (AMTF), DESY scientists have been preparing European XFEL accelerator modules (yellow) for installation in the linear accelerator tunnel.

In March 2014, more components for the undulator systems were delivered as in-kind contributions via the 17-institute Accelerator Consortium: the vacuum systems for the intersection, the undulator vacuum chambers, beam position monitors and their electronics, beam loss monitors, and quadrupole magnets. The installation of the first undulator system SASE1 began, including cooling water infrastructure, concrete pillars, support columns, and control racks. At the end of September, 35 control systems for the undulator segments and intersection components were installed. In the following months, the first parts of the air conditioning system and the vacuum pipe of the laser alignment system were installed. For SASE3, installation began about 5 months after SASE1. The SASE2 system is scheduled to begin installation in March 2015 and the sequence of the installation will be similar to that of SASE1 this year.

Further up the facility's length towards the DESY campus, the accelerator installations have begun. The DESY-led Accelerator Consortium set into place one section of four modules, called L1, and began to assemble the main accelerator, L3, along with parts of their associated waveguide components, pulse transformers, and klystrons. Meanwhile, tests and further installations continued on the injector, which is expected to be operational in May 2015 when injector commissioning will commence.

Next year will come installations of the L2 section, which will close the gap between the injector and L3, and the installation of further sections of the main accelerator. Additional components for the injector and accelerator cryogenic lines are also expected next year. Completion of the accelerator installation is foreseen for summer 2016.

Construction of the European XFEL laboratory and office building began in April. The three-floor structure is built directly atop the underground experiment hall in Schenefeld and will feature laboratories for specimen preparation, lasers, electron microscopy, and biology on the ground floor and offices on the two floors above. The ground floor and second floor are structurally complete and doors and windows will be added early next year. Two important nearby buildings that will maintain precise humidity levels and temperatures in the underground tunnels and experiment hall are also complete and due to be fully functional by next summer. A large effort in the coming year will also be renaturation of the construction site and compensation measures in its surroundings, including restoration work on the river Düpenau. These efforts are being discussed with local environmentalists.

European XFEL hosted the 6th Hard X-Ray FEL Collaboration Meeting in May 2014. This meeting brought together scientists from the hard X-ray free-electron laser (FEL) facilities around the world – the Linac Coherent Light Source in Menlo Park, California; SACLA in Harima, Japan; SwissFEL in Villigen, Switzerland; and PAL-XFEL in Pohang, Korea – most of which are either under construction or undergoing upgrades. The meeting focused on operational experience with the functioning FELs. Results of measurements at FLASH were presented as an outlook to the European XFEL accelerator performance. Collaborations in the area of accelerator and photon beam systems were discussed.

Over the course of 2014, the European XFEL GmbH workforce grew to about 210 employees in December 2014 from 196 in December 2013. When all positions are filled, the company will have around 280 employees and 25 longterm guests, with an additional 230 DESY employees operating the accelerator.

Looking to next year, installations will continue. After climatization of the underground structures, critical parts of the scientific infrastructure, such as optical components, will be installed. The undulator group will begin installations of sensitive components in SASE1 early in the year, such as beam position monitors, intersection control racks, quadrupole movers, quadrupoles, and vacuum systems, leading to the installation of the first undulator segments at the end of summer. Next year will likewise be an intense push towards opening what will be the world's brightest light source to users in 2017.

Contact: Massimo Altarelli, massimo.altarelli@xfel.eu

Figure 4

Several infrastructure installations have been made in the SASE1 tunnel, including cooling water infrastructure, concrete pillars, support columns, and control racks.

New Technologies and Developments.

- Tuning the phase 104
- Ultrashort FLASHes gauged 106
- Mutual coherence function of FLASH via Wigner formalism 108
- Happy CAMPer 110
- Smooth operator 112
- New material by high pressure synthesis at PETRA III 114
- NeXus integration at PETRA III 116

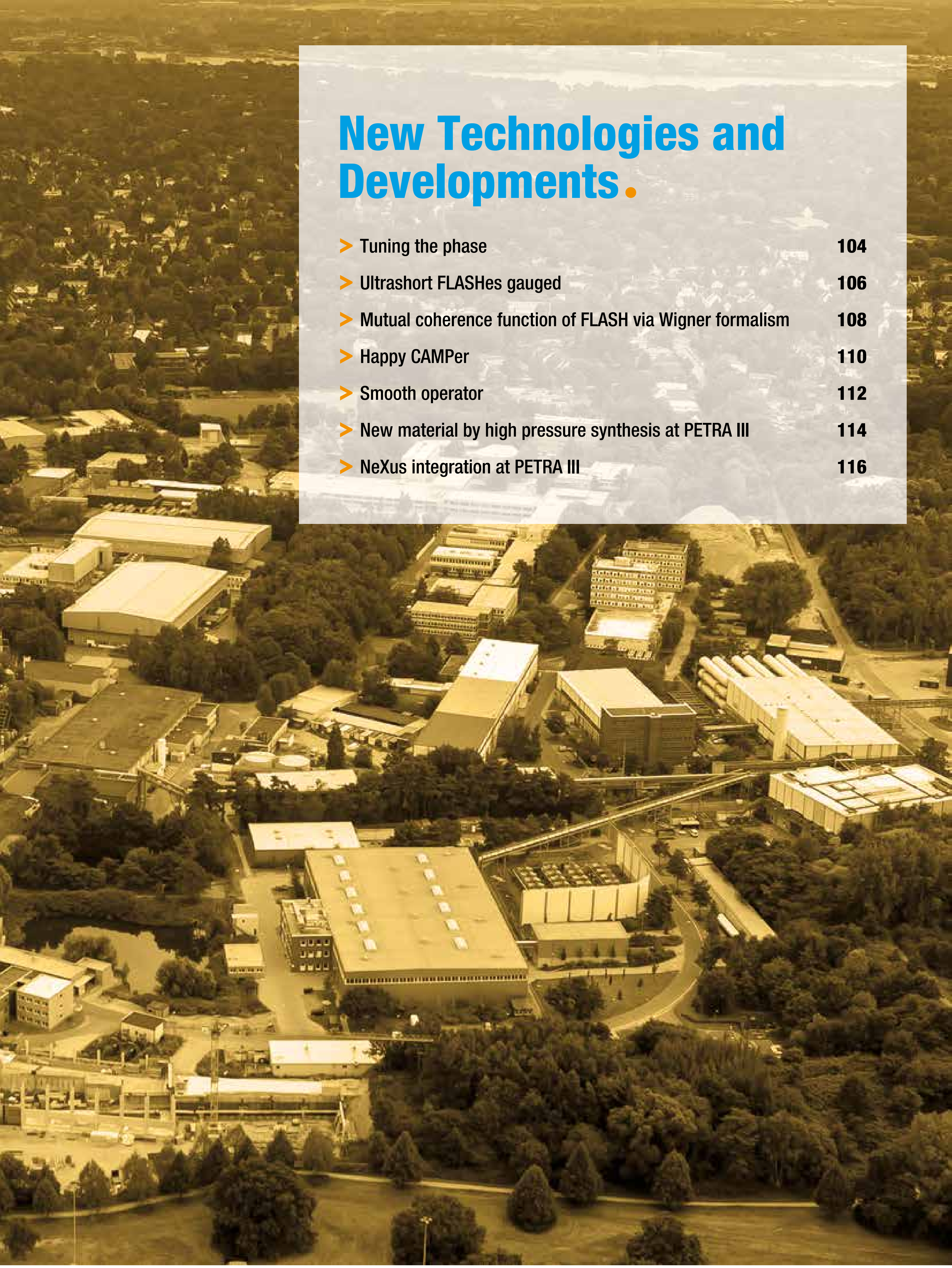

Tuning the phase.

Tuning and characterization of the FLASH2 undulators and phase shifters

Figure 1

Part of the FLASH2 SASE section comprising 12 undulators and corresponding intersections

In order to double the capacity for user beamtime, a second undulator line was added to the FLASH facility. To assure saturation for the entire wavelength range of 4 to 60 nm and to match the lattice, in total 12 insertion devices (IDs) of 2.5 m length were installed in the FLASH2 tunnel. They have a period length of 31.4 mm, provide a maximum field of 0.96 T and a K-parameter of 2.81 at minimum gap. The variable gaps allow for energy tuning independently from FLASH1 operation. Before installation, each ID was tuned for minimum phase error and trajectory roughness over the entire gap range, based on Hall probe measurements. Thereby a RMS phase error below 2° and a trajectory flatness of 6 Tmm^2 (~2 μm at 1 GeV) was achieved [1].

Each intersection between the IDs comprises a phase shifter and various components for diagnostics and beam steering. The phase shifters are compact electromagnetic chicanes and have to assure constructive interference of the radiation of adjacent undulators for all wavelengths. Their magnetic performance, field errors and the hysteresis behaviour have been investigated and were found to be within the required accuracy. From these data, tables for steering each phase shifter's current as a function of adjacent undulator gaps were derived and implemented in the control system [2].

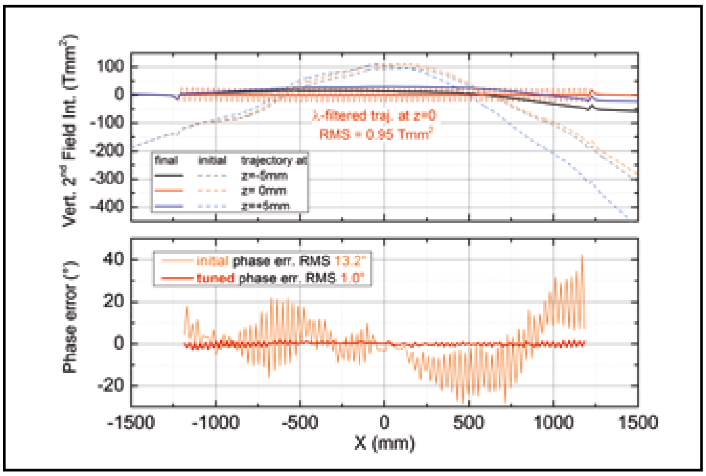

Figure 2

Examples for the tuning results of one FLASH2 undulator: vertical 2nd field integral ("trajectory", top) and phase error (bottom). Tuning was not only done on axis (z = 0), but also for horizontal offsets of up to z = 5 mm.

While manufacturing of the undulator support frames and magnet modules was done by industrial partners, the final assembly, magnetic measurements and tuning were performed in the FS undulator lab in order to meet the stringent specifications. Magnets were sorted according to data provided by the manufacturer and in the initial state all poles were positioned precisely 100 μm above the magnet surfaces, which already provided a good starting value for the tuning procedure. After an accurate mechanical alignment to the measurement bench according to Hall probe data, the fine tuning of the vertical and horizontal field integral was then realized by shifting and tilting each pole individually on the μm- and sub-mrad scale.

Vertical magnetic fields were measured by a Hall-probe and horizontal ones by a small pick-up coil, both with an accuracy of 10^{-5}. The related data were used to ascribe any imperfections to particular poles and calculate the pole shift or tilt required for correction. Within a few iterative tuning steps, horizontal and vertical trajectories straightness and phase error could be improved simultaneously to values below 6 Tmm^2 and 1° RMS, respectively. Figure 2 shows examples for the tuning of trajectory straightness and phase error from the initial to the final state at minimum gap while Figure 3 gives an overview of the results for the entire gap range of all 12 FLASH2 undulators.

The pole shifting and tilting was also used to correct for local quadrupole contributions based on off-axis trajectory measurements. Although multipole components like these are usually not considered to be crucial for FELs, even higher order multipoles have been compensated in a limited transverse range of ±5 mm by means of small "magic finger" corrector magnets at each end of the ID. The arrangement of magnets in these arrays is based on measurements of horizontal and vertical field integrals with a stretched wire setup along the undulator. Thus, the transverse variation of the field integrals in this range could be reduced to 0.03 Tmm. The remaining gap dependence of the end-kicks was below 0.05 Tmm and will be corrected by small air coils at both ends of each ID.

In order to assure constructive interference of the radiation by two consecutive undulator segments, a phase shifting chicane magnet is required, which extends the drift length of the electron beam. In case of FLASH2 (Fig. 1), this chicane consists of three electromagnetic coils on a yoke of laminated relay iron, which are powered in series and create a –½, 1, –½ triangular bump. They comprise an additional corrector winding, which is used for cancellation of residual kicks and as a horizontal steerer.

The total phase advance Φ_{Tot} between photons and electrons consists of the vacuum phase advance in the drift section Φ_D, the phase advance induced by the end field termination of the insertion devices Φ_{IDends} and the contribution of the phase shifters Φ_{PS}. The first two components can be described in a way that they only depend on the undulator K-parameter. The current of the phase shifter needs then to be chosen such that its contribution Φ_{PS} adjusts the total phase advance to a multiple of 2π.

$$\Phi_{Tot} = \Phi_D\,(K) + \Phi_{IDends}\,(K) + \Phi_{PS}\,(K,I) = n\,2\pi$$

The drift length between two IDs at FLASH2 is 800 mm and the values for Φ_D add up to values from $5 \cdot 2\pi$ to $23 \cdot 2\pi$ for the entire K-range. It needs to be known quite precisely, since an error of 0.5 mm induces an uncertainty of 1° to 5° in Φ_D, respectively. The phase advance induced by the two ends of an undulator Φ_{IDends} of up to 10° can be calculated from measured magnetic field maps and represented by a polynomial in terms of K and thus be calculated during operation.

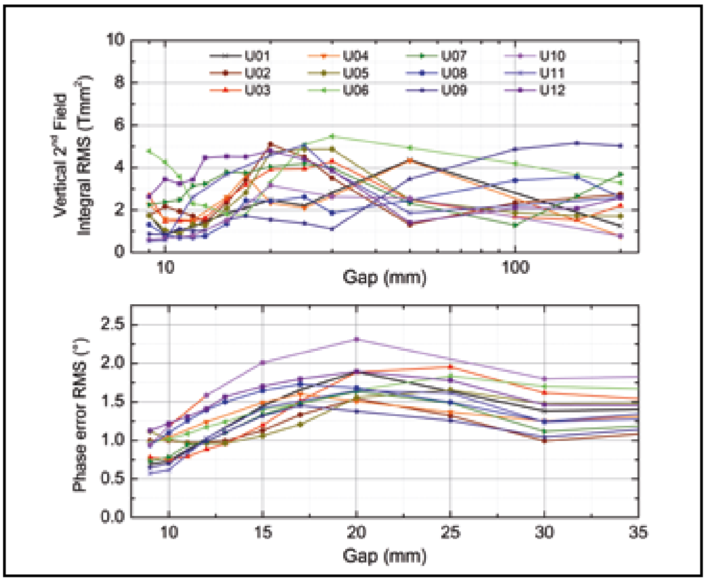

Figure 3

Summary of the tuning results for all FLASH2 IDs: RMS values for vertical 2nd field integral ("trajectory roughness", top) and phase error (bottom) as a function of the undulator gap.

The contribution to the delay of the electrons by the phase shifter Φ_{PS} can be described by its 1st field integral and terms of the undulator K-parameter. Therefore all phase shifters have been characterized by Hall-probe and stretched wire measurements to determine phase integral and kick errors as a function of operating current. Since for the maximum field of 0.12 T there should be no saturation effects in the yoke, a parabolic behaviour of the phase integral is expected up to the maximum current of 8.8 A. The data normalised to I^2 shows good agreement with this assumption for currents above 2 A, but becomes poor below. Therefore, the phase shifter operation will be limited to currents above this value. Thus the devices will cover a phase advance of $1.9 \cdot 2\pi$ to $8.5 \cdot 2\pi$ for undulator K-values from 2.8 to 0.5. The residual field integrals of the phase shifters due to manufacturing imperfections have been independently calculated from Hall-probe data and measured by a stretched wire setup and can be compensated by the integrated corrector coil.

The magnetic tuning of the undulators was done beyond specifications by including off-axis trajectories and higher order multipoles. This and the thorough characterization of the phase shifters allowed for very smooth commissioning of FLASH2. First lasing was achieved "at the push of a button" without orbit corrections in the SASE section [3].

Contact: Markus Tischer, markus.tischer@desy.de
Andreas Schöps, andreas.schoeps@desy.de

Authors

A. Schöps
Deutsches Elektronen-Synchrotron DESY, 22607 Hamburg, Germany

References

1. O. Bilani, P. Neumann, A. Schöps, M. Tischer, S. Tripathi, P. Vagin, T. Vielitz, "Magnetic Tuning of FLASH2 Undulators", IPAC'14, Dresden (Germany), June 2014, p. 1235 (2014).
2. M. Tischer, P. Neumann, A. Schöps, P. Vagin, "Phase Shifters for the FLASH2 FEL", IPAC'14, Dresden (Germany), June 2014, p. 2010 (2014).
3. J. Feldhaus, "Simultaneous lasing of the two FEL lines FLASH1 and FLASH2", this report.

Ultrashort FLASHes gauged.

An XUV pulse duration measurement campaign verified ultra-short FLASH pulses

The ultra-short pulse duration in the femtosecond range is characteristic for the new generation of XUV and X-ray free-electron lasers. With these new sources ultrafast reaction dynamics as well as the investigation of multi-photon processes in the XUV to the X-ray range are accessible, which has not been possible before. The accurate knowledge of the FEL key parameters such as pulse peak power, radiance, and on-target irradiance is crucial for the analysis of experimental data. It turns out that the number of photons, the focal spot size and the spectral content in such short pulses can be measured reliably, while the pulse duration is still the most difficult parameter to be determined.

At FLASH the duration of the generated photon pulses can be varied over a range of few tens of femtoseconds up to several hundreds of fs. Still, a reliable method to measure pulse durations for the entire parameter range is not yet available. In a campaign nine different techniques – three electron bunch duration measurements and six photon based methods – have been used to determine the photon pulse duration (see Fig. 1). They are either performed in a *direct* way by measuring the photon pulse duration at the experimental end stations or by *indirect* methods measuring only parameters which are linked – by theoretical models – to the actual pulse duration. From the measured data the actual XUV pulse duration can be calculated using these models. From the experimental point of view, indirect methods are typically simpler to realize as compared to the direct approaches. However, they have to be verified and calibrated by direct methods.

The goal was to tune the FEL to generate ~ 50 fs short pulses at 13.5 nm. The measured pulse duration of 50 +/– 10 fs agreed remarkably good with the target value (with a slight increase at the end of the campaign). Most of all the used indirect methods reveal the same results as the direct methods and thus the assumptions made for the analysis of the indirect methods seem to be valid for this case. In agreement with our expectations the XUV photon pulse was shorter by a factor of 0.6, as compared to the length of the electron bunch from which it was generated. Thus, the knowledge of the electron bunch duration also yields important information for the determination of the XUV pulse length.

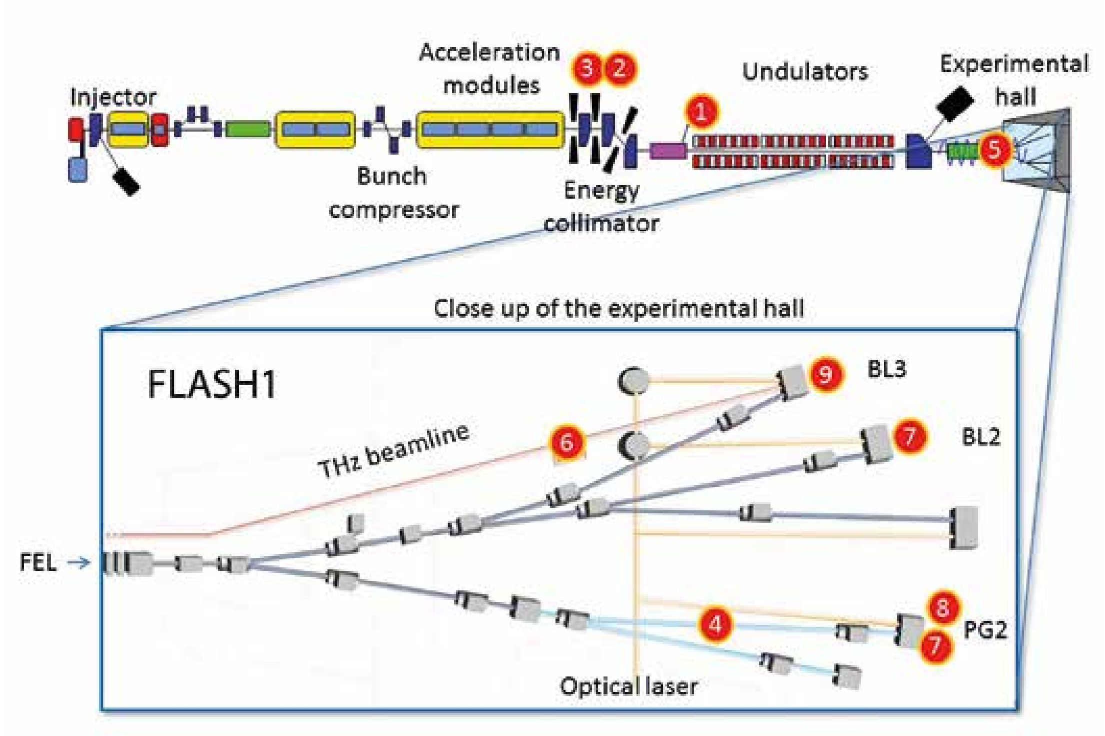

Figure 1

The positions of the various techniques in the FLASH FEL tunnel and hall for electron bunch or photon pulse duration measurements are indicated by numbers [4]:

(1) Transverse Deflecting RF Structure (TDS)
(2) Bunch Compression Monitors (BCM)
(3) THz Spectrometer CRISP
(4) XUV Spectra
(5) XUV Statistics
(6) Optical Replica (Afterburner)
(7) XUV Autocorrelation (gas phase)
(8) XUV Autocorrelation (solid state)
(9) THz Streaking
(all figures adopted from [4]; Copyright (2014) by The American Physical Society)

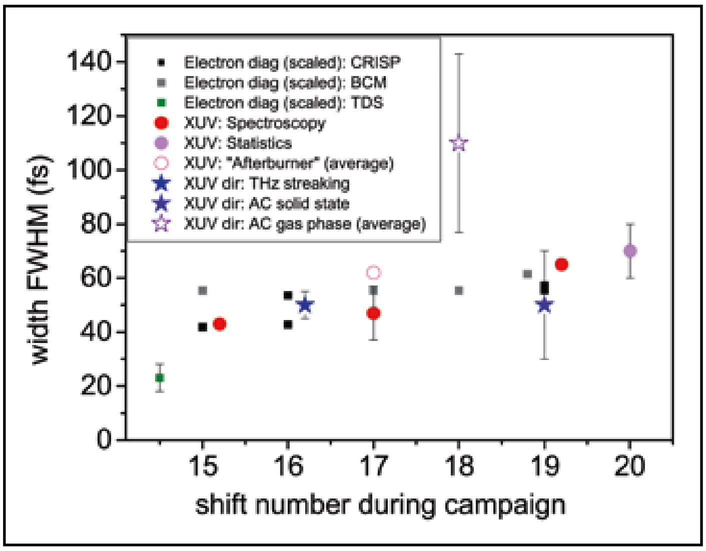

Figure 2

XUV pulse and electron bunch duration (FWHM) measured at FLASH by various methods at a wavelength of 13.5 nm. The electron bunch measurements were scaled by a factor of 0.6. The deviation of two methods (TDS, AC gas) can be explained by different accelerator settings and low signal-to-noise ratio in the experiment, respectively. A shift lasts 8 hours [4].

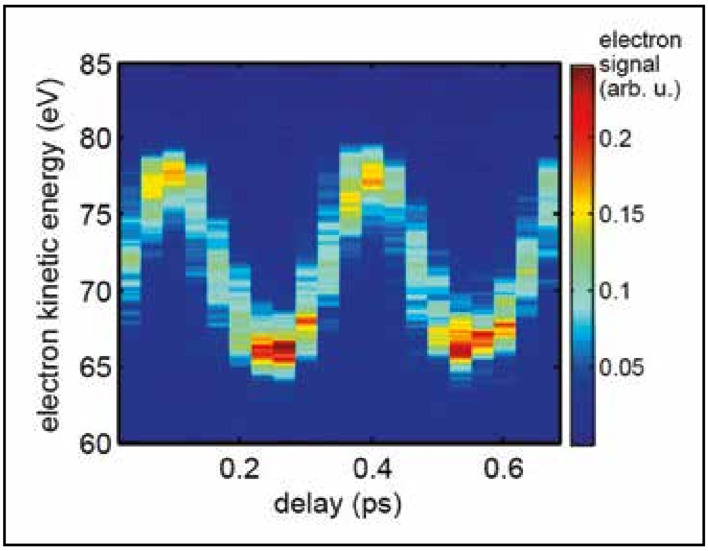

Figure 3

THz streaking scan as example for a pulse duration measurement. Shown are photoelectron spectra measured for different delay times between the THz radiation and the XUV pulses. The energy shift represents the vector potential of the THz field, while the widths of the spectra represent a measure of the XUV pulse duration [4].

In conclusion, for FLASH we will further develop and automatize the electron based diagnostics as monitor for changes within a bunch train as well as for long term drifts in the pulse duration. In order to use the electron pulse duration techniques to state reliable XUV pulse durations more investigations on the various dependencies of the scaling factor on the wavelength and other FEL parameters have to be undertaken. In addition we will further automatize the usage of THz afterburner measurements and spectral analysis as future standard diagnostics. Finally, for SASE FELs like FLASH it is essential to also develop tools being able to deliver on a single-shot basis the pulse profile and the substructure as well as the arrival time in respect to an external laser source. The methods considered for future development are based on the XUV induced reflectivity changes (see e.g. Refs. [1,2] and THz streaking techniques (see Fig. 3) in particular with optical laser based THz sources as described in Ref. [3].

The detailed description of all methods and the comparison of the various approaches can be found in Ref. [4].

Contact: Stefan Düsterer, stefan.duesterer@desy.de

References

1. T. Maltezopoulos, S. Cunovic, M. Wieland, M. Beye, A. Azima, H. Redlin, M. Krikunova, R. Kalms, U. Fruehling, F. Budzyn, W. Wurth, A. Foehlisch, M. Drescher,"Single-shot timing measurement of extreme-ultraviolet free-electron laser pulses", New Journal of Physics 10, 033026 (2008).
2. R. Riedel, A. Al-Shemmary, M. Gensch, T. Golz, M. Harmand, N. Medvedev, M. J. Prandolini, K. Sokolowski-Tinten, S. Toleikis, U. Wegner, B. Ziaja, N. Stojanovic and F. Tavella,"Single-shot pulse duration monitor for extreme ultraviolet and X-ray free-electron lasers", Nature Communications 4, 1731 (2013).
3. I. Grguras, A.R. Maier, C. Behrens, T. Mazza, T J. Kelly, P. Radcliffe, S. Duesterer, A. K. Kazansky, N.M. Kabachnik, Th. Tschentscher, J.T. Costello, M. Meyer, M.C. Hoffmann, H. Schlarb and A.L. Cavalieri, "Ultrafast X-ray pulse characterization at free-electron lasers", Nature Photonics 6, 852-857 (2012).
4. S. Düsterer, M. Rehders, A. Al-Shemmary, C. Behrens, G. Brenner, O. Brovko, M. DellAngela, M. Drescher, B. Faatz, J. Feldhaus, U. Frühling, N. Gerasimova, N. Gerken, C. Gerth, T. Golz, A. Grebentsov, E. Hass, K. Honkavaara, V. Kocharian, M. Kurka, Th. Limberg, R. Mitzner,R. Moshammer, E. Plönjes, M. Richter, J. Rönsch-Schulenburg, A. Rudenko, H. Schlarb, B. Schmidt, A. Senftleben, E. Schneidmiller, B. Siemer, F. Sorgenfrei, A. Sorokin, N. Stojanovic, K. Tiedtke, R. Treusch, M. Vogt, M. Wieland, W. Wurth, S. Wesch, M. Yan, M. Yurkov, H. Zacharias, and S. Schreiber. "Development of experimental techniques for the characterization of ultrashort photon pulses of XUV free-electron lasers", Phys. Rev. ST Accel. Beams 17, 120702 (2014).

Mutual coherence function of FLASH via Wigner formalism.

4D phase space tomography of an FEL beam

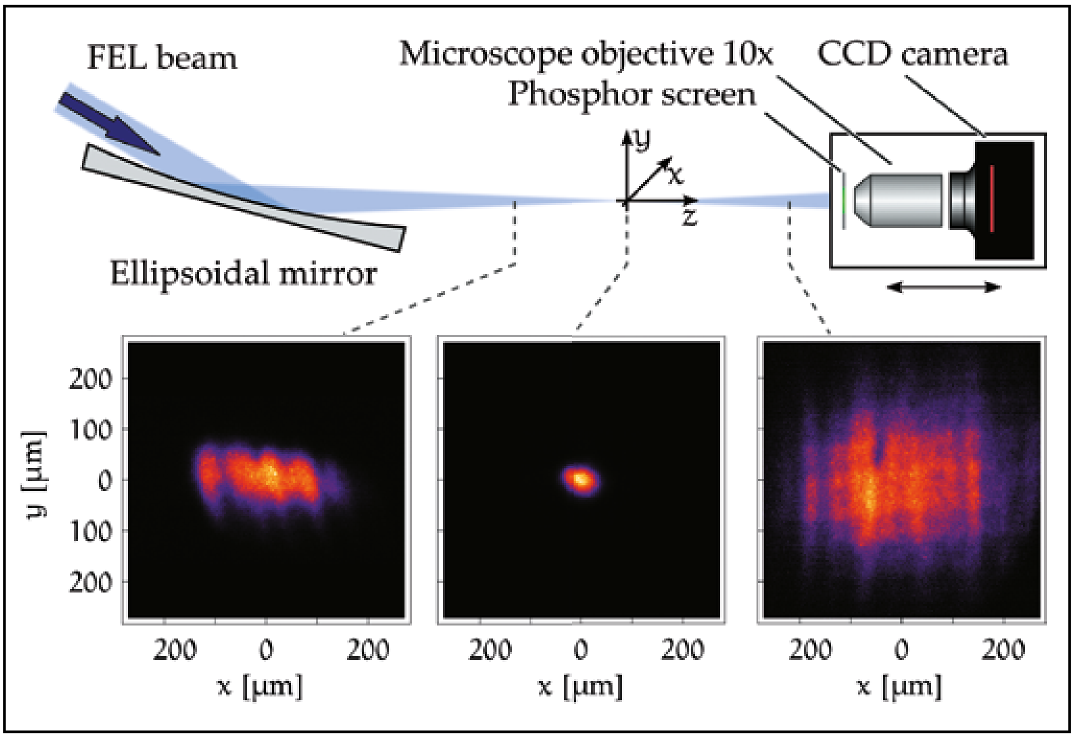

Figure 1
Experimental setup for the measurement of the Wigner distribution at FLASH with a selection of spatial intensity profiles at different positions around the beam waist (wavelength λ = 24.7nm).

Free-electron lasers (FELs) are unique beam sources in the extreme UV and soft X-ray spectral range. They produce ultrashort pulses with the highest brilliance available and a high degree of spatial coherence, enabling groundbreaking experiments, e.g. in the field of coherent diffractive imaging. As long as the lateral coherence length of the photon beam exceeds the dimensions of the investigated object, it can be properly recovered from the diffraction pattern [1]. On the contrary, in case of larger samples the assumption of full coherence does not apply anymore and the coherent reconstruction will fail [2]. It has been demonstrated, however, that exact knowledge of the mutual coherence function (MCF) can provide a remedy [3]. Here, fundamental coherence parameters for FLASH are derived from a reconstruction of the four-dimensional MCF within the scope of phase-space tomography.

A photon beam can be described entirely by the Wigner distribution function $h(\vec{x},\vec{u})$ which is defined as two-dimensional Fourier transform of the mutual coherence function $\Gamma(\vec{x},\vec{s})$, where $\vec{x} = (x,y)$ and $\vec{s} = (s_x,s_y)$ are vectors in a plane perpendicular to the mean propagation axis and $\vec{u}=(u,v)$ describes a direction [4]. $h(\vec{x},\vec{u})$ can be denoted as generalized radiance [5], which implies the interpretation as an amplitude of a ray passing through the point $\vec{x}$ in the direction of $\vec{u}$. However, $h(\vec{x},\vec{u})$ may assume negative values, which limits this interpretation to a certain extent. From the Wigner distribution, the mutual coherence function can be derived by a two-dimensional Fourier back-transformation. In that context, the coherence lengths l_x and l_y describe the decay of $\Gamma(\vec{x},\vec{s})$ in s_x- and s_y-direction, and the global degree of coherence K can be considered as the inverse phase-space volume occupied by $h(\vec{x},\vec{u})$.

The Wigner distribution can be reconstructed tomographically from a measurement of several intensity profiles. At FLASH, a phosphor screen is employed to convert EUV radiation at a wavelength of 24.7 nm into visible green light, and a 10x magnifying objective images the resulting beam profile to a CCD camera (Fig. 1). This system probes the FEL beam behind the focusing ellipsoidal mirror of beam line BL3 at 145 different positions in vicinity of the beam waist and thus, the three-dimensional radiation field is captured. As a consequence of the projection slice theorem of tomography, in Fourier space each measured intensity profile corresponds to a certain 2D slice through the 4D-Wigner distribution of the beam. Numerically, the phase space of the Wigner distribution is constituted by a four-dimensional regular grid that contains 129^4 cells. However, the described measurement suffices to

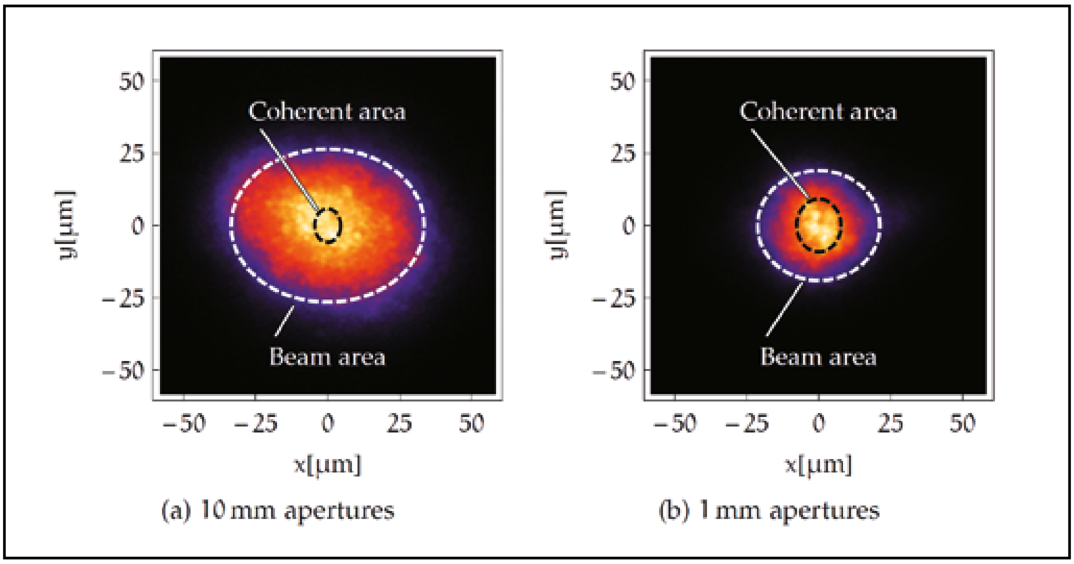

(a) 10 mm apertures

(b) 1 mm apertures

Figure 2

Intensity profiles of the FLASH beam at mean waist position. The beam area is confined by the beam diameters (given in terms of 4σ values) as indicated by the white ellipse. Correspondingly, the coherence lengths define the coherent area, signified by the black ellipse. It is apparent, that the application of small apertures to the FEL photon beam leads to an increased coherent fraction.

reconstruct a three-dimensional sub-manifold only. This issue is addressed by an interpolation procedure for those cells that remain empty after the mapping. Finally, the coherence parameters are derived from the reconstructed Wigner distribution, and a two-dimensional Fourier transform of the latter yields the mutual coherence function.

According to our evaluations, the photon beam of FLASH exhibits coherence lengths of $l_x = 9.0\ \mu m$ and $l_y = 11.6\ \mu m$ at its mean waist position, where the beam diameters are found to be $d_x = 67\ \mu m$ and $d_x = 53\ \mu m$ (derived by second moments of the intensity distribution $dx = 4(<x^2>)^{1/2}$). Thus, fractions of 9.0 / 67 = 0.13 and 11.6 / 53 = 0.22 of the beam can be regarded as coherent. An illustration of this result is shown in Figure 2, where the coherent area is indicated in the intensity profile. The global degree of coherence, derived from the Wigner distribution, is K = 0.032. This value stands in contradiction to previous coherence studies employing double pinhole interferograms [6] or Hanbury Brown-Twiss interferometry [7], where values of K = 0.43 and K = 0.78 are found for wavelengths of 8.0 nm and 5.5 nm. Consequently, at the present situation it seems that the beam coherence strongly depends on its wavelength, although three fundamentally different approaches are compared to each other. Furthermore, deviations might result from different techniques to determine beam sizes (Wigner: phosphor screen vs. double pinhole: PMMA imprints) which play a major role in the determination of the coherence.

In further experiments at BL2, we improved the coherence by two identical circular apertures of different diameters, ranging down to 1 mm, positioned 18.8 m and 23.3 m behind the center of the last undulator. As a result, we observe an increase in the coherence length (up to $l_x = 15.3\ \mu m$ and $l_y = 18.3\ \mu m$) whereas the beam diameter decreases (down to $d_x = 38\ \mu m$ and $d_y = 34\ \mu m$) (see Fig. 2). These two effects in combination lead to a considerable improvement of the global degree of coherence to K = 0.198 in case of the smallest apertures.

In summary, with respect to previous studies, our investigations imply that the coherence of FEL radiation shows a dependence on the photon wavelength. This involves comparably low coherence values as resulting from the Wigner measurements which have been conducted at relatively large wavelengths. This particular correlation should be further explored by future experiments. A deeper insight with respect to that context might qualify the wavelength as an interesting control parameter of the coherence properties.

Contact: Tobias Mey, tobias.mey@llg-ev.de
Barbara Keitel, barbara.keitel@desy.de

Authors

Tobias Mey[1], Barbara Keitel[2], Marion Kuhlmann[2], Elke Plönjes[2], Bernd Schäfer[1], Klaus Mann[1]

1. Laser-Laboratorium Göttingen e.V., 37077 Göttingen, Germany
2. Deutsches Elektronen-Synchrotron DESY, 22607 Hamburg, Germany

Original publication

"Wigner distribution measurements of the spatial coherence properties of the free-electron laser FLASH", Optics Express 22, Issue 13, 16571-16584 (2014).
DOI: 10.1364/OE.22.016571

References

1. J. C. H. Spence, U. Weiterstall, M. Howells, "Coherence and sampling requirements for diffractive imaging," Ultramicroscopy 101, 149-152 (2004).
2. B. Chen, B. Abbey, R. Dilanian et al., "Diffraction imaging: The limits of partial coherence," Phys. Rev. B 86, 235401 (2012).
3. L. W. Whitehead, G. J. Williams, H. M. Quiney et al., "Diffractive Imaging Using Partially Coherent X Rays," Phys. Rev. Lett. 103, 243902 (2009).
4. M. J. Bastiaans, "Application of the Wigner distribution function to partially coherent light," JOSA A 3, 1227-1238 (1986).
5. A. Walther, "Radiometry and coherence," JOSA 58, 1256-1259 (1968).
6. A. Singer, F. Sorgenfrei, A. P. Mancuso, et al., "Spatial and temporal coherence properties of single free-electron laser pulses," Opt. Expr. 20, 17480-17495 (2012).
7. A. Singer, U. Lorenz, F. Sorgenfrei, et al., "Hanbury Brown-Twiss Interferometry at a Free-Electron Laser," Phys. Rev. Lett. 111, 034802 (2013).

Happy CAMPer.

A permanently installed multi-purpose end station for user experiments at FLASH

The increasing complexity of the experimental setups for many free-electron laser (FEL) experiments together with the tighter scheduling to satisfy the growing beamtime demand has led to the realization that permanently installed end stations, which can host a variety of different user experiments, can, in some cases, increase the productivity of heavily oversubscribed FEL facilities. This worldwide trend has also been realized at FLASH, where CAMP, a multi-purpose instrument for electron and ion spectroscopy, pump-probe, and imaging experiments with FELs, has just been installed as a permanent user end station at beamline BL1 (see Fig. 1).

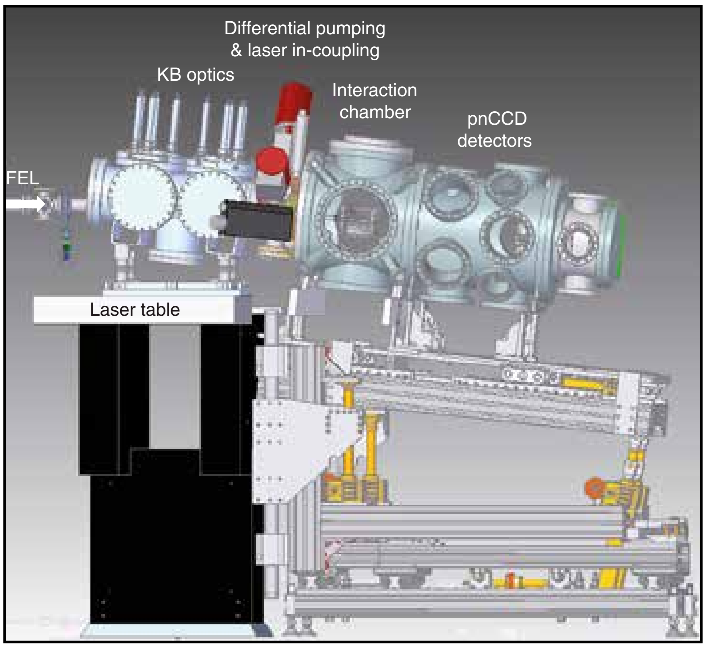

Figure 1

Layout of the CAMP end station at FLASH BL1 including KB focusing optics, laser in-coupling unit, and the experimental interaction chamber with pnCCD photon detectors attached.

CAMP was developed by the Max Planck Advanced Study Group within the Center for Free-Electron Laser Science (CFEL) at DESY together with various Max Planck Institutes and a number of international user groups [1]. After three extremely successful years at the AMO beamline of LCLS, where it has enabled a wide variety of ground-breaking FEL experiments [2-10] in atomic, molecular, and optical physics, material and energy science, chemistry, and biology, CAMP has now found a permanent home at FLASH, where it is available to all users.

Through a BMBF collaborative research project led by the TU Berlin, the CAMP instrument including large-area pnCCD photon detectors is made available at FLASH by the Max-Planck-Gesellschaft, and BL1 has been equipped with new nickel-coated Kirkpatrick-Baez (KB) optics providing a tight focus of about 4 x 5 μm^2 (FWHM) over the entire wavelength range available at FLASH. The optics are optimized for wavelengths of 13 nm and shorter, including the carbon K-edge, and have been commissioned and characterized during FEL studies time in October 2014 using a FLASH wavefront sensor [11] as well as by imprint measurements. A typical imprint of the FLASH beam on a PMMA substrate in the BL1 focus position is shown in Figure 2.

The modular and flexible design of the CAMP end station allows combining various spectrometers and detectors, e.g. large-area pnCCD photon-detectors and momentum imaging ion and electron spectrometers (Fig. 3), with a large variety of targets ranging from gas-phase atoms, molecules, and clusters to nano-particles and viruses in aerosol and liquid jets, and solid-state samples. Dedicated laser in-coupling optics and diagnostics for the FLASH pump-probe laser are also available.

The pnCCD photon detectors

Two large-area (78 x 74 mm^2), single-photon counting 1-Megapixel pnCCD detectors (75 x 75 μm^2 pixel size) can be installed

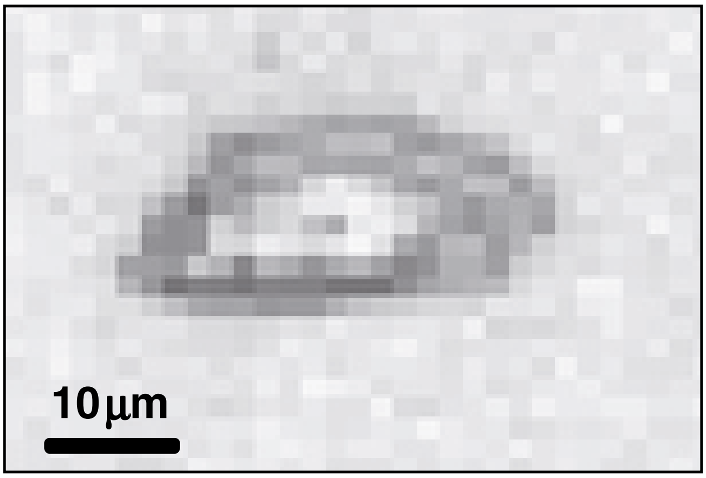

Figure 2

Imprint of the FLASH beam on a PMMA substrate in the focus of BL1. The elongated shape in the horizontal direction is due to the angle of 60° in which the substrate was mounted with respect to the FEL beam and which stretches the imprint by a factor of two in the horizontal direction.

Figure 3

View into the CAMP chamber with the electron-ion coincidence spectrometer (left) and the pnCCD photon detectors (right).

into the CAMP end station. These detectors collect scattered and fluorescent photons with high quantum efficiency and an energy resolution of 40 to 200 eV between <100 eV and 25 keV at a frame read-out rate up to 200 Hz. A variable-sized gap with a hole in the centre of the first CCD camera allows the direct FEL beam (and a high-power pump-probe laser, if applicable) to pass through the detector, while the small-angle scattering signal within the area of the hole can be detected on the second CCD, which has a fixed-diameter hole for the direct FEL beam. Both pnCCD cameras can be removed individually if they are not needed in order to provide more flexibility inside the chamber.

Electron and ion spectrometers

A suite of doubled-sided electron and ion imaging spectrometers (time-of-flight, velocity map imaging (VMI), and COLTRIMS / "reaction microscope" spectrometers) are available to detect ions and / or electrons of up to several hundred eV kinetic energy covering the full 4π solid angle. Special conical electrodes of the spectrometers provide an unrestricted line-of-sight from the interaction region to the pnCCD detectors. The spectrometers use 80-mm MCP detectors that can be operated with delay-line anodes for coincident, momentum-resolved single particle detection or with MCP / phosphor screen detectors that are read-out by CCD cameras.

Gas jets and particle injectors

A variety of (supersonic) gas and cluster jets, liquid and droplet jets, aerodynamic lenses as well as fixed-target holders have been developed and adapted to fit the CAMP chamber. A supersonic gas jet is available to all CAMP users, other jets and injectors have to be provided by the user or brought in through collaborations.

Contact: Daniel Rolles, daniel.rolles@desy.de
Benjamin Erk, benjamin.erk@desy.de

Authors

Daniel Rolles[1,2], Benjamin Erk[1,2], Jan P. Müller[3], Angad Swiderski[1], Rolf Treusch[1], Cédric Bomme[1], Evgeny Savelyev[1], Rebecca Boll[1,2,4], Barbara Keitel[1], Elke Plönjes[1], Günter Brenner[1], Siarhei Dziarzhytski[1], Marion Kuhlmann[1], Stefan Düsterer[1], Kai Tiedtke[1], Jonathan Correa[1], Heinz Graafsma[1], Thomas Tilp[5], Lars Gumprecht[5], Henry Chapman[5], Mario Sauppe[2], Daniela Rupp[2], Thomas Zeschke[6], Frank Siebert[6], Robert Hartmann[7], Lothar Strüder[7], Günter Hauser[8], Simone Techert[1,9], Ilme Schlichting[10], Stefan Eisebitt[3], Joachim Ullrich[2,4,11], Robert Moshammer[2,4], Thomas Möller[3]

1. Deutsches Elektronen-Synchrotron DESY, 22607 Hamburg, Germany
2. Max Planck Advanced Study Group at Center for Free-Electron Laser Science (CFEL), 22607 Hamburg, Germany
3. Technische Universität Berlin, 10623 Berlin, Germany
4. Max-Planck-Institut für Kernphysik, 69117 Heidelberg, Germany
5. Center for Free-Electron Laser Science (CFEL), DESY, 22607 Hamburg, Germany
6. Helmholtz-Zentrum Berlin für Materialien und Energie, 12489 Berlin, Germany
7. PNSensor GmbH, 81739 München, Germany
8. Max-Planck-Institut für extraterrestrische Physik, 85741 Garching, Germany
9. Max-Planck-Institut für biophysikalische Chemie, 37077 Göttingen, Germany
10. Max-Planck-Institut für medizinische Forschung, 69120 Heidelberg, Germany
11. Physikalisch-Technische Bundesanstalt, 38116 Braunschweig, Germany

References

1. L. Strüder et al., "Large-format, high-speed, x-ray pnCCDs combined with electron and ion imaging spectrometers in a multipurpose chamber for experiments at 4th generation light sources", Nucl. Instr. and Meth. in Phys. Res. A 614, 483-496 (2010).
2. B. Rudek et al., "Ultra-efficient ionization of heavy atoms by intense X-ray free-electron laser pulses", Nature Photonics 6, 858-865 (2012).
3. T. Gorkover et al., "Nanoplasma dynamics of single large xenon clusters irradiated with superintense X-ray pulses from the Linac Coherent Light Source free-electron laser", Phys. Rev. Lett. 108, 245005 (2012).
4. H. N Chapman et al., "Femtosecond X-ray protein nanocrystallography", Nature 470, 73-77 (2011).
5. N. D. Loh et al., "Fractal morphology, imaging and mass spectrometry of single aerosol particles in flight", Nature 486, 513-517 (2012).
6. M. M. Seibert et al., "Single mimivirus particles intercepted and imaged with an X-ray laser", Nature 470, 78-81 (2011).
7. S. Hau-Riege et al., "Ultrafast disintegration of X-ray-heated solids", Phys. Rev. Lett. 108, 217402 (2012).
8. L. F. Gomez et al., "Shapes and vorticities of superfluid helium nanodroplets", Science 345, 906 (2014).
9. B. Erk et al., "Imaging Charge Transfer in Iodomethane upon X-Ray Photoabsorption" Science 345, 288 (2014).
10. J. Küpper et al., "X-ray diffraction from isolated and strongly aligned gas-phase molecules with a free-electron laser", Phys. Rev. Lett. 112, 083002 (2014).
11. photon-science.desy.de/facilities/flash/photon_diagnostics/wavefront_sensor/index_eng.html

Smooth operator.

A fast sample changing robot for high-throughput macromolecular crystallography at beamline P11

The "Bio-Imaging and Diffraction Beamline" P11 is dedicated to structural investigations of biological samples. The beamline provides two different experiments: an X-ray crystallography endstation and an X-ray microscope.

Basis of design for beamline P11 was to make full use of the outstanding source properties of the PETRA III storage ring and to provide a state-of-the-art endstation for macromolecular X-ray crystallography. The flexible X-ray optics of beamline P11 allow for tailoring the beam properties to the needs of the experiment: A micrometre sized beam is available for structure determinations from microcrystals. For the investigation of large molecular complexes and viruses a large parallel beam can be generated. Common to both configurations is the high photon flux of more than 1×10^{13} ph/s at the sample position. In combination with a PILATUS 6M-F detector installed at P11 a full data set can be typically collected in less than two minutes. With such short data collection times and a highly automated software sample exchange time became a limiting factor for efficient use of beamline P11. The new sample changing robot makes beamline P11 ideally suited for high-throughput crystallography experiments and allows for screening a large number of samples in a short time in order to identify and collect data from the best diffracting crystals.

For X-ray diffraction experiments crystals are typically mounted in nylon loops which are attached to a so-called magnetic cap as shown in Fig. 1A. In order to prevent crystals from dehydration and to reduce radiation damage effects, samples are stored in liquid nitrogen (LN_2) and kept at cryogenic temperatures for data collection using e.g. so-called uni-pucks (see Fig. 1B). During sample loading these cryogenic temperatures have to be maintained in order to prevent crystal degradation.

Since commercially available sample changing robots were too slow, provided not enough storage capacity for a large number of samples, and suffered from icing of the crystals it was decided to develop a new sample changing robot for beamline P11 [1]. The sample changer is already fully implemented into the experimental infrastructure of beamline P11 and in user operation since December 2013. A picture of the installation at P11 is shown in Fig. 2A. It consists of a large storage Dewar with a load capacity of 368 samples. The robot is based on a Stäubli-TX60L robotic arm equipped with an in-house developed flexure-based sample gripper with integrated sample cooling. In the following the individual components are described in more detail:

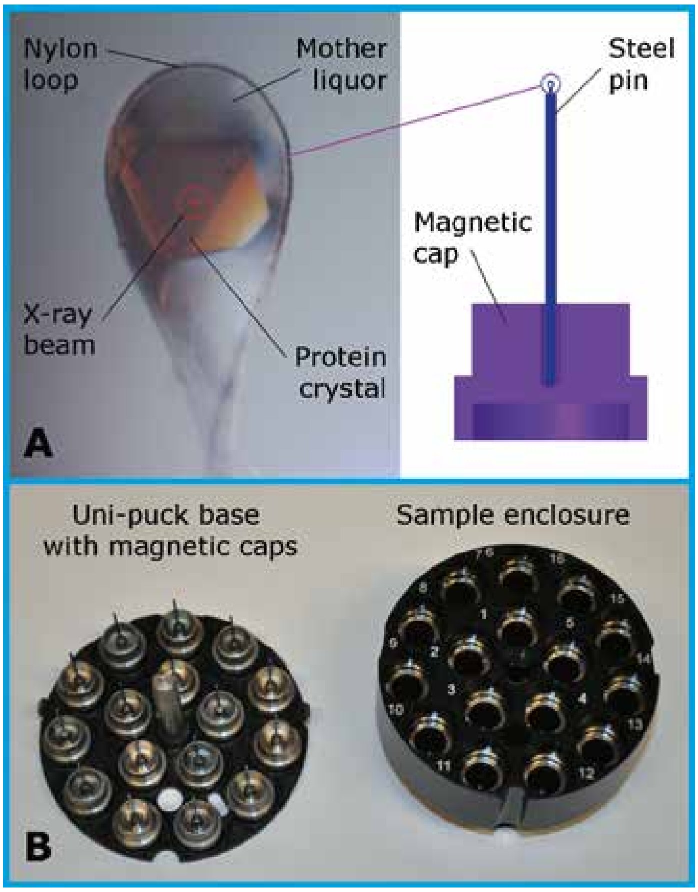

Figure 1

A) Macromolecular crystals are mounted in a nylon loop (left). The surrounding mother liquor prevents the crystals from dehydration. The loop is located on the tip of a steel pin which is inserted into the magnetic base (right).

B) Uni-pucks used for cryogenic transfer and sample storage.

Large capacity storage Dewar

The P11 storage Dewar is based on the universal puck (uni-puck) standard (see Fig. 1B). Here 16 magnetic caps carrying the samples are mounted on one common magnetic base, the so-called uni-puck base [2]. For transport from the home lab to the experiment the uni-puck bases are protected with a so-called sample enclosure (puck). The base plate located on the bottom of our storage Dewar can carry up to 23 of these uni-pucks (see Fig. 2B). So the Dewar has a total load capacity of 23 × 16 = 368 samples which is enough to perform measurements for several hours without the need to load the Dewar with new samples.

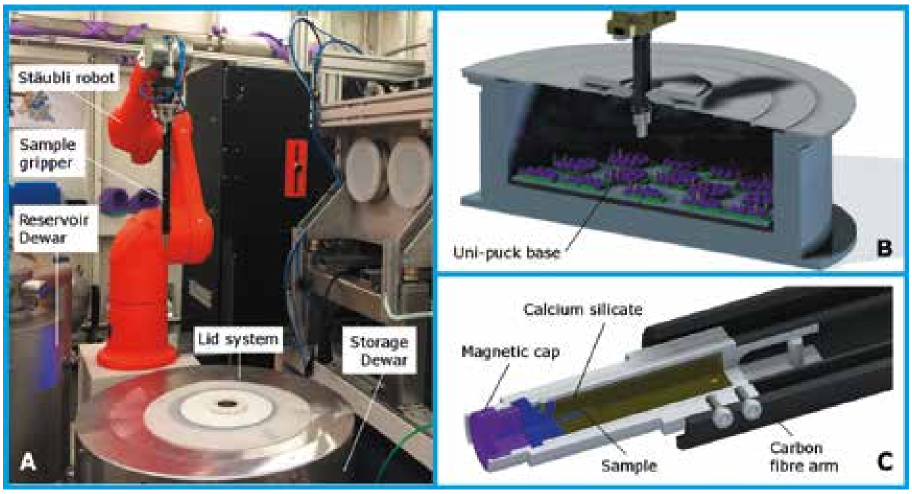

Figure 2

A) Automatic sample changing robot installed at the P11 crystallography endstation;

B) Uni-pucks stored under LN_2 in the large sample Dewar;

C) Sample gripper equipped with calcium silicate for cryogenic sample cooling during mounting.

In order to keep the crystals at cryogenic temperatures they are covered with LN_2. The LN_2 level in the storage Dewar is kept at a constant level by continuous refilling from a phase separator located on the roof of the P11 experimental hutch. Filling is performed indirectly via a second transfer Dewar (reservoir Dewar) which is attached to the storage Dewar by a communicating vessel. Due to this indirect filling the cold exhaust gas is not released into the storage Dewar where it would cause extensive icing of the samples. In order to prevent ice formation the storage Dewar is covered with a flexible lid system which can be easily moved by the gripper during sample-picking. For effective operation the lid opening is identified by pattern recognition using a CCD camera. To further prevent ice formation in the storage Dewar it is permanently floated with nitrogen gas (T = 25 °C) and the outer rim of the Dewar is constantly heated.

Robotic arm and sample gripper

The sample gripper is mounted on the robotic arm and used to grip the magnetic caps and to transfer them to the goniometer whilst maintaining cryogenic temperatures. In contrast to other grippers our design allows sample gripping from beneath as illustrated in Fig. 2C. This requires very accurate positioning but reduces the holding force to a minimum which allows using relatively thin carbon fibre arms with a much lower heat conductivity than the steel arms commonly used. The use of low thermal conductivity materials reduces the heat transfer from the gripper into the Dewar and thereby significantly reduces the LN_2 consumption. The gripping mechanism is operated with pressurized air. The joints for the gripper are based on flexural hinges which are ideally suited for operation at cryogenic temperatures since their action is based on elastic deformation only.

To keep the sample at cryogenic temperatures during sample transfer the gripper head is fitted with a calcium silicate tube acting as an LN_2 reservoir. Whenever the gripper is inserted into the LN_2 in order to grip a sample the reservoir is filled with LN_2 and the sample is surrounded by this reservoir. Once the gripper is moved out of the Dewar the temperature raises and cold nitrogen gas is slowly released from the calcium silicate. This keeps the sample at cryogenic temperatures during the mounting procedure and also prevents ice formation on the sample surface by forming a continuous cold gas stream surrounding the sample. After numerous sample mounts condensation of air moisture can lead to ice formation on the cold gripper surface. For deicing the gripper is automatically exposed to a stream of hot air.

The robotic arm is fully integrated into the Tango control software environment and into the P11 data collection software. Several safety interlocks are in place for equipment protection. For personnel safety robot operation is linked to the P11 interlock system.

After X-ray data collection the sample is transferred back to the storage Dewar (demounting). Overall an automatic sample exchange at P11 can be realized in less than 25 seconds. A video showing the mounting and demounting and also the deicing procedure of the gripper can be found at [3].

In summary, the P11 sample changing robot allows rapid sample exchange in a very reliable way in less than 25 seconds. This compares very well to typical data collection times of 120 seconds and below. Icing of the crystals is prevented in a very efficient way by a continuous release of cold nitrogen gas in the gripper head during sample transfer onto the goniometer. The large capacity of the storage Dewar allows for several hours of operation before loading new samples.

Contact: Anja Burkhardt, anja.burkhardt@desy.de
Alke Meents, alke.meents@desy.de

Authors

Nicolas Stübe, David Kellermann, Jan Meyer, Pontus Fischer, Bernd Reime, Tim Pakendorf, Julia Danckert, Anja Burkhardt, and Alke Meents

Deutsches Elektronen-Synchrotron DESY, 22607 Hamburg, Germany

References

1. D. Kellermann, “Entwicklung einer Robotersteuerung für den automatischen Wechsel tiefgefrorener Proben”, Bachelor thesis, Hamburg University of Applied Sciences
2. smb.slac.stanford.edu/robosync/Universal_Puck/
3. www.youtube.com/watch?v=G5iZYSULUy4

New material by high pressure synthesis at PETRA III.

The new offline large volume press instrument

High-pressure high-temperature synthesis is one of the most important techniques to produce new materials, especially super-hard materials [1]. An offline large volume press (LVP) laboratory has been setup in the former DORIS III experimental hall and is available since May 2013. The LVP laboratory which is part of the PETRA III extension project includes a press which allows for synthesizing samples under high pressure up to 20 GPa and temperatures up to 2000 °C (see Fig. 1). The LVP laboratory consists of several instruments: the offline LVP (Max Voggenreiter, mavo press LPR 1000-400/50), machining tools to prepare high-pressure cells, and a desk-top X-ray diffraction instrument (Rigaku, MiniFlex 600).

The LVP instrument has eight tungsten carbide (WC) anvils which squeeze an octahedral high-pressure cell (Fig. 2a) [2]. The anvil assembly is located in a split cylinder that is composed of six wedges (Fig. 2b and c). The split cylinder with the anvil assembly is compressed by a die and pistons (Fig. 2d).

Figure 1

The offline large volume press instrument in the former DORIS III experimental hall.

Figure 3 shows a schematic illustration of a representative high-pressure cell. The high-pressure cell has a cylindrical resistive heater ($LaCrO_3$). A sample (powder or a bulk chunk) is usually embedded into a metal capsule (gold or platinum) and magnesia is used for electrical insulation between the heater and the sample capsule. Molybdenum disks and rods are used as electrodes.

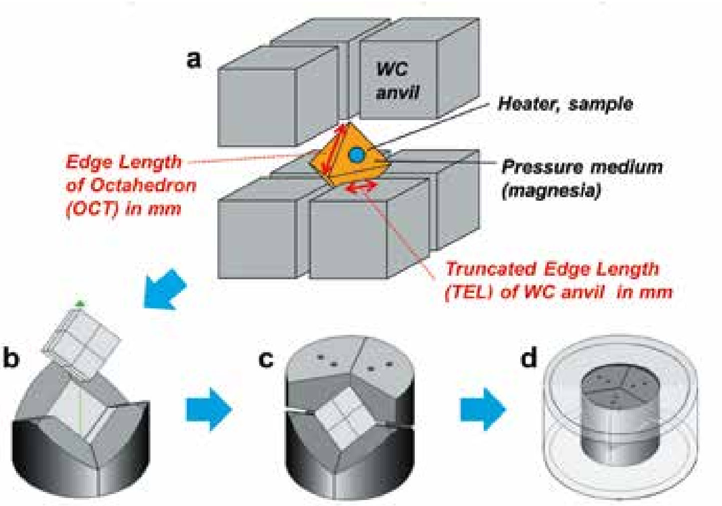

Figure 2

High-pressure anvil assembly and a split cylinder system.

The generated pressure is a function of the truncated edge length (TEL) of the WC anvils: the smaller the TEL, the higher the pressure. Three types of high-pressure cells corresponding to different pressure ranges are available: an 18/11 cell (an edge length of an octahedral pressure medium is 18 mm and TEL is 11 mm), a 14/7 cell, and a 10/4 cell.

Figure 4 shows relationships between generated pressure and oil pressure of the hydraulic system. 600 bar corresponds to 900 tonf. The 18/11 cell is suitable for generating pressures of 5–10 GPa with a rather large sample volume. Typical sample dimensions are 4.5 mm in diameter and 3 mm in height. The 14/7 cell is suitable for a pressure range of 10–16 GPa. The 10/4 cell is available for generating pressure of ~20 GPa. In this case, the sample chamber is relatively small: 1.5 mm in diameter and 1.2 mm in height.

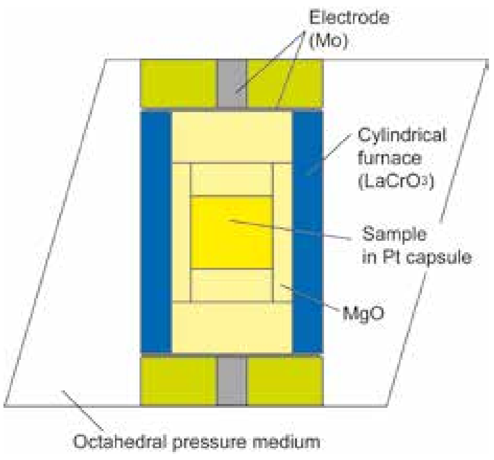

Figure 3

A schematic illustration of a high-pressure cell.

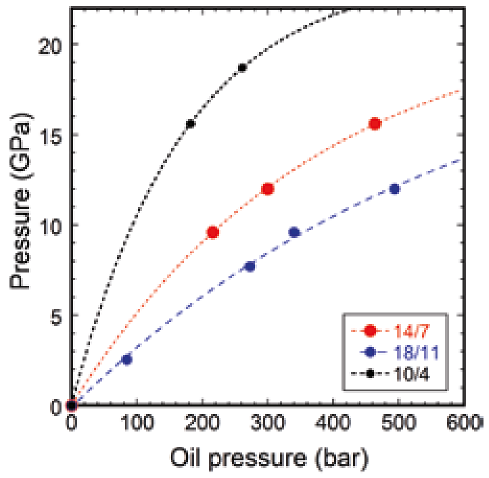

Figure 4

Pressure generation curves of the three high-pressure cells of different dimensions.

Figure 5 shows a representative relationship between input power and generated pressure for the 14/7 cell at 15.6 GPa. The temperature (T) was measured by a thermocouple consisting of W0.95Re0.05–W0.74Re0.26. T increases almost linearly with the input power up to temperatures above 2000 °C. In all the cell assemblies we confirmed temperature generation of more than 2000 °C.

Using the newly installed LVP system, we can synthesize high-pressure samples up to 20 GPa and 2000 °C. Recently, we have used the LVP successfully to synthesize stishovite, SiO_2 at 15.6 GPa and 1100–2000°C [3].

Contact: Norimasa Nishiyama, norimasa.nishiyama@desy.de
Eleonora Kulik, eleonora.kulik@desy.de

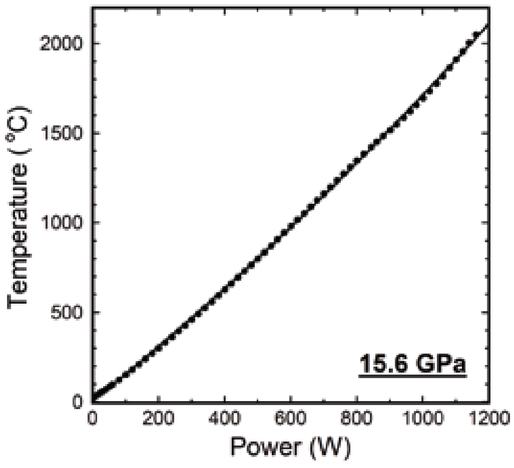

Figure 5

A representative power vs. temperature plot (14/7 cell at 15.6 GPa).

Authors

N. Nishiyama and E. Kulik
Deutsches Elektronen-Synchrotron DESY, 22607 Hamburg, Germany

References

1. F. P. Bundy, H. T. Hall, H. M. Strong, R. H. Wentorf, “Man-made diamonds”, Nature 176, 51-55 (1955).
2. N. Kawai, S. Endo, “The generation of ultrahigh hydrostatic pressures by a split sphere apparatus”, Rev. Scientific Instruments 41, 1178-1181 (1970).
3. N. Nishiyama et al., “Fracture-induced amorphization of polycrystalline SiO_2 stishovite: a potential platform for toughening in ceramics”, Scientific Reports 4, 6558 (2014).

NeXus integration at PETRA III.

The deployment of a common file format including configuration procedures and user interfaces

Experimental data should be recorded in a way that the information necessary to understand the measurement is captured in the output files. This comprises the source parameters, the optical components of the beamline and all details of the sample environment. All information is needed for a comprehensive analysis and visualization of the measured data. The biggest part of the data is generated by the readout of detectors, motion controllers and other electronics equipment. However, information describing the experimental setup and the precise experimental procedure is of equal importance. The output files should also contain details about the facility, the beamtime and the scientists involved. To allow for a verification of published results, derived data have to be accompanied by a documentation of how they were achieved. NeXus/HDF5 [1, 2] has been chosen as the standard data format for the PETRA III experiments at DESY because it is capable to manage the aforementioned raw/derived data and associated metadata. The work described in this report has been carried out within the PaN-data ODI [3] project which is an initiative of European photon and neutron sources.

The following paragraphs focus on integration issues. The central part is the configuration of the NeXus files which is a complex task especially for experimental stations with frequently changing setups. It is discussed how the configuration is prepared depending on the applied experimental technique and how the data acquisition process implements the NeXus configuration.

Data acquisition process

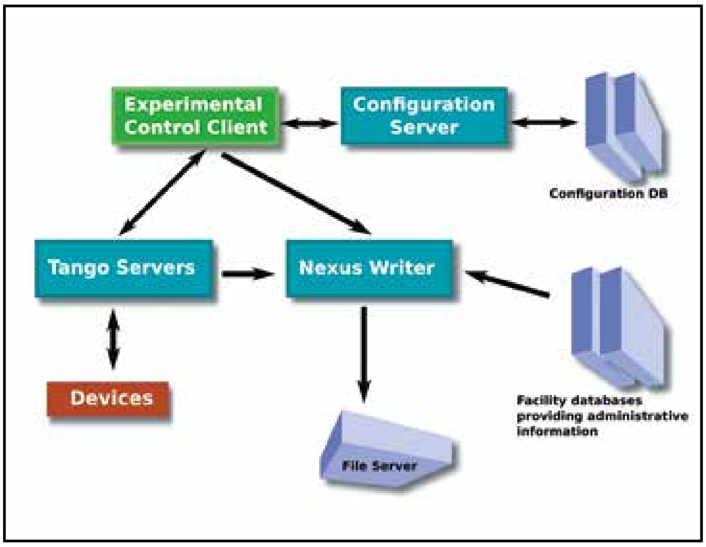

Figure 1

Data acquisition framework

The PETRA III data acquisition system is a modular framework consisting of applications and servers that communicate through standardized interfaces (Fig. 1). *Experiment control clients (ECC)* are used by researchers to conduct measurements. They have graphical and command line interfaces. Scripts may also act as ECCs.

Since *Tango* [4] is the communication layer all devices are exported via Tango servers with interfaces consisting of properties, commands and attributes. Attributes are of special interest because they provide data being read by the NeXus Writer, e.g. motor positions, counter readings or MCAs.
The *NeXus Writer* is a Tango server which opens NeXus files, creates the internal structures and fills them with data coming from the ECC, other Tango servers, database queries or Python scripts. The NeXus Writer is controlled by the ECC.
The *Configuration Server* is a Tango server managing the information necessary to build the structure of the NeXus files. It has access to a configuration database. The *facility database* provides administrative information stored in the NeXus files.

NeXus configuration

The key idea of the NeXus configuration is that the internal file structure is expressed in terms of components and data sources. Components are objects constructed of NeXus base classes representing simple devices (e.g. counter, MCA), composite devices (e.g. molecular beam epitaxy chambers mounted in a beam path) or structures only holding metadata (e.g. mandatory metadata). The available data sources are listed below. The whole concept is inspired by the following correspondence between scientific notions and technical terms:

measurement ↔ file
experimental setup ↔ NeXus configuration
device ↔ component
device attribute ↔ data source

The central point is the relation between devices and components. Devices are selected or de-selected depending on the experimental technique applied. Likewise components are inserted into a configuration or deleted from it.

Components consist of:
Names identify the component.
Data sources specify where the data to be stored in NeXus

fields have to be fetched from. The available data source types are: Tango attributes, database queries, data supplied by the experiment control client (ECC) and output of python scripts. *Strategies* indicate when the data have to be captured. Four strategy types are implemented: INIT, STEP, FINAL and POSTRUN. A NeXus field or attribute is marked with the POSTRUN tag, if the information is inserted by a subsequent data processing step.
NeXus paths specify the absolute position of the data inside the file. It is expressed in terms of NeXus groups.
Since components contain absolute path names, they can be merged to obtain the complete configuration. In practice, NeXus files typically consist of 20 to 40 components.

The preparation of components and data sources is a rather tedious task and therefore an application has been developed that creates new components and data sources, edits existing ones or links data sources to components.

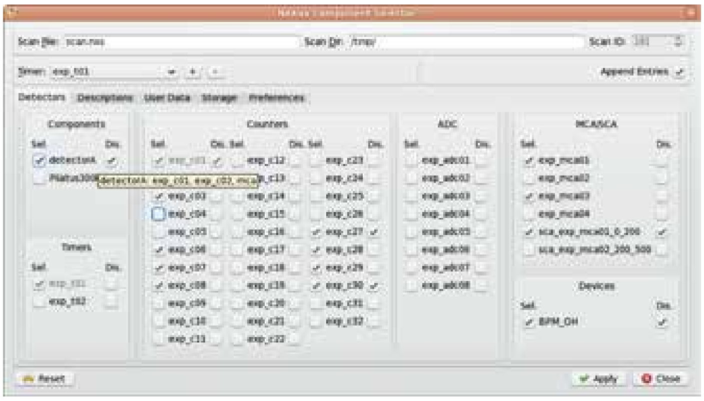

Scan File: scan.nxs
Scan Dir: /tmp/
Timer: exp_t01

Figure 2

Component Selector

NeXus integration

Before a measurement is started components (aka devices) have to be selected. This can be done by scripts from the command line or by a graphical user interface, the Component Selector (CS, Figure 2). Components with multiple data sources appear in the leftmost part of the window. The other components are distributed in the frames labelled Counters, ADC, MCA, etc. Simple components may be part of composite components. As a consequence, selecting a composite component may implicitly select one or more simple components. The CS makes this dependency visible to the user.

Ideally all devices are contained in components ensuring that they have sensible NeXus paths and meaningful metadata associated with them. In practice this is not always possible. In order to handle this situation, dynamical components have been introduced. They are automatically created whenever a selected device is not covered by a component. The CS also offers a window for user-supplied metadata like title, sample name and comments.

The selected components are stored on a dedicated Tango server making them available for experiment control clients. The most important of these is Sardana [5] which has a full implementation of the described NeXus file production. Other experiment control clients like Python scripts or Online [6] can also create NeXus files by means of the described framework.

Mandatory metadata

Certain metadata contained in NeXus files are common to all PETRA III experiments, the mandatory metadata (MMD). They comprise the beamtime id, the beamline, a title, etc. This information is used by the ingestion procedure inserting files into the metadata catalogue where the files can be discovered and downloaded by scientists.

Conclusion

At PETRA III, a framework supporting the production of NeXus/HDF5 files has been developed and implemented. A configuration procedure based on components and data sources allows for a complete description of the data stored. Interfaces to all relevant experiment control clients are provided.

Contact: Jan Kotanski, jan.kotanski@desy.de
Thorsten Kracht, thorsten.kracht@desy.de

References

1. NeXus, www.nexusformat.org
2. HDF5, www.hdfgroup.org
3. PaN-data ODI, pan-data.eu
4. Tango Control System www.tango-controls.org.
5. J. Klora, T. Coutinho et al., “The architecture of the ALBA Control System”, Proceedings NOBUGS (2008).
6. Online, Data Acquisition and Beamline Control, photon-science.desy.de/research/technical_groups/experiment_control/index_eng.html

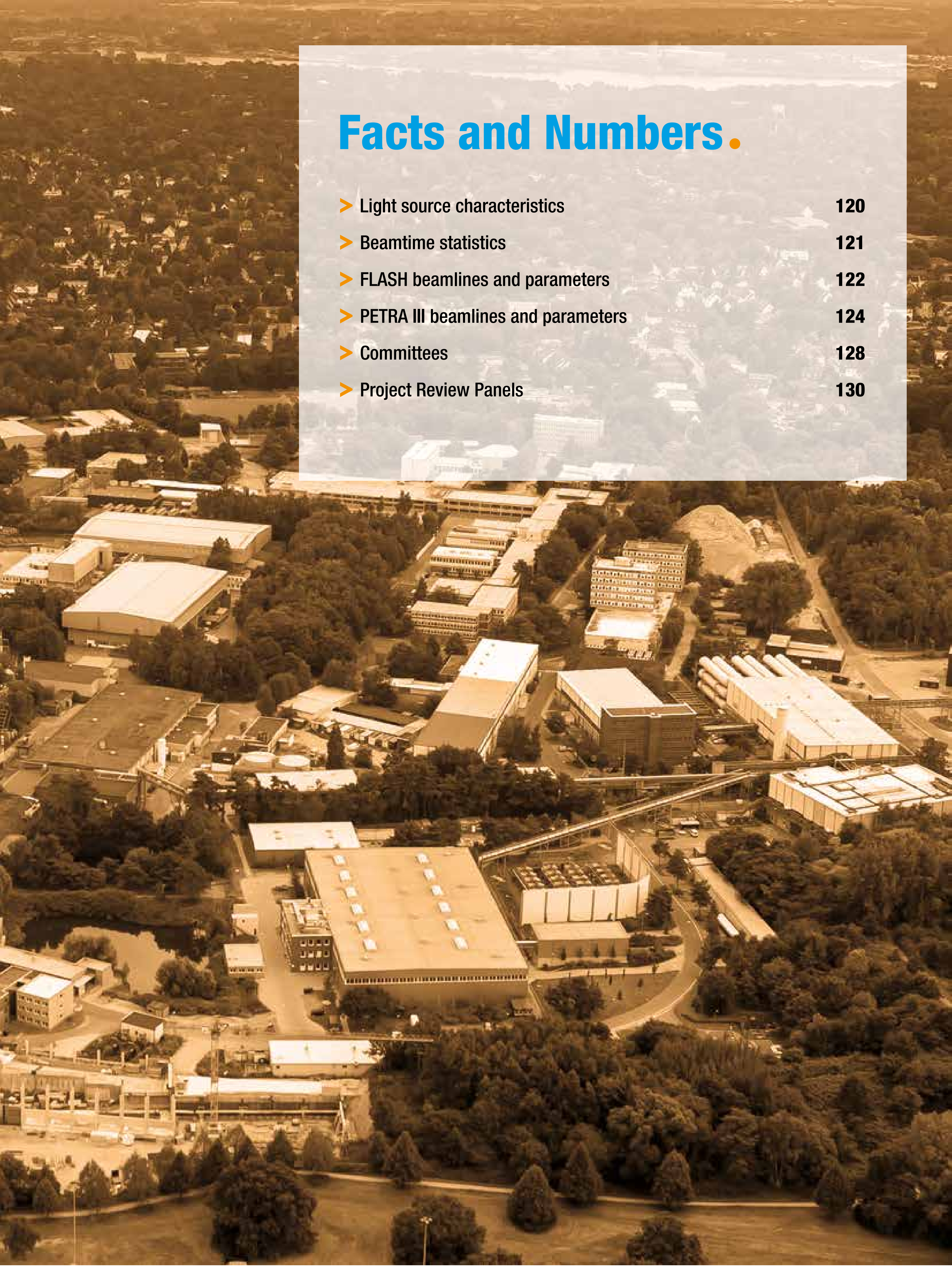

Facts and Numbers.

> Light source characteristics 120

> Beamtime statistics 121

> FLASH beamlines and parameters 122

> PETRA III beamlines and parameters 124

> Committees 128

> Project Review Panels 130

Light source characteristics.

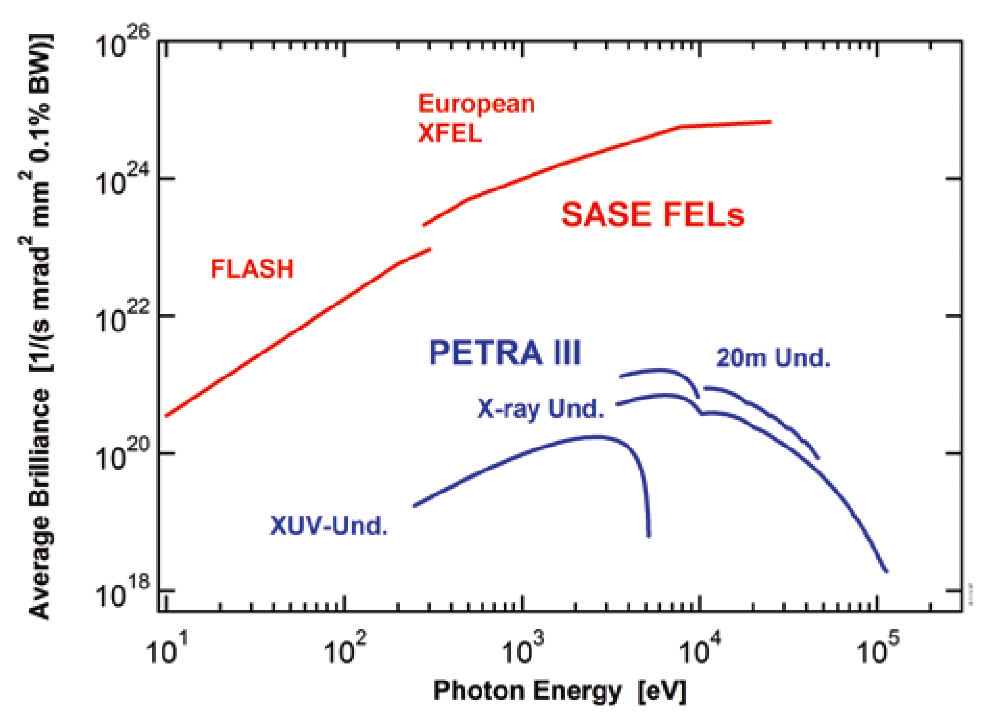

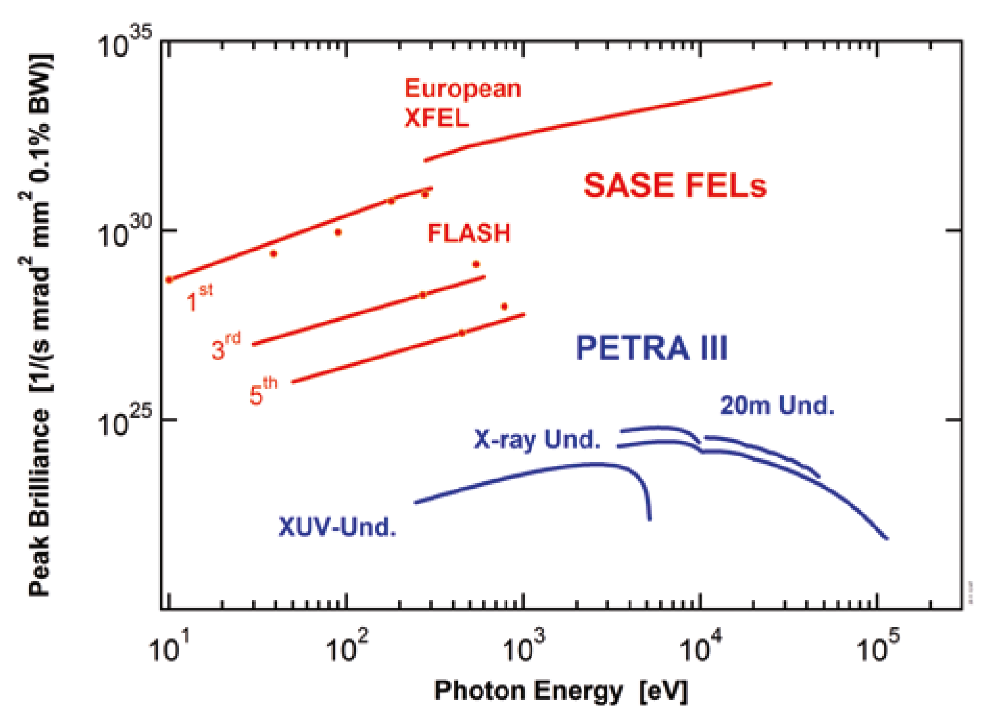

Average and peak brilliance values for FLASH, PETRA III and European XFEL. Peak brilliance values are given for the optimum bunch charge at the respective photon energies. Dots represent experimentally measured values at FLASH.

Beamtime statistics 2014.

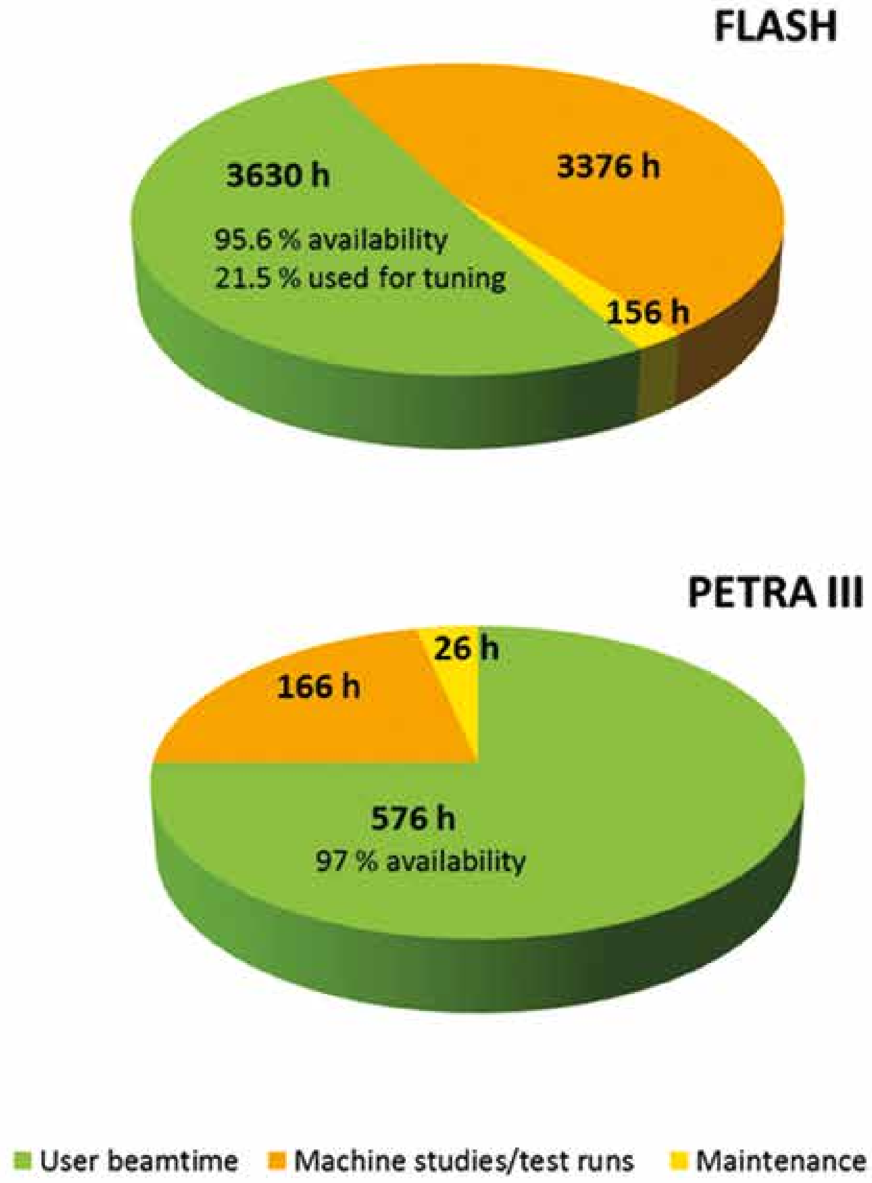

Operation periods 2014

FLASH	01.01. - 01.12.2014 not included: - last user beamtime block in December: ca. 500 h - shutdown and commissioning: 861 h
PETRA III	02.01. - 03.02.2014 shutdown for the rest of the year 2014

FLASH.

Beamlines and parameters

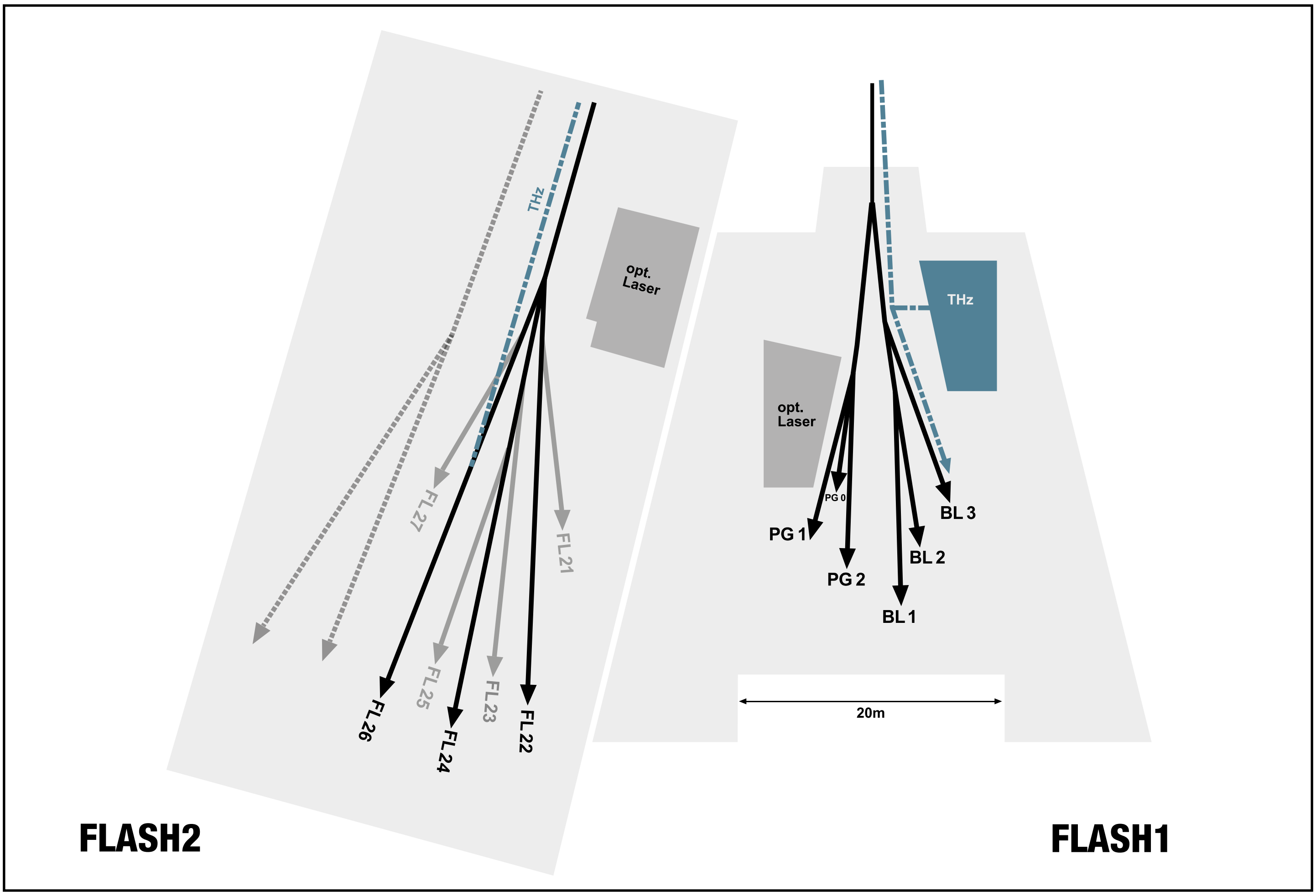

Machine parameters FLASH

Electron energy (max.)	1.25 GeV
Length of the facility	315 m
Normalized emittance	1.5 mm mrad (rms)
Emittance	0.6 nm rad (rms)
Bunch charge	0.1 – 1 nC
Peak current	1 – 2 kA
Bunches per second (typ. and max.)	300 and 6000

FLASH Lasing parameters

Photon energy (max.)	301 eV (fundamental)
Wavelength (min.)	4.12 nm (fundamental)
Pulse duration (FWHM)	50 – 200 fs
Peak power	1 – 3 GW
Bunch energy (average)	up to 500 μJ
Photons per bunch	10^{11} – 10^{13}
Average brilliance	10^{17} – 10^{21} photons/sec/mm^2/mrad^2/0.1%
Peak brilliance	10^{29} – 10^{31} photons/sec/mm^2/mrad^2/0.1%

FLASH beamlines

FLASH1

BL 1	non-monochromatic FEL photons Kirkpatrick-Baez (KB) focusing optics, FEL focal spot of ~3 µm x 4 µm (FWHM)	_TU Berlin*_
	split-and-delay unit for XUV pump - XUV probe experiments (planned, up to ns delay)	_TU Berlin*_
	optional pump - probe experiments using FLASH1 optical laser system	
	permanent end station: multipurpose CAMP chamber with two pnCCD detectors, electron and ion spectrometers and collinear incoupling optics for optical laser, optional supersonic gas jet (as sample)	
BL 2	non-monochromatic FEL photons focused to ~20 µm/unfocussed beam size ~5-10 mm (FWHM, depending on wavelength)	
	XUV beam splitter with variable delay (-3 ps to 15 ps) for photon diagnostics and XUV pump - XUV probe experiments	_Univ. Münster*_
	optional pump-probe experiments using FLASH1 optical laser system	
	about 3 x 4 m footprint for user-provided end station	
BL 3	non-monochromatic FEL photons, spectral range: >4.5 nm (carbon coated optics) focused to ~20 µm/unfocussed beam size ~5-10 mm (FWHM, depending on wavelength)	
	optional pump - probe experiments using FLASH1 optical laser system	
	optional pump - probe experiments using **THz radiation** (unique to BL3): - tunable: 10 – 230 µm; up to 100 µJ/pulse; ~10 % bandwidth - broadband at 200 µm, up to 10µJ/pulse; ~100 % bandwidth - synchronized and phase stable to X-ray pulses (down to 5 fs) - delivered to the experiment via vacuum beamline as: (i) ultra-high vacuum (~10^{-8} mbar), shorter delay between THz and X-ray (~4 m path difference), can accommodate up to 0.3 m wide setup (ii) high vacuum (~10^{-6} mbar), longer delay between THz and X-ray (~7 m path difference); can accommodate up to 2 m wide setup	
	about 3 x 4 m footprint for user-provided end station	
PG1	high resolution plane grating XUV monochromator (SX 700 type, <10^{-4} bandwidth, carbon coated optics): - variable combination of photon flux and resolution (from high flux to high resolution) - controlled temporal-spectral properties at moderate resolution for pump - probe experiments - high photon flux with harmonic filtering Kirkpatrick-Baez (KB) refocusing optics, FEL focal spot of 5 µm (vertically)	_Univ. Hamburg*_
	permanent end station: two-stage VUV-Raman spectrometer for high-resolution measurements close to Rayleigh line	_Univ. Hamburg*_
PG2	uses the same monochromator as PG1 50 µm focus	
	XUV beamsplitter with variable time delay (±6 ps) for time resolved studies	_Univ. Hamburg*_
	optional pump - probe experiments using FLASH1 optical laser system	
	about 3 x 4 m platform for user-provided end station	

FLASH1 optical / NIR laser system for pump - probe experiments

10 Hz	single pulse 3.5 mJ, 90 fs synchronization to FEL better than 100 fs r.m.s.
Burst-mode	up to 400 pulses / burst 20 µJ, 110 fs synchronization to FEL better than 100 fs r.m.s.

FLASH2 - under commissioning -

FL22	wavelength range: 6 – 40 nm with 6σ, up to 80 nm with 3σ acceptance	
FL24	wavelength range: 4 – 16 nm for the fundamental with 6σ acceptance, for harmonics down to 0.8 nm	
	grazing incidence (1.8 °) split-and-delay unit with ±12 ps delay	_Univ. Münster_
FL26	wavelength range: 6 – 40 nm with 6σ, up to 80 nm with 3σ acceptance	
	permanent end station: - split multilayer mirror & reaction microscope (REMI) for time-resolved spectroscopy - grazing incidence delay-line and refocusing optics for a second experiment in-line behind the REMI (under development)	_MPI-K Heidelberg_

All FLASH beamlines provide online photon diagnostics for intensity, wavelength, and beam position; fast shutter, aperture and filter sets.

*We would like to acknowledge all contributions to instrument development and operation provided within the framework of BMBF Verbundforschung.

PETRA III.

Beamlines and parameters

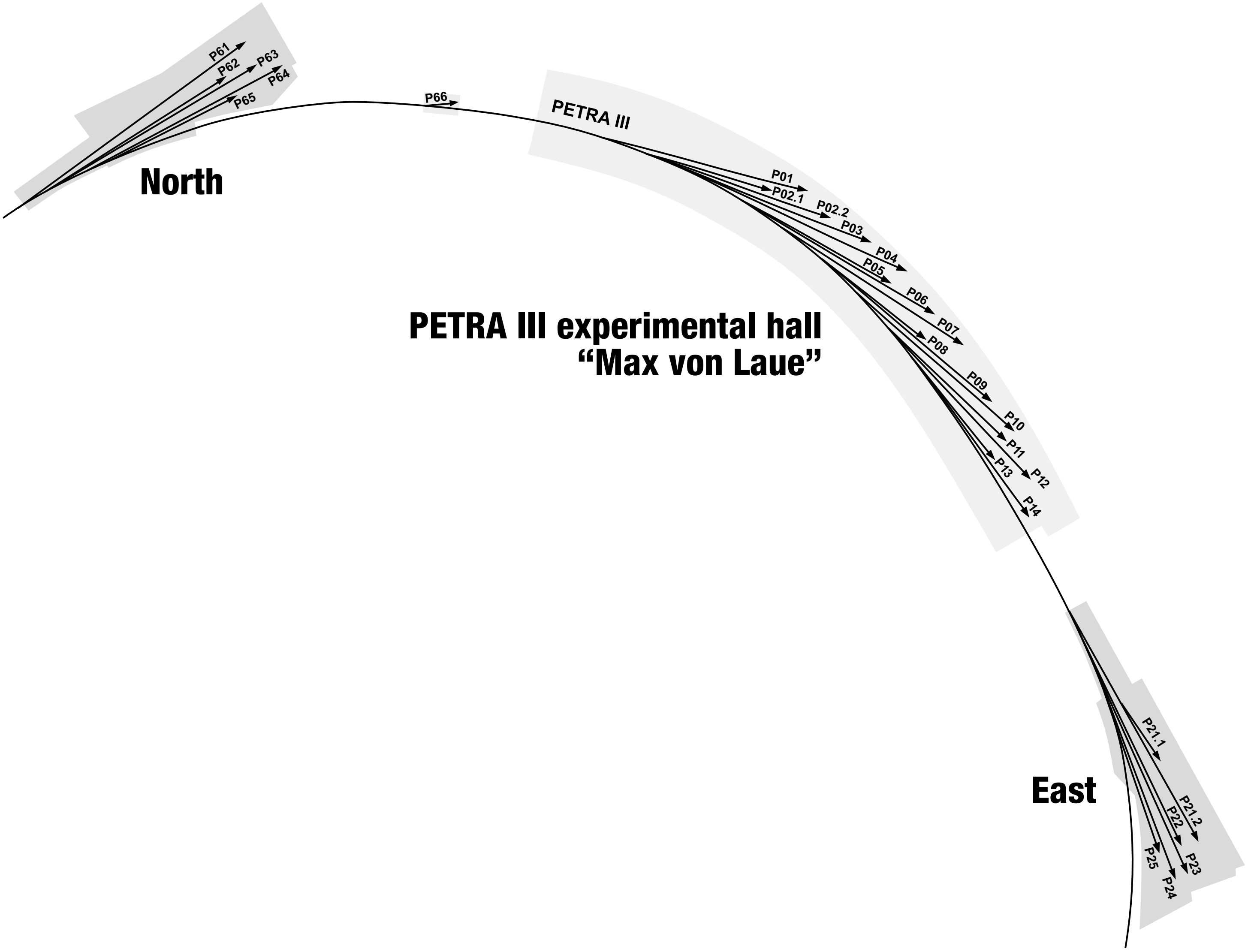

Machine parameters PETRA III

Electron energy	6.08 GeV
Circumference of the storage ring	2304 m
Number of buckets	3840
Number of bunches	960, 60, and 40
Bunch separation	8 ns, 128 ns, and 192 ns
Electron beam current	100 mA (top-up)
Horizontal positron beam emittance	1.0 nmrad (rms)
Coupling factor	1.0%
Vertical electron beam emittance	0.01 nmrad (rms)
Electron beam energy spread	0.1% (rms)
Horizontal x vertical beam size at 5 m undulator (12 keV, high β section)	141 μm x 5.2 μm
Horizontal x vertical beam size at 5 m undulator (12 keV, low β section)	36 μm x 5.7 μm

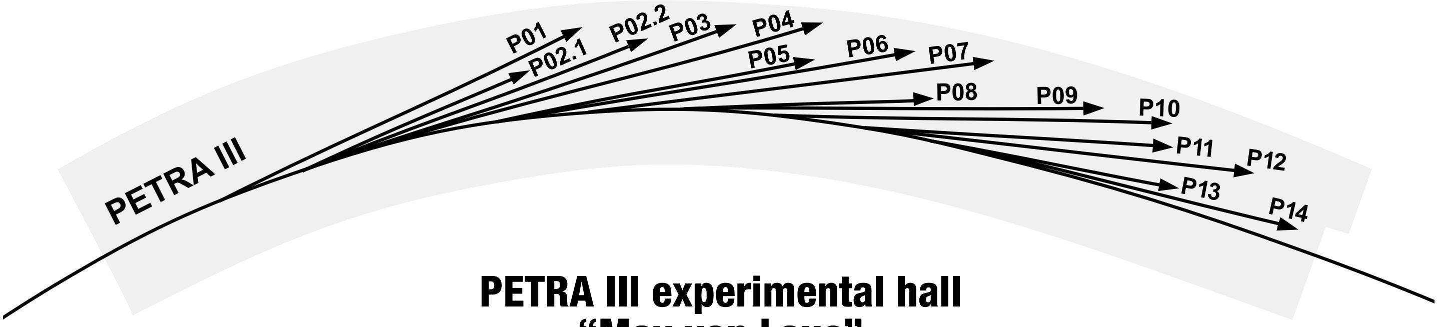

**PETRA III experimental hall
“Max von Laue”**

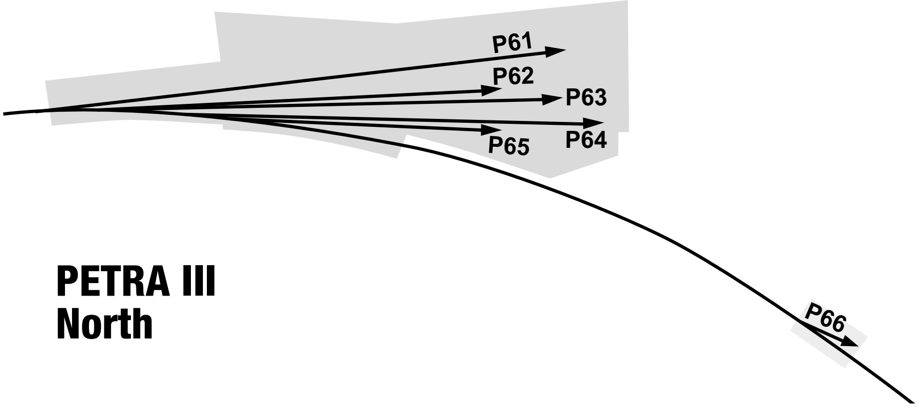

**PETRA III
North**

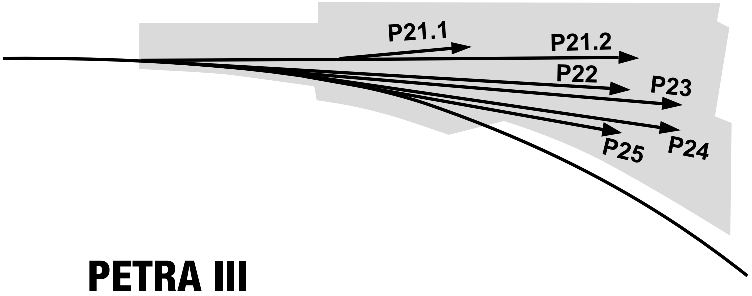

**PETRA III
East**

PETRA III beamlines

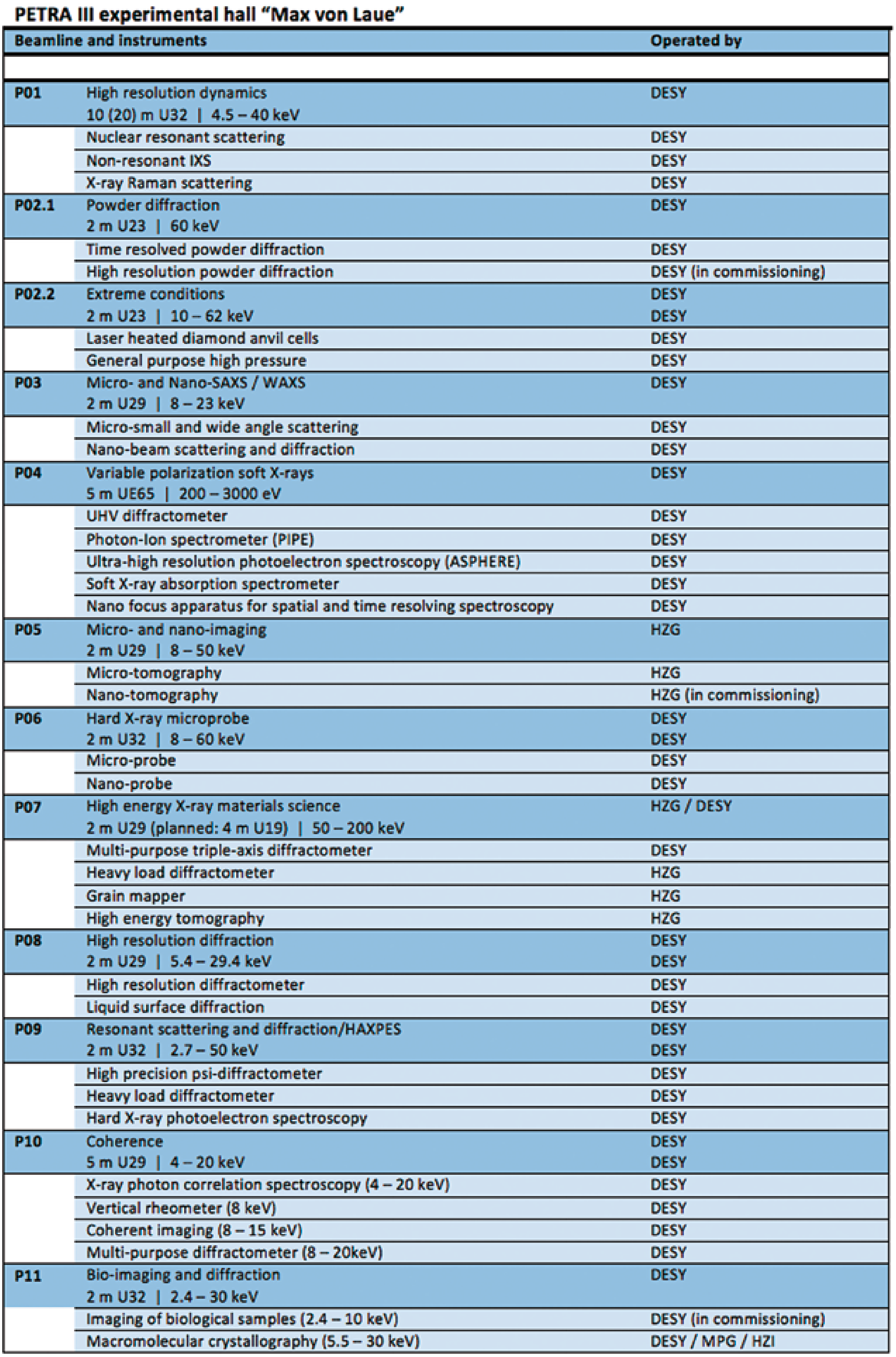

PETRA III experimental hall "Max von Laue"

Beamline and instruments		Operated by
P01	High resolution dynamics 10 (20) m U32 | 4.5 – 40 keV	DESY
	Nuclear resonant scattering	DESY
	Non-resonant IXS	DESY
	X-ray Raman scattering	DESY
P02.1	Powder diffraction 2 m U23 | 60 keV	DESY
	Time resolved powder diffraction	DESY
	High resolution powder diffraction	DESY (in commissioning)
P02.2	Extreme conditions 2 m U23 | 10 – 62 keV	DESY DESY
	Laser heated diamond anvil cells	DESY
	General purpose high pressure	DESY
P03	Micro- and Nano-SAXS / WAXS 2 m U29 | 8 – 23 keV	DESY
	Micro-small and wide angle scattering	DESY
	Nano-beam scattering and diffraction	DESY
P04	Variable polarization soft X-rays 5 m UE65 | 200 – 3000 eV	DESY
	UHV diffractometer	DESY
	Photon-Ion spectrometer (PIPE)	DESY
	Ultra-high resolution photoelectron spectroscopy (ASPHERE)	DESY
	Soft X-ray absorption spectrometer	DESY
	Nano focus apparatus for spatial and time resolving spectroscopy	DESY
P05	Micro- and nano-imaging 2 m U29 | 8 – 50 keV	HZG
	Micro-tomography	HZG
	Nano-tomography	HZG (in commissioning)
P06	Hard X-ray microprobe 2 m U32 | 8 – 60 keV	DESY DESY
	Micro-probe	DESY
	Nano-probe	DESY
P07	High energy X-ray materials science 2 m U29 (planned: 4 m U19) | 50 – 200 keV	HZG / DESY
	Multi-purpose triple-axis diffractometer	DESY
	Heavy load diffractometer	HZG
	Grain mapper	HZG
	High energy tomography	HZG
P08	High resolution diffraction 2 m U29 | 5.4 – 29.4 keV	DESY DESY
	High resolution diffractometer	DESY
	Liquid surface diffraction	DESY
P09	Resonant scattering and diffraction/HAXPES 2 m U32 | 2.7 – 50 keV	DESY DESY
	High precision psi-diffractometer	DESY
	Heavy load diffractometer	DESY
	Hard X-ray photoelectron spectroscopy	DESY
P10	Coherence 5 m U29 | 4 – 20 keV	DESY DESY
	X-ray photon correlation spectroscopy (4 – 20 keV)	DESY
	Vertical rheometer (8 keV)	DESY
	Coherent imaging (8 – 15 keV)	DESY
	Multi-purpose diffractometer (8 – 20keV)	DESY
P11	Bio-imaging and diffraction 2 m U32 | 2.4 – 30 keV	DESY
	Imaging of biological samples (2.4 – 10 keV)	DESY (in commissioning)
	Macromolecular crystallography (5.5 – 30 keV)	DESY / MPG / HZI

Beamline and instruments		Operated by
P12	Bio SAXS 2 m U29 | 4 – 20 keV	EMBL
	Solution small-angle scattering	EMBL
P13	Macromolecular crystallography I 2 m U29 | 4 – 16 keV	EMBL
	Macromolecular crystallography	EMBL
P14	Macromolecular crystallography II 2 m U29 | 10 keV	EMBL
	Macromolecular crystallography	EMBL

PETRA III Extensions East and North

Beamline and instruments		Operated by
P21.1	Swedish high-energy materials science beamline (side branch) 2 m U29 | 50, 80, 100 keV	Swedish institution / DESY
	Broad band diffraction	Swedish institution / DESY (operation planned 2016/17)
P21.2	Swedish high-energy materials science beamline 4 m IVU21 | 40 – 150 keV	Swedish institution / DESY
	Diffraction and imaging	Swedish institution / DESY (operation planned 2016/17)
P22	Nano X-ray spectroscopy (India-motivated beamline) 2 m U33 | 2.4 – 15 keV	DESY
	Hard X-ray photoelectron spectroscopy (relocated from P09)	DESY (operation planned 2016)
	2nd hutch instrument tbd	not yet funded
P23	Russian-German nano-diffraction beamline 2 m U32 | 5 – 35 keV	DESY
	Nano-XRD, in situ and complex environments	DESY (operation planned 2016)
	2nd hutch instrument tbd	not yet funded
P24	Chemical crystallography 2 m U29 | 8, 15 – 45 keV	DESY
	Single crystal diffraction in complex sample environments	DESY (operation planned 2016)
	Small molecule crystallography	DESY (operation planned 2016)
P25	Education & testing	not yet funded
P61	High-energy materials science 40 m damping wiggler | 50 – 200 keV / pink beam	DESY
	High-energy engineering materials science	HZG
	Extreme conditions in the large volume press	DESY (operation planned 2016/17)
P62	Small-angle X-ray scattering (tentative)	DESY (not yet funded)
P63	Instrument tbd	DESY (not yet funded)
P64	Time-resolved X-ray absorption 2 m U32 | 4 – 44 keV	DESY
	Time-resolved *in situ* XAFS, QEXAFS, bioXAFS	DESY (operation planned 2015)
P65	X-ray absorption Short U32 | 4 – 44 keV	DESY
	Ex situ and *in situ* XAFS of bulk samples	DESY (operation planned 2015)
P66	Superlumi Bending magnet | 4 – 40 eV	DESY
	Time-resolved luminescence spectroscopy	DESY (operation planned 2016)

We would like to acknowledge all contributions to instrument development and operation provided within the framework of BMBF-Verbundforschung, the Röntgen-Ångström-Cluster (RAC), the Ioffe-Röntgen-Institute (IRI), and the Ruprecht-Haensel-Laboratory (University of Kiel).

Committees 2014.

Photon Science Committee PSC — advises the DESY Photon Science management

Markus Drescher (chair)	Universität Hamburg, DE
Melissa A. Denecke (vice chair)	University of Manchester, UK
Christian David	Paul Scherrer Institute, Villigen, CH
Stefan Eisebitt	Technische Universität, Berlin, DE
Gwyndaf Evans	Diamond Lights Source Ltd., Oxford, GB
Maya Kiskinova	Sincrotrone Trieste, IT
Franz Pfeiffer	Technische Universität München, DE
Henning Friis Poulsen	DTU Fysik, Lyngby, DK
Harald Reichert	ESRF, Grenoble, FR
Anthony J. Ryan, OBE	University of Sheffield, GB
Bernd Schmitt	Paul Scherrer Institute, Villigen, CH
Andrea Somogyi	Synchrotron Soleil, FR
Julian Stangl	Johannes Kepler Universität Linz, AT
Lucia Incoccia-Hermes (PSC secretary)	DESY, Hamburg, DE

PSC members from the right:
Julian Stangl, Bernd Schmitt, Christian David.
In the middle: Stefan Eisebitt, Maya Kiskinova,
Gwyndaf Evans, Henning Friis Poulsen.
On the left: Harald Reichert, Markus Drescher (chair),
Melissa A. Denecke (vice chair), Andrea Somogyi.
Here absent: Anthony J. Ryan, Franz Pfeiffer

Laser Advisory Committee LAC — shared between DESY and the European XFEL

Uwe Morgner (Chair)	Universität Hannover, DE
Giulio Cerullo	Politecnico di Milano, IT
Mike Dunne	SLAC, Menlo Park, CA, US
Patrick Georges	CNRS, FR
Alfred Leitenstorfer	Universität Konstanz, DE
Robert Schoenlein	LBNL, US
William E. White	SLAC, Menlo Park, CA, US
Andreas Galler (European XFEL LAC secretary)	European XFEL GmbH, Hamburg, DE
Oliver D. Mücke (DESY-CFEL LAC secretary)	DESY, Hamburg, DE

DESY Photon Science User Committee DPS-UC — represents the user community

Peter Müller-Buschbaum (Chair)	Technische Universität München, DE
Thomas Möller	Technische Universität Berlin, DE
Julian Stangl	Johannes Kepler Universität, Linz, AT
Gregor Witte	Ludwig-Maximilians-Universität, München, DE
Joachim Wollschläger	Universität Osnabrück, DE

Komitee Forschung mit Synchrotronstrahlung KFS
representative body of the German synchrotron radiation and FEL user community

Stefan Eisebitt (chair)	Universität Hamburg, DE
Bridget Murphy (vice chair)	Universität Kiel, DE
Ronald Frahm	Universität Wuppertal, DE
Jan-Dierk Grunwaldt	KIT Karlsruhe, DE
Christian Gutt	Universität Siegen, DE
Birgit Kanngießer	Technische Universität Berlin, DE
Lutz Kipp	Universität Kiel, DE
Tim Salditt	Universität Göttingen, DE
Hermann Schindelein	Universität Würzburg, DE
Andreas Schreyer	Helmholtz-Zentrum Geesthacht, DE
Peter Albers	AQura GmbH, DE

Project Review Panels 2014.

PRP1: VUV- and Soft X-Ray

Lucia Aballe	CELLS-ALBA Barcelona, ES
Stephan Fritzsche	Helmholtz Institut Jena, DE
Michael Meyer	European XFEL GmbH, Hamburg, DE
Luc Patthey	PSI, Villigen, CH
Jens Viefhaus (PRP Secretary)	DESY, Hamburg, DE

PRP2: X-Ray Spectroscopy

Ralph Claessen	Julius-Maximilians-Universität Würzburg, DE
Melissa A. Denecke	University of Manchester, GB
Joerg Evers	MPI für Kernphysik, Heidelberg, DE
Raphael Hermann	FZ Jülich, DE
Håkan Rensmo	Uppsala University, SE
Sebastian Schoeder	Synchrotron Soleil, FR
Max Wilke	GFZ Potsdam, DE
Wolfgang Drube (PRP secretary)	DESY, Hamburg, DE

PRP3: X-Ray Diffraction/Scattering – Hard Condensed Matter

Denis Andrault	Université Clermont-Ferrand, FR
Johan Chang	EPFL, Villigen, CH
Robert Dinnebier	MPI für Festkörperforschung, Stuttgart, DE
Leonid Dubrovinsky	Bayrisches Geoinstitut, Bayreuth, DE
Lars Ehm	Stony Brook University, Stony Brook, NY, US
Jochen Geck	IFW Dresden, DE
Hermann Gies	Ruhr-Universität Bochum, DE
Lars Gustafson	Lund University, SE
Helmut Klein	GZG Universität Göttingen, DE
Ulrich Schwarz	MPI für Chem. Phys. fester Stoffe, Dresden, DE
Sergio Speziale	GFZ Potsdam, DE
Helen Walker	ISIS, Didcot, GB
Hanns-Peter Liermann (PRP secretary)	DESY, Hamburg, DE

PRP4: X-Ray Diffraction/Scattering – Engineering Materials Science

Jens Gibmeier	Karlsruher Institut für Technologie KIT, DE
Jozef Keckes	Montanuniversität Leoben, AT
Svea Mayer	Montanuniversität Leoben, AT
Walter Reimers	Technische Universität Berlin, DE
Guillermo Requena	Technische Universität Wien, AT
Gerold Schneider	Technische Universität Hamburg-Harburg, DE
Bernd Schönfeld	ETH Zürich, CH
Carsten Siemers	Technische Universität Braunschweig, DE
Axel Steuwer	MAX IV Laboratory, Lund, SE
Martin Müller (PRP secretary)	HZG, Geesthacht, DE
Ralf Röhlsberger (DESY representative)	DESY, Hamburg, DE

PRP5: X-Ray Diffraction/Scattering – Soft Materials (Bulk)

Francisco José Baltá-Calleja	CSIC, Madrid, ES
Wim de Jeu	RWTH Aachen, DE
Uwe Klemradt	RWTH Aachen, DE
Yongfeng Men	Changchun Inst. of Applied Chemistry, CN
Christine M. Papadakis	Technische Universität München, DE
Michael Paulus	Technische Universität Dortmund, DE
Joachim Wagner	Universität Rostock, DE
Rainer Gehrke (PRP secretary)	DESY, Hamburg, DE

PRP6: X-Ray Diffraction/Scattering – Soft Materials (Surfaces and Interfaces)

Gerald Brezesinski	MPI Kolloid- u. Grenzflächenforsch., Potsdam, DE
Moshe Deutsch	Bar-Ilan University, Ramat Gan, IL
Tiberio A. Ezquerra	CSIC, Madrid, ES
Thomas Gutsmann	Leibniz-Zentrum Borstel, DE
Hyunjung Kim	Sogang University, Seoul, KR
Mark Schlossmann	University of Illinois, Chicago IL, US
Frank Schreiber	Universität Tübingen, DE
Oliver Seeck (PRP Secretary)	DESY, Hamburg, DE

PRP7: Imaging

Oliver Bunk	PSI, Villigen, CH
Peter Cloetens	ESRF, Grenoble, FR
Koen Janssens	University Antwerpen, BE
Hendrik Küpper	Universität Konstanz, DE
Bert Müller	University Basel, CH
Michael Nickel	Friedrich-Schiller-Universität Jena, DE
Stefan Vogt	APS, Argonne, US
Gerald Falkenberg (PRP secretary)	DESY, Hamburg, DE
Felix Beckmann (HZG representative)	HZG, Geesthacht, DE

PRP8: Methods and Instrumentation

Rolf Follath	PSI, Villigen, CH
Tim Salditt	Universität Göttingen, DE
Anatoly Snigirev	ESRF, Grenoble, FR
Horst Schulte-Schrepping (PRP secretary)	DESY, Hamburg, DE

PEC / PRP9: Bio-crystallography at P11 (coordinated by EMBL Hamburg)

Pau Bernadó	CBS/CNRS, Montpellier, FR
Kristina Djinovic-Carugo	Universität Wien, AT
Gwyndaf Evans	Diamond Light Source, GB
Bob Fischetti	Argonne National Laboratory, USA
Mariusz Jaskolski	University of Poznan, PL
Poul Nissen (Chair)	University of Aarhus, DK
Javier Pérez	Synchrotron SOLEIL, FR
Savvas Savvides	Ghent University, BE
Joel Sussman	Weizmann Institute of Sciences, Rehovot, IL
Maria Vanoni	University of Milano, IT
Bente Vestergaard	University of Copenhagen, DK
Hermann Franz (DESY observer)	DESY, Hamburg, DE

PRP11: Soft X-Ray – FEL Experiments (FLASH)

Katharina Al-Shamery	Universität Oldenburg, DE
Michael Bonitz	Universität Kiel, DE
Christoph Bostedt	SLAC, Menlo Park, CA, US
Chris Jacobsen	APS, Argonne, IL, US
Steven Johnson	ETH Zürich, CH
Maya Kiskinova	Sincrotrone Trieste, IT
Jonathan Marangos	Imperial College London, GB
Ronald Redmer	Universität Rostock, DE
Jan-Michael Rost	MPI für Physik komplexer Systeme, Dresden, DE
Robert W. Schoenlein	Lawrence Berkeley Nat. Lab., US
Bernd Sonntag	Universität Hamburg, DE
Urs Staub	PSI, Villigen, CH
Kiyoshi Ueda	Tohoku University, Sendai, JP
Marc Vrakking	MBI, Berlin, DE
Martin Weinelt	FU Berlin, DE
Gwyn P. Williams	Jefferson Laboratory, Newport News, VA, US
Josef Feldhaus (PRP secretary)	DESY, Hamburg, DE

Photographs and Graphics:
Rainer Becker Architekten, Berlin
Lars Berg, Hamburg
Daniel Bockwoldt / dpa
Gesine Born, Berlin
CFEL
Class 5 Photonics
CUI Hamburg
DESY
EMBL
European XFEL
hammeskrause architekten, Stuttgart
HZG
Thomas Kleinteich, Universität Kiel
MPG
EMBL Photolab / Hugo Neves
Reimo Schaaf, Hamburg
Universität Hamburg

Figures of the Research Highlights were reproduced by permission from authors or journals.

Acknowledgement

We would like to thank all authors and all those who helped in the realization of this annual report.

Imprint

Publishing and Contact:
Deutsches Elektronen-Synchrotron DESY
A Research Centre of the Helmholtz Association

Hamburg location:
Notkestr. 85, 22607 Hamburg, Germany
Tel.: +49 40 8998-0, Fax: +49 40 8998-3282
desyinfo@desy.de

Zeuthen location:
Platanenallee 6, 15738 Zeuthen, Germany
Tel.: +49 33762 7-70, Fax: +49 33762 7-7413
desyinfo.zeuthen@desy.de

Photon Science at DESY
Tel.: +49 40 8998-2304, Fax: +49 40 8998-4475
photon-science@desy.de
photon-science.desy.de

www.desy.de

ISBN 978-3-935702-93-5

Online version:
photon-science.desy.de/annual_report

Realization:
Wiebke Laasch, Ralf Röhlsberger, Daniela Unger

Editing:
Lars Bocklage, Rainer Gehrke, Lucia Incoccia-Hermes,
Wiebke Laasch, Tim Laarmann, Wolfgang Morgenroth,
Elke Plönjes, Ralf Röhlsberger, Daniela Unger, Jens Viefhaus,
Hans-Christian Wille, Martin von Zimmermann

Layout: Diana Schröder, bunteaussicht mediengestaltung,
Hamburg

Printing: EHS Druck GmbH, Schenefeld

Copy deadline: December 2014

HELMHOLTZ
ASSOCIATION

Deutsches Elektronen-Synchrotron
A Research Centre of the Helmholtz Association

The Helmholtz Association is a community of 18 scientific-technical and biological-medical research centres. These centres have been commissioned with pursuing long-term research goals on behalf of the state and society. The Association strives to gain insights and knowledge so that it can help to preserve and improve the foundations of human life. It does this by identifying and working on the grand challenges faced by society, science and industry. Helmholtz Centres perform top-class research in strategic programmes in six core fields: Energy, Earth and Environment, Health, Key Technologies, Structure of Matter, Aeronautics, Space and Transport.

www.helmholtz.de